Magnetic and Dielectric Investigations in Rare Earth Iron Garnet Ceramics: Unravelling Multifunctional Properties

A Thesis Submitted

By

Shalini Verma

Roll Number: 206121027

In Partial Fulfillment of the Requirements for the Award of the Degree of

Doctor of Philosophy in Physics

Department of Physics

Indian Institute of Technology Guwahati

Guwahati-781039, India

April, 2025

TH-3713_206121027


भारतीय प्रौद्योगिकी संस्थान गुवाहाटी
Indian Institute of Technology Guwahati

भारतीय प्रौद्योगिकी संस्थान गुवाहाटी • Indian Institute of Technology Guwahati •

Magnetic and Dielectric Investigations in Rare Earth Iron Garnet Ceramics: Unravelling Multifunctional Properties

A Thesis Submitted

By

Shalini Verma

Roll Number: 206121027

In Partial Fulfillment of the Requirements for the Award of the Degree of

Doctor of Philosophy in Physics

Department of Physics

Indian Institute of Technology Guwahati

Guwahati-781039, India

April, 2025

TH-3713_206121027


भारतीय प्रौद्योगिकी संस्थान गुवाहाटी
Indian Institute of Technology Guwahati

Statement

The work contained in the thesis entitled “**Magnetic and Dielectric Investigations in Rare Earth Iron Garnet Ceramics: Unravelling Multifunctional Properties**” has been carried out by me under the supervision of Prof. S. Ravi, Department of Physics, Indian Institute of Technology Guwahati. This work has not been submitted elsewhere for the award of any degree.

April, 2025

Shalini Verma
Department of Physics
Indian Institute of Technology Guwahati
Guwahati – 781039, India

Certificate

It is certified that the work contained in the thesis entitled **"Magnetic and Dielectric Investigations in Rare Earth Iron Garnet Ceramics: Unravelling Multifunctional Properties"** by Ms. Shalini Verma, a Ph.D. student of the Department of Physics, Indian Institute of Technology Guwahati for the award of the degree of *Doctor of Philosophy* has been carried out under my supervision. This work has not been submitted elsewhere for the award of any degree.

April, 2025

Prof. S. Ravi
Professor, Department of Physics
Indian Institute of Technology Guwahati
Guwahati – 781 039, India

Indian Institute of Technology Guwahati

This thesis is dedicated to my family

Acknowledgements

Life is enriched by experiences and I feel incredibly fortunate to have spent five unforgettable years at IIT Guwahati during my Ph.D. journey. I take this opportunity to sincerely thank all those who contributed to my growth, both personally and professionally during this transformative phase of my life.

First and foremost, I would like to express my gratitude to Prof. S. Ravi for his supervision and providing me an opportunity to conduct my Ph.D. work in a very well-equipped laboratory. Additionally, his invaluable insights into various technical concepts and his extensive experience in this field helped me to resolve challenges raised during the experiments. Apart from research, his calm nature, gentle behaviour and continuous support not only inspired me but also created a positive and motivating environment that helped me to stay focused and driven throughout the process.

I am very much obliged to my doctoral committee (DC) members i.e., Prof. D. Pamu (Chairperson), Prof. S. Thota, and Prof. G. Pugazhenthi for their insightful suggestions and invaluable encouragement which greatly contributed to enhancing my thesis work in multiple perspectives.

I am deeply grateful to CEFIPRA for awarding me the Raman-Charpak Fellowship which provided me with the invaluable opportunity to conduct research at the CRISMAT Laboratory in Caen, France for a duration of six months. I am sincerely thankful to Dr. Wilfrid Prellier for hosting me at the CRISMAT lab, an experience that offered me a unique global perspective. This opportunity has been not only advanced my professional growth but also enriched my personal experiences.

I am highly thankful to former and present Head of the Department (HoD) of Physics i.e., Prof. S. Ghosh, Prof. A. Perumal and Prof. B. R. Boruah for their cooperation in my entire Ph.D. tenure. I am also grateful to all the faculty and staff members of the Department of Physics for their support at different stages.

I would also like to acknowledge Dr. Dolly Gogoi and Dr. Sidananda Sarma for allowing me to assist FESEM machine as an operator for about 2 years. I am also thankful to the present Head of the Central Instrumentation Facility (CIF), Prof. G. Kumar and the former Head of CIF, Prof. G. Pugazhenthi for their support. I extend my gratitude to the scientific officers and technical staff of CIF, IIT Guwahati for their invaluable assistance in facilitating my experiments using advanced instruments throughout my Ph.D. period.

I would like to extend my heartfelt thanks to all my labmates for creating such a collaborative and inspiring environment. I am grateful to my seniors and juniors including Dr. Junmoni Barman, Dr. Pratap Behera, Dr. Aakansha, Dr. Ritupan Borah, Dr. K. Pushpanjali Patra, Dr. Rimpi Chakravarty, Debabrata, Nibedita, Deepak, Bivek and Shubhajit for their support and encouragement. I would also like to give special thanks to Dr. Ritupan Borah for his consistence advice and discussions and to Nibedita, with whom I have shared a special bond and supporting each other through all the highs and lows.

I feel truly fortunate to be surrounded by wonderful friends and seniors, including Fatima, Rakshanda, Manish, Rahul, Harshita, Debtanay, Debu bhaiya, Subham, Shilpa, Subingya, Camelia, Likun for their invaluable help and companionship. I will always cherish the memories we've created together, from our unforgettable trips and other fun games.

I am deeply grateful to my family and relatives for their constant love, blessings, care, and constant support throughout my life.

Lastly, I am highly thankful to the Ministry of Human Resource Development (MHRD) and the Indian Institute of Technology Guwahati for their financial support throughout my Ph.D. tenure. I also sincerely acknowledge the Department of Science and Technology (DST), New Delhi for providing financial assistance for various experimental facilities.

Shalini Verma

IIT Guwahati

Abstract

Ferrites or magnetic ceramics are advanced materials with tailored magnetic and dielectric properties and they are widely used in transformers, telecommunication, sensors and data or energy storage devices. Their unique composition and versatility drive ongoing research for enhanced performance. The complexity in ferrites arises from the interplay of magnetic phenomena and ceramic microstructures. Their process of synthesis, crystal structure, magnetic and physical properties intricately linked with each other. Ferrites are particularly appealing for applications in microwave and energy storage devices due to their exceptional magnetic and dielectric properties.

Ferrites were introduced by Louis Néel in 1948 and they are composed of ferric oxide $(\alpha - Fe_2O_3)$. Ferrites are magnetic ceramics that are broadly classified based on their crystal structures into spinels, garnets and hexaferrites. Spinel ferrites, with a general formula of MFe_2O_4 (where M is a divalent metal ion like Zn, Mn, or Ni) are widely used in high-frequency applications due to their low electrical conductivity and high magnetic permeability. Garnet ferrites are known for their superior magnetic, dielectric and optical properties making them suitable for microwave devices and magneto-optical applications. Hexaferrites, such as barium ferrite $BaFe_{12}O_{19}$ and strontium ferrite $SrFe_{12}O_{19}$ are hexagonal in structure and exhibit high coercivity making them ideal for permanent magnets and data storage.

We will be focusing on Rare earth iron garnet (RIG) due to high resistivity, low resonance line width, low dielectric loss and good thermal stability as they are annealed at high sintering temperature of $1400°C$ to avoid impurities like Fe_2O_3 and $RFeO_3$. RIG posses magnetic compensation, magnetization reversal, spin reorientation, magneto-electric, magneto-dielectric, and relaxor-ferroelectric type behaviours. Based on the literature review and current understanding, exploring the magnetic and dielectric properties in depth offers significant potential to enhance the functional characteristics of RIG materials. Therefore, we have selected Gadolinium, Samarium and Dysprosium iron garnets and high entropy garnet ceramics for a detailed investigation.

All Gd, Sm and Dy iron garnets show ferrimagnetic ordering as the magnetic moment of garnets originates from the antiferromagnetic interaction between Fe^{3+} ions at the octahedral and tetrahedral sites and the resultant moments are antiferromagnetically coupled with the magnetic moment of rare-earth ions at the dodecahedral site. Their ferrimagnetic transition temperature is around $550K$ which is not affected much by substitution at rare earth site. Interestingly, all three of them show spin reorientation transition between $20K$ to $60K$. Additionally, Gd and Dy iron garnets undergoes magnetic compensation around $298K$ and $225K$, respectively. Other than Gd and Dy iron garnets, $Ho_3Fe_5O_{12}, Tb_3Fe_5O_{12}, Er_3Fe_5O_{12}, Yb_3Fe_5O_{12}$ also exhibit magnetic compensation. Further, substitution of Bi in $Ho_3Fe_5O_{12}$ and $Tb_3Fe_5O_{12}$, Sm in $Gd_3Fe_5O_{12}$ has introduced magnetization reversal below their respective magnetic compensation temperature. Apart from magnetic transitions, RIGs also hold excellent dielectric characteristics as well. They are known for having high dielectric constant along with low dielectric loss. Some of them also inhibits magneto-electric or magneto-dielectric coupling. In 2015, Rost has introduced high-entropy oxides which are made up of five or more elements in nearly equal amounts within a single solid solution. High-entropy oxide ceramics stand out from traditional materials by offering a range of functional properties including a high dielectric constant, low thermal conductivity, excellent electrocatalytic performance and robust mechanical strength. Hence, this thesis includes magnetic, dielectric and magneto-dielectric investigations of GdIG, SmIG, DyIG and high entropy garnets.

The chosen garnet series for the above-mentioned analysis is as follows:

1. $(Gd_{1-x}Ho_x)_3Fe_5O_{12}$ ($x = 0.0$ to 1.0)
2. $(Gd_{1-x}Nd_x)_3Fe_5O_{12}$ ($x = 0.0$ to 0.4)
3. $(Sm_{1-x}Ho_x)_3Fe_5O_{12}$ ($x = 0.0$ to 1.0)
4. $(Dy_{1-x}Ho_x)_3Fe_5O_{12}$ ($x = 0.0$ to 1.0)
5. High entropy garnet ceramics i.e., $(Gd_{0.2}Y_{0.2}Nd_{0.2}Dy_{0.2}R_{0.2})_3Fe_5O_{12}$ ($R = Er, Sm$ and Pr)

The crystalline behaviour and the purity of phase are studied with X-Ray diffraction (XRD) patterns. Surface morphology and detailing of microstructure were investigated with field emission scanning electron microscope (FESEM) and transmission electron microscope (TEM), respectively. Further, possible active phonons modes were detected with Raman spectroscopy and the electronic states of the individual cations were determined by X-Ray photoelectron spectroscopy (XPS). Magnetic measurements were carried out with Vibrating sample magnetometer (VSM) connected with high temperature oven and physical property measurement system (PPMS) equipped with Quantum design Dynacool cryostat . The dielectric measurements were extracted from LCR meter externally connected with a high-temperature furnace.

This thesis contains six chapters:

1. **Introduction**
2. **Synthesis and Experimental Techniques**
3. **Magneto-dielectric studies in Ho and Nd substituted Gadolinium iron garnet**
4. **Magnetic and dielectric properties in Ho substituted Samarium and Dysprosium iron garnet**
5. **Magnetic and dielectric investigations in $(Gd_{0.2}Y_{0.2}Nd_{0.2}Dy_{0.2}R_{0.2})_3Fe_5O_{12}$ $(R = Er, Sm, \mathrm{Pr})$ high entropy garnet**
6. **Conclusion**

Chapter 1 deals with the origin of RIGs and the literature review of their technological applicability in various fields of research. The crystal structure of RIG and the crystal field theory are discussed. Thereafter, different types of magnetic interactions possible in any ferrite material are demonstrated. Further, different types of magnetic anisotropy affecting the magnetic interactions are presented in connection with magnetic compensation and magnetization reversal phenomena. The theory behind spin-reorientation phenomenon is shown. A brief discussion on dielectric properties including complex electric impedance, complex dielectric constant, and ac conductivity are provided. A review of previous studies on GdIG, SmIG, DyIG, and high-entropy garnet ceramics focusing on their structural, magnetic, and dielectric properties is conducted. Additionally, the primary motivations for the present thesis work is briefly outlined.

Chapter 2 covers different experimental techniques used in synthesizing the sample and characterizing their structural, magnetic and dielectric properties. The solid-state reaction route with all the technical details starting from weighing to sintering in the furnace are discussed. The working principles of various sophisticated instruments such as the X-ray Diffractometer (XRD) that was used for the phase purity test, and Field Emission Scanning Electron Microscope (FESEM) and Energy Dispersive X-ray (EDX) spectrometer which are utilized for surface morphology and composition analysis. Further, Transmission Electron Microscopy (TEM) was used for studying microstructure and diffraction patterns in related area. Moreover, analysis of different phonon active modes were detected by Raman spectroscopy and the oxidation state of individual elements was extracted from X-ray Photoelectron Spectroscopy (XPS). Both the spectroscopies are discussed one after the other. Finally, the working principles of the Vibrating Sample Magnetometer (VSM), physical property measurement system (PPMS) and dielectric set with LCR meter used to measure magnetic and dielectric properties are discussed.

Chapter 3 focuses on the study of magnetic, dielectric and magneto-dielectric properties on Ho and Nd substituted Gadolinium iron garnet (GdIG).

$(Gd_{1-x}Ho_x)_3Fe_5O_{12}$ $(x = 0.0$ to $1.0)$ (Ho-GdIG) samples were prepared by solid-state reaction method and the phase purity was verified by Rietveld refinement using Fullprof software. The lattice constant decreases from 12.4846 (1) Å to 12.3871 (1) Å as x goes from 0.0 to 1.0. Average grain size is estimated by fitting the frequency of particle size count to log-normal function and it comes out to be 4.88 μm to 2.59 μm for $x = 0.0$ to 1.0 samples. Further, the Raman spectra demonstrate the peaks at the desired wavenumbers, which again confirmed the garnet phase of Ho-GdIG samples. Then, we performed XPS analysis that revealed the $+3$ oxidation state of Gd and Ho. On the other hand, Fe is available in a mixed valance state i.e., $+2$ and $+3$. The bond length between $Fe(a) - Fe(d)$ and the bond angle among $Fe(a) - O - Fe(d)$ get weaker with Ho substitution in GdIG. Consequently, the ferrimagnetic T_c also reduces from 553 K $(x = 0.0)$ to 543 K $(x = 1.0)$. In addition, all the samples of Ho-GdIG series represent magnetic compensation, and the parent sample's compensation temperature is found to be 295 K which is decreased to 145 K for $x = 1.0$ sample. Moreover, the M_s and effective anisotropy constant (K_1) both enhance drastically when the temperature goes from room temperature to 5 K. The anisotropy is raised from 10^3 to 10^6 erg/cc with the temperature reduction. Further, the deviation of Nyquist plots from ideal Debye-type relaxation is claimed because of the formation of depressed semi-circles with their centers not lying on the Z' axis. The ac conductivity remains almost constant for all the concentrations of Ho-GdIG samples that fluctuates the concentration of charge carriers. Based on the fitting of ac conductivity to Jonscher's Power Law, both small and large polaron tunneling models are observed among the charge carriers. Interestingly, Arrhenius plots show deviation around FIM T_c, and that anomaly can be attributed to magneto-electric coupling in Ho-GdIG samples.

Moreover, $(Gd_{1-x}Nd_x)_3Fe_5O_{12}$ ($x = 0.0$ to 0.4) (Nd-GdIG) samples are formed in single phase with no secondary impurity across the temperature range of $80\ K$ to $300\ K$. The lattice constant has increased from 12.4961 Å for $x = 0.0$ to 12.5496 Å for $x = 0.4$ which can be attributed to differences in ionic radii. Similarly, the average grain size is also enhanced from $1.77\ \mu m$ ($x = 0.0$) to $2.72\ \mu m$ ($x = 0.4$) sample as Nd has larger ionic radii than Gd. Additionally, the phase purity is supported by the observed Raman active phonons which are in good agreement with the predicted ones. A spin reorientation transition is observed between $10\ K$ and $60\ K$, while magnetic compensation temperatures for $x = 0.0$ to 0.2 shifted from $291\ K$ to $200\ K$ as the Nd concentration increased. The room-temperature saturation magnetization exhibited a significant increase from $0.71\ emu/g$ to $10.76\ emu/g$ with higher x values. Additionally, the dielectric constant shows a temperature-dependent increase which is independent of the applied magnetic field $(0 - 3\ T)$ and it is attributed to thermally activated charge carriers. The dielectric loss curves are found to be aligned with magnetic transitions indicating a magneto-dielectric coupling in these materials. This garnet series demonstrates remarkable advantages including high thermal stability, tunable magnetic properties, and strong magneto-dielectric coupling making it a promising candidate for advanced multifunctional applications.

Chapter 4 includes the studies of magnetization reversal and dielectric phenomenon in Ho substituted Samarium iron garnet (SmIG) samples and magneto-caloric effect investigation in Ho substituted Dysprosium iron garnet (DyIG) samples.

The polycrystalline $(Sm_{1-x}Ho_x)_3Fe_5O_{12}$ ($x = 0.0$ to 1.0) (Ho-SmIG) samples were synthesized by solid-state reaction method by sintering the pellets at $1400°C$ for 8 hours. The phase purity examination is conducted with the Rietveld refinement technique using a cubic crystal structure and $Ia\bar{3}d$ space group. The obtained lattice parameters are found to be reduced with Ho substitution from 12.5375(1)Å ($x = 0.0$) to 12.3936(1)Å ($x = 1.0$) due to the smaller ionic radii of Ho^{3+} (1.015Å) as compared to Sm^{3+}(1.079Å) ions. The average grain size follows the trend from $7.47\mu m$ to $8.56\mu m$ for $x = 0.0$ to 1.0 samples. Further, we have carried out Raman spectra analysis and found that the Ho^{3+} ions are successfully substituted at Sm^{3+} ions site. SmIG exhibits FIM ordering with a T_c around $561\ K$ it is reduced to $541\ K$ for $x = 1.0$ sample. This reduction in T_c can be attributed to the lowering of superexchange interaction between $Fe(a) - O - Fe(d)$ networks. Apart from this, all the samples of Ho-SmIG series represent spin reorientation transition and the transition temperature varies from 65 K $(x = 0.0)$ to 20 K $(x = 1.0)$. In addition to this, the $x = 0.0$ and 0.2 samples undergo an additional magnetic transition, below which the magnetic moment reduces sharply. This transition disappears for $x \geq 0.4$ samples, as it shifts to lower temperatures and falls outside the measured temperature range for these samples. Interestingly, $x = 0.4$ sample exhibits magnetization reversal under FC condition. This reversal can be attributed to the strong magnetocrystalline anisotropy introduced by Ho^{3+} ions in SmIG. The FC magnetization at $\pm 500\, Oe$ magnetic field forms a mirror reflection, leading us to conclude that negative magnetization is an inherent property of the $x = 0.4$ sample in the Ho-SmIG series. Furthermore, both the $x = 0.6$ and 0.8 samples exhibit two magnetic compensation temperatures, after which their magnetic moments become entirely positive. In contrast, the $x = 1.0$ sample shows only one magnetic compensation temperature. The saturation magnetization (M_s) is found to be reduced from 19.83 emu/g $(x = 0.0)$ to 6.98 emu/g $(x = 1.0)$. The decrease in M_s value can be explained in terms of the AFM alignment of Ho^{3+} ions to the net magnetic moment of Fe^{3+} ions. The complex impedance spectra were analyzed using Nyquist plots, revealing that both grains and grain boundaries contribute to the relaxation dynamics. The asymmetric or depressed nature of the Nyquist plots indicates a deviation from ideal Debye-type relaxation. Moreover, the order of dielectric constant at 100 Hz frequency has increased from 10^4 to 10^6 with $x = 0.0$ to 1.0 samples which makes this garnet series well suited for microwave device applications.

The $(Dy_{1-x}Ho_x)_3Fe_5O_{12}$ $(x = 0.0$ to $1.0)$ (Ho-DyIG) samples were synthesized by conventional solid-state reaction route and the final sintering was held at 1200°C for 24 hours. All the samples are formed in single garnet phase and have cubic structure and $Ia\bar{3}d$ space group. The lattice constant is estimated as 12.4181 Å for $x = 0.0$ sample and it is reduced to 12.3858 Å for $x = 1.0$ sample. The smaller ionic radii of Ho^{3+}(1.015Å) ions compared to Dy^{3+} (1.052Å) is responsible for the decrement in lattice constant. Further, the average crystallite size is evaluated from Debye-Scherrer's relation and lies between $90 - 270\ nm$ for all the samples. The morphology of the samples is highly compact with low porosity and the average grain size varies from $0.87 \pm 0.03 \mu m$ to $1.13 \pm 0.09 \mu m$ for $x = 0.0$ to 1.0 sample. The electronic states of all the elements were determined from XPS analysis. The ferrimagnetic ordering of Ho-DyIG samples gets converted to paramagnetic at a T_c 555 K ($x = 0.0$) to 545 K ($x = 1.0$). The distortion of $Fe(a) - O - Fe(d)$ bonding reduces the ferrimagnetic T_c. As the temperature decreases further, these samples exhibit magnetic compensation which is explained by the interaction among different sublattices at octahedral, tetrahedral, and dodecahedral sites. Continuing to lower the temperature leads to the Belov transition, which arises due to weakly ordered exchange coupling between rare earth ions and Fe^{3+} ions at the octahedral site magnetic moments. This Belov transition lies in the range of $34 - 44\ K$ for all the samples. Upon decreasing the temperature even more, SRT has been observed to vary from 10 to 18 K for Ho-DyIG samples. We studied the order of the magnetic phase transition and the magnetocaloric effect by recording a series of isothermal magnetization measurements for $x = 0.4$ and 0.8 samples over the temperature range of $10 - 300\ K$. The maximum magnetic entropy change ($-\Delta S_M$) increased from 3.92 to 4.30 J/kgK for the $x = 0.4$ and 0.8 samples at a $5T$ magnetic field. The peaks in $-\Delta S_M$ are observed near the Belov transition temperature. The relative cooling power was calculated to be 364.6 J/kg and 313.0 J/kg at $5T$ for the $x = 0.4$ and 0.8 samples, respectively, indicating the material's potential for magnetic refrigeration applications. The positive slope of the Arrott plots (M^2 vs H/M) confirms the second-order ferrimagnetic-paramagnetic transition in these systems.

Chapter 5 involves the study of magnetic, impedance and magneto-dielectric characteristics of $(Gd_{0.2}Y_{0.2}Nd_{0.2}Dy_{0.2}R_{0.2})_3Fe_5O_{12}$ ($R = Er, Sm$ and Pr) high entropy garnet ceramics.

The synthesis of $(Gd_{0.2}Y_{0.2}Nd_{0.2}Dy_{0.2}R_{0.2})_3Fe_5O_{12}$ ($R = Er, Sm$ and Pr) (GYNDR) high entropy garnet ceramic samples were carried out with solid-state reaction route. The samples are formed in single phase with $Ia\bar{3}d$ space group. The XRD patterns reveal that the lattice constant values are 12.4458(2) Å, 12.4834(4) Å and 12.5062(2) Å for GYNDE, GYNDS and GYNDP samples, respectively. These values of lattice constant are consistent with the order of the substituted element's ionic radii, i.e., Er^{3+} (0.86Å) < Sm^{3+} (1.07Å) < Pr^{3+}(1.13Å). Further, the average grain size obtained around 1 μm for all the high entropy samples. This similarity in grain size is attributed to the low doping concentration of the substituent which is insufficient to significantly affect the mobility of the grain boundary. Moreover, the interplanar spacing is evaluated by HRTEM micrographs that comes out to be 0.26 nm, 0.31 nm and 0.29 nm for GYNDE, GYNDS and GYNDP samples, respectively. These values of interplanar spacing correspond to

(420) and (400) planes are comparable to our XRD data. Additionally, the formation of concentric circles in SAED patterns reveals the polycrystalline behavior of the high entropy garnet samples. Then, the Raman active modes are analyzed by fitting them to the Gaussian function and we have observed a red shift in the Raman spectra from GYNDE to GYNDP. From magnetic characteristics, the saturation magnetization is found to be $13.67\ emu/g$ for GYNDE sample whereas, it comes out to nearly $16\ emu/g$ for the rest of the two samples. The variation of saturation magnetization is understood with Dionne's sublattice magnetization model. Since Sm and Pr are lighter elements, their magnetic moments will align parallelly with the net moment of Fe^{3+} ions at octahedral and tetrahedral sites, which increases the net magnetization. In contrast, Er being heavier element has its moment aligned antiparallel to the moment of Fe^{3+} ions, which relatively decreases the overall magnetic moment. Further, the impedance data are analyzed using Nyquist plots which show incomplete semi-circles due to the lack of a relaxation phenomenon at room temperature. This absence of relaxation can be attributed to immobile charge carriers or impurities within the material. We have observed a short semicircle at a higher frequency side which arises due to grains contribution and is followed by a straight line, indicative of the effect of grain boundaries. The Nyquist plot of GYNDS sample is fitted to $(RQ1)Q2$ equivalent circuit and $[(RQ1C)Q2]$ is fitted to GYNDE and GYNDP sample. Moreover, the dielectric constant (ε') is found as highest for GYNDP sample as compared to others. Interestingly, the ε' versus temperature plot shows some anomaly around ferrimagnetic T_c that represents the magneto-electric coupling in these high entropy garnet ceramics. This multiple functionality behavior of these materials makes them useful in microwave devices, sensors, spintronics, energy storage devices, capacitors, etc.

Chapter 6 is devoted to the overall summary of the important findings in all the synthesized series. We have successfully tuned the magnetic and dielectric properties of various rare earth iron garnet systems by substitution at rare earth site or characterizing high entropy garnets. Interestingly, magneto-electric coupling is noticed in the vicinity of ferrimagnetic T_c in Ho-substituted GdIG, Nd substituted GdIG and high entropy garnet systems. On the other hand, negative magnetization is observed in $\mathrm{Sm}_{1.8}Ho_{1.2}Fe_5O_{12}$ sample at $500\ Oe$ magnetic field. Moreover, normal and inverse magnetocaloric effects are identified in Ho substituted DyIG. Impedance spectroscopic studies identify grains and grain boundaries contribution towards the dielectric relaxation of the samples. The pattern

of dielectric constant follows Maxwell-Wagner type relation model. In addition, ac conductivity follows the Jonscher Power Law and reveals the nature of the charge carriers.

भारतीय प्रौद्योगिकी संस्थान गुवाहाटी • Indian Institute of Technology Guwahati •

भारतीय प्रौद्योगिकी संस्थान गुवाहाटी • Indian Institute of Technology Guwahati •

Abbreviations used in this thesis

RIG	Rare earth iron garnet
AFM	Antiferromagnetic
FM	Ferromagnetic
FIM	Ferrimagnetic
DM	Dzyaloshinskii-Moriya
RKKY	Ruderman-Kittel-Kasuya-Yosida
MR	Magnetization Reversal
XRD	X-Ray Diffraction
FESEM	Field Emission Scanning Electron Microscope
TEM	Transmission Electron Microscope
EDX	Energy Dispersive X-Ray
XPS	X-Ray photoelectron microscopy
VSM	Vibrating Sample Magnetometer
PPMS	Physical Properties Measurement System
G	Grain
GB	Grain boundary
HN	Havriliak-Negami
JPL	Jonscher's Power Law
$\boldsymbol{T_c}$	Ferrimagnetic transition temperature
$\boldsymbol{T_{comp}}$	Magnetic compensation temperature
$\boldsymbol{T_{sr}}$	Spin reorientation transition temperature
$\boldsymbol{M_s}$	Saturation magnetization
LAS	Law of Approach to Saturation

TH-3713_206121027

ZFC	Zero Field Cooled
FC	Field cooled
UDR	Universal Dielectric Response
MD	Magneto-dielectric
SRT	Spin reorientation transition
FOPT	First order phase transition
SOPT	Second order phase transition
CPE	Constant phase element

Contents of thesis

TH-3713_206121027

Chapter 3: Magneto-dielectric studies in Ho and Nd substituted Gadolinium iron garnet……………………………………………………………………….………49

Chapter 4: Magnetic and dielectric properties in Ho substituted Samarium and Dysprosium iron garnet………………………………………………...……….…..95

Indian Institute of Technology Guwahati

भारतीय प्रौद्योगिकी संस्थान गुवाहाटी • Indian Institute of Technology Guwahati •

List of Figures

Chapter 1

Chapter 2

Chapter 3

Chapter 4

Chapter 5

List of Tables

Chapter 1

Chapter 3

Chapter 4

Chapter 5

Chapter 1

Introduction

The growing advancements in communication technology are driving an increasing demand for ferrites that exhibit excellent magnetic and dielectric characteristics. In this context, the historical utilization of spinel ferrites was predominantly confined to microwave applications. However, the compelling attribute of low dielectric loss exhibited by garnet materials has sparked a growing interest in their adoption within the broader spectrum of microwave and radio frequency domains. In addition, the tuning of magnetic and dielectric properties makes them useful in various technological applications such as telecommunication, isolators in near and mid-infrared regions [1], dielectric resonator antennas [2], magneto-optical and passive microwave devices [3], tunable filters [4], spin-orbit torque devices [5], magnetic refrigeration [6] etc.

Ferrites are ceramic-like magnetic materials made from iron oxide (Fe_2O_3) or alongwith other transition element oxides with mettalic elements and they are valued for their high magnetic permeability and electrical resistance. Spinel ferrites, with a cubic crystal structure are used in transformers and inductors due to their stability and desirable magnetic properties [7-9]. Garnet ferrites have a more complex cubic structure and are known for their excellent performance in microwave and optical applications, due to their high magnetic anisotropy and low dielectric loss [10,11]. Hexaferrites, characterized by a hexagonal crystal structure exhibit high coercivity making them ideal for permanent magnets used in motors, data storage, and other applications requiring durable magnetic fields.

RIGs are magnetic materials with a cubic crystal structure and they are well-known for their high magnetic anisotropy, low dielectric loss, and wide bandwidth. These properties make garnets highly effective at frequencies in the microwave range, offering minimal energy loss in electromagnetic signal transmission. Additionally, garnets have excellent thermal stability, chemical durability, and low magnetic damping, which contributes to their reliability in high-frequency applications. As a result, garnets are widely used in microwave devices, optical isolators, circulators, and phase shifters, as well as in magneto-optical storage and telecommunications equipment, where efficient and stable signal processing is essential [12-16].

This thesis investigates the magnetic and dielectric properties of RIGs. The first chapter provides an introduction that includes the theoretical background and explores the different types of magnetism and electric polarization present in these systems. Following this, a comprehensive literature survey on various rare-earth based garnet compounds by highlighting their characteristics and significance is presented.

1.1 Crystal structure

Ferrites primarily consist of ferric oxides and were initially identified by French physicist Louis Néel in 1948 [7]. Menzer in 1928 [8] has discovered the general chemical formula for the geological silicates as $Ca_3Al_2(SiO_4)_3$ with X-Ray powder photograph. Further, in the early $1950's$ Bertaut and Forrat, and Geller and Gilleo [19,20] have observed that the chemical formula of RIGs i.e., $R_3(Fe1)_2[Fe2]_3O_{12}$ is resembling with that of natural silicates. Here, R represents rare earth element which belongs to the lanthanide series of the periodic table such as $Y, Gd, Sm, Dy, Ho, Er, Ce, Pr\ etc.$ and it is situated at the dodecahedral site. Moreover, $Fe1\ (a)$ and $Fe2\ (d)$ are the iron atoms at the octahedral and tetrahedral sites, respectively [9]. RIGs have cubic centrosymmetric space group $O_h^{10}: Ia\bar{3}d$ that belongs to a Body-centred Bravais lattice. Additionaly, RIG contains 160 atoms in a unit cell and have 8 formula units per unit cell [10]. The Wyckoff positions (x, y, z) of $R, Fe1$ and $Fe2$ atoms are given as $24c\ (1/8, 0, 1/4), 16a\ (0, 0, 0)$ and $24d\ (3/8, 0, 1/4)$ [11]. The atomic positions of all the sublattices are shown in Table 1.1. These positions of different cations influence the properties of the magnetic oxides and thus their applicability in soft and hard magnet applications. The basic crystal structure of RIGs and bonding in different polyhedra is shown in Fig. 1.1. The exchange coupling strength follows a hierarchical pattern, with the strongest coupling observed among transition metal ions. The coupling between rare earth and transition metal ions is of intermediate strength, while the coupling between rare earth ions is comparatively weaker. The dodecaherdal, octahedral and teterahedral bonding among rare earth and transition metal cations with oxygen (red coloured atoms) is represented in Fig. 1.2.

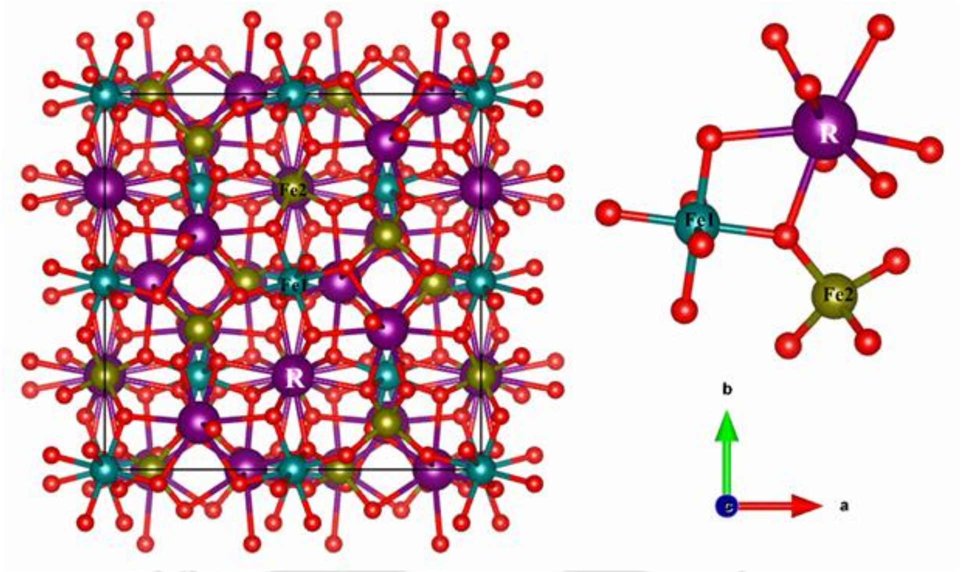

Fig. 1.1: The crystal structure of RIGs and the bonding among different sublattices of garnet system.

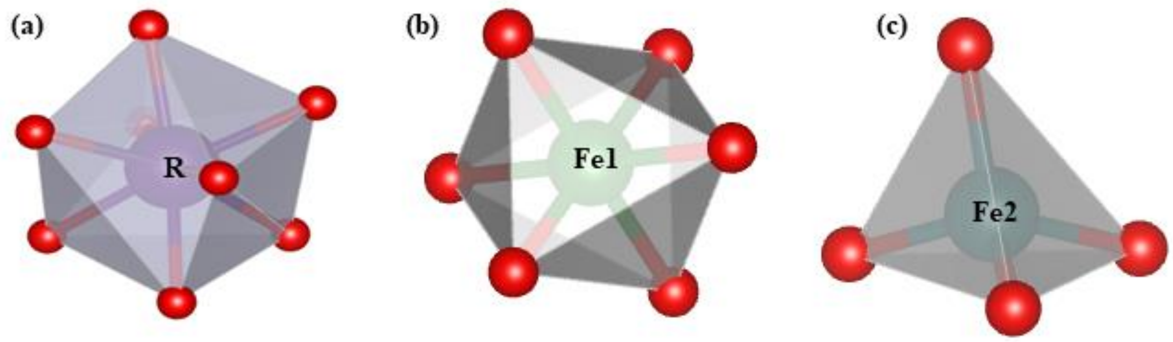

Fig. 1.2: Bonding of cations in polyhedra of (a) Rare earth element at dodecahedral site, (b) $Fe1$ atoms at octahderal and (c) $Fe2$ atoms at tetrahedral positions.

Table 1.1: Atomic coordination of different atoms of RIGs as per $Ia\bar{3}d$ space group.

Atoms	Wycoff position	Coordination to Oxygen	(x, y, z)
R	$24c$	8	$(1/8, 0, 1/4)$
$Fe1$	$16a$	6	$(0, 0, 0)$
$Fe2$	$24d$	4	$(3/8, 0, 1/4)$
O	$96h$	$-$	$(-0.029, 0.057, 0.149)$

RIGs have gained researchers attention because of their excellent magnetic and dielectric properties such as tunable saturation magnetization, magnetic compensation, negative magnetization, spin reorientation, ferroelectricity, magneto-caloric, magnetooptic, magneto-electric, and magneto-dielectric effect [24-27]. Moreover, these materials exhibit advantageous attributes like high resistivity, narrow resonance line width, high dielectric constant along with low dielectric loss [10,28]. These useful properties make RIGs desirable in diverse applications in microwave devices (telecommunication, radar, patch antennas, RF measurement systems), bubble-storage memory devices (solid-state drives i.e., SSD), spintronics devices, oscillators, circulators, isolators, switches, phase shifters, screen printers, humidity gas sensors, drug delivery in cancer treatment and many more [14,29-31].

1.2 Crystal Field Theory (CFT)

CFT explains how the electronic structure of metal ions in ferrites is influenced by the surrounding crystal field created by nearby ions. The crystal field effect lifts the degernercies of d-orbitals of transition elements and hence impacting the magnetic and electronic properties of ferrites. In general, the d-orbital has five degenerate energy levels that are split into two groups: the t_{2g} and e_g orbitals. The t_{2g} group contains three orbitals d_{xy}, d_{yz} and d_{zx} which are oriented in between the x, y and z axes. Meanwhile, the e_g group consists of the $d_{x^2-y^2}$ and d_{z^2} orbitals, which are aligned along the x, y and z directions, as illustrated in Fig. 1.3. In most oxides involving transition metals, the $3d$-orbitals of the metal ions overlap with the $2p$-orbitals of nearby oxygen ions. The oxygen $2p$-orbitals p_x, p_y and p_z extended along the x, y and z directions, respectively facilitate this overlap and influences the electronic properties of the material.

In a tetrahedral environment, the t_{2g} orbitals are raised in energy because they overlap more extensively with the neighboring p-orbitals of oxygen ions, as seen in compounds like MnO_4 [4]. Conversely, in an octahedral environment, the e_g orbitals experience stronger overlap with the p-orbitals of nearby oxygen ions compared to the t_{2g} orbitals, resulting in a higher e_g level relative to the t_{2g} level. This effect is depicted in the energy level diagram for CrO_6 in Fig. 1.4. The arrangement of electrons in the $3d$ orbitals is influenced by a competition between the crystal field energy (Δ_t or Δ_o) and Hund's coupling energy (Δ_{H}). When the crystal field energy is greater than Hund's coupling energy i.e., ($\Delta_{\mathrm{H}} < \Delta_{\mathrm{t},o}$), a low-spin state is favored, while a high-spin state is favored if Hund's coupling energy dominates ($\Delta_{\mathrm{H}} > \Delta_{\mathrm{t},o}$). This crystal field effect directly impacts the magnetic moment of transition elements within the solid.

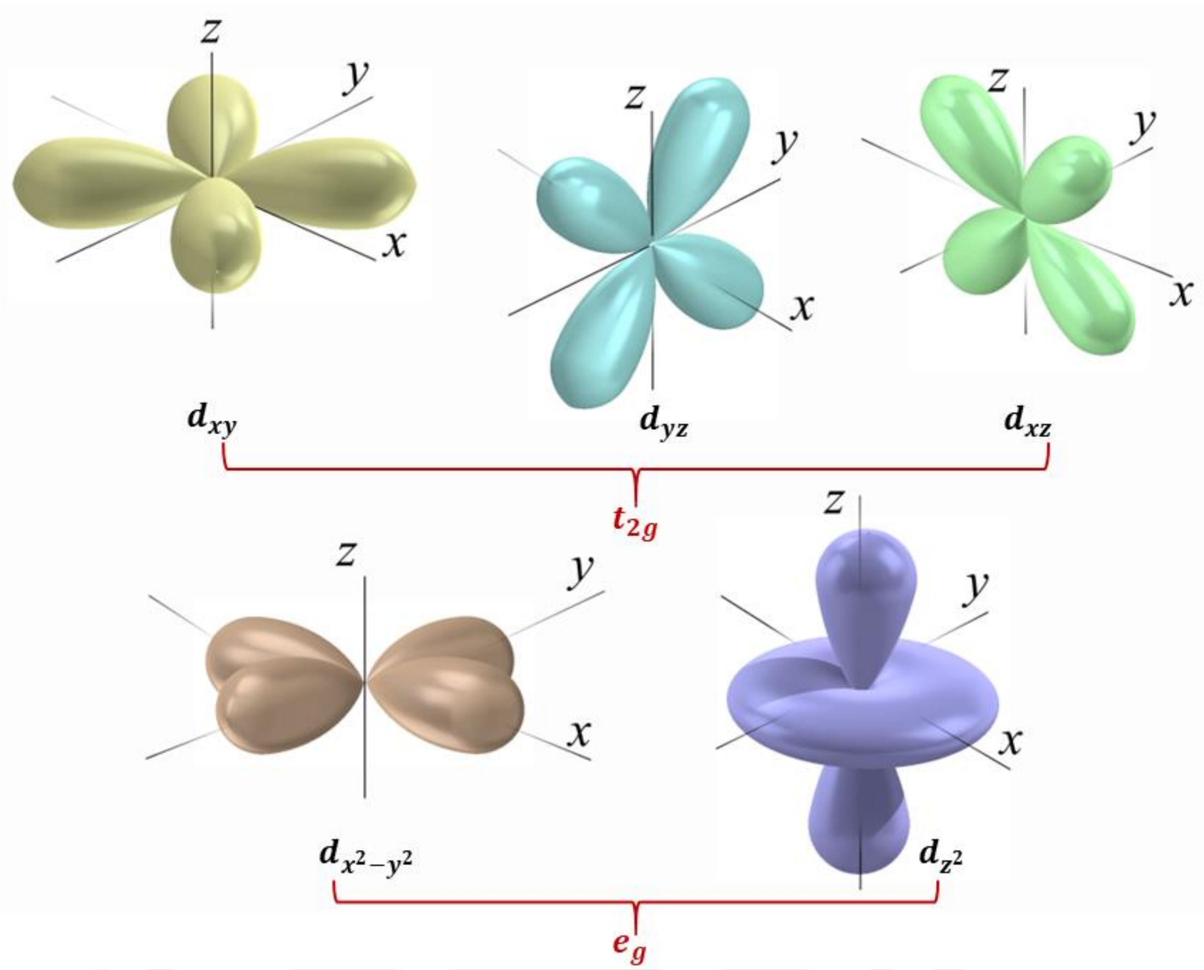

Fig. 1.3: Electronic distribution of $3d$ orbitals.

The magnitude of effective magnetic moment (μ_{eff}) of an ion can be theoretically calculated using the formula $\mu_{eff} = g\sqrt{J\,(J+1)}\mu_B$, where J is the total angular momentum quantum number and μ_B is the Bohr magneton. This formula accounts for both the spin and orbital contributions to the magnetic moment. However, for most transition elements, the experimentally observed magnetic moment often deviates from this theoretical prediction. This discrepancy arises due to the "quenching" of the orbital magnetic moment, where the orbital contribution is suppressed by the crystal field environment, leaving only the spin contribution significant. As a result, the magnetic moment for transition elements is generally estimated using the spin-only formula: $\mu_{eff} = g\sqrt{S\,(S+1)}\mu_B$, where S represents the spin quantum number. This approach provides a more accurate estimate of the magnetic moment in these cases by focusing solely on the spin component.

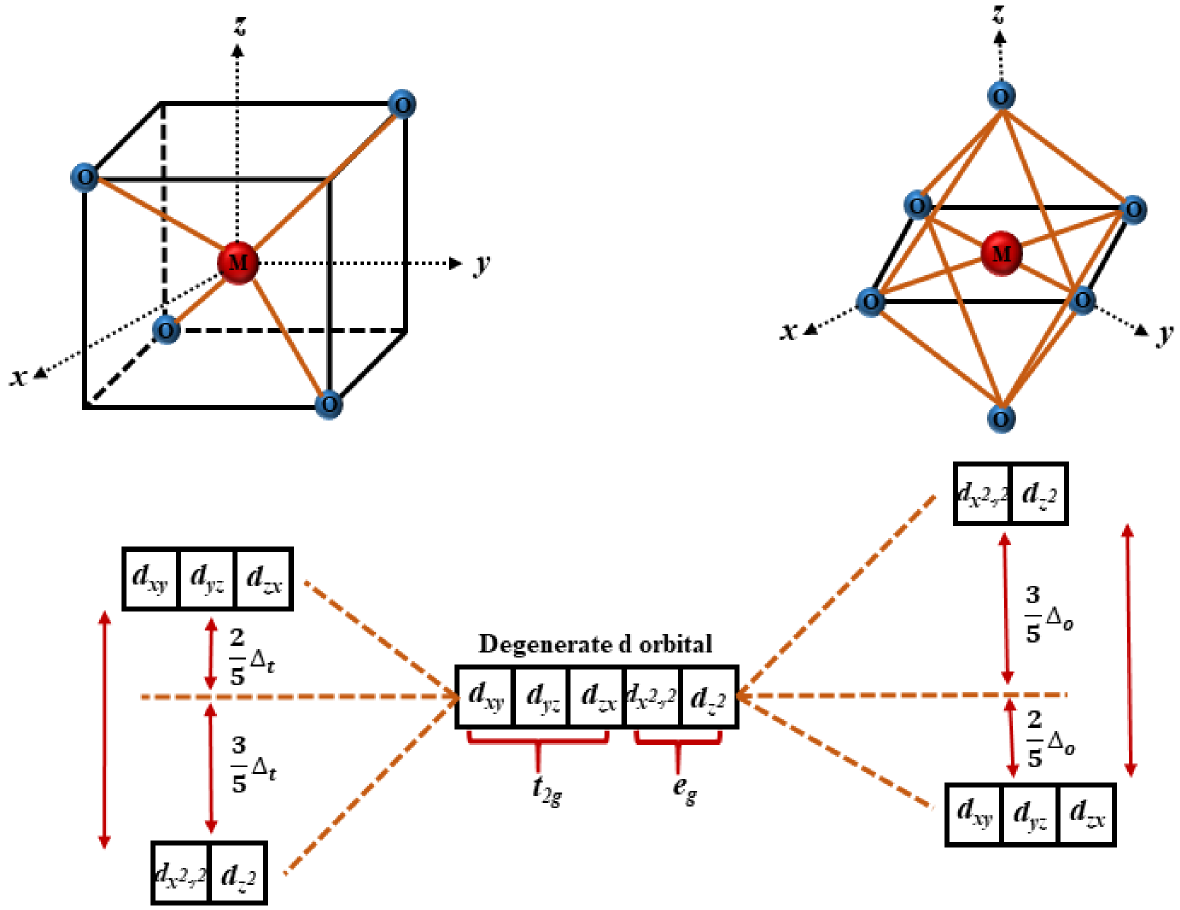

Fig. 1.4: Crystal field splitting in terahedral and octahedral ambience.

1.3 Magnetic exchange interaction

The Heisenberg exchange interaction describes the quantum mechanical exchange of spins across magnetic ions through a non-magnetic ion, which influences the alignment of their magnetic moments. This interaction arises from the Pauli exclusion principle and the wavefunction overlap between adjacent atoms, leading to either ferromagnetic (parallel spin alignment) or antiferromagnetic (anti-parallel spin alignment) ordering, depending on the nature of the exchange integral. In magnetic materials, the Heisenberg exchange interaction plays a crucial role in determining the overall magnetic structure, contributing to the formation of spin configurations and the stability of magnetic phases. The exchange interaction between the localized spins of two atoms labelled as ‘a’ and ‘b’ is described by the Heisenberg model as follows:

$$E_{ex} = -2J_{ab}\left(\vec{S_a}.\vec{S_b}\right) \tag{1.1}$$

The alignment of magnetic dipoles relies on this exchange energy in such a manner that the overall energy of the system must be minimized. So, when the exchange integral factor i.e., $J_{ab} > 0$, the spins of both atoms i.e., $\overrightarrow{S_a}$ and $\overrightarrow{S_b}$ must be parallel to each other to reduce exchange energy and hence leading to ferromagnetism in the material. In contrast, when $J_{ab} < 0$, the exchange energy will remain minimum when both of the spins remain antiparallel to each other. This type of configuration stands for ferrimagnetic and antiferromagnetic ordering in the ferrites. Further, different types of exchange interactions play a different role in the magnetism and they are discussed below:

1.3.1 Direct exchange interaction

Direct exchange interaction occurs when unpaired electrons on neighboring atoms interact through the overlap of their atomic orbitals, without the mediation of any intermediate ion or atom. This overlap leads to a direct Coulomb exchange between the electron spins, favoring either parallel or anti-parallel alignment depending on the sign and strength of the exchange integral. Such interactions are generally significant at low temperatures.

1.3.2 Superexchange interaction

The superexchange interaction is an indirect exchange mechanism in which magnetic ions interact through a non-magnetic intermediary atom, often an oxygen ion [12]. This interaction is commonly found in transition metal oxides where metal ions such as iron or manganese, are separated by oxygen atoms. In superexchange interaction, the magnetic interaction between neighboring metal ions is mediated through the overlap of their unpaired d-orbitals with the p-orbitals of the oxygen atom. The concept of superexchange is explained by Anderson-Goodenough-Kanamori [13] through a semi-covalent bonding model. Taking the $Mn - O - Mn$ network as an example, there are typically three bonding types: (1) covalent or semi-covalent bonding, where the empty $Mn\ 3d$ orbital points toward the $O\ 2p$ orbital; (2) ionic bonding, where the empty $Mn\ 3d$ orbital points away from the $O\ 2p$ orbital; and (3) metallic bonding where the O^{2-} ion sits between Mn^{3+} and Mn^{4+} ions.

In a specific case of semi-covalent bonding between $Mn - O - Mn$ (shown in Fig. 1.5 (a)), the core spins of Mn ions are opposite to each other. According to Hund's rule, the oxygen atom's up-spin $2p$ electron is shared with the empty $3d$ state of Mn that has a core up-spin, and the down-spin $2p$ electron is shared with the Mn ion having a down-spin core. This results in an AFM superexchange interaction as the spin alignment between the two Mn ions become antiparallel.

However, if the core spins of the Mn ions are parallel (shown in Fig. 1.5 (b)) and undergo semi-covalent bonding, such bonding is prohibited due to Hund's rule. This leads to the absence of magnetic ordering. In a mixed bonding case, where one Mn exhibits semi-covalent bonding and the other ionic bonding, below the ordering temperature, the result is a FM superexchange interaction. In such a case, the $Mn-O$ in one side undergoes semi-covalent bonding causing FM alignment between the spins of Mn and O. The $Mn-O$ on the other side exhibits ionic bonding which leads to AFM interaction between Mn and O. The combined effect would lead to net FM interaction between the two Mn ions.

Therefore, a combination of semi-covalent interaction on one side and ionic exchange on the other leads to an overall FM superexchange interaction. Hence, the nature of magnetic ordering (whether FM or AFM) depends on the environment and the type of bonding present in the system. The spin configurations corresponding to FM and AFM superexchange interactions further illustrate how electron alignment governs the magnetic behavior in these systems.

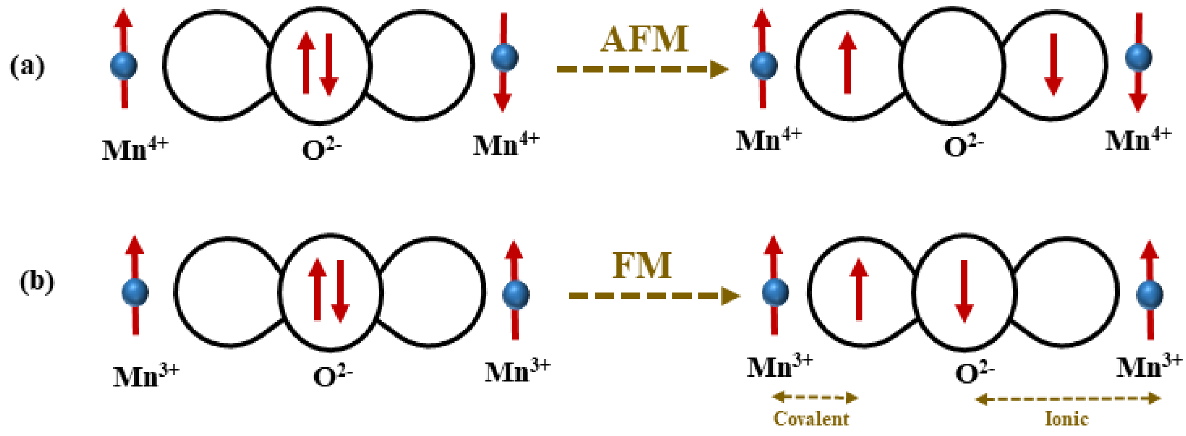

Fig. 1.5: Schematic representation of (a) AFM and (b) FM superexchange interaction.

1.3.3 Dzyaloshinskii-Moriya (DM) Exchange Interaction

The DM exchange interaction is an antisymmetric magnetic exchange interaction that arises in systems with strong spin-orbit coupling and a lack of inversion symmetry between neighbouring magnetic ions. Unlike conventional exchange interactions which align spins parallel or antiparallel, the DM interaction favors a non-collinear canted spin arrangement and their exchange energy can be given as:

$$H_{DM} = \vec{D}.(\vec{S_1} \times \vec{S_2}) \tag{1.2}$$

where, $\vec{D}$ is the DM vector and $\vec{S_1}$ and $\vec{S_2}$ are the spins of two interacting ions. If there is an inversion symmetry with respect to the central point connecting the two magnetic ions, the $\vec{D}$ becomes zero. The DM interaction primarily occurs in AFM materials that sometimes results in a weak FM component. Certain AFM crystals, such as $\alpha - Fe_2O_3$ and Cr_2O_3, display this weak FM behavior [14]. In multiferroic systems, the antisymmetric exchange interaction is a key factor contributing to magnetism-induced electric polarization.

1.3.4 Ruderman-Kittel-Kasuya-Yosida (RKKY) Interaction

The RKKY interaction describes an indirect exchange interaction between localized magnetic moments in a metal mediated by conduction electrons. The magnetic moment of a localized spin polarizes the surrounding conduction electrons, and this polarization, in turn, interacts with another localized magnetic ion located a distance r away. This is a long-range type of interaction that results in either AFM or FM ordering depending upon the distance between the magnetic ions.

1.4 Magnetic ordering

Magnetic ordering arises from the interactions between atomic orbital and spin magnetic moments within a material. These moments are derived from the orbital and spin momentum of electrons in atoms/ions. Depending on how these moments align with each other, various types of magnetic ordering emerge such as diamagnetic, paramagnetic (PM), ferromagnetic (FM), antiferromagnetic (AFM) and ferrimagnetic (FIM).

1.4.1 Diamagnetic materials

Diamagnetic materials are substances that create a weak and negative magnetic moment in response to an applied magnetic field. In these materials, all electron spins are paired resulting in no atomic dipole moment. However, when placed in a magnetic field, they produce a small opposing field, thereby exhibiting a negative susceptibility. This behavior is due to changes in electron orbital motion, which slightly offsets the applied field. Common examples of diamagnetic materials include He, Ne, Ar, N_2, NaCl. Unlike paramagnetic or ferromagnetic materials, diamagnetism is independent of temperature. The susceptibility of diamagnetic material having N number of atoms per unit volume and Z fully filled electron per atom can be given as [15]:

$$\chi = -\frac{N\mu_0 Z e^2}{6m}\bar{r}^2 \tag{1.3}$$

here, μ_0, e, m and $\bar{r}^2$ are the permeability in free space, electronic charge, mass and the mean square radius of electrons orbit.

1.4.2 Paramagnetic materials

Paramagnetic materials are those that exhibit a weak attraction to an external magnetic field due to the presence of unpaired electrons. In these materials, individual magnetic moments tend to align with an external magnetic field resulting in a small and positive magnetization. However, thermal motion disrupts this alignment, so paramagnetism is generally weak and decreases as temperature increases. The magnetic susceptibility χ of paramagnetic materials as per Langevin approach is given as [16]:

$$\chi = \frac{N\mu^2\mu_0}{3k_BT} \tag{1.4}$$

here, μ and k_B are the magnetic moment of atoms or ions and Boltzman constant, respectively. This equation is better known as Curie's law that reflects the dependence of susceptibility on temperature [17]. As per Quantum mechanical approach, the susceptibility of paramagnets in low magnetic fields can be expressed as:

$$\chi = \frac{N\mu_0 g^2\mu_B^2 J(J+1)}{3k_BT} \tag{1.5}$$

With g representing the Lande's g factor:

$$g = 1 + \frac{J(J+1)+S(S+1)-L(L+1)}{2J(J+1)} \tag{1.6}$$

Some commonly known paramagnets are $Al, Pt, Mn, Mg, , W, Li$, salts of transition metals and some rare earth elements such as La, Ce, Pr.

1.4.3 Ferromagnetic materials

FM materials are those that exhibit strong, permanent magnetization due to the alignment of magnetic moments in the same direction. In these materials, unpaired electron spins within certain regions (domains) spontaneously align parallel to each other because of strong exchange interactions. This alignment produces a large net magnetic moment even without an external field. Common examples include Fe, Co and Ni. The magnetic susceptibility of ferromagnetic materials does not follow Curie's Law directly but instead follows the Curie-Weiss Law:

$$\chi = \frac{C}{T-T_c} \tag{1.7}$$

where C is the Curie constant, T is the absolute temperature and T_c is the transition temperature. Here,

$$C = \frac{N\mu_0 g^2 \mu_B^2 J(J+1)}{3k_B} \quad \text{or} \quad C = \frac{N\mu_0 g^2 \mu^2}{3k_B} \tag{1.8}$$

Below T_c, the susceptibility of ferromagnets increases rapidly contributing to their strong, temperature-dependent magnetic properties. Above T_c, ferromagnetic materials lose their magnetization and become paramagnetic.

1.4.4 Antiferromagnetic materials

AFM materials are those in which neighboring magnetic moments align in opposite directions, resulting in no net magnetization under normal conditions. This arrangement occurs because of strong antiferromagnetic exchange interactions which favor an antiparallel spin alignment. Examples of AFM materials include MnO, FeO and Cr. The magnetic susceptibility of these materials typically follows the Curie-Weiss Law [18]:

$$\chi = \frac{C}{T+T_N} \tag{1.9}$$

where T_N exhibit a characteristic temperature called the Néel temperature, below which they show AFM ordering. Above T_N, thermal energy disrupts this ordering and the material becomes paramagnetic.

1.4.5 Ferrimagnetic materials

FIM materials have magnetic moments that align in an antiparallel arrangement, similar to antiferromagnets but with unequal opposing moments. These unequal moments result in a net magnetic moment and thereby exhibiting appreciable magnetization. Ferrimagnets are typically composed of different magnetic ions with varying magnitudes of magnetization and their net magnetization is determined as $M_{net} = M_A - M_B$ with M_A and M_B representing the magnetization due to A and B sublattices. Common examples of

FIM materials include $Fe_3O_4, MnFe_2O_4$ and $NiFe_2O_4$. Ferrimagnets exhibit a transition temperature (T_c), above which they lose their ferrimagnetic order and become paramagnetic. FIM materials are widely used in applications such as permanent magnets, transformers, and magnetic recording media due to their strong net magnetic moment and unique magnetic properties.

Spinel, hexaferrite and garnet are also example of FIM materials. The magnetic moment of garnets arises from the AFM interaction of Fe^{3+} ions at octahedral (a) and tetrahedral (d) sites and the net moment gets antiferromagnetically coupled with the moment of rare earth ion (c). The ordering of rare earth ion gets stronger drastically with the decrease in temperature whereas, the moment of a and d sublattices remains almost constant as shown in Fig. 1.6 (a). Overall, the FIM nature gets vanished around T_c of 550 K for various RIGs and the material turns into PM. Typical M-T plots for various RIGs are shown in Fig. 1.6 (b), with T_c around 550 K.

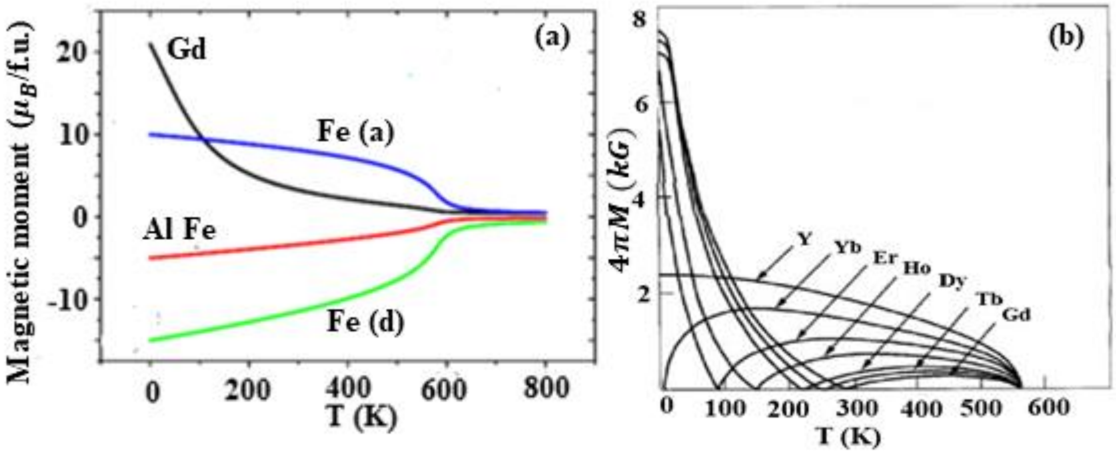

Fig. 1.6: (a) Temperature dependent magnetization for different sublattice of GdIG and (b) for various rare earth based garnets [39,4].

1.5 Magnetic anisotropy

Magnetic anisotropy refers to the directional dependence of a material's magnetic properties meaning that the energy required to magnetize the material varies based on the direction of the applied magnetic field. This property arises due to the material’s atomic structure, spin-orbit coupling, crystal lattice, or external factors like shape or stress causing certain orientations to be energetically favorable for magnetization. Magnetic anisotropy plays a crucial role in magnetic storage devices and permanent magnets as it helps stabilize magnetic domains and affects the coercivity, or the resistance to demagnetization of the material. Some commonly known magnetic anisotropies are magnetocrystalline anisotropy, shape anisotropy, stress anisotropy and exchange anisotropy.

1.5.1 Magnetocrystalline anisotropy

The ability of magnetic moments to orient themselves in a particular crystallographic direction is named as magnetocrystalline anisotropy. This effect arises from the interaction between electron spins and the atomic lattice structure causing the material to have "easy" and "hard" axes of magnetization. Aligning the magnetic moment along an easy axis requires less energy, while aligning it along a hard axis requires more. In a crystal, electron coupling occurs through several mechanisms that shape its magnetic and structural properties. Spin-spin coupling aligns neighboring spins affecting magnetic ordering, while spin-lattice coupling transfers energy between spins and lattice vibrations aiding magnetic relaxation. Lattice-orbit coupling impacts electronic band structure by interacting with the atomic lattice. Spin-orbit coupling links electron spin with orbital motion and the energy required to overcome the spin-orbit coupling is known as anisotropy energy (E). In 1929, a Russian physicist Akulov [19] formulated the energy E as a series expansion involving the direction cosines α_i of the saturation magnetization (M_s) with respect to the crystal axes, expressed as:

$$E = K_0 + K_1(\alpha_1^2\alpha_2^2 + \alpha_2^2\alpha_3^2 + \alpha_3^2\alpha_1^2) + K_2(\alpha_1^2\alpha_2^2\alpha_3^2) + \cdots \tag{1.10}$$

In this expression, K_0, K_1 and K_2 denote the anisotropy constants for a specific crystal at a given temperature. The terms α_1, α_2 and α_3 are the direction cosines of the saturation magnetization M_s along the crystallographic axes a, b and c, respectively. The effect of K_0 is minimal, as it is independent of orientation. When $K_2 = 0$, the easy axis can be determined by the sign of K_1. If K_1 is positive, the energy order follows $E_{100} < E_{110} < E_{111}$ making $< 100 >$ the easy axis. In contrast, if K_1 is negative, the energy order becomes $E_{111} < E_{110} < E_{100}$ with $< 111 >$ as the easy axis. When $K_2 \neq 0$, both K_1 and K_2 together dictate the direction of the easy axis.

1.5.2 Shape anisotropy

The shape anisotropy refers to the influence that how easily a material can be magnetized along different directions. For example, in a long needle-like shape, the magnetic moments are more likely to align along the length of the material, as this configuration minimizes the demagnetizing field. In contrast, in a spherical or cubic shape, the demagnetizing field is more uniform and the material tends to have easier magnetization along certain axes. The shape anisotropy of any material can be estimated in form of demagnetization field (H_d) and can be expressed as follows [20]:

$$H_d = -N_d M \tag{1.11}$$

With N_d and M representing demagnetization factor and magnetization, respectively. This demagnetization field is strong around short dimension as compared to its larger dimension.

1.5.3 Stress anisotropy

When a material is subjected to stress, either externally or internally (such as during fabrication or under operating conditions), the lattice structure may be distorted affecting the alignment and interaction of magnetic moments. This results in a stress anisotropic behavior, where the magnetic properties depend on the direction of the applied stress relative to the crystallographic axes. The energy of such anisotropy can be written as [21]:

$$E_\sigma = K_\sigma \sin^2 \theta \tag{1.12}$$

here, K_σ is the stress anisotropy constant and θ is the angle between magnetization and direction of applied stress.

1.5.4 Exchange anisotropy

Exchange anisotropy typically arises from the exchange interaction between two dissimilar materials, such as at the interface of FM and an AFM material or within a heterostructure. This type of anisotropy also leads to exchange bias phenomenon in these compounds.

1.6 Magnetic Compensation and Magnetization Reversal (MR)

Magnetic compensation occurs in RIGs at a specific temperature called compensation temperature (T_{comp}), when the magnetization of the rare-earth sublattice and the iron sublattice cancel each other out at a specific temperature leading to a net zero magnetization at that point. Magnetic compensation behavior is reported in various garnet systems such as GdIG, HoIG, TbIG, DyIG, ErIG, YbIG [26,43,44].

Magnetization reversal (MR) refers to the phenomenon where the dc magnetization changes sign from positive to negative as the temperature is varied under applied magnetic field. Unlike diamagnetism, MR is typically observed under field-cooled (FC) conditions but may also occur by varying the strength of the applied magnetic field at a fixed temperature below T_{comp}. This behavior can result from various factors, including crystal distortions, lattice defects, exchange interactions, magnetic anisotropy, or the temperature dependence of sublattice magnetizations. It was first observed by Néel in 1948 in FIM materials [22] and then later observed in various other systems such as FM or canted AFM compounds [23]. MR leads to numerous technological applications, including thermally assisted magnetoresistive random access memory (TAMRAM) devices, thermomagnetic switches, spin valves, and magnetic tunnel junctions, etc.

Chukalkin *et al.* [24] reported the occurrence of negative magnetization in polycrystalline $Y_{2.25}Gd_{0.75}Fe_5O_{12}$ garnet sample under FC conditions, with a compensation temperature (T_{comp}) of 50 K and at a cooling field H_{FC} of 15 Oe. They attributed this behavior to the distinct temperature dependencies of the magnetic moments of the Gd and Fe sublattices. Interestingly, magnetization reversal can also occur when the magnetocrystalline anisotropy is strong enough to reorient the magnetic spins in the opposite direction. For example, when Hong $et\ al.$ [25] measured the FC magnetization of TbIG at 100 and 5000 Oe and observed only magnetic compensation. But when TbIG was doped with Bi ($Tb_{3-x}Bi_xFe_5O_{12}$ ($x = 0.0 - 1.0$)), they noticed a magnetization reversal at a field of 100 Oe. The authors explained that this happens because Bi^{3+} ions create strong magnetocrystalline anisotropy, which makes it harder for the magnetic spins to rotate [26]. Similarly, Bi substitution also leads to MR phenomenon in HoIG ($Ho_2Bi_1Fe_5O_{12}$) compound [27]. The occurrence of MR in TbIG and HoIG with Bi substitution is shown in Fig. 1.7. Additionally, $Gd_1Sm_2Fe_5O_{12}$ compound also exhibits MR which is further confirmed by applying 100 to 600 Oe magnetic field.

MR occurs in various material systems due to unique interactions between different magnetic ions sublattices. In spinel ferrites like $CoFe_2O_4$ and $Mn_{0.2}Co_{0.8}Fe_2O_4$, magnetization reversal is observed and it results from the interactions between ions in tetrahedral and octahedral sites as per Néel hypothesis [28]. Similarly, orthoferrites ($RFeO_3$) orthochromites ($RCrO_3$) exhibit magnetization reversal influenced by strong spin-orbit coupling and exchange interactions [52,53]. In perovskites such as $La_{0.75}Nd_{0.25}CrO_3$, competing ferromagnetic and antiferromagnetic interactions between transition metals drive reversal behaviors [29]. Additionally, magnetization reversal is observed in alloy systems with ferromagnetic and antiferromagnetic phases, such as Fe/FeMn thin films, where exchange bias at the ferromagnetic–antiferromagnetic interface is exploited in magnetic memory technologies [30].

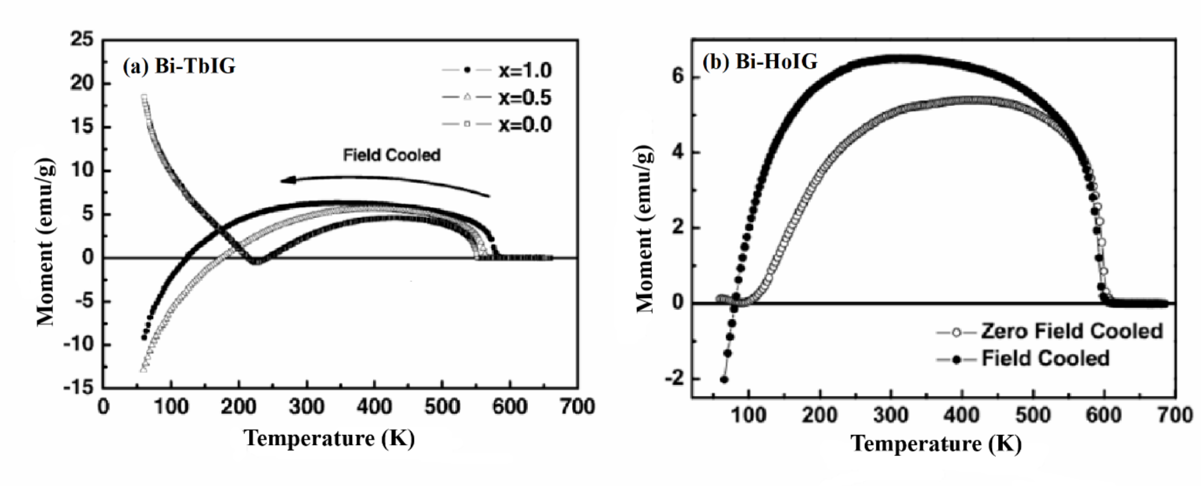

Fig. 1.7: Variation in magnetization with temperature under (a) FC condition at $H_{FC} = 100Oe$ for $Tb_{3-x}Bi_xFe_5O_{12}$ and (b) ZFC and FC magnetization curves of $Ho_2Bi_1Fe_5O_{12}$ compound [49,50].

1.7 Spin reorientation

Spin reorientation is a magnetic phenomenon where the direction of magnetic moments in a material changes or "reorients" due to variations in temperature, external magnetic field, or internal structural changes. This reorientation is driven by competing anisotropies, typically magnetocrystalline anisotropy which determine the preferred orientation of spins in different temperature or field regimes. The anisotropic exchange interaction between Fe^{3+} ions and rare-earth ions generates an effective field at the tetrahedral and octahedral sites, helping the Fe^{3+} ions sustain their antiferromagnetic ordering. As the temperature decreases, the rare-earth ions become more magnetically ordered which enhances their magnetization. This strengthened magnetization creates a more powerful effective magnetic field that influences the Fe^{3+} ions within the material. Under normal conditions, Fe^{3+} ions align their spins in a preferred direction due to magnetic anisotropy which resists reorientation. However, when the effective field from the rare-earth ions becomes sufficiently strong, it can overcome the anisotropy energy of the Fe^{3+} ions. At this point, the Fe^{3+} ions reorient their magnetization to align with the stronger field, a process known as spin reorientation [31]. This reorientation takes place at a specific temperature characteristic of the material which is called as spin reorientation transition (SRT) that is denoted as T_{sr}.

Spin reorientation occurs in a variety of magnetic systems each with distinct characteristics influenced by factors like temperature, magnetic anisotropy, and external fields. In rare-earth–transition metal compounds (e.g., $Dy_3Fe_5O_{12}$), reorientation arises from the temperature-dependent competition between rare-earth and transition-metal sublattice anisotropies [32]. It is further confirmed with an anomaly observed in the specific heat (C_p) plot around $15K$ as shown in Fig. 1.8. In ferromagnetic thin films, reorientation can be driven by film thickness, strain, or temperature, causing spins to switch from in-plane to out-of-plane orientations [33]. AFM systems like Mn_2Au show reorientation due to anisotropic exchange interactions, which can be influenced by magnetic fields or spin currents [34].

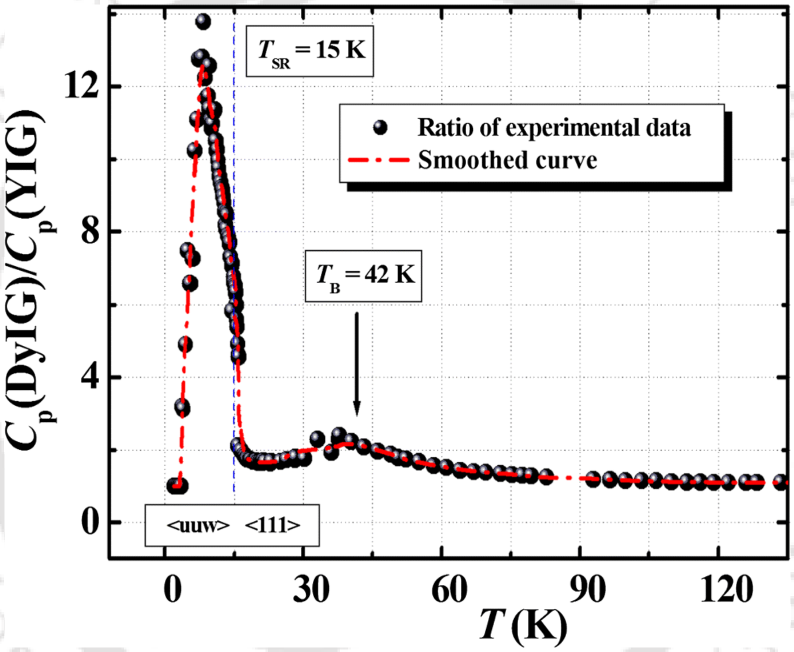

Fig. 1.8: Temperature dependent specific heat for $Dy_3Fe_5O_{12}$ garnet system [32].

Indian Institute of Technology Guwahati

1.8 Magnetocaloric effect (MCE)

The MCE is a phenomenon observed in certain materials where a change in temperature occurs due to the application or removal of a magnetic field. When a magnetic field is applied, the magnetic dipoles within the material tend to align reducing magnetic entropy and releasing heat. Conversely, when the magnetic field is removed, the dipoles become disordered that increases the magnetic entropy and causing the material to cool down. Materials exhibiting a strong MCE such as gadolinium and some intermetallic compounds are key to creating practical magnetocaloric cooling systems. The strength of the MCE depends on the type of material and its magnetic phase transition temperature.

Near this transition, changes in entropy and temperature are more pronounced making these materials ideal candidates for efficient cooling. The MCE can be quantified using thermodynamic equations, particularly the Maxwell relations. One way to express the isothermal entropy change ΔS_M due to a change in magnetic field is by the following Maxwell relation [35]:

$$\Delta S_M(T,H) = \int_0^H \left(\frac{\partial M}{\partial T}\right)_H dH \quad (1.13)$$

or,

$$\Delta S_M = \sum \frac{M_i - M_{i+1}}{T_{i+1} - T_i} \Delta H_i \quad (1.14)$$

here, the terms M_i and M_{i+1} refers to the magnetic moment at T_i and T_{i+1} temperature, respectively in ΔH_i change in magnetic field. Further, the efficiency of any magnetocaloric material can be quantified in terms of Relative Cooling Power (RCP) and can be expressed as [36]:

$$RCP = |\Delta S_M^{max}| \times \delta T_{FWHM} \quad (1.15)$$

The variable δT_{FWHM} shows the full width half maxima of magnetic entropy versus temperature plot. Then, the order of phase transition can be determined from the slope of Arrott plots i.e., M^2 vs. H/M curves. The positive slope stands for second order phase transition (SOPT), while a negative slope indicates first order phase transition (FOPT) [37]. Further, the order of the phase transition is confirmed with fitting of $-\Delta S_M^{max}$ vs. H plot to $\Delta S_M^{max}\ \alpha\ H^n$ relation. In a magnetic system with a single transition temperature, the exponent n varies by region: near zero temperature, $n \approx 1$; at the critical temperature T_c, $n \approx 2/3$; and in the paramagnetic region, $n \approx 2$. Additionally, values $0 < n < 1$ indicate a SOPT, while $n > 1$ signifies a FOPT [38].

1.9 Dielectric properties

Dielectrics are insulating materials that do not conduct electricity but can be polarized in the presence of an electric field. When a dielectric is placed in an electric field, positive and negative charges within the material shift slightly that creates an internal electric field that opposes the applied field. This polarization ability makes dielectrics essential in capacitors, where they increase capacitance by storing energy in the form of an electric field. Common dielectric materials include ceramics, glass, and various polymers.

The polarization (P) depends upon the strength of the applied electric field (E) and can be determined as [39]:

$$P = \varepsilon_0 \chi E \tag{1.16}$$

where, ε_0 represents the permittivity in free space ($8.854 \times 10^{-12}\ F/m$) and χ is the susceptibility of dielectric. Further, polarization in dielectrics can be classified by the mechanism through which dipole moments are created and they are of four types: (i) electronic, (ii) ionic/atomic, (iii) Orientational and (d) space charge polarization. All different types of polarization are demonstrated in Fig. 1.9.

Electronic polarization occurs in all materials when an electric field displaces the electron cloud relative to the nucleus within atoms forming temporary dipoles; for instance, this effect is seen in noble gases. This type of polarization occurs in 10^{-15} seconds. Ionic polarization is present in ionic materials, like NaCl, where an electric field causes positive and negative ions to shift in opposite directions creating a dipole moment. Orientational (dipolar) polarization occurs in materials with permanent dipoles, such as H_2O, NH_3, HF where dipoles align with an electric field, although they resist alignment due to thermal motion. This polarization takes 10^{-10} seconds to happen [40]. Lastly, space charge polarization arises in heterogeneous materials or composites such as ceramics with grain boundaries, where charges accumulate at interfaces under an electric field, producing polarization. This polarization occurs relatively quickly in 10^{-2} seconds and that is why, it can be found in lower frequency zone. Each type responds to an applied field at different speeds, with electronic polarization being the fastest and space charge the slowest [41].

The dielectric permittivity or dielectric constant (ε_r) can be estimated through the known dielectric permittivity of the medium (ε) as follows [42]:

$$\varepsilon_r = \frac{\varepsilon}{\varepsilon_0} \tag{1.17}$$

The ε_r is generally influenced by the material's chemical structure, imperfections (defects), and other physical factors such as temperature and pressure. The polarization mechanism in dielectrics can be analyzed through two primary approaches: the time-domain and the frequency-domain [43]. In the time-domain approach, the polarization's time dependence is observed immediately after the application of an electric field, or as the system returns to its initial state upon removal of the field. This process is generally known as dielectric relaxation. In the frequency-domain approach, the dielectric constant is measured at various frequencies of an alternating electric field. Both approaches are theoretically interconnected and, in principle, should yield consistent results.

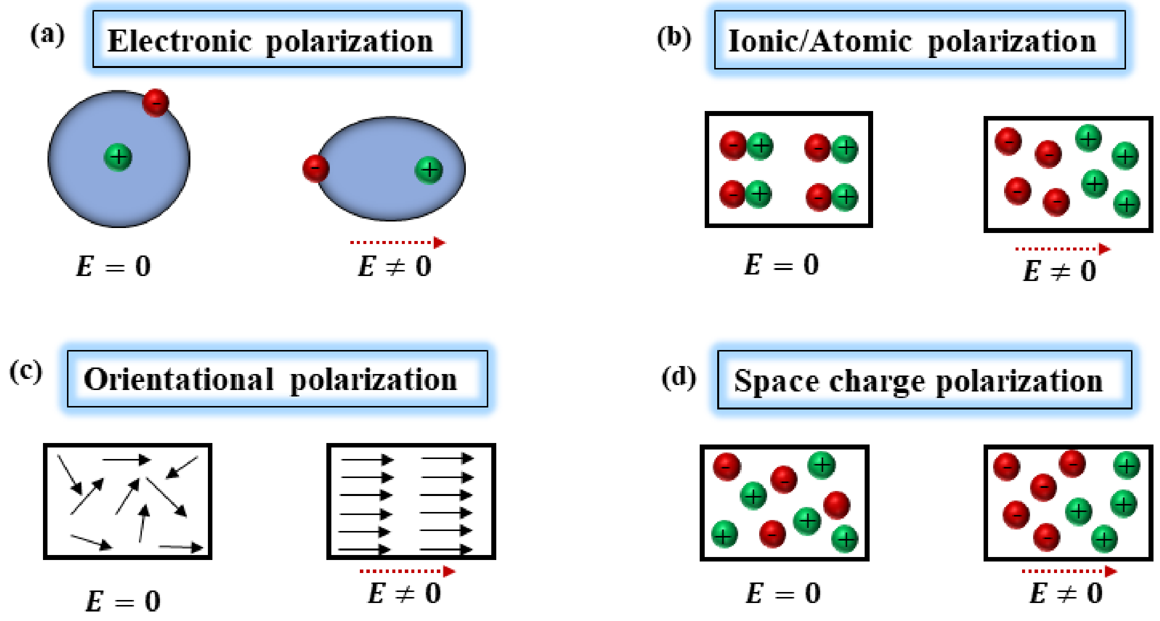

Fig. 1.9: Schematic demonstration of different types of polarization present in any dielectric material such as (a) electronic, (b) ionic, (c) orientational and (d) space charge polarization.

1.9.1 Complex Impedance Spectroscopy

Complex impedance spectroscopy is an analytical technique used to study the electrical properties of materials by measuring their impedance over a range of frequencies. This method provides insights into various processes within a material, including conduction, polarization, and dielectric relaxation by separating the real (Z') and imaginary (Z'') components of impedance. The variation of both Z' and Z'' with the dispersion of frequency are displayed in Fig. 1.10. The concept of complex impedance (Z^*) was first introduced by Heaviside in 1880 and further detailed by Kennelly and Steinmertz [44]. In complex impedance spectroscopy, an alternating current is applied across the sample and the resulting impedance response is recorded as a function of frequency. As per Ohm's law, the complex impedance can be calculated as:

$$Z^* = Z' - jZ'' = \frac{V^*(\omega)}{I^*(\omega)} \tag{1.18}$$

here, $V^*(\omega)$ is the voltage across dielectric material and $I^*(\omega)$ is the current through it. In an ideal dielectric, the real part of impedance $Z' = 0$, so the total impedance is purely capacitive. It can be expressed as $Z^*(\omega) = -j/\omega C$, where ω is the angular frequency and

C is the capacitance. In the lower frequency region, mostly space charge polarization dominates and with the passage of frequency in higher frequency zone ($\sim 1MHz$), orientational polarization leads. The Z' curve shows a dispersion with frequency and a peak appears in the Z'' curve around the same frequency. The frequency at which this peak occurs is known as the relaxation frequency of charge carriers, as shown in Fig. 1.10. This relaxation frequency can be related to the relaxation time τ by the equation $\tau = 1/2\pi f_{max}$ [45].

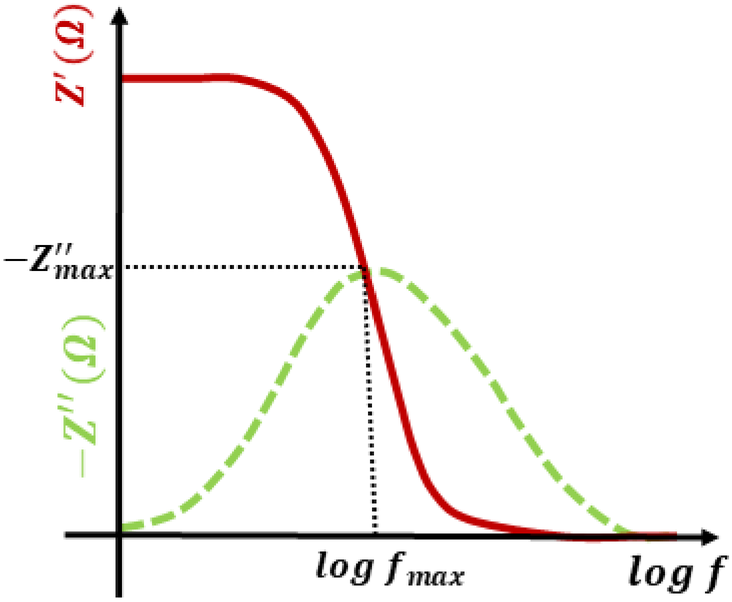

Fig. 1.10: Representation of real and imaginary components of impedance with respect to logarithmic frequency.

Nyquist plots are graphical representations used in impedance spectroscopy to visualize the complex impedance (Z^*) of a material. In a Nyquist plot, the real part of the impedance (Z') is plotted on the x-axis, while the imaginary part ($-Z''$) is plotted on the y-axis as shown in Fig. 1.11. This plot typically forms a semicircular or arc-like shape where the diameter of the semicircle represents the resistance or impedance of the material. It is particularly useful for distinguishing between different contributions to the impedance, such as bulk resistance, interfacial effects, and capacitive behaviour. In an ideal case, the Nyquist plot forms perfect semicircle with its centre lying on the Z' axis (as displayed in Fig. 1.11 (a)). However, in a non-ideal scenario (refer to Fig. 1.11 (b)), a depressed semicircle is formed that do not follow ideal Debye type relaxation behavior [46]. The departure from ideal case is measured in terms of constant phase element (CPE) denoted as Q [47]:

Indian Institute of Technology Guwahati

$$Z_{CPE} = \frac{1}{A}(j\omega^{-m}) \tag{1.19}$$

here, A is a constant, and m represents the distribution of relaxation times ranging from $0 \leq m \leq 1$. When $m = 0$, the CPE behaves like a resistor, while at $m = 1$, it behaves like a capacitor.

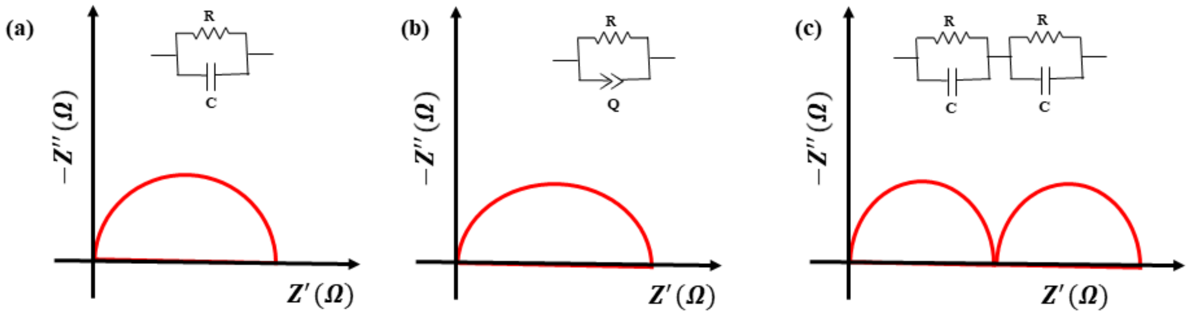

Fig. 1.11: Pictorial representation of Nyquist plots with different conditions.

In polycrystalline materials, both the grains (G) and grain boundaries (GB) contribute to the overall electrical response. Grains typically exhibit higher conductivity and lower capacitance in comparison to GB which can act as barriers to charge transport. When the impedance response of such a material is plotted, a single semicircular arc generally represents an equivalent circuit with a parallel combination of resistance (R) and capacitance (C). If two semicircular arcs appear, they are usually indicative of separate contributions from the G and GB and the system can be modelled with two parallel R-C elements in series (as shown in Fig. 1.11 (c)). The arc observed at higher frequencies (lower Z') typically corresponds to the G, representing short-range motion of charge carriers. Conversely, the arc at lower frequencies (higher Z') corresponds to the GB reflecting a long-range charge migration. The diameters of these semicircles allow estimation of the resistances for both the G and GB regions, with the grain resistance usually being lower than that of the grain boundary. This impedance behaviour offers valuable insights into the internal microstructure of polycrystalline materials and helps in understanding how G and GB characteristics influence the overall conductivity.

1.9.2 Complex Dielectric Spectroscopy

The dielectric constant which is also known as the dielectric permittivity (ε_r) is a fundamental property that characterizes a material's ability to polarize in response to an applied electric field, thereby storing electrical energy. It reflects how much the electric field within the material is reduced compared to the field in a vacuum. So, ε_r is measured with the capacitance of free space and that of any medium by following relation [48]:

$$\varepsilon_r = \frac{C}{C_0} \tag{1.20}$$

here, C_0 is the geometrical capacitance that can be determined by area (A) and thickness (t) of the pellet by the relation $C_0 = A\varepsilon_0/t$. The complex dielectric permittivity $\varepsilon^*(\omega)$ captures both the energy storage and energy loss behaviors of a material and is frequency-dependent that offers insight into different polarization mechanisms at various frequencies. The complex permittivity can be expressed in terms of real in imaginary component as follows [49]:

$$\varepsilon^*(\omega) = \varepsilon'(\omega) - j\varepsilon''(\omega) \tag{1.21}$$

where $\varepsilon'(\omega)$ is the real part that represents the material's ability to store energy (the dielectric constant), while $\varepsilon''(\omega)$, the imaginary part which is associated with energy dissipation such as through dielectric losses or relaxation processes. These components can be estimated via impedance and is given as [50]:

$$\varepsilon' = \frac{-Z''}{\omega C_0\,(Z'^2+Z''^2)} \tag{1.22}$$

$$\varepsilon'' = \frac{Z'}{\omega C_0\,(Z'^2+Z''^2)} \tag{1.23}$$

The dielectric constant typically depends on frequency and at higher frequencies, it decreases because the electric field changes too quickly for the dipoles in the material to respond that leads to reduced polarization. In dielectric materials having G and GB, distinct dielectric relaxation processes can be observed at two different frequencies. The dissipation factor or loss tangent, defined as [51]:

$$tan\delta = \frac{\varepsilon''}{\varepsilon'} \tag{1.24}$$

This serves as a measure of the efficiency of energy storage versus energy loss, where a higher $tan\delta$ indicates greater losses. Since no dielectric material is truly ideal (i.e., with conductivity $\sigma \rightarrow 0$), there is typically some presence of free charges in addition to bound charges leading to non-ideal behaviour (ideal case is shown in Fig. 1.12 (a)). Consequently, more than one relaxation process is often observed. To account for these complexities, Havriliak–Negami (HN) has modified the standard relaxation model of the dielectric constant, incorporating the effects of electrical conductivity (as illustrated in Fig.1.12 (b)). The HN model is given as follows [52]:

$$\varepsilon^* = \varepsilon_\infty + \frac{\varepsilon_s - \varepsilon_\infty}{(1+(j\omega\tau)^{1-\alpha})^\beta} - j\frac{\sigma^*}{\varepsilon_0 \omega^s} \tag{1.25}$$

The terms ε_s and ε_∞ represent the dielectric constant at low and high frequency regimes, respectively. The exponents α and β in the above equation represent the breadth and asymmetry of the dielectric spectrum. In an ideal Debye relaxation, $\alpha = 0$ and $\beta = 1$ indicating a single and symmetric relaxation process. The complex conductivity, $\sigma^* = \sigma_1 + j\sigma_2$ includes contributions from both free charge carriers (σ_1) and space charges (σ_2).

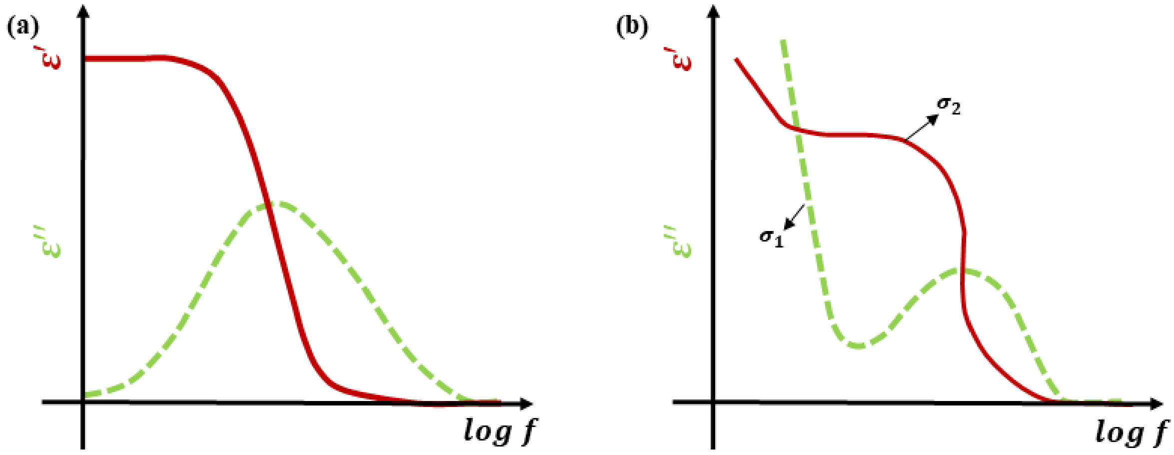

Fig. 1.12: The schematic representation of real and imaginary components of dielectric constant with logarithmic frequency in (a) an ideal Debye type relaxation and (b) non-ideal Debye case.

1.9.3 ac conductivity

ac conductivity σ_{ac} in dielectric materials is related to the imaginary component of the dielectric constant (ε'') which reflects energy losses due to polarization and relaxation processes. The relationship is given by [53]:

$$\sigma_{ac}(\omega) = \omega\varepsilon_0\varepsilon'' \tag{1.26}$$

here, ε_0 is $8.854 \times 10^{-12}\, F/m$ showing the permittivity in free space. ac conductivity in dielectric materials typically displays two distinct frequency-dependent regions as shown in Fig. 1.13 (a). In the low-frequency region, conductivity tends to show dc like behaviour where it remains relatively constant. This stability is attributed to the translation motion of free charges over longer distances which is often dominated by bulk or grain boundary contributions (displayed in Fig. 1.13 (b)). As the frequency increases, σ_{ac} begins to increase with frequency. This rise in conductivity is often associated with localized or short-range hopping of charge carriers. At these higher frequencies, charges cannot migrate over long distances but instead oscillate in response to the alternating field with mechanisms such as dipole relaxation or ion hopping coming into play (refer to Fig. 1.13 (c)). These two distinct regions offer valuable insight into the transport mechanisms and structural characteristics of materials, including the roles of grain boundaries, defect sites and other microstructural features.

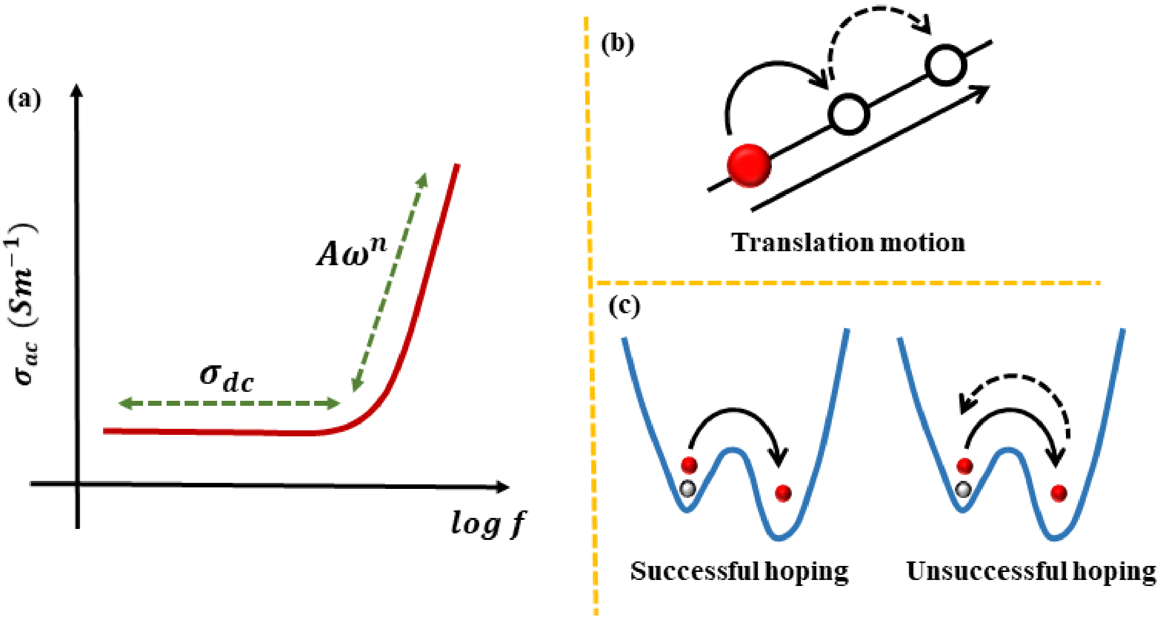

Fig. 1.13: Pictorial diagram of (a) variation in ac conductivity with frequency, (b,c) different types of motion of charge carriers within dielectric material.

At constant temperature, the AC conductivity can be investigated by Jonscher's Power law (JPL) as follows [54]:

$$\sigma_{ac}(\omega) = \sigma_{dc} + A\omega^n \tag{1.27}$$

where, σ_{dc} is the frequency independent region or plateau region while, the secondary term of the equation represents the frequency dependent dispersion phenomenon. Also, A is a constant and n represents frequency exponent which shows the amount of interaction between lattice and mobile ions within that lattice. Generally, n lies between 0 and 1 but sometimes it exceeds. When $n < 1$, the conductivity is associated with the translational movement of charge carriers. Conversely, for $n > 1$, it is linked to localized or reorientational hopping motion where electrons move back and forth between two charge defect sites [55].

1.10 Literature survey on Rare Earth Iron Garnets

RIGs are discovered way back in 1956 by Bertaut and Forrat. Further, in 1957 Bertaut and Pauthenet have studied the structural and magnetic properties of various rare earth-based garnets such as $Y, Sm, Ho, Gd, Tb, Er, Lu, Bi, Dy, Yb$ and Tm [56]. Initially, they gained attention for applications in magneto-optics, microwave devices, and magnetic storage. Over time, their tunable magnetic, dielectric, and optical characteristics made them valuable in areas like telecommunications, sensing, and spintronics. Research continues to explore new compositions to enhance their functionality for advanced electronic and photonic applications.

In RIG, the moment of three Fe^{3+} (d) (up spin) ions get antiferromagnetically coupled with two Fe^{3+} (a) (down spin) ions which results in net one Fe^{3+} ion moment i.e., $5\mu B$. This resultant moment will also be coupled antiferromagnetically with the rare earth ion moment. The arrangement of magnetic spins is demonstrated in Fig. 1.14. So, overall RIGs exhibit ferrimagnetic ordering with a T_c at around $550\ K$. Hence, the receding and strengthening of superexchange interaction among $Fe(a) - O - Fe(d)$ network primarily decides the trend of T_c. The overall magnetic moment of RIG can be interpreted as:

$$M_{net} = 3M_{Fe(d)} - 2M_{Fe(a)} - 3M_{R(c)} \tag{1.28}$$

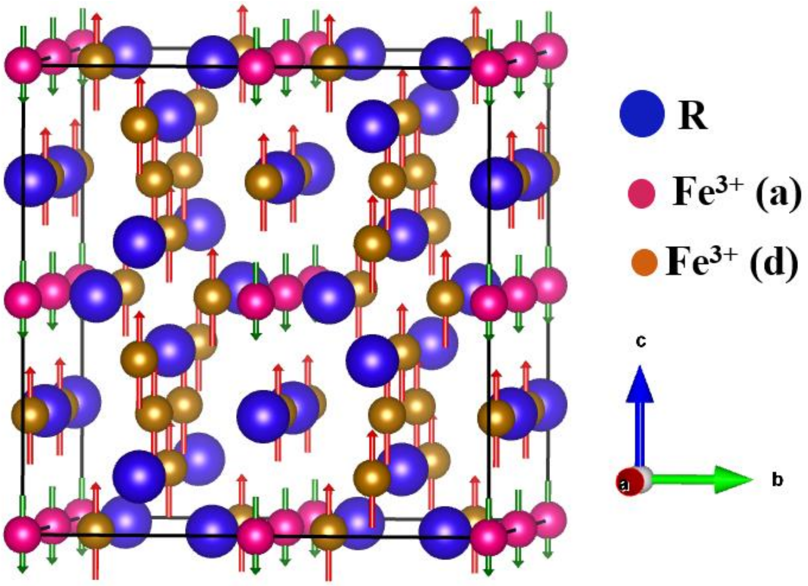

Fig. 1.14: The arrangement of magnetic spins of Fe^{3+} (a) and Fe^{3+} (d) site as down and up spins, respectively in a rare earth iron garnet system.

The magnetic moment of Sm^{3+} ions interacts with Fe^{3+} ions in Samarium iron garnet (SmIG) and leads to the spin reorientation transition (SRT) at around $65\ K$. It has been reported that substituting Al in SmIG does not significantly affect this SRT temperature due to doping of non-magnetic element [57]. Other than SmIG, only a few garnet systems exhibit spin reorientation transition that are HoIG, ErIG, DyIG [26,81]. Rivera *et al*. [58] discovered that synthesizing $Sm_2Gd_1Fe_5O_{12}$ using the citrate method enhances its magnetic properties that reduces the coercivity to 90 Oe and increases the remnant magnetization to above $0.33\ \mu B/f.u$. This makes the material useful for cost-effective transformers and microwave switches. Additionally, Huang *et al*. [59] observed two dielectric relaxations in SmIG. The hopping of electrons between Fe^{2+} and Fe^{3+} ions is responsible for the relaxation in the high frequency zone and the relaxation in the low frequency region is due to translation motion of charge carriers. In the low frequency band $(< 10^4\ Hz)$, they noticed high dielectric permittivity and minimal dielectric loss which makes SmIG an important material for microwave applications.

Gadolinium iron garnet (GdIG) exhibits interesting magnetic and dielectric properties due to the presence of magnetic rare-earth element (Gd) and its weak interaction with the net ferrimagnetic moment of Fe^{3+} ions [60]. A magnetic compensation around $290\ K$ is reported in this compound and it is mostly due to the competition between moments of Fe ions at two different sublattices. In addition, it is reported to exhibit room temperature magneto-caloric effect for potential application in magnetic refrigeration [61]. Other RIGs (R = Dy, Ho, Tb and Er) undergo magnetic compensation but with a lower compensation temperature as compared to that of GdIG [62]. Even though magnetic compensation is observed in the above discussed RIG, they generally do not show negative magnetization below magnetic compensation temperature (T_{comp}) but the magnetization starts increasing for $T < T_{comp}$. This can be attributed to the flipping of magnetic spins of all three magnetic sublattices due to a relatively small magnetic anisotropy [63]. On the other hand, $Gd_1Sm_2Fe_5O_{12}$ exhibits negative magnetization below T_{comp} due to the strong magnetocrystalline anisotropy introduced by Sm^{3+} ions. Similarly, some of the other RIG, such as Bi substituted $Tb_3Fe_5O_{12}$ and $Ho_3Fe_5O_{12}$ also hold magnetization reversal below T_{comp} [49,88]. Rajan *et al.* [64] have reported that Bi-substitution at Gd site gives rise to enhanced dielectric constant and bigger grain size.

The high value of magnetic moment of Dysprosium iron garnet (DyIG) i.e., 10.6 μB is responsible for its applicability in energy storage devices. Additionally, nanosized DyIG demonstrates approximately 2 kOe higher coercivity than bulk DyIG rendering it suitable for hard magnet applications [65]. Many researchers have studied the magnetic and dielectric properties of DyIG either by substitution or by using different synthesis processes. For instance, Ahmed *et al.* [66] have used the citrate auto-combustion technique to produce nanocrystals of Strontium substituted DyIG. They noticed that introducing Sr into DyIG increased its T_c to 610 K. Additionally, they found that the dielectric constant rises from 10^2 at room temperature to 10^4 at 850 K. Tholkappiyan *et al.* [67] observed that Co substituted DyIG improved saturation magnetization, remnant magnetization, coercivity, and anisotropy. Moreover, Lahoubi et al. [68] confirmed the SRT in DyIG material by detecting an anomaly in the specific heat plot around the SRT temperature which is approximately 14.5 K.

In 2015, Rost *et al.* [69] introduced the concept of high-entropy oxides that consist of five or more elements with nearly equimolar ratios within a unified solid solution. Since then, research on these high-entropy oxides has expanded significantly, leading to the development of a wide range of high-entropy materials. For instance, high entropy spinels [70], high entropy perovskites [71], fluorite and bixbyite structured high entropy oxides [72], high entropy pyrochlores [73], magnetoplumbite structured high entropy oxides [74], lanthanide sesquioxides [75], alkali doped $(Co, Cu, Mg, Ni, Zn)_{1-x}M_xO$ $(M = Li, Na, K)$

monoxides [76] and many more are reported. Unlike other traditional materials, high entropy oxide ceramics possess multiple functional physical properties such as profound dielectric constant, low thermal conductivity, electrocatalysis along with mechanical properties [102,103]. In this context, Liu *et al.* [77] have investigated the dielectric properties among $(Y_{0.2}Eu_{0.2}Er_{0.2}Dy_{0.2}Lu_{0.2})_3(Al_xFe_{1-x})_5O_{12}$ high entropy garnet ceramics and found that the dielectric constant gets reduced from 10^4 to 10^2 at 100 Hz frequency with Al substitution. Likewise, Dąbrowa *et al.* [78] have tested the transport properties of $(Dy, Er, Gd, Ho, Y)_3Fe_5O_{12}$ samples and found that the electrical conduction in lower temperature region is very low due to the Fe^{3+} ions present at distorted octahedral and tetrahedral sites. On the other hand, Chen *et al.* [79] have studied the structural and magnetic characteristics of $(Gd_{0.2}Dy_{0.2}Er_{0.2}Y_{0.2}RE_{0.2})_3Fe_5O_{12}$ $(RE = Sm, Eu, Tm, Yb)$ garnet ferrite samples and reported the saturation magnetization values around 13 emu/g for these samples.

1.11 Motivation

Based on the above literature survey, we can conclude that GdIG, SmIG, DyIG, and high entropy garnet ceramics exhibit remarkable magnetic and dielectric properties. However, there is a lack of detailed investigation into the magneto-electric coupling, the magneto-caloric effect and thorough magnetization and dielectric studies. Specifically, the exploration of these phenomena by tuning magnetic exchange interactions through the substitution of suitable magnetic or non-magnetic ions at rare earth site is insufficient. As per our literature survey, GdIG substituted with Ho and Nd, as well as DyIG substituted with Ho, have not yet been synthesized for magnetic and dielectric characterizations. However, few reports are available for Ho substituted SmIG series but detailed investigation is still required. Moreover, in general, ferroelectric materials exhibit magneto-electric coupling. However, recent studies have shown that non-ferroelectric material such as $CaCu_3Ti_4O_{12}$ also exhibits a large dielectric constant that can be attributed to Maxwell-Wagner type polarization.

Interestingly, the Ho and Nd substitution in GdIG leads to the magneto-dielectric coupling. Further, Ho substitution in SmIG resulted in novel negative magnetization introduced by the high magnetocrystalline anisotropy of Ho^{3+} ions. Moreover, the magneto-caloric effect was already reported for DyIG samples but when it is doped with Ho, the magnetic entropy change has been raised which reflects their suitability for magnetic refrigeration applications. The dielectric properties of polycrystalline materials are greatly influenced by their microstructure and heterogeneity, including grains and grain boundaries. Therefore, we have also attempted to tune the impedance spectra of Ho substituted SmIG and GdIG series. Furthermore, the high entropy garnets are rarely studied so far hence, they require in depth investigation on magnetic and dielectric characteristics. Interestingly, we have again obtained magneto-dielectric relations in the synthesized high entropy garnet compounds. So, the substitution of these cations will also tune rest of the properties like magnetic saturation, magnetocrystalline anisotropy, different magnetic transition temperatures including spin reorientation transition and magnetic compensation, conductivity and permittivity for specific type of applications. In the present thesis, we have conducted an extensive investigation into the magnetic and dielectric properties of several rare earth iron garnet compounds. The chosen samples for above investigation are as follows:

5. $(Gd_{1-x}Ho_x)_3Fe_5O_{12}$ ($x =$ 0.0 to 1.0)
6. $(Gd_{1-x}Nd_x)_3Fe_5O_{12}$ ($x =$ 0.0 to 0.4)
7. $(Sm_{1-x}Ho_x)_3Fe_5O_{12}$ ($x =$ 0.0 to 1.0)
8. $(Dy_{1-x}Ho_x)_3Fe_5O_{12}$ ($x =$ 0.0 to 1.0)
9. High entropy garnet ceramics i.e., $(Gd_{0.2}Y_{0.2}Nd_{0.2}Dy_{0.2}R_{0.2})_3Fe_5O_{12}$ ($R = Er, Sm,$ Pr)

All the above-mentioned samples were characterized by various sophisticated instruments. The phase purity is tested with X-Ray diffractometer (XRD), surface morphological studies are carried out with Field Emission Scanning Electron Microscope (FESEM) and Transmission Electron microscopy (TEM), phonon modes are detected with Raman Spectrometer and the oxidation states of different cations are determined with X-Ray Photoelectron Spectroscopy (XPS). Further, the low and high temperature magnetic measurement were held with Physical Property Measurement System (PPMS) and Vibrating Sample Magnetometer (VSM), respectively. The furnace connected with LCR meter is utilized for the dielectric measurements. So, the sample preparation technique and detailed explanation of all the instrumentation has been briefly discussed in Chapter 2.

Chapter 2

Synthesis and Experimental Techniques

This chapter outlines the various experimental methods and equipment employed for material synthesis, characterization and physical property measurements. In our research, we used solid-state method to synthesize samples. All the powder precursors were manually grinded and kept for presintering and sintering in high-temperature commercial furnaces. The synthesized samples were then characterized using advanced instrumentation. XRD was used to analyze powder diffraction patterns, assessing phase purity and crystal structure. Microstructural morphology was examined with a FESEM and compositional analysis was performed through Energy Dispersive X-ray (EDX) Spectroscopy. Raman spectra were measured using a Micro-Raman spectrometer to investigate vibrational modes and the oxidation states of different cations were determined by XPS. Magnetic properties were assessed by measuring temperature and field-dependent magnetization using a VSM and PPMS. Additionally, an LCR meter was utilized to record the complex impedance spectra across various frequencies and temperatures. Each of these experimental techniques is detailed in the following sections.

2.1 Sample preparation methodology

Generally, materials typically do not form as a single phase at ambient temperature due to limited diffusion among constituent elements. To overcome these kinetic barriers, heat treatment is applied through two processes: presintering and sintering. Presintering is an initial heat treatment stage where the starting compounds are decomposed and the intended phase starts forming. It helps to remove binders, reduce porosity and initiate the formation of bonds between particles. Then, sintering is the subsequent higher-temperature process where the material is heated close to its melting point leading to densification and strong bonding between particles. This final stage improves the material's structural integrity resulting in a dense, solid product with enhanced mechanical and physical properties.

Solid-state reaction method

All the samples presented this thesis were synthesized via solid-state reaction approach. This method offers several advantages. It is a relatively simple and cost-effective approach making it suitable for large-scale production. This method enables the production of high-purity and homogenous materials as the process parameters can be controlled to influence particle size and morphology. Solid-state reactions are versatile and applicable to a broad range of materials, including ceramics, magnetic materials and other compounds that require precise structural and compositional control.

First of all, the precursors were taken in oxide forms such as Gadolinium oxide (Gd_2O_3), Holmium oxide (Ho_2O_3), Neodymium oxide (Nd_2O_3), Samarium oxide (Sm_2O_3), Dysprosium oxide (Dy_2O_3), and iron oxide (Fe_2O_3) with purity more than 99%. The required oxides were weighed in stoichiometric ratio with Mettler Toledo (model no. AG135) make electronic weighing balance with an accuracy of $\pm 0.01\,mg$. All the oxides were mixed uniformly in the acetone medium for about 3 to 4 hours using agate mortar pestle. The grinded powder is then transferred to an alumina crucible and kept for presintering at $800°C$ for 12 hours. Further, the obtained powder was pressed in form of pellets in KBr press provided by Techno-search instruments by applying a pressure of $2.98 \times 10^8\ N/cm^2$. These pellets were prepared using a stainless-steel die of $10mm$ diameter and the thickness is kept almost $1.5mm$. These pellets were then sintered in a temperature range of $1473K$ to $1673K$ that may vary for different series. In between presintering and sintering process, the samples were grinded and kept in furnace over and again to achieve a dense morphology. The schematic representation of the solid-state reaction method is shown in Fig. 2.1.

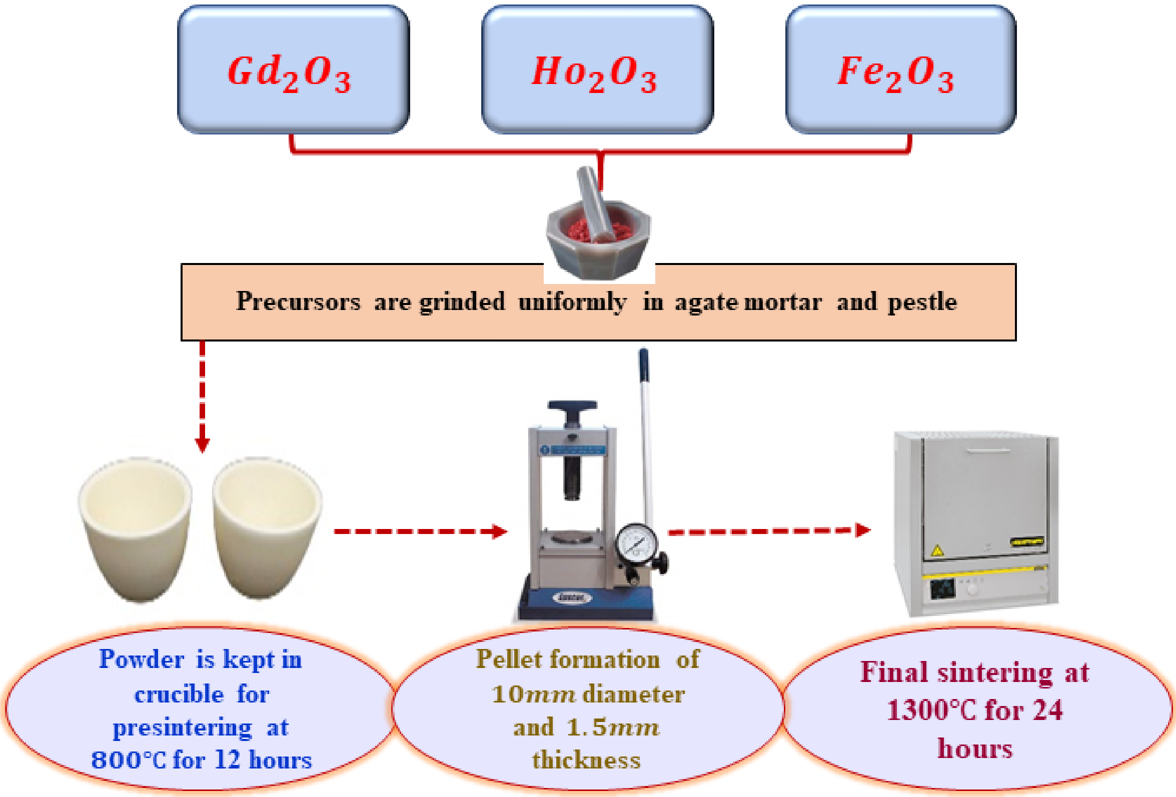

Fig. 2.1: Schematic diagram of solid-state reaction method.

2.2 High Temperature Furnace

In this thesis, the heat treatment of precursors was conducted using commercial tabletop high-temperature furnaces (model HTCT 03/15) with a maximum operating temperature of 1873 K. These furnaces were supplied by K.G. Projects and Equipment and manufactured by Nabertherm, Germany. A labelled diagram of the high-temperature furnace along with its accessories is presented in Fig. 2.2. The furnace body was constructed from stainless steel and featured a dual-shell design to minimize heat transfer to the outer surface and surrounding environment. The temperature is regulated with a PID controller with model no. $C450$ and a S-type thermocouple (Platinum Rhodium - 10% Platinum) was used as the temperature sensor. High-quality silicon carbide (Si-C) rods served as the heating elements, while a solid-state relay managed the switching system that controls to turn on the power of Si-C rods. The temperature controller offers an accuracy of $\pm 1\ K$. The furnace operates at $380\ V\ -\ 400\ V$ ($50\ Hz, 3$ −phase) with a current rating of $20\ A$.

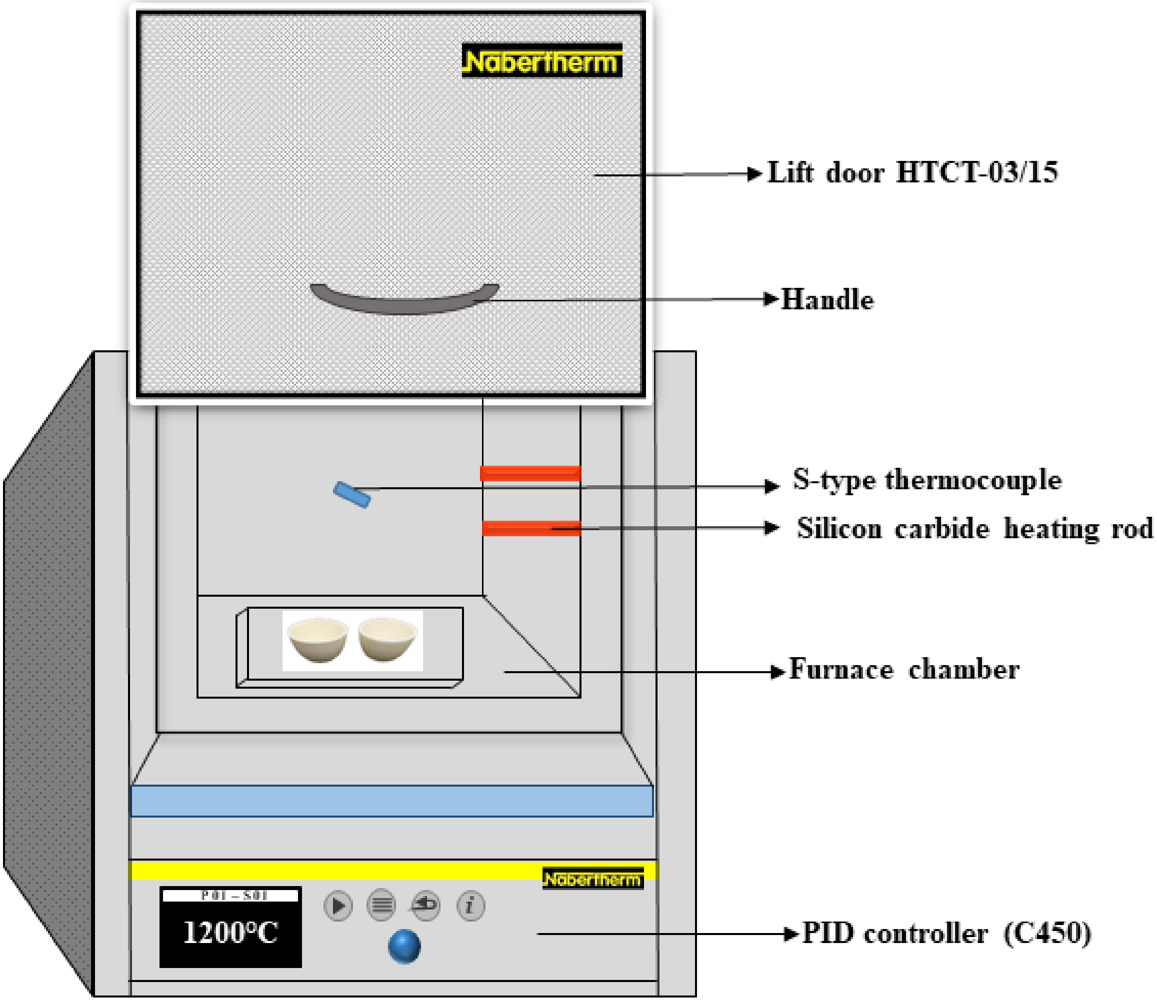

Fig. 2.2: Pictorial diagram of high temperature furnace with all the elements.

2.3 Structural characterization

2.3.1 X-Ray Diffraction

Powder X-ray diffraction (XRD) is a technique used to study the crystal structure of crystalline materials. When X-rays are directed onto a powdered sample, they are scattered by the atoms in a way that creates a unique diffraction pattern. This pattern can be analyzed to determine the crystal structure, lattice parameters, crystallite size, phase composition, and other structural information about the sample. The principle of X-Ray diffraction pattern is explained by the Bragg's law and it provides the fundamental relationship governing diffraction patterns. It states that constructive interference of X-rays occurs when the path difference between rays scattered by atomic planes is an integer multiple of the X-ray wavelength. Mathematically, Bragg's Law is given by [80]:

$$2dsin\theta = n\lambda \tag{2.1}$$

where n is an integer (order of reflection), λ is the wavelength of the X-Ray, d is the distance between atomic planes and θ is the glancing angle also known as Bragg angle. This law forms the basis of crystallographic analysis in XRD. The entire process involved in diffraction of X-Rays has been demonstrated in Fig. 2.3 (a).

For this thesis, XRD patterns were recorded at room temperature using a Rigaku TTRAX III X-ray diffractometer with a $\theta - 2\theta$ rotating anode configuration. The instrument utilizes $CuK\alpha$ radiation with a wavelength of 1.5406 Å generated by maintaining the X-ray source at a voltage of 50 kV and a current of 220 mA. The principles of powder XRD in the Bragg-Brentano geometry are depicted in Fig. 2.3 (b). In this setup, both the X-ray source and detector are positioned equidistantly from the sample holder. The X-ray source (F1), the sample, and the detector slit (F2) are aligned along a circle ensuring that X-rays diffracted by an angle of 2θ arrive precisely at the detector. This arrangement, with the X-ray tube and detector aligned around the sample creates optimal focusing conditions. Data collection was performed in a standard $\theta - \theta$ scan mode, spanning 2θ angles from 20° to 80°, with a step size ($\Delta\theta$) of approximately 0.02° and a scan speed of 3° per minute.

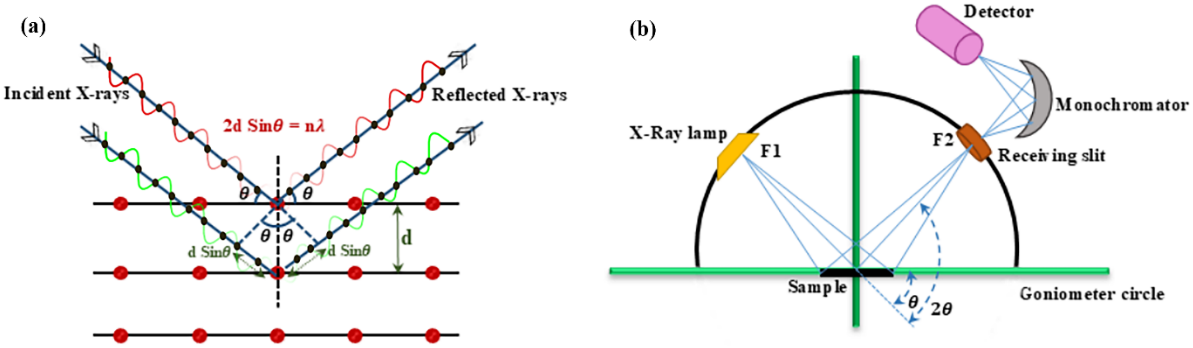

Fig. 2.3: (a) Bragg's law schematic and (b) representation of ray diagram of XRD or Bragg-Brentano geometry.

The XRD patterns of the samples were analyzed using the Rietveld refinement technique via the FullProf suite program [81]. The background intensity was modelled with a polynomial function while the peak shapes were fitted using the Pseudo-Voigt function. During refinement, the global parameters such as the polynomial coefficients for background, scaling factor, peak width parameters (u, v, w) and lattice constants (a, b, c) were varied. Additionally, nuclear structure variables including fractional atomic coordinates (x, y, z), isotropic displacement parameters, and occupancy values were refined. Here, occupancy refers to the normalized chemical occupancy relative to the multiplicity of general positions in the space group. Oxygen occupancy was fixed at 1 (100%) and not varied during refinement. The refinement quality was assessed based on several reliability factors, such as $R_p, R_{wp}, R_{exp}, R_{Bragg}, R_F$ and χ^2, which are defined below one by one [82].

Profile factor is defined as follows:

$$R_p = \frac{\sum_{i=1,n}|y_i - y_{c,i}|}{\sum_{i=1,n} y_i} \times 100 \tag{2.2}$$

here, y_i represents the observed data, $y_{c,i}$ is the calculated data and n denotes the total number of data points. Then, weighed profile factor is given as:

$$R_{wp} = \left[\frac{\sum_{i=1,n}\omega_i|y_i - y_{c,i}|^2}{\sum_{i=1,n}\omega_i y_i^2}\right]^{1/2} \times 100 \tag{2.3}$$

here, $\omega_i = \frac{1}{\sigma_i^2}$ and σ_i is the variance of y_i. Expected weight factor is:

$$R_{exp} = \left[\frac{|n-p|}{\sum_{i=1,n}\omega_i y_i^2}\right]^{1/2} \times 100 \tag{2.4}$$

where, the degree of freedom is presented by $|n - p|$ with n be the total number of data points and p is the refined parameters. Then, goodness of fit or reduced chi-square is given as:

$$\chi^2 = \left[\frac{R_{wp}}{R_{exp}}\right]^2 \tag{2.5}$$

Bragg factor is deduced as follows:

$$R_{Bragg} = \frac{\sum_h |I_{obs,h} - I_{cal,h}|}{\sum_h I_{obs,h}} \times 100 \tag{2.6}$$

here, h denotes a specific hkl Bragg peak, while $I_{obs,h}$ and $I_{cal,h}$ represent the observed and calculated integrated intensities, respectively. Further, crystallographic R_F factor can be determined as follows:

$$R_F = \frac{\sum_h |F_{obs,h} - F_{cal,h}|}{\sum_h F_{obs,h}} \times 100 \tag{2.7}$$

here, $F_{obs,h}$ and $F_{calc,h}$ represent the observed and calculated structural factors, respectively. The crystal structure of RIGs was generated using Visualization for Electronic and Structural Analysis (VESTA, version 4.3.0) software.

2.3.2 Field Emission Scanning Electron Microscope

Field Emission Scanning Electron Microscopy (FESEM) is an advanced imaging technique used to obtain high-resolution images of the surface morphology and microstructure of materials. It uses a field emission gun as an electron source which produces a highly focused, low-energy electron beam, allowing for enhanced surface detail and clarity especially at nanoscale resolutions. It provides information about the surface morphology of variety of samples such as chemical, biological, magnetic materials etc. up to very high magnification from $10X$ to $300kX$. The in-lens FESEM enables imaging at ultra-high magnifications.

The used electron gun is a zirconium oxide-coated tungsten (ZrO_2/W) emitter which operates in thermally assisted Schottky emission mode. This type of gun generates a narrow, high-energy electron beam, enhancing spatial resolution while reducing sample damage from charging effects. An extreme vacuum and high electric field gradient are applied for electron acceleration with an acceleration voltage between the electron gun and anode typically ranging from 0.5 to 30 kV. In high vacuum conditions, primary electrons are focused and directed by the second condenser lens (a magnetic lens) to produce a narrow scanning beam that bombards the specimen. This bombardment generates various types of emitted electrons, as shown in Fig. 2.4.

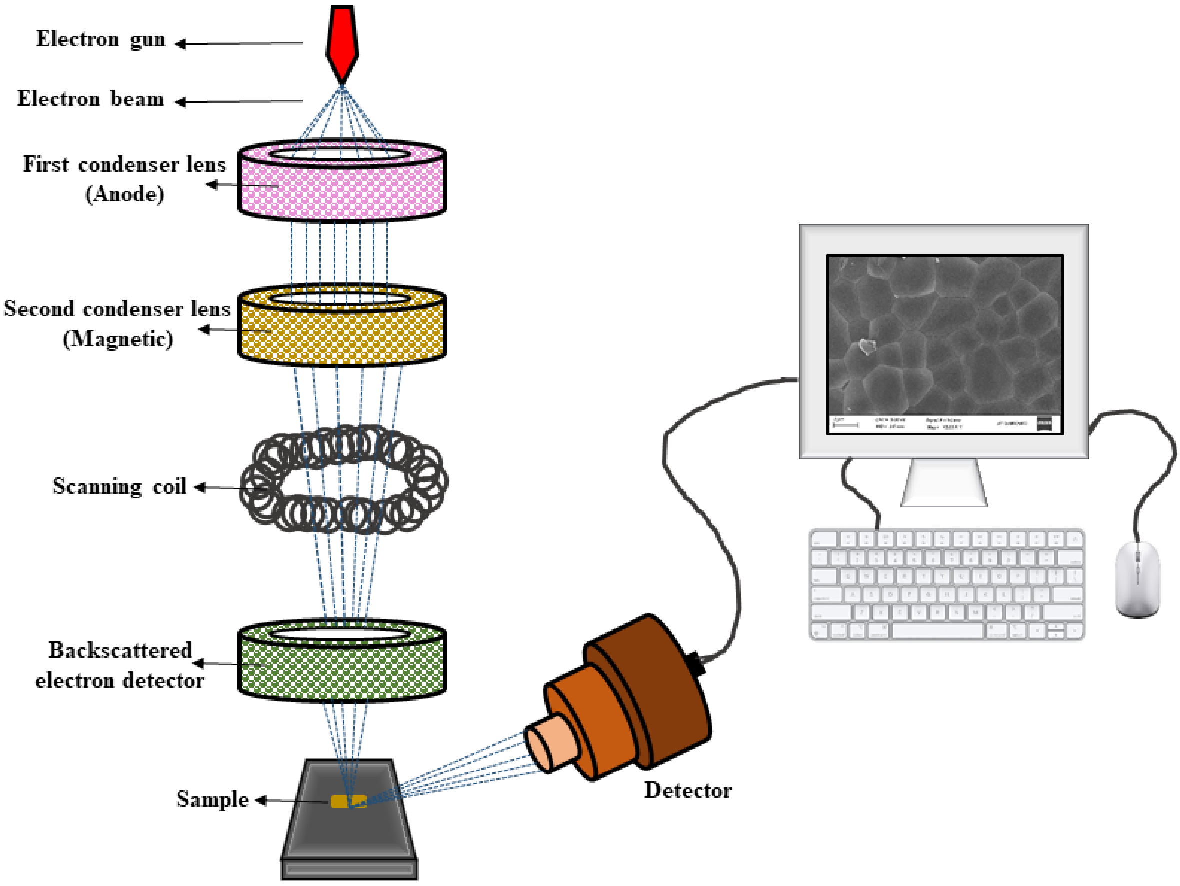

Fig. 2.4: Schematic diagram of FESEM with all the lens.

Upon electron impact, the interaction volume within the sample takes on a droplet shape and electrons dislodged from the surface are known as secondary electrons (SE). A highly efficient annular in-lens detector captures these SEs to create a detailed image of the sample surface. In addition to SEs, other emissions including backscattered electrons (BSE), characteristic X-rays, cathode luminescence, Auger electrons, and continuum X-rays are also produced. BSEs, which are more energetic than SEs and have a specific directional path are classified as any emissions above $50\,eV$. These electrons are not collected by the SE detector unless it is directly in their path. BSE imaging is particularly valuable for differentiating materials as its yield increases monotonically with the atomic number (Z) of the specimen (approximately $\sim 0.05\, Z^{1/2}$). This technique can differentiate between elements with atomic number differences of at least three. The energy spectrum of the electrons emitted from the specimen surface is illustrated in Fig. 2.5. To make the samples conductive, they were coated with a thin layer ($1.5 - 3.0\, nm$) of gold. The FESEM analysis for this thesis was conducted using a ZEISS Sigma 300 model.

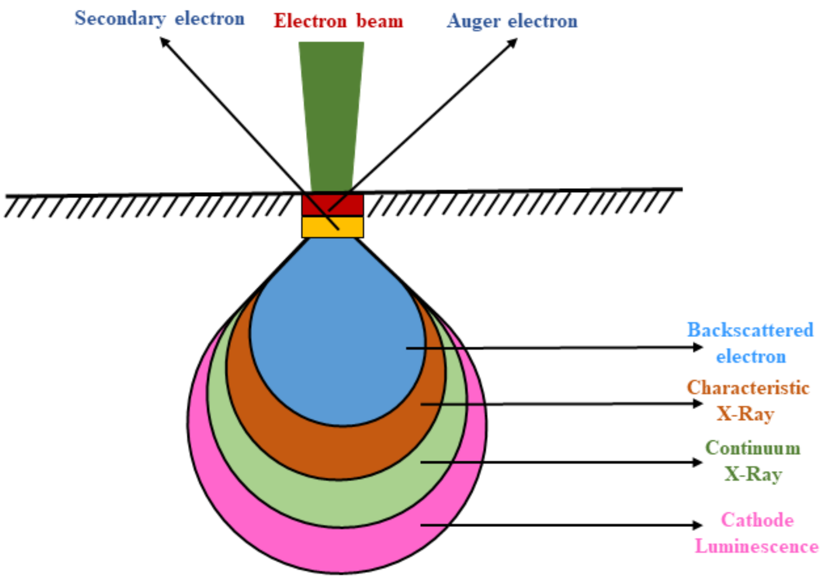

Fig. 2.5: Scattering of electrons and photons from the droplet-shaped interaction volume within the sample.

2.3.3 Energy Dispersive X-Ray Spectroscopy

The Energy Dispersive X-ray spectrometer (EDX) attached to the FESEM, provides elemental and compositional information about the specimen under investigation. Each element has a unique atomic structure that emits characteristic X-rays. To induce this emission, a high-energy beam of charged particles such as electrons or protons or an X-ray beam, is focused on the sample. This excitation dislodges some inner-shell electrons which are then replaced by outer-shell electrons, releasing characteristic X-rays in the process. The elements within the sample can be identified by measuring the energy of these emitted X-rays. The resulting EDX spectrum displays peaks corresponding to specific energy levels with peak position and intensity indicating the elements present and their relative concentrations. For this thesis, the EDX spectra of samples were recorded using a ZEISS SIGMA FESEM equipped with an Oxford EDX system.

2.3.4 Transmission Electron Microscopy

Transmission electron microscopy (TEM) is a technique where an image is created by passing an electron beam through a thin sample (usually less than 100 nm thick) suspended on a grid. The interaction of the electron beam with the sample is similar to that in FESEM; however, TEM uses transmitted electrons to form an image instead of secondary electrons. This transmitted image is then magnified and projected onto an imaging device such as a fluorescent screen connected to a sensor. Fig. 2.6 illustrates the structure of a TEM which comprises four main components: (i) an electron gun, (ii) condenser system, (iii) an imaging system and (iv) an image recording system. Similar to FESEM, the TEM's electron beam is generated by an electron gun which consists of a heated tungsten filament acting as a cathode. The beam is accelerated by an anode and directed through an aperture. The condenser system focuses the electron beam onto the sample after which the imaging system consisting of objective and intermediate lenses, focuses the transmitted electrons to create a highly magnified image of the sample. This magnification is further enhanced by the projector lenses. Finally, the image recording system converts the electron image into a visible format using a fluorescent screen for viewing. For the measurements in this thesis, a JEOL TEM (model 2100 F) was used.

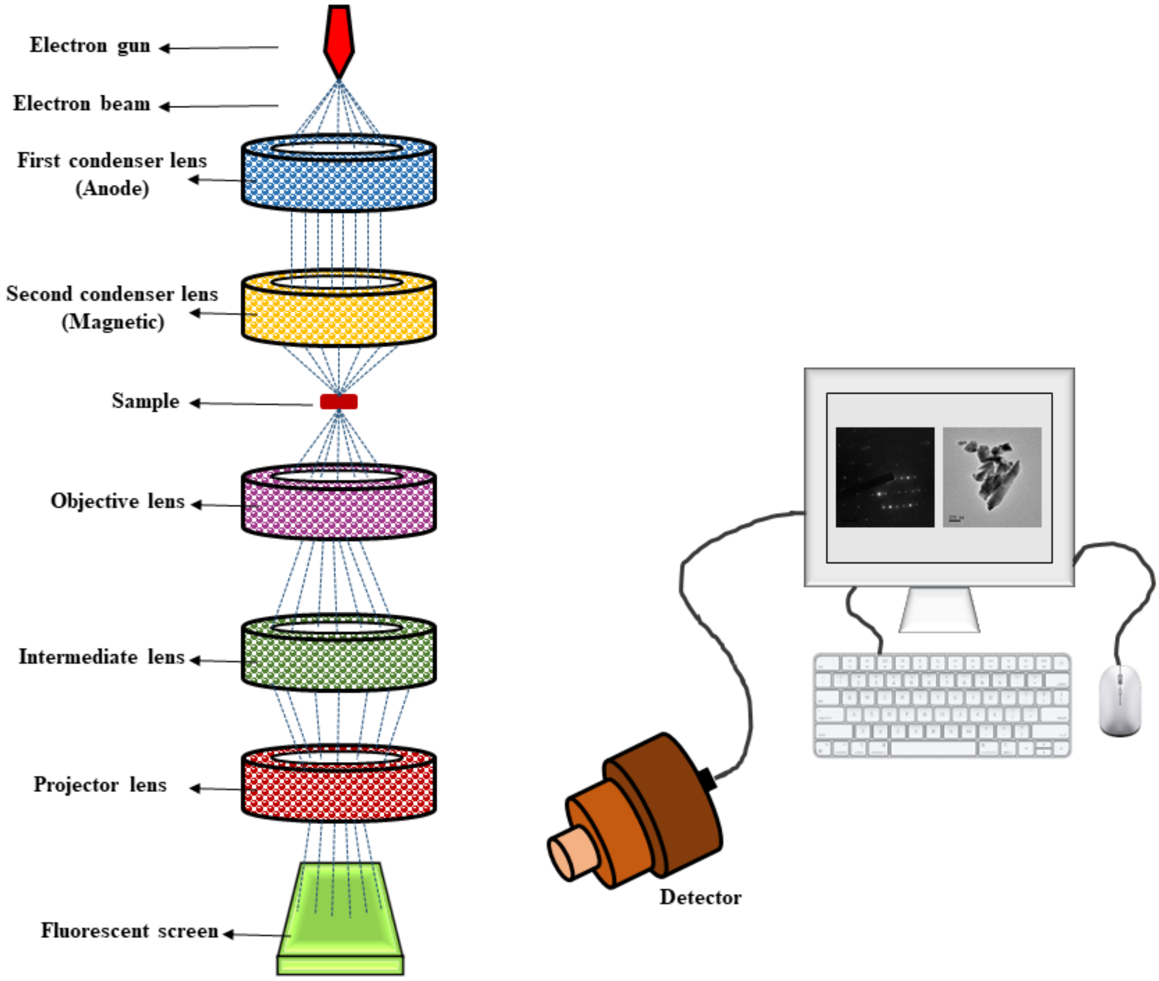

Fig. 2.6: Schematic for the instrumental setup of TEM.

2.3.5 Raman Spectroscopy

Raman scattering was discovered by C. V. Raman in 1928, an achievement that led to him being awarded the Nobel Prize in 1930. Raman spectroscopy is a powerful analytical technique used to observe translational, vibrational, rotational, and other low-frequency modes in molecules. By measuring the inelastic scattering of monochromatic light (usually from a laser), it provides a molecular "fingerprint" that can identify substances and analyze molecular composition and structure.

The principle of Raman scattering originates from the quantum theory of radiation. When monochromatic light of frequency ν_0 interacts with a sample, it engages with the molecular vibrations within. In case of elastic scattering better known as Rayleigh scattering, the frequency of the scattered light remains the same as that of the incident light. However, a small fraction of incident photons either transfer or absorb energy from the sample due to molecular vibrational or rotational changes resulting in a frequency shift in the scattered light. This phenomenon is known as Raman scattering. The frequency shift, or Raman shift, can be expressed as $\Delta\nu = \nu_0 - \nu_s$, where ν_s is the frequency of the scattered light. If energy is transferred from the incident light to the molecules, the scattered light undergoes a red-shifted frequency, known as a Stokes shift ($\Delta\nu = +ve$). Conversely, if the molecules are already in an excited state and transfer energy to the incident photons, the scattered light exhibits a blue-shifted frequency which is referred to as an anti-Stokes shift ($\Delta\nu = -ve$). The Raman activity of a compound depends on the polarizability of its molecules. The intensity of Raman scattering is directly related to the degree of molecular polarization which arises from the stretching or bending of bonds. According to the Raman selection rule, molecular vibrations occur when the constituent atoms displace from equilibrium positions, leading to a change in molecular polarizability, thus enabling Raman scattering.

Raman spectrometers are generally categorized into two types: dispersive and non-dispersive. Dispersive spectrometers utilize a diffraction grating to analyze the light scattered from a sample, whereas non-dispersive spectrometers rely on a Michelson interferometer. In this thesis, the dispersive Raman spectra of the samples were recorded using a micro-Raman spectrometer (LabRam HR 800, Horiba Jobin Yvon) at room temperature, with an argon laser operating at a 514 nm or 633 nm wavelength as the excitation source. A schematic diagram of a dispersive Raman spectrometer is shown in Fig. 2.7. In this setup, a beam splitter divides the laser beam from the source into two equal parts. When the laser interacts with the sample, both Rayleigh and Raman scattering occur; however, a notch filter selectively permits only the Raman-scattered wavelengths to pass. The scattered light then passes through a grating and an etalon which effectively resolve the weak inelastic scattered wavelengths from the sample. Finally, the beam enters a charge-coupled device (CCD), where the system detects changes in the sample's polarizability based on wavelength shifts and converts this information into an intensity profile.

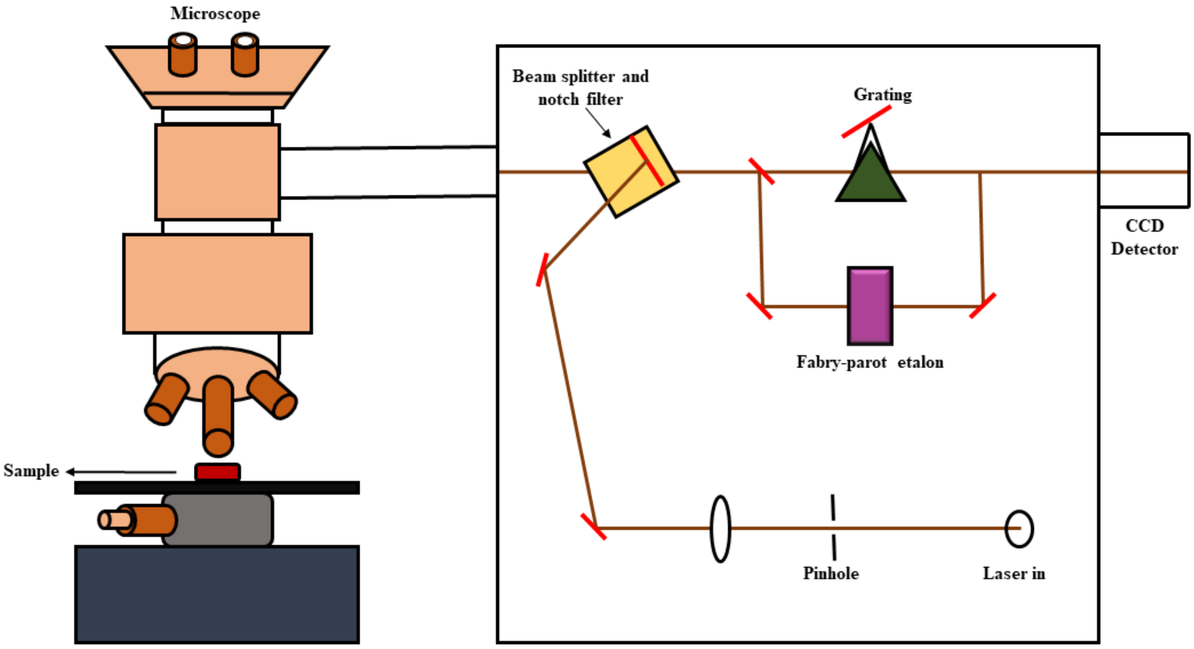

Fig. 2.7: Schematic diagram of Raman spectrometer and the related ray diagram.

2.3.6 X-Ray Photoelectron Spectroscopy

X-ray photoelectron spectroscopy (XPS) is an analytical technique used to study the elemental composition, oxidation states and their binding energy of a material's surface. When a material is irradiated with X-rays, it emits photoelectrons and XPS measures the kinetic energy of these emitted electrons to determine the binding energies characteristic of specific elements and their chemical states. With a typical analysis depth of just a few nanometers, XPS provides precise and surface-sensitive information. The binding energy along with the intensity of these peaks, allows for the identification of the electron configuration ($e.g., 1s, 2s, 2p, 3s,$ etc.) and the elements present in the material. The relationship between the various energy parameters is expressed by the following equation [83]:

$$E_{kinetic} = E_{photon(hv)} - E_{binding} - \phi \tag{2.8}$$

where, $E_{kinetic}$ and E_{photon} are the kinetic and incident energies of photon, respectively. $E_{binding}$ is the binding energy of any electron to hold it in its state and ϕ is the work function that shows the difference in vacuum energy level (E_v) and Fermi energy level (E_F).

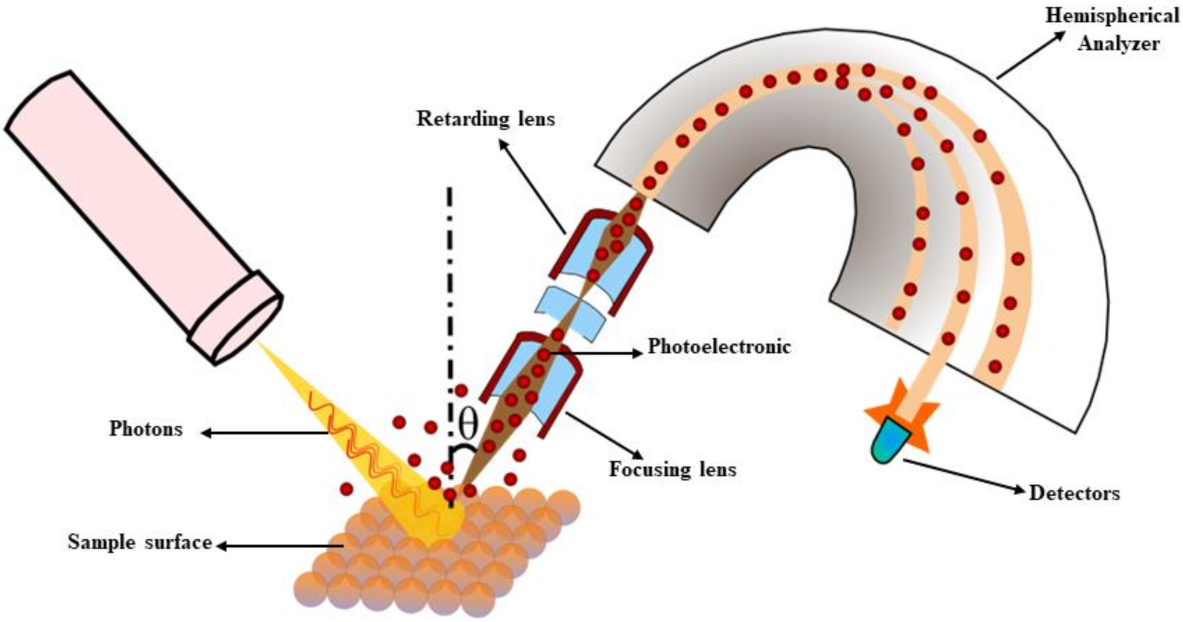

Fig. 2.8: Pictorial representation of XPS setup.

An X-ray beam illuminates the sample, causing electrons to be emitted from the surface with various energies and directions as shown in Fig. 2.8. A portion of these photoelectrons is collected by a system of magnetic and multi-element electrostatic input lenses which direct them to an analyzer. The hemispherical analyzer uses electrostatic fields to selectively permit electrons of a specific energy to reach the detector. To measure electrons of a defined initial kinetic energy, the lens system voltages are adjusted, focusing the electrons onto the entrance slit corresponding to the targeted initial energy. This system also decelerates the electrons so that their kinetic energy aligns with the pass energy of the hemispherical analyzer. For this thesis, measurements were conducted using a ULVAC-PHI, Inc. make PHI5000 VersaProbe III X-Ray Photoelectron Spectrometer with a monochromatic $Al\ K\alpha$ source having a pass energy of $1486.6\ eV$. The binding energy calibration was referenced to the $C\ 1s$ peak at $284.8\ eV$. XPS data fitting was carried out using a Pseudo-Voigt function which combines Lorentzian and Gaussian profiles, via the "XPS Peak41" software. For background fitting of the XPS spectrum, a Shirley function was applied.

2.4 Magnetic characterization

2.4.1 Vibrating Sample Magnetometer

A Vibrating Sample Magnetometer (VSM) is an instrument used to measure the magnetic properties of materials. VSM was first discovered by a scientist named Foner [84]. In VSM, a sample is magnetized within a controlled magnetic field and vibrated at a fixed frequency. The resulting changes in magnetic flux are detected by sensing coils which allow the magnetization of the sample to be quantified. The accuracy to measure magnetic moment by VSM is $5 \times 10^{-6}\ emu$.

The working principle of a Vibrating Sample Magnetometer (VSM) is based on Faraday's law, which states that an electromotive force (emf) is induced in a coil when there is a change in magnetic flux through it. When a small magnetic sample is placed in a uniform magnetic field produced by an electromagnet, a magnetic dipole moment is induced in the sample. By vibrating either the sample or the pickup coil in this magnetic field, a varying magnetic flux is generated leading to an induced voltage in the pickup coils positioned on the electromagnet's pole pieces. This induced voltage is directly proportional to the sample's magnetic moment. The voltage $V(t)$ is detected using a VSM signal detector, typically a Lock-in Amplifier which ensures accurate signal measurement. The magnetic field strength is monitored with a Gauss-meter equipped with analog output capabilities, while a Hall probe that is positioned between the magnetic pole pieces near the sample, provides precise field measurements. A block diagram of the VSM setup and its components is illustrated in Fig. 2.9. In this setup, the sample is kept fixed and coil is vibrating. For high-temperature measurements, a high-temperature oven (Lakeshore, Model 74034) is placed in between the electromagnets. This setup includes a temperature controller that allows precise temperature adjustment from $300\ K$ to $1273\ K$. During these high-temperature experiments, Argon or Nitrogen gas is continuously flowed into the oven to maintain an inert atmosphere. The temperature is monitored with a K-type thermocouple attached to the oven, ensuring accurate readings throughout the experiment.

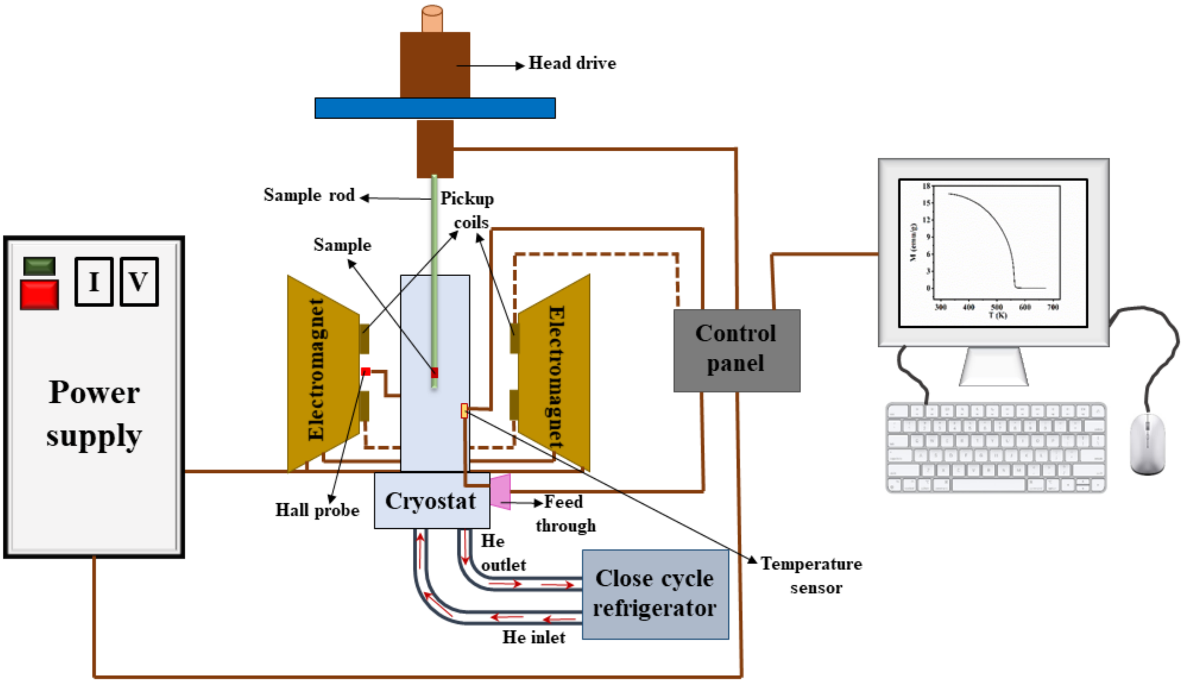

Fig. 2.9: Block diagram of VSM and its accessories.

2.4.2 Physical property measurement system

To measure the magnetic properties of our samples, we used a Quantum Design DynaCool Physical Properties Measurement System (PPMS) equipped with a VSM. This DynaCool PPMS system provides a quick, accurate and fully automated approach for analyzing the magnetic characteristics of materials in bulk, thin film, and powder forms. By oscillating the sample within a pickup coil and synchronously detecting the induced voltage, this setup allows for precise magnetic measurements. The system can detect magnetic moments as low as $10^{-6}\,emu$ at a data rate of $1\,Hz$, utilizing a compact gradiometer pickup coil configuration. This configuration provides a relatively large oscillation amplitude and operates at a frequency of $40\,Hz$. The VSM in the Quantum Design system includes similar components to standard VSMs but uses a superconducting solenoid rather than an electromagnet to generate the magnetic field. A linear transport motor controls both sample vibration and positioning and the pickup coils are housed within the VSM coil section. Fig. 2.10 shows the arrangement of the pickup coils with their protective cover removed.

The pickup coils in the VSM are arranged in a first-order gradiometer configuration with coils wound clockwise and anticlockwise, separated by approximately $1\,cm$. This setup enables faster vibrations with a smaller amplitude of $2\,mm$ and a typical frequency of 40 Hz. The first-order gradiometer, shown here with the Cernox thermometer is part of the measurement setup. The VSM includes two types of pickup coils with different internal bore sizes. One is a standard coil set with a 6 mm bore that offers a sensitivity of around $6 \times 10^{-7} emu$, while the other is a larger coil set with a 12 mm bore and a sensitivity of approximately $1.5 \times 10^{-6} emu$. Moreover, the sample rod is placed into the chamber with the sample mounted at its end. After calibration, the sample is positioned at the centre of the gradiometer pickup coils. The output voltage from the pickup coil is connected to a preamplifier and the VSM module, which includes a lock-in amplifier for phase-sensitive detection. The PPMS system operates with high precision, enabling temperature control in the range of 1.8 K to 300 K.

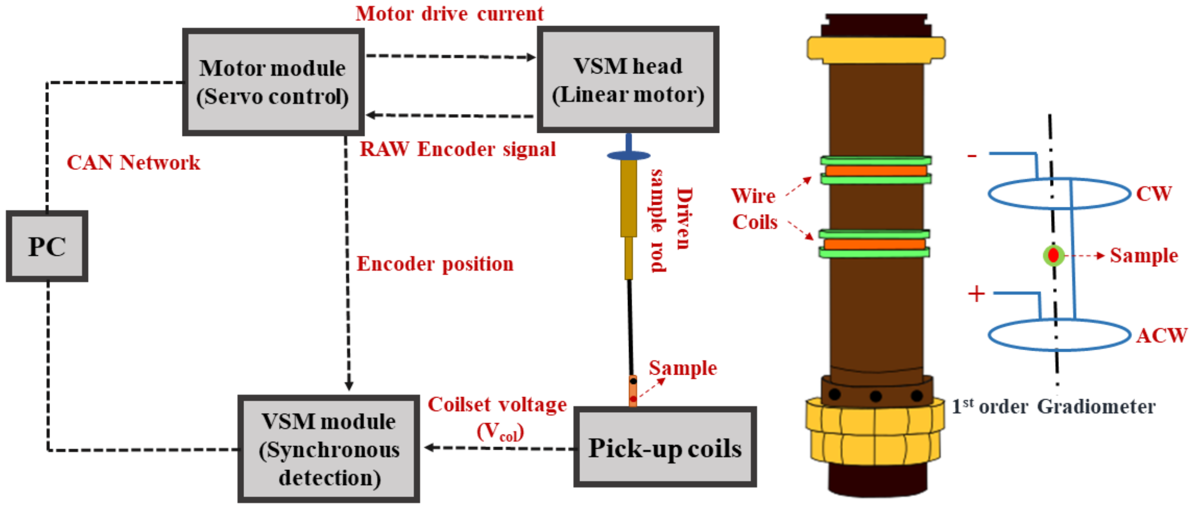

Fig. 2.10: Schematic of pickup coils with two distinct coil sets.

2.5 Dielectric characterization

Impedance measurements were performed using a Wayne Kerr LCR meter (Model $43100R$) across a frequency range of 10^2 Hz to 10^6 Hz with an AC voltage of 1.0 V_{rms}. Data collection was facilitated by software provided by Wayne Kerr, allowing connection between the LCR meter and a computer via an $RS232$ interface. A high-temperature oven from Wayne Kerr was employed for temperature-dependent impedance measurements. Temperature control was managed using a Chromal-Alumel (Cr-Al) thermocouple along with a Eurotherm temperature controller (Model 3216). For dielectric measurements, samples were prepared in cylindrical pellet form with typical dimensions of $1 - 1.5$ mm in thickness and $9 - 10$ mm in diameter. The thickness and diameter were measured using a Vernier calliper. Prior to measurement, calibration was conducted using a Kelvin clip with open and closed-circuit models to eliminate stray impedance effects. Silver paste (Sigma Aldrich) was applied to both surfaces of the pellets to form electrodes.

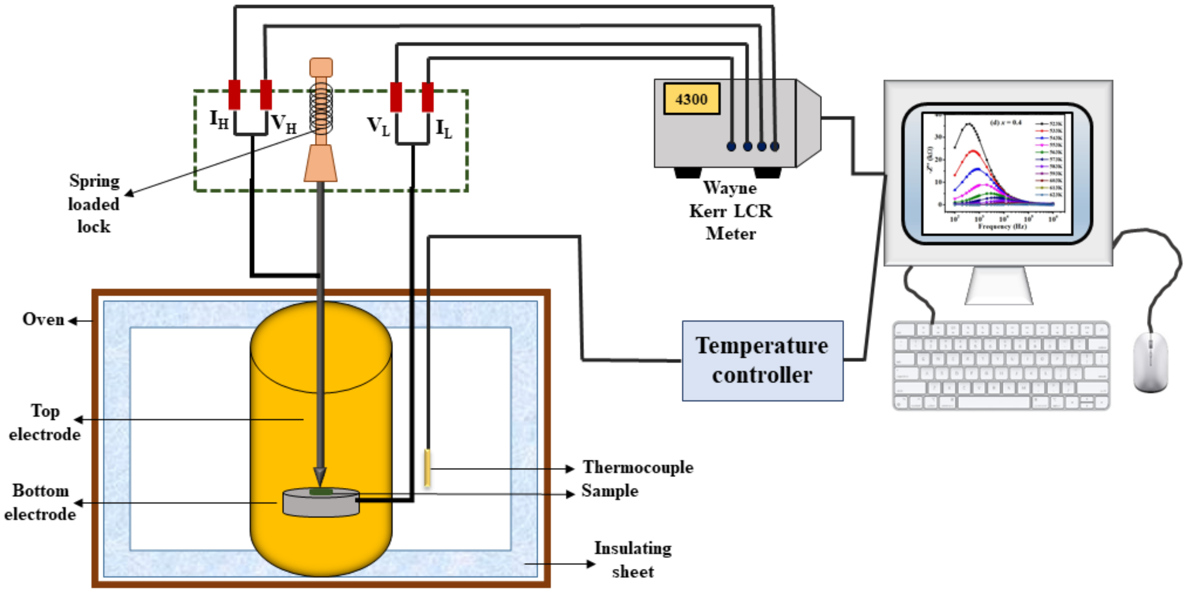

Fig. 2.11: Setup of dielectric system along with LCR meter and high temperature furnace.

The setup of dielectric includes an LCR meter connected to a sample holder through four BNC connectors. The sample holder which is constructed from stainless steel, operates in a parallel plate capacitor configuration using the four-terminal method. The top electrode is spring-loaded to ensure a reliable electrical contact for samples of varying dimensions. In this configuration, the LCR meter is linked to the sample holder via four leads: the top electrode connects to the I_H and V_H terminals, while the bottom electrode connects to the I_L and V_L terminals. The bottom electrode is mounted on an insulating base. The I_H/I_L pair is connected to the signal generator to apply current through the sample, whereas the V_H/V_L pair is used to measure voltage. The LCR meter then calculates the sample's impedance by applying a current at a specific frequency (f) and measuring the voltage across the device. The schematic diagram of the impedance measurement setup is shown in Fig. 2.11.

Hence, this chapter provides a comprehensive overview of the experimental techniques used for sample synthesis, structural and microstructural characterization, and measurement of physical properties. From solid-state synthesis to advanced tools like XRD, FESEM-EDX, Raman spectroscopy, XPS, VSM, PPMS, and dielectric setup, played a key role in analyzing the structural, magnetic, and dielectric behavior of the materials studied.

भारतीय प्रौद्योगिकी संस्थान गुवाहाटी • Indian Institute of Technology Guwahati •

Chapter 3

Magneto-dielectric studies in Ho and Nd substituted Gadolinium iron garnet

This chapter focuses on Gadolinium iron garnet (GdIG) due to its excellent thermal stability and power-handling capabilities. GdIG exhibits magnetic compensation at room temperature which arises from the weak exchange interactions between the magnetic moments of Gd and Fe ions [61]. Additionally, Canglong *et al*. [85] reported a significant magnetocaloric effect in GdIG, along with a reversal in the sign of magnetic entropy change near the compensation temperature. While the net moment in RIGs typically increases beyond the compensation point, Aakansha *et al*. [86] observed magnetization reversal in GdIG upon substituting Sm. Substituting cobalt at the Fe site in GdIG results in an expanded band gap and the introduction of intermediate defect levels within the band structure [87]. Bi-doped GdIG samples exhibit exchange bias behavior near the compensation temperature, with the exchange bias field significantly exceeding the coercive field ($H_{EB} = 6.4H_C$) [88]. Moreover, Bi substitution induces relaxor ferroelectric properties in GdIG [89]. Fechine *et al*. [90] reported that GdIG demonstrates a high dielectric constant coupled with low dielectric loss that further enhances its multifunctional potential. Magneto-electric coupling effects have also been observed in rare-earth-doped BiIG thin films deposited on gallium-gadolinium garnet substrates [91].

The RIG family has recently garnered significant attention for applications in dielectric resonator antennas and advanced devices utilizing magneto-dielectric properties [2,119]. A comprehensive understanding of the dielectric response is critical for these cutting-edge applications. High dielectric permittivity can arise from two primary mechanisms: structural distortions enhancing electrical polarizability or hopping of charge carriers. These mechanisms interact uniquely with an external magnetic field that produces distinct magneto-dielectric effects. In the first mechanism, the magneto-dielectric response is attributed to magnetostriction effects [92]. Conversely, in the second mechanism, the effect emerges from the reorganization of spin-coupled dipole moments at hopping sites under an applied magnetic field [93]. While the magnetic behavior of GdIG is complex, as highlighted in numerous studies. The spin-lattice coupling is anticipated to significantly influence dielectric permittivity, particularly near temperatures associated with magnetic transitions. This coupling suggests a strong connection between the material's magnetic and dielectric properties. In this chapter, we will tune the structural, magnetic, and dielectric properties of Ho- and Nd-substituted GdIG, with a focus on uncovering the interrelationships among these characteristics.

3.1 Ho substituted Gadolinium iron garnet

We have synthesized $(Gd_{1-x}Ho_x)_3Fe_5O_{12}$ for $x =$ 0.0, 0.2, 0.4, 0.6, 0.8, 1.0 garnet samples via solid-state reaction method. For this, all the precursors i.e., Gd_2O_3, Ho_2O_3 and Fe_2O_3 were weighed in stoichiometric proportion and then grinded in acetone medium. Presintering is carried out at $800°C$ for 12 hours followed by final sintering of pellets to $1400°C$ for 8 hours. In between presintering and sintering, the samples were sintered over and again at different temperatures to attain good homogeneity.

3.1.1 Structural characterization

The room temperature X-Ray diffraction patterns for $(Gd_{1-x}Ho_x)_3Fe_5O_{12}$ for $x =$ 0.0, 0.2, 0.4, 0.6, 0.8, 1.0 samples are shown in Fig. 3.1. These XRD patterns are Rietveld refined with $Ia\bar{3}d$ (O_h^{10}) space group and cubic crystal structure. The refined plots are demonstrated in Fig. 3.2 and Fig. 3.3 for all the concentrations. The recorded patterns are represented with red open circles and black solid line is for the Rietveld refined XRD patterns. The reliability parameters of the refined plots such as $R_p, R_{wp,}\ R_F, R_{Bragg}$ and χ^2 are tabulated in Table 3.1. The refined data reveal that all the samples are formed in pure garnet phase with cubic crystal structure. Additionally, occupancy of all the cations are refined and they are in accordance with the initial compositions of the respective sample. The lattice constant and unit cell volume are decreasing systematically with Ho substitution as shown in Table 3.1. The lattice constant of the parent sample is comparable to that reported in literature [94]. The decrement in lattice parameters can be attributed to the smaller ionic radii of Ho^{3+} $(1.041\ \text{Å})$ as compared to Gd^{3+} (1.078 Å) ions. Further, the bond length $Fe\ (a) - Fe\ (d)$ and bond angle $Fe\ (a) - O - Fe(d)$ are also determined using Rietveld refined data in Vesta software as shown in Fig. 3.4. The bond length is decreasing from $3.48\ \text{Å}\ (x = 0.0)$ to $3.46\ \text{Å}\ (x = 1.0)$ because of contraction of interatomic distance due to smaller ion substitution at larger ion site. These values of bond length and bond angle for parent sample i.e., $x = 0.0$ are comparable with the literature [86].

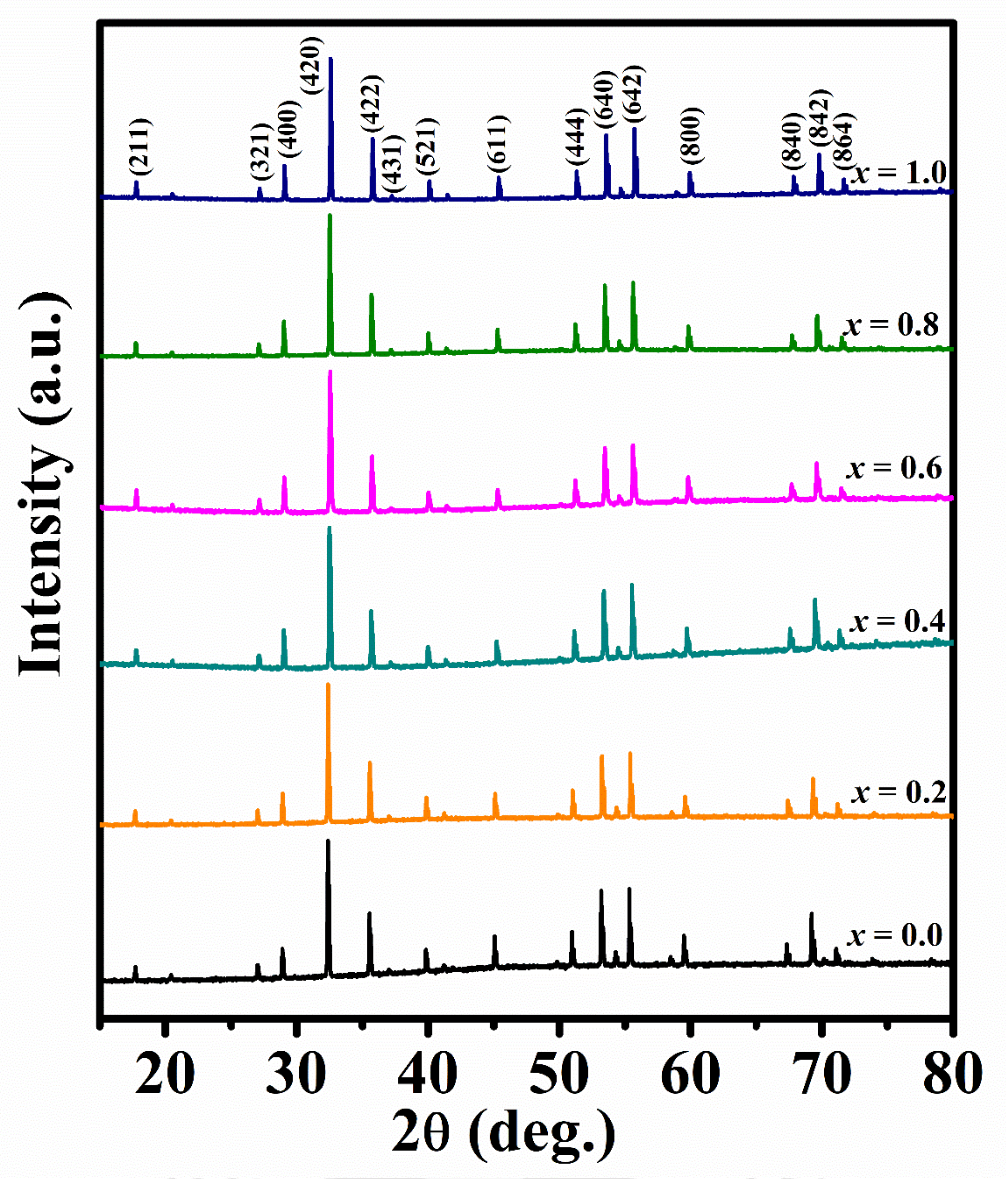

Fig. 3.1: The XRD data patterns of Ho-GdIG samples for $x = 0.0$ to $x = 1.0$.

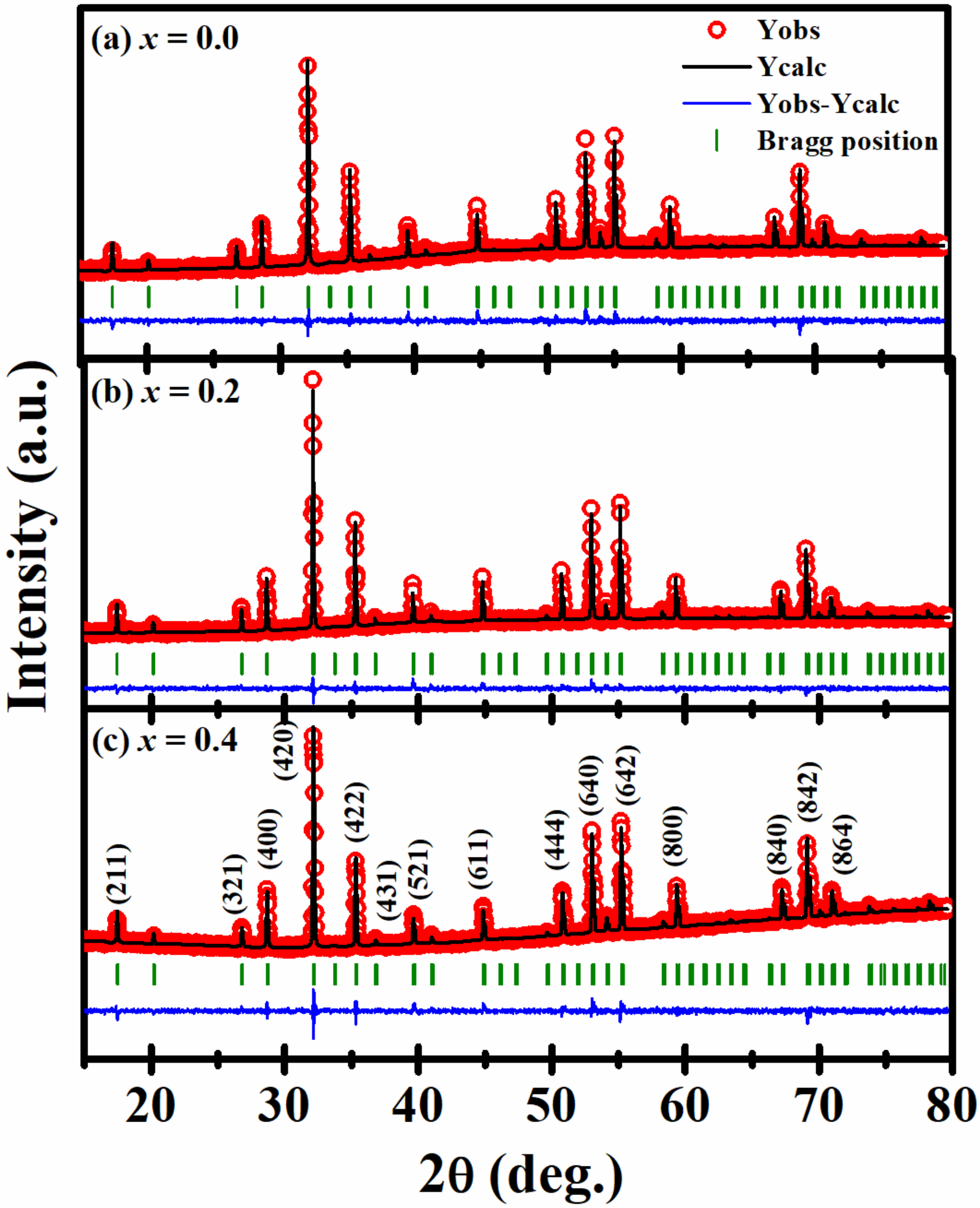

Fig. 3.2: Rietveld refined plots of $(Gd_{1-x}Ho_xFe_5O_{12})$ with $x = 0.0, 0.2$ and 0.4 samples.

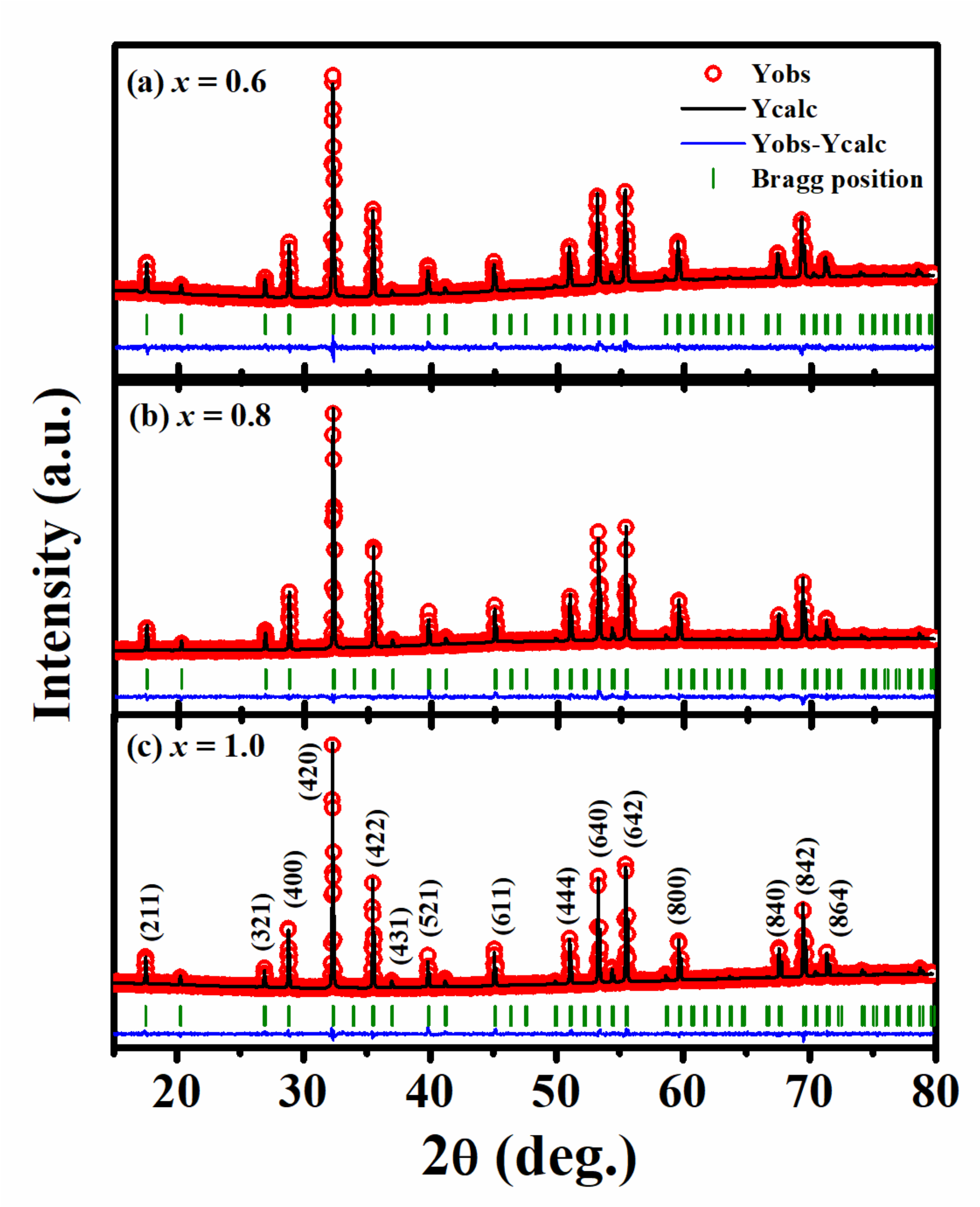

Fig. 3.3: Rietveld refined plots of $(Gd_{1-x}Ho_xFe_5O_{12})$ with $x = 0.6, 0.8$ and 1.0 samples.

Table 3.1: Reliability and structural parameters evaluated from Rietveld refinement of XRD patterns for Ho-GdIG samples.

Sample → Parameters ↓	$x = 0.0$	$x = 0.2$	$x = 0.4$	$x = 0.6$	$x = 0.8$	$x = 1.0$
Space group	$Ia\bar{3}d$	$Ia\bar{3}d$	$Ia\bar{3}d$	$Ia\bar{3}d$	$Ia\bar{3}d$	$Ia\bar{3}d$
$a = b = c$ (Å)	12.4846 (1)	12.4604 (2)	12.4448 (2)	12.4231 (1)	12.4074 (1)	12.3871 (1)
Volume (Å^3)	1945.9	1934.6	1927.3	1917.3	1910.0	1900.6
R_p (%)	12.2	11.0	15.9	11.5	16.2	10.8
R_{wp} (%)	11.5	9.2	13.2	12.0	8.2	13.2
R_F (%)	16.6	10.2	16.8	14.9	17.5	12.6
R_{Bragg} (%)	15.5	11.7	13.8	10.9	14.6	11.2
χ^2	1.9	1.8	1.9	1.7	2.3	2.5
Occupancy						
Gd	2.98	2.38	1.77	1.19	0.58	0.0
Ho	0.0	0.56	1.18	1.76	2.37	2.97
Fe	4.97	4.99	4.84	4.96	4.92	4.98

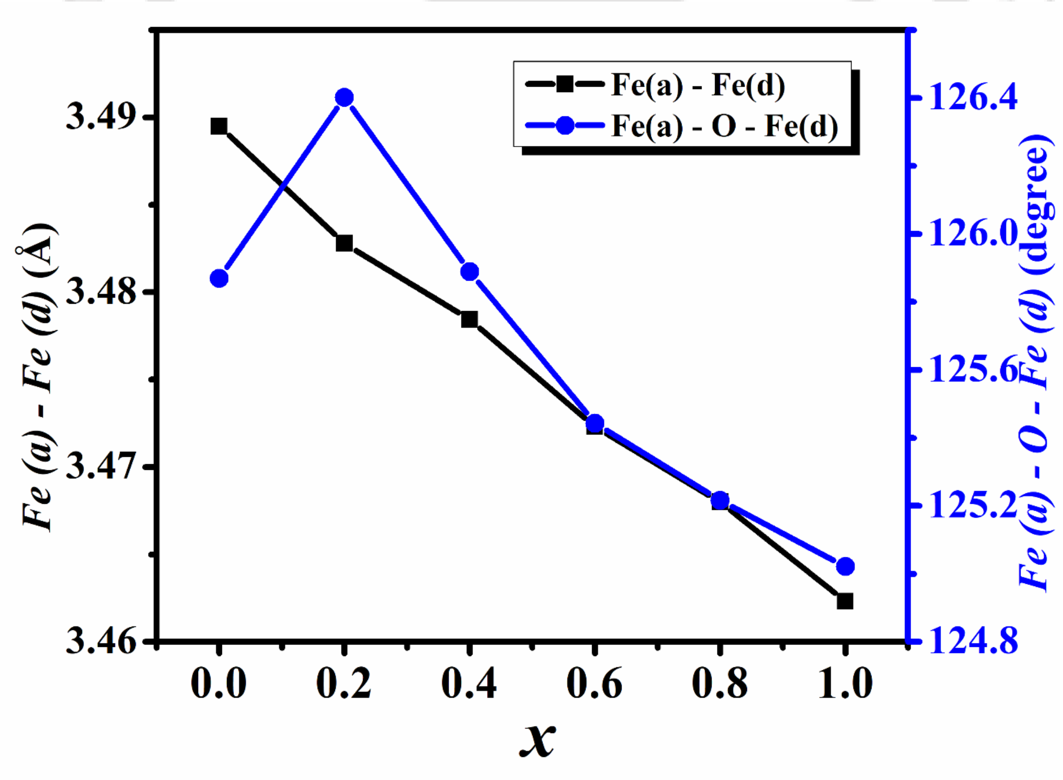

Fig. 3.4: Variation of $Fe(a) - Fe(d)$ bond length and $Fe(a) - O - Fe(d)$ bond angle with change in Ho concentration.

The FESEM micrographs for $x = 0.0, 0.2, 0.6$ and 1.0 samples are shown in Fig. 3.5 (a-d) with their corresponding fitted histogram demonstrated in Fig. 3.5 (e-h). As reported by Odo [95], the size distribution histograms are fitted to log-normal function which is given as follows:

$$f(l,\mu,\sigma_s) = \frac{1}{l\sigma_s\sqrt{2\pi}}\exp\left(-\frac{(lnl-\mu)^2}{2\sigma_s^2}\right) \tag{3.1}$$

Here, l represents the cross-sectional length of the grain, μ is the logarithmic mean and σ_s is the standard deviation. All the micrographs are analyzed using ImageJ software. The FESEM pictures show highly dense microstructure with clear grains and grain boundaries due to which they are expected to show good dielectric properties. The density of these materials is calculated by Archimedes principle and they are obtained as $6.175, 6.276, 6.451, 6.484, 6.138, 6.494\ g/cm^3$ for $x = 0.0, 0.2, 0.4, 0.6, 0.8, 1.0$ samples, respectively. They all lie in the range of 90 to 95% of their theoretical density. The estimated values of average grain size are $4.88, 3.47, 4.56, 3.79, 3.57, 2.59\ \mu m$ for $x = 0.0, 0.2, 0.4, 0.6, 0.8, 1.0$ samples, respectively. The average reduction in grain size can be attributed to the smaller ionic radii of substituted Ho^{3+} ions at host Gd^{3+} site.

The elemental composition is calculated by EDS spectra which is shown for two of the compositions i.e., for the parent and $x = 0.6$ concentration as shown in Fig. 3.6. Elemental compositions are calculated from the atomic percentage provided and they are obtained as $2.98{:}\ 0.0{:}\ 4.99$ and $1.09{:}\ 1.6{:}\ 4.98$ (Gd: Ho: Fe) for $x = 0.0$ and 0.6 samples, respectively. These compositions are significantly comparable to the original compositions.

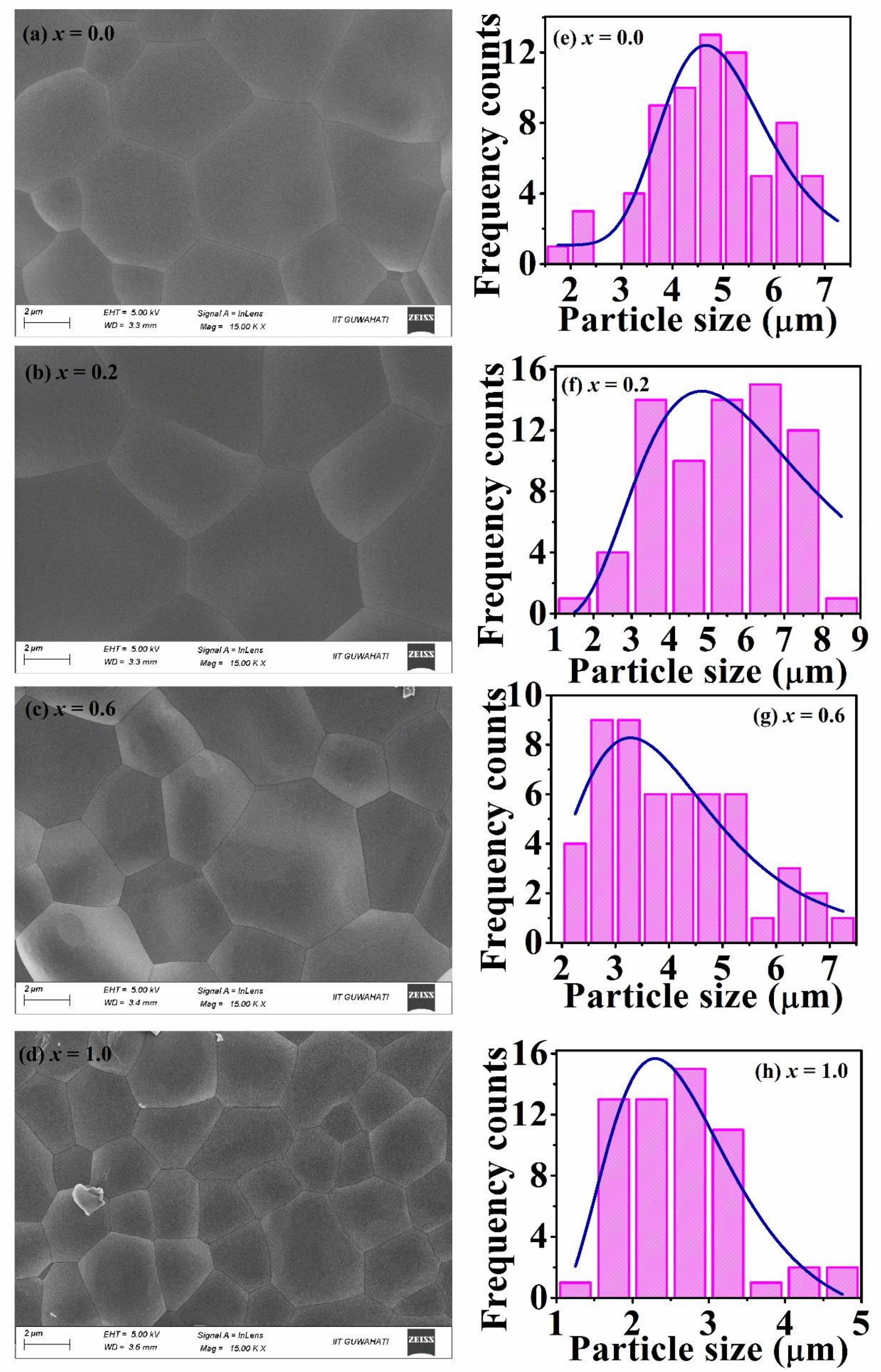

Fig. 3.5: (a-d) FESEM micrographs and (e-h) fitting of particle size distribution to the log-normal function for $x = 0.0, 0.2, 0.6$ and 1.0 samples.

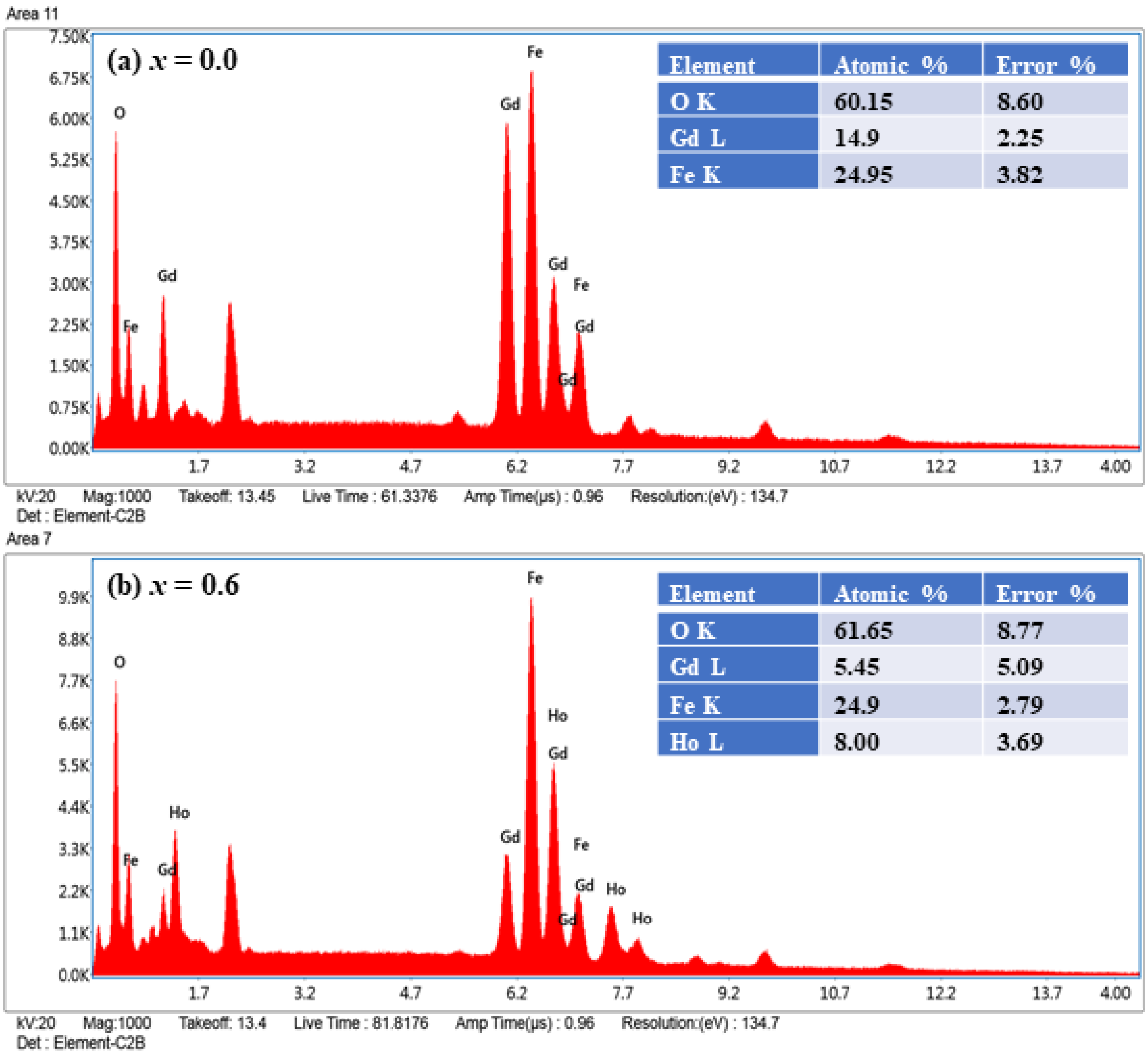

Element	Atomic %	Error %
O K	60.15	8.60
Gd L	14.9	2.25
Fe K	24.95	3.82

Element	Atomic %	Error %
O K	61.65	8.77
Gd L	5.45	5.09
Fe K	24.9	2.79
Ho L	8.00	3.69

Fig. 3.6: EDS plots for (a) $x = 0.0$ and (b) $x = 0.6$ samples with inset showing their atomic percentage with corresponding percentage error.

The Raman spectrum for all the samples of Ho-GdIG series by using a radiation having excitation wavelength of 633 nm are recorded and shown in Fig. 3.7. In total, there exists 98 vibration modes at the center of Brillouin zone of RIGs out of which 55 are silent modes and only F_{1u} is the acoustic mode. According to Group theory, the garnet system contains 160 atoms in a unit cell that corresponds to 17 ($17F_{1u}$) infrared modes and 25 active Raman modes i.e., $3A_{1g}, 8E_g$ and $14F_{2g}$ [96]. These Raman modes corresponds to internal, translational and rotatory modes, respectively. The peaks arising below 300 cm^{-1} are due to the translation motion of either of the rare earth ion, whereas the peaks in between 300 cm^{-1} to 800 cm^{-1} are coming because of internal vibration of FeO_4 molecular group [97]. Since we are replacing a lighter element with a heavier one, the effective mass will increase and the peak will shift to a lower wavenumber. This type of shift is named as Red shift in Raman spectroscopy.

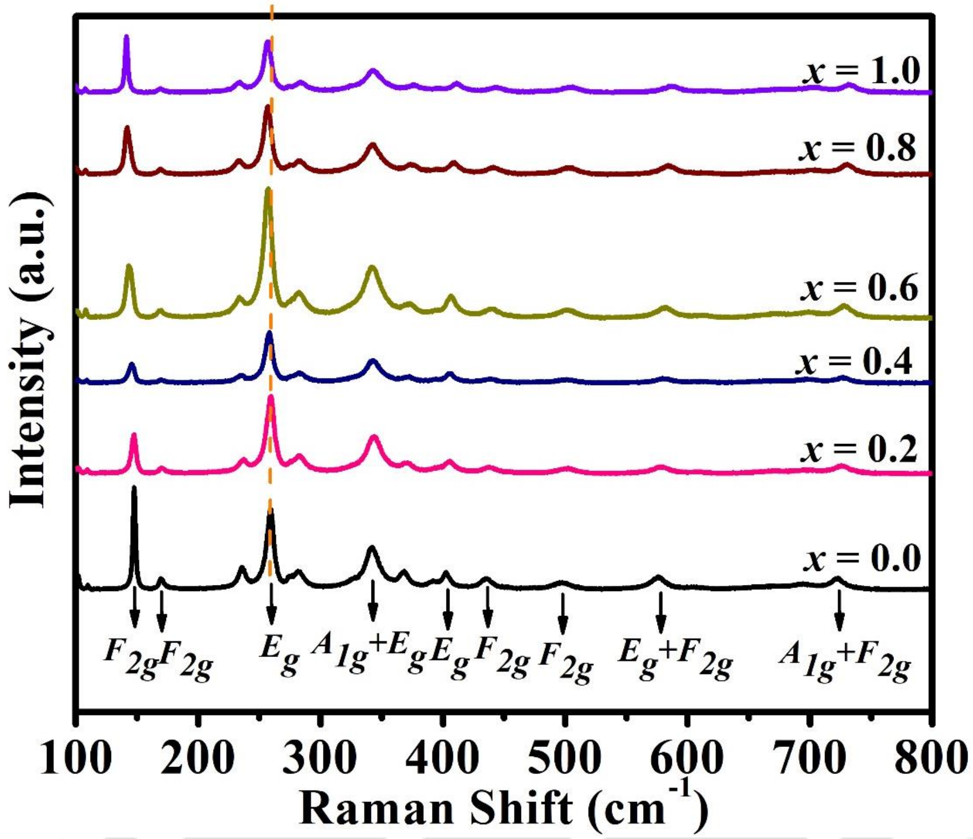

Fig. 3.7: Room temperature Raman spectra of Ho-GdIG samples with an excitation wavelength of 633nm.

We have further used XPS to identify the electronic and chemical states of all the atoms. The XPS spectra with its fitting to Gaussian and Lorentzian function together are shown in Fig. 3.8 for $x = 0.0$ and 0.6 compositions. The binding energy peaks of Gd^{3+} and Ho^{3+} ions correspond to two spin-orbit doublet i.e. $4d_{5/2}$ and $4d_{3/2}$ levels. Whereas, the binding energy peaks for Fe^{2+} and Fe^{3+} ions are obtained for $2p_{3/2}$ and $2p_{1/2}$ levels [86]. Additionally, a satellite peak is also found at $\sim 719\ eV$ that occur due to energy loss processes, such as inelastic scattering or multiplet splitting. Further, we can clearly see that for $x = 0.0$ sample, the peaks are obtained at $142.2\ eV$ and $147.2\ eV$ for $4d_{5/2}$ and $4d_{3/2}$ levels, respectively. Similarly, for Ho doped sample ($x = 0.6$), we have also observed two peaks of Gd^{3+} at $160.8\ eV$ and $162.8\ eV$ and they correspond to $4d_{5/2}$ and $4d_{3/2}$ levels, respectively (shown in Fig. 3.8(c)). Moreover, the prominent peaks for Fe stands for $2p_{3/2}$ and $2p_{1/2}$ energy doublets and they show the ionic states of Fe as $2+$ and $3+$. These two peaks are observed at $710.4\ eV$ and $724.5\ eV$ for $2p_{3/2}$ and $2p_{1/2}$ level, respectively and each of them splits into two energy peaks which further confirms the presence of Fe^{2+} and Fe^{3+} ions in both the samples. The ratio of Fe^{2+}/Fe^{3+} ions is determined from the area under the respective Fe^{2+} and Fe^{3+} peaks in the deconvoluted $Fe\ 2p$ spectra. It was found to decrease from 0.95 $(x = 0.0)$ to 0.73 $(x = 0.6)$ sample. This decline in the Fe^{2+}/Fe^{3+} ratio suggests a suppression in the hopping conductivity as the conduction mechanism in such systems relies heavily on the presence of Fe^{2+} ions.

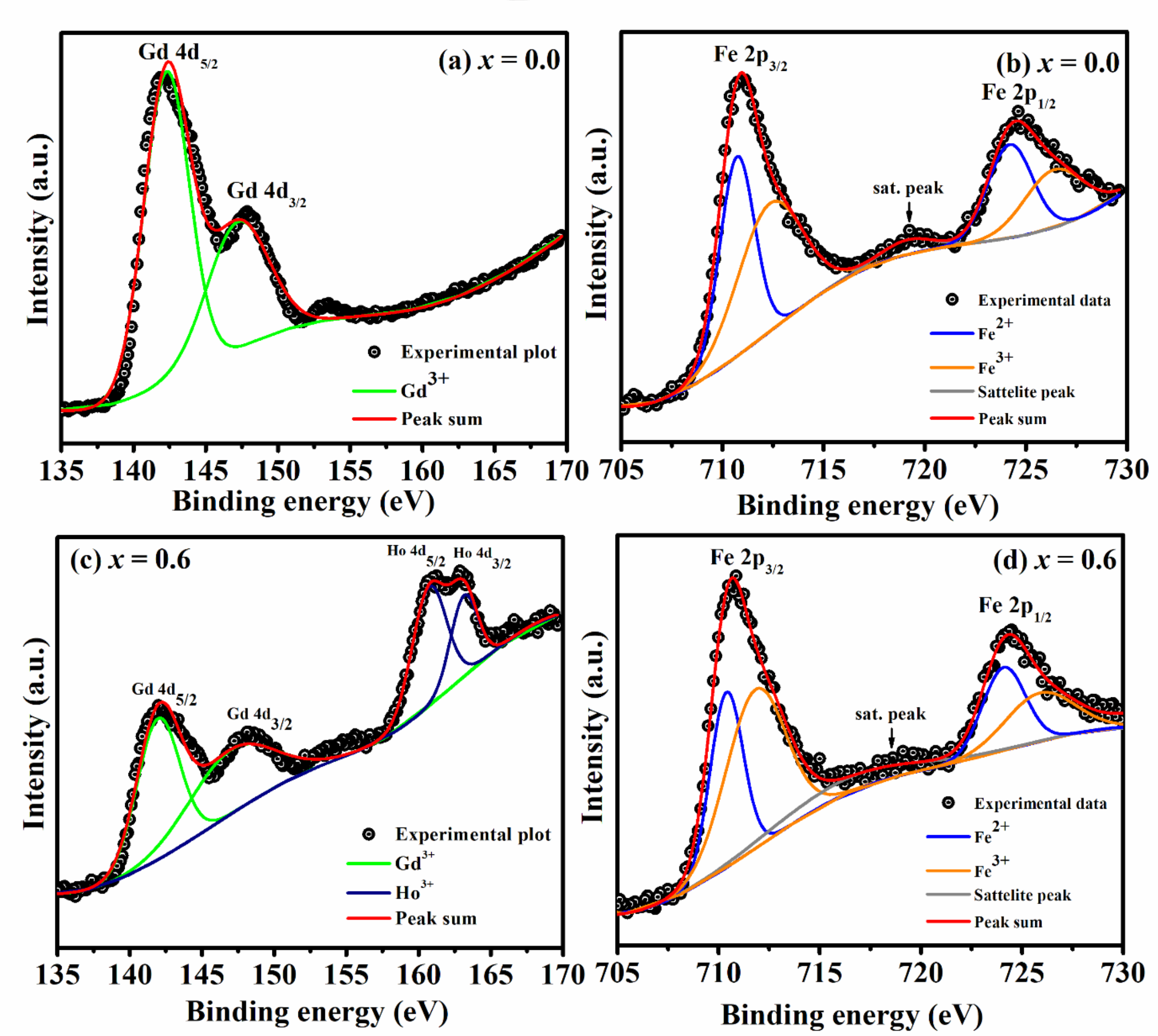

Fig. 3.8: XPS spectrum of Gd, Ho and Fe with their different oxidation states of cations in $x = 0.0$ and 0.6 samples.

If multiple cationic species are introduced exclusively on a single crystallographic sublattice in a complex oxide, the resulting configurational entropy (ΔS_{conf}) arises solely from their mixing on that specific site. It can be expressed as follows [10]:

$$(\Delta S_{conf}) = -R\sum_{i=1}^{n} x_i lnx_i \tag{3.2}$$

where, R is the gas constant and x_i is the mole fraction of each species occupying the same type of site for n atomic constituents. As we are substituting Dy^{3+} site with Ho^{3+}ions at the dodecahedral $(24c)$ site and each formula unit of garnet has 3 rare-earth sites, leading to net configurational entropy as:

$$(\Delta S_{conf}) = -3R(xlnx + (1-x)\ln(1-x)) \tag{3.3}$$

Hence, ΔS_{conf} is evaualted and it comes out to be $0.0, 12.48, 16.79, 16.79, 12.48,$ and 0.0 for $x = 0.0, 0.2, 0.4, 0.6, 0.8$ and 1.0 composition, respecticely. These values are solely determined by the statistical distribution of cations at the rare-earth site and are independent of the specific elements involved. As a result, the ΔS_{conf} trend remains identical across different substitution series such as Ho–SmIG and Ho–DyIG. Here, for $x =$ 0.0 and 1.0 samples, ΔS_{conf} is 0.0, as the system is fully ordered (only Dy or only Ho present, no mixing). The entropy is maximum for $x = 0.4$ and 0.6 samples, indicating highest cationic disorder at the rare-earth site, which can significantly influence the material's functional properties. At intermediate substitution levels, the enhanced entropy may lead to more active dielectric relaxation due to space charge polarization, and reduced magnetic ordering temperature due to spin disorder. The above effect may lead to altered conductivity. This highlights the importance of configurational entropy as a key parameter in designing multifunctional garnet materials.

3.1.2 Magnetic characterization

In order to study the FIM transition point, we have carried out magnetization vs. temperature plots from $300K$ to $773K$ by applying an external field of $200\ Oe$ as shown in Fig. 3.9 (a). All these plots show typical ferrimagnetic behavior and the transition temperature (T_c) is calculated by dM/dT vs. temperature plots as shown in Fig. 3.9 (b). The T_c is varying from $553K$ to $543K$ as x goes from 0.0 to 1.0. The decrease in T_c can be related to the distortion of the superexchange interaction between the $Fe\ (a) - O - Fe(d)$ bond as in accordance with XRD data.

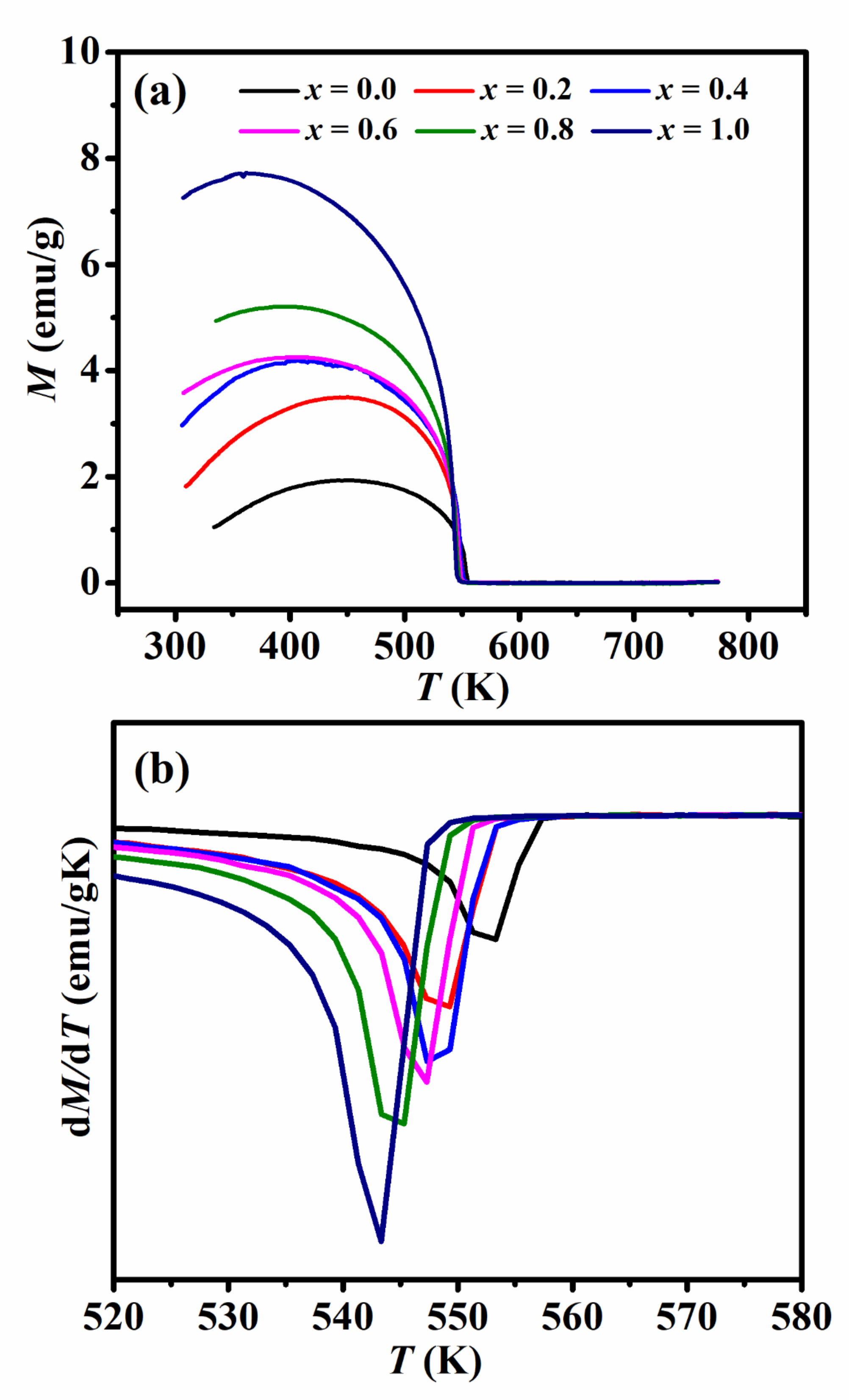

Fig. 3.9: (a) $M - T$ plots in the temperature ranging between $300K$ to $773K$ by applying an external magnetic field of $200\ Oe$ and (b) derivative of magnetization with temperature i.e., dM/dT vs. T plots for Ho-GdIG samples.

Further, the zero-field cooled (ZFC) and field cooled (FC) $M - T$ plots from $5\ K$ to $300\ K$ by applying a magnetic field of $200\ Oe$ are extracted as depicted in Fig. 3.10 for $x = 0.0, 0.4, 0.8$ and 1.0 samples. When $x = 0.0$ sample is cooled below T_c, the magnetization exhibits a broad increment at $450\ K$ (shown in Fig. 3.9). On further cooling, the magnetization drops systematically and at room temperature the moment remains $0.98\ emu/g$ which becomes zero at $295\ K$. The compensation effect results from the collinear FIM ordering of the Fe ions at the tetrahedral and octahedral sites and small contribution from rare earth ion at the dodecahedral site. Similar trend of magnetization is also observed for Ho-doped samples. However, T_{comp} reduces drastically with the addition of Ho i.e., from $295\ K$ for $x = 0.0$ to $145\ K$ for $x = 1.0$ sample. The reason for the decrement in T_{comp} can be attributed to the strong magnetocrystalline anisotropy which is induced with Ho substitution at lower temperature. This substitution also strongly influences the alignment and thermal behavior of magnetic moments in the garnet structure.

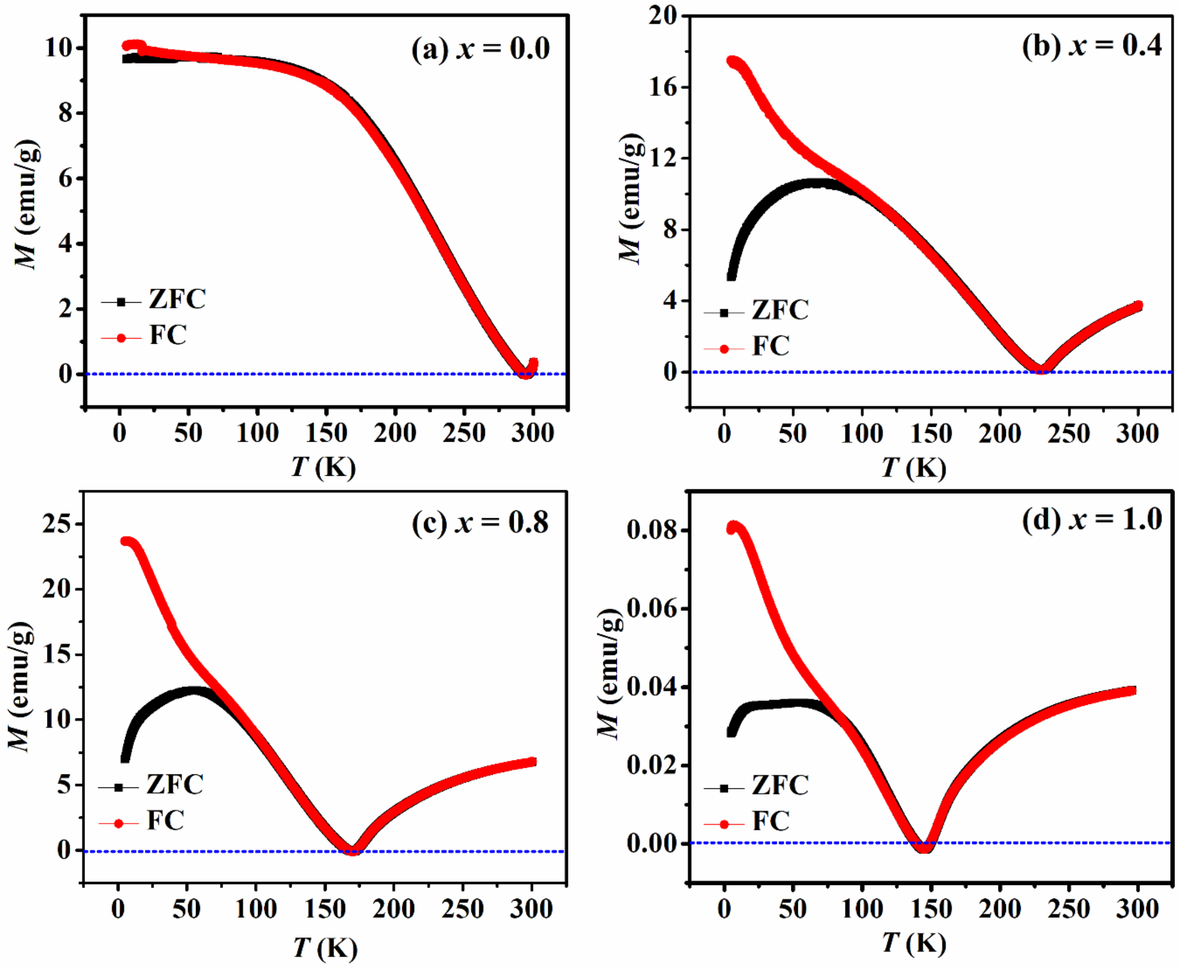

Fig. 3.10: (a-d) ZFC and FC $M - T$ plots in the low temperature range $(5K - 300K)$ for $x = 0.0, 0.4, 0.8$ and 1.0 samples at an applied field of 200 Oe.

The room temperature (RT) hysteresis loops for Ho-GdIG samples are collected as shown in Fig. 3.11 (a). All the loops are getting partially saturated as their T_{comp} is very close to RT. We have evaluated the saturation magnetization (M_s) and effective anisotropy (K_1) constant for these samples using Law of approach to saturation (LAS) [98], which shows the dependence of magnetization on the applied field H as:

$$M = M_s\left(1 - \frac{8K_1^2}{105\mu_0^2 M_s^2 H^2}\right) + cH \tag{3.4}$$

here, $8/105$ represents a numeric constant for some random polycrystalline material and the last term cH is forced magnetization due to higher fields. We can see that the saturation magnetization is increasing from 0.29 emu/g for $x = 0.0$ (as shown in inset of Fig. 3.11 (a)) to 9.36 emu/g for $x = 1.0$ sample at $T = 300\ K$. As we are measuring the $M - H$ loops at RT and T_{comp} value for $x = 0.0$ is 295 K which is very close to RT that makes the magnetization value of this sample small. Whereas, T_{comp} for Ho-doped samples is away from RT, so higher magnetization is observed at RT. The effective anisotropy constant K_1 at ambient temperature is found to be increased from $2.4 \times 10^3\ erg/cc$ ($x = 0.0$) to $3.73 \times 10^4\ erg/cc$ ($x = 1.0$) as shown in Table 3.2. The anisotropy constant of the parent sample is in good agreement with the literature reported by Calhoun *et al.* [99] where they confirmed the obtained anisotropy theoretically as well as experimentally.

We have also analyzed hysteresis loops at 5 K as shown in Fig. 3.11 (c,d) and they show perfect saturated magnetization as their T_{comp} is far away from 5 K. All the curves are perfectly fitted to LAS and saturation magnetization as well as anisotropy constant K_1 are calculated as listed in Table 3.2. The magnetization drops from 93.53 emu/g to 57.36 emu/g for $x = 0.0$ to $x = 1.0$ samples, respectively due to the distortion in exchange interaction. For any particular concentration, we have also observed a large increment in effective anisotropy as well as coercivity compared to those of RT as shown in Table 3.2. The $x = 1.0$ sample exhibits the lowest M_s and the highest H_c at 5 K among all the samples which can be attributed to the presence of competing magnetic interactions.

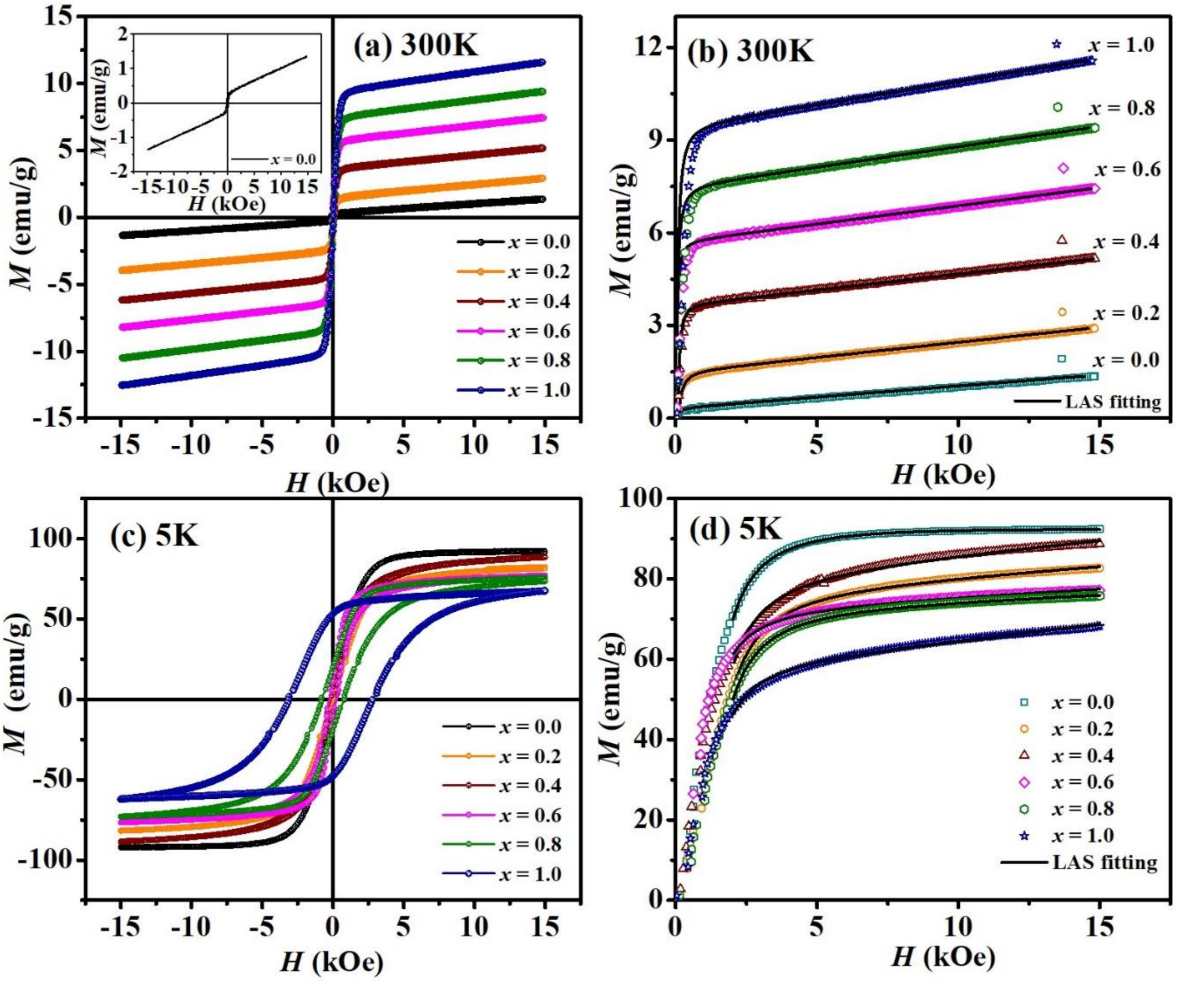

Fig. 3.11: (a,c) Magnetic hysteresis loop $(M-H)$ at room temperature and $5K$ and (b,d) fitting of $M-H$ loops to Law of Approach to Saturation (LAS) equation for $x = 0.0$ to 1.0 samples.

Table 3.2: Saturation magnetization, coercivity and magnetocrystalline anisotropy constant for Ho doped GdIG samples at $300K$ and $5K$.

x	T_{comp}		$300K$			$5K$	
	(K)	$M_s\ (emu/g)$	$H_c\ (Oe)$	$K_1\ (10^3)$ (erg/cc)	$M_s\ (emu/g)$	$H_c\ (Oe)$	$K_1\ (10^6)$ (erg/cc)
0.0	295	0.286±0.002	154.9	2.4	93.53±0.04	29.6	2.11
0.2	265	1.458±0.001	86.4	9.04	75.74±0.09	81.4	1.97
0.4	231	3.628±0.002	70.6	11.1	79.38±0.23	168.5	2.01
0.6	197	5.678±0.002	50.2	13.7	71.63±0.09	258.3	1.35
0.8	170	7.435±0.001	58.1	24.9	69.92±0.05	810.5	1.33
1.0	145	9.362±0.002	53.3	37.3	57.36±0.13	3137.6	1.28

3.1.3 Complex impedance spectroscopy

Complex impedance spectroscopy is a versatile technique for analyzing the electrical properties of materials and systems across frequencies. It provides insights into resistive, capacitive, and inductive behaviours that enables the study of charge transport, dielectric properties, and interfacial phenomena across grains, grain boundaries and electrode effects. The frequency variation of the real component (Z') of the complex impedance (Z^*) for samples with $x = 0.0, 0.2, 0.6$ and 1.0 at temperature ranging from $523K - 623K$ is shown in Fig. 3.12. For a particular temperature, we have observed step like decrease in Z' vs. frequency plots. Z' initially decreases gradually as frequency rises up to $10^3\ Hz$, then suddenly drops off at higher frequencies. The discharge of space charges causes Z' to drop in the low frequency regime [100]. Whereas, the sudden fall in Z' is arising because of dielectric relaxation process at that frequency. For a specific composition, Z' is decreasing with the increase in temperature indicating negative temperature coefficient of impedance. Z' is increasing with Ho doping suggesting the decrease in electrical conductivity of the samples. Such an increase in Z' value is consistent with more grain boundaries available in Ho doped samples due to the reduction in grain size [101]. Also, the observed increase in resistivity with increasing Ho concentration can be attributed to the reduction of charge carrier mobility. This is closely linked to the decreasing Fe^{2+}/Fe^{3+} ratio, as confirmed by XPS analysis. A lower concentration of Fe^{2+} ions hinder the electron hopping process between Fe^{2+} and Fe^{3+} sites, which is the primary mechanism for electrical conduction in these materials. As a result, the overall conductivity decreases, leading to higher resistivity in the Ho-substituted samples.

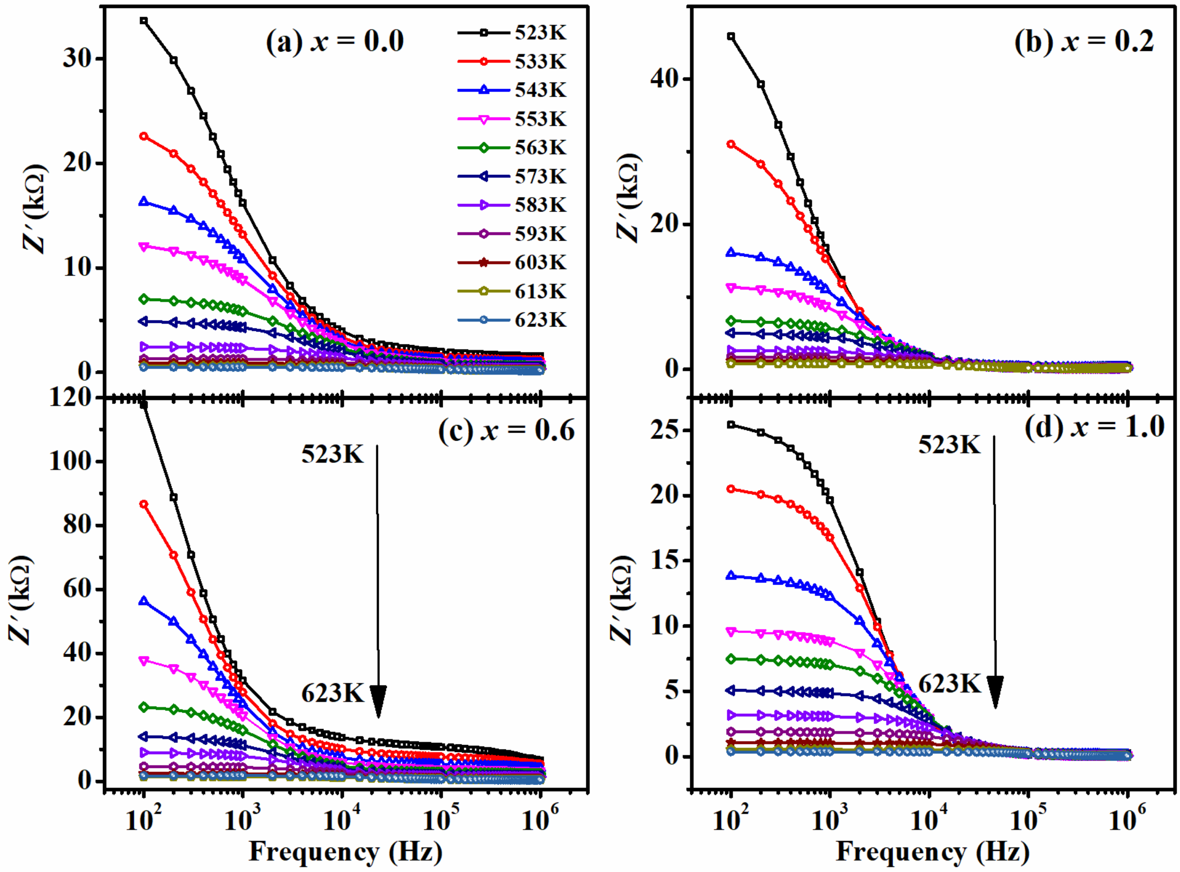

Fig. 3.12: (a-d) Variation in real component of impedance (Z') with frequency measured between $523\ K$ to $623\ K$ for $x = 0.0, 0.2, 0.6$ and 1.0 sample.

We have measured imaginary part (Z'') of complex impedance with respect to frequency $(100Hz - 1MHz)$ and varying the temperature from $523K$ to $623K$, in order to investigate the dielectric relaxation behavior in Ho-GdIG samples as shown in Fig. 3.13. These plots consist of a characteristic peak at a particular frequency indicating the presence of dielectric relaxation across grain boundaries. The shape of the peak is not uniform throughout the measured temperature range and it gets broadened with the increase in temperature. This asymmetric pattern of Z'' peaks shows that the relaxation not obeying ideal Debye type relaxation. For $x = 0.0$ sample, the relaxation occurred around $10^4 Hz$ frequency at $623K$ which can be ascribed to the relaxation across grain boundaries. Since, long range hopping happens at higher temperatures due to thermally activated charge carriers and it results in broad relaxation times. As the temperature increases from $523\ K$ to $623\ K$, the relaxation peaks are found to shift towards higher frequency signifying the existence of thermal activation of charge carriers [102].

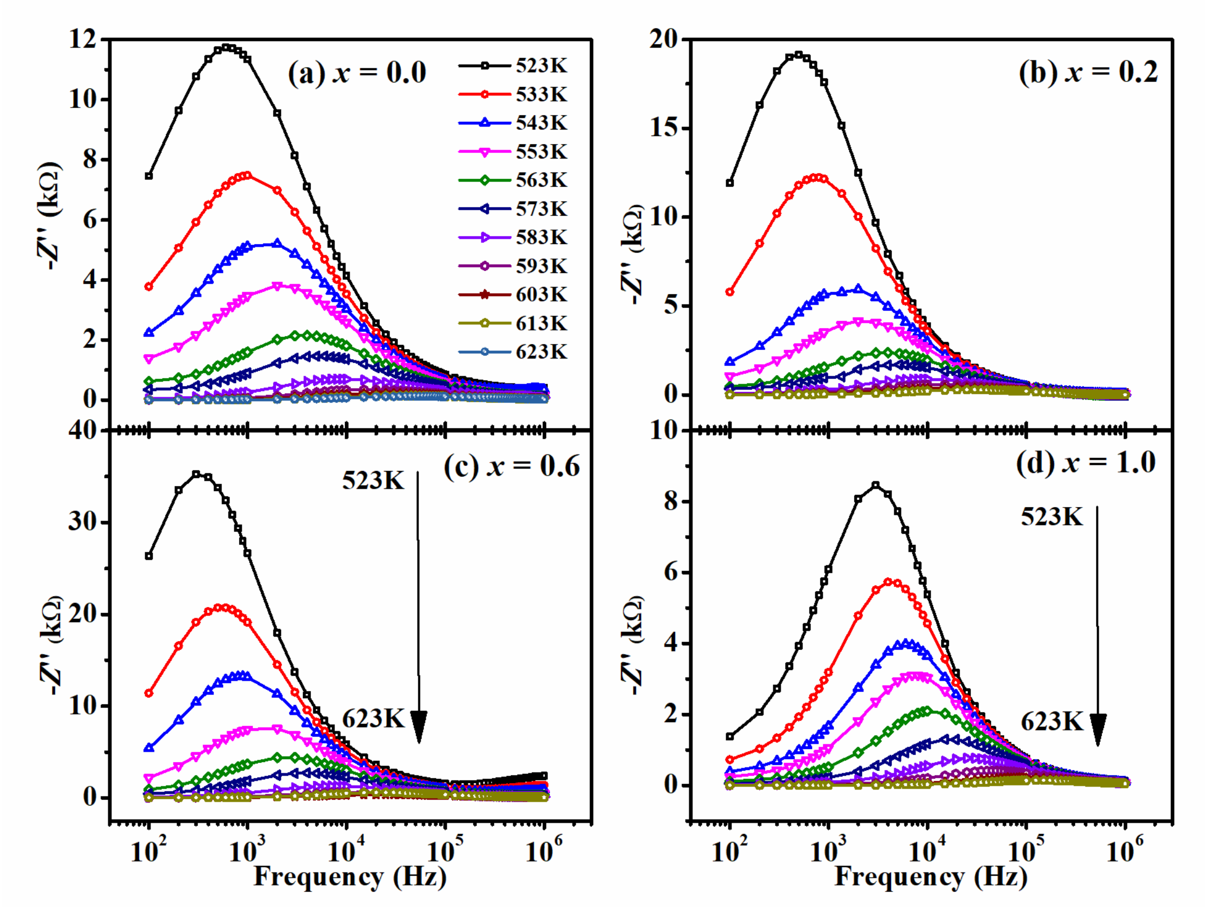

Fig. 3.13: (a-d) Frequency dependence on imaginary component of impedance (Z'') when measured between $523K - 623K$ for $x = 0.0, 0.2, 0.6$ and 1.0 sample.

Nyquist plots were constructed to determine the distinct contributions of grains and grain boundaries towards relaxation behavior in dielectric materials. The Nyquist plots of Ho-GdIG samples are measured at different temperatures from $523K$ to $623K$ and they are shown in Fig. 3.14 (a-c) for $x = 0.0, 0.6$ and 1.0 sample. We can see the depressed semicircles i.e.; the center of the semicircles lies below Z' axis and it signifies the deviation from ideal Debe type relaxation. This deviation from ideal Debye type behavior can be interpreted in terms of constant phase element (CPE denoted by Q) with impedance $Z_{CPE} = \frac{1}{A}(j\omega)^{-n}$. Here, A is a constant and n is distribution of relaxation time $(0 \leq n \leq 1)$. For a perfect capacitor $n = 1$ and for perfect resistor $n = 0$. In general, we expect two semicircles (one is due to grains and another due to grain boundaries) for polycrystalline materials with their center lying on Z' axis and they are fitted to two sets of parallel R and C circuits connected in series (as discussed in Section 1.9.1). The insets of Fig. 3.14 (a-c) depict the Nyquist plots for temperature less than $523\,K$ and we can clearly see the contribution of grains and grain boundaries in the high and low frequency regime, respectively. But as the temperature rises, the contribution of grains gets out of the measured range of frequency and only grain boundaries contribution remains. Due to the reduction in average grain size and increase in grain boundaries volume, as determined by FESEM analysis, the predominant effect of grain boundary can be seen instead of grains in the Nyquist plots with the doping of Ho. An equivalent circuit was fitted to each of the Nyquist plots which consists grain resistance (R_g), grain boundary resistance (R_{gb}), electrode resistance (R_{el}) and grain boundary capacitance (C_{gb}) as shown in Fig. 3.14 (d).

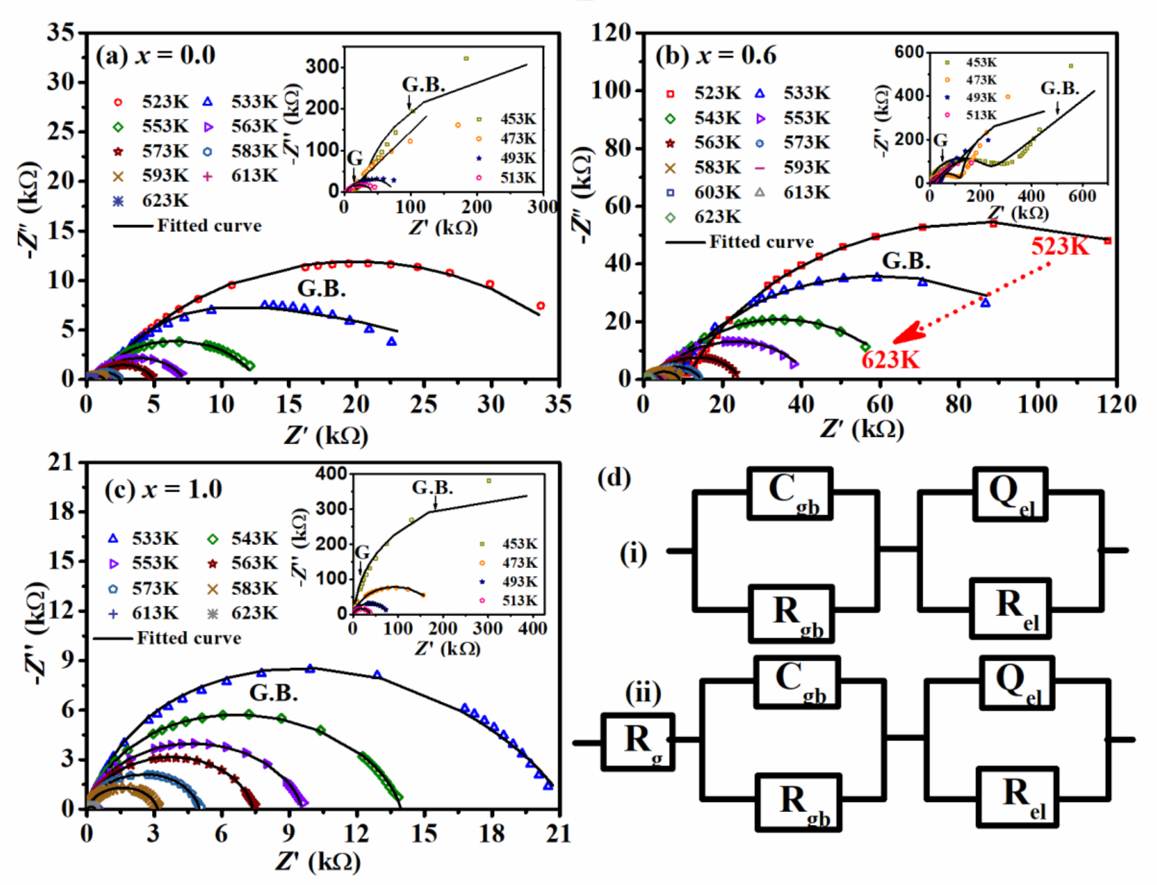

Fig. 3.14: (a–c) Nyquist plots for Ho-GdIG samples with $x = 0.0, 0.6$ and 1.0 at temperatures above $523K$; the insets show the corresponding Nyquist plots below $523K$. (d) Equivalent circuit models used to fit the Nyquist data: (i) for $T < 523\ K$ and (ii) for $T \geq 523\ K$.

3.1.4 Complex dielectric spectroscopy

The real (ε') and imaginary (ε'') components of complex dielectric constant can be determined as follows [50]:

$$\varepsilon' = \frac{-Z''}{\omega C_o\,(Z'^2+Z''^2)} \tag{3.5}$$

$$\varepsilon'' = \frac{Z'}{\omega C_o\,(Z'^2+Z''^2)} \tag{3.6}$$

here, C_o is the geometrical capacitance which is calculated from the diameter and thickness of the pellet. The temperature dependant ε' with frequency variation is displayed in Fig. 3.15 (a,b) for $x = 0.0$ and 0.6 samples. It is observed that for $x = 0.0$ sample, ε' is about 10^5 at lower frequency region that can be attributed to the Maxwell-Wagner type relaxation. Such relaxation can be generally found in heterogenous systems where the impedance results from the contribution of grains, grain boundaries or electrode effects. With the increase in frequency, ε' drops drastically indicating an increase in ac conductivity of the system. Moreover, the flat region in the lower frequency zone at high temperature can be attributed to the accumulation of space charge carriers across grain boundaries. The value of ε' is 50 at $1MHz$ frequency for the parent sample that has found to be increased with the increase in temperature. However, for $623K$, the trend gets reversed due to structural distortions at higher temperatures. Additionally, ε' drops from 10^5 to 10^4 with Ho doping in GdIG in low frequency region which is possibly because of the reduction in oxygen vacancies.

Further, the frequency dependence on ε'' is studied at different temperature range $(523\ K - 623\ K)$ and shown in Fig. 3.15 (b,d). At lower frequencies, the slope of the linear region in the logarithmic plot of ε'' versus frequency is approximately -1 that indicates that the conductivity follows the Universal Dielectric Response (UDR) behavior [103]. According to UDR, the dependencies of the dielectric constant and loss factor on frequency can be expressed as $\varepsilon' \propto \omega^{(s-1)}$ and $\varepsilon'' \propto \omega^{(s-1)}$, where $s < 1$. A higher value of ε'' at elevated temperatures reflects increased conductivity which arises from a greater number of thermally generated charge carriers. This temperature-dependent enhancement in ε'' has been observed in Yttrium iron garnet as well [104]. The conduction losses contributing to ε'' are likely due to leakage currents influenced by factors such as vacancies.

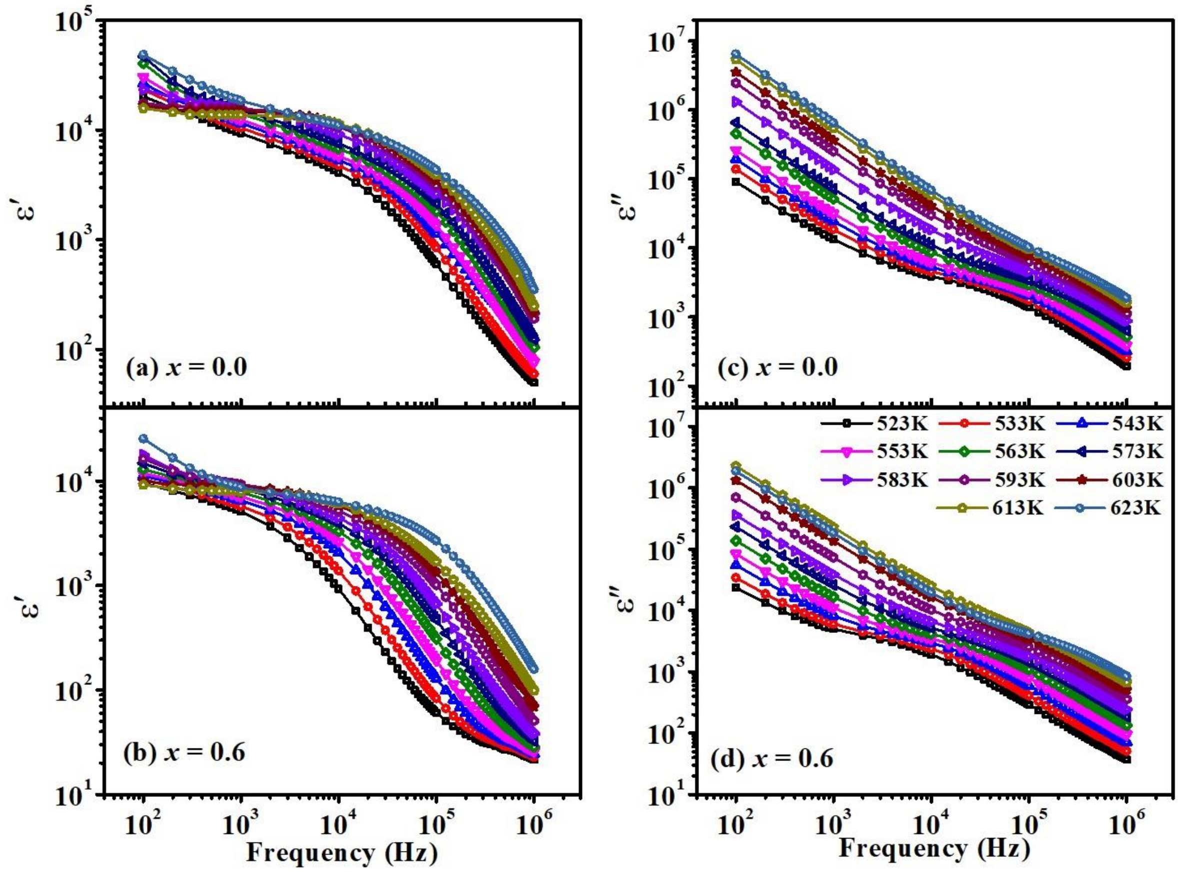

Fig. 3.15: (a,b) Variation in real part of dielectric constant (ε') and (c,d) imaginary part of dielectric constant (ε'') with frequency in $523K$ to $623K$ range for $x = 0.0$ and 0.6 samples.

3.1.5 ac conductivity

We have examined conductivity in order to comprehend the mechanism of mobility of charge carriers inside the material. The ac conductivity (σ_{ac}) is calculated using imaginary component of dielectric constant (ε'') at different temperatures varying from $523K$ to $623K$ and are demonstrated in Fig. 3.16 for all the samples of Ho-GdIG series. Following relation is used to determine the ac conductivity [105]:

$$\sigma_{ac} = \omega\varepsilon''\varepsilon_0 \qquad (3.7)$$

here ε_0 is the permittivity in free space and its numeric value is $8.854 \times 10^{-12} F/m$. The ac conductivity rises with temperature for all concentrations due to thermally active charge carriers. Knowing that our samples were sintered at a high temperature in air for a considerable amount of time, it is extremely logical to assume that there are oxygen vacancies in them [106]. These oxygen vacancies after ionization converts some Fe^{3+} ions to Fe^{2+} states and this leads to hopping of electrons between Fe^{3+} and Fe^{2+} site. This hopping mechanism affects the conductivity of the system. We have observed a decrease in conductivity for Ho doped samples because of the decrement in oxygen vacancies and as a result decrement in the hopping of charge carriers in Fe^{2+} and Fe^{3+} ions site. The existence of Fe^{2+} and Fe^{3+} ions can be verified from XPS plots. According to XRD data, the lattice constant and unit cell volume are both falling which requires fewer oxygen vacancies in the expansion and contraction of $Fe-O$ network and hence less Fe^{2+} ions are formed. As Z' is increasing for Ho doped samples due to the accumulation of charges at grain boundaries and it leads to decrement in ac conductivity.

Generally, we observe two regions in the ac conductivity plots. One flat region is frequency independent and is observed at lower frequency regime which is known as the dc conductivity or dc plateau zone. This region arises due to long range translation motion of charge carries due to the successful hopping of charge carriers in the neighboring vacant sites i.e., from Fe^{2+} to Fe^{3+} ions and vice versa. Another one arises at high frequency zone and it shows continuous increment in conductivity with increase in frequency. This frequency-dependent zone has developed as a result of more successful hopping of electrons compared to those of unsuccessful hopping. The ratio of successful to unsuccessful hopping of electrons rises with frequency resulting an increase in ac conductivity. The Jump Relaxation Model refers to this occurrence (JRM). The ac conductivity curves are fitted and analyzed using Jonscher Power Law (JPL) which is given as follows [107]:

$$\sigma_{ac} = \sigma_{dc} + A\omega^n \tag{3.8}$$

where, σ_{dc} is the conductivity in the lower frequency region, A is a constant and n is frequency exponent term. n represents the nature of the charge carriers and generally n lies between 0 and 2. The temperature dependence of n with the error bar is shown in Fig. 3.17 (a).

There are different models to explain the nature of charge carriers on the basis of variation of n with temperature. (1). The quantum tunnelling model (QMT), in which n is roughly 0.8 and stays nearly constant with temperature fluctuation, (2). In Correlated barrier hopping model (CBH) n decreases as the temperature rises, (3). In the Overlapping Large Polaron Tunnelling Model (OLPT), n drops until it reaches a minimal value, after that point it begins to grow in response to further temperature increases, (4). In Small polaron tunnelling model (SPT), n rises as the temperature rises [108]. In the presented series, for $x = 0.0, 0.2$ and 0.8 samples, the process is regulated by a small polaron tunnelling model as n increases with temperature. For $x = 0.4$ and 1.0 samples, small polaron tunnelling model governs up to $570\ K$ and after that n starts decreasing and the phenomenon is governed by large polaron tunneling model. For $x = 0.6$ sample, n decreases up to 0.54 and then it starts increasing with the increase in temperature. So, we can conclude that overlapping large polaron tunnelling model is responsible for the motion of charge carriers in this sample.

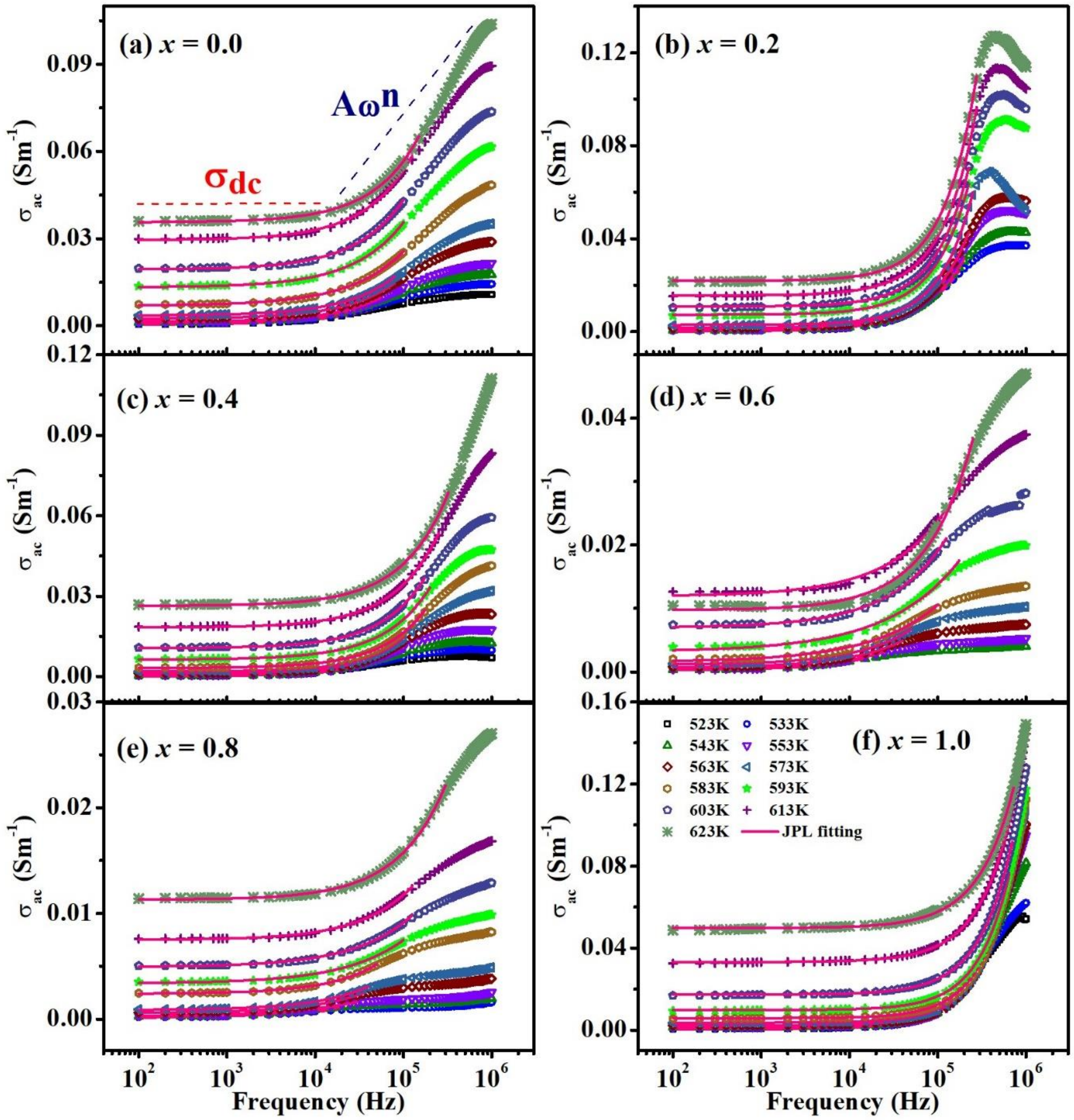

Fig. 3.16: (a-f) Fitting of Jonscher's power law to the ac conductivity plots up to maximum $1MHz$ frequency with the variation of temperature from $523K$ to $623K$.

We have plotted logarithmic relaxation time ($\tau = 1/2\pi f_{max}$) with the inverse of temperature (shown in Figure 3.17 (b)) in order to determine the activation energy (E_a) of charge carriers. Where, f_{max} is the maximum frequency at which relaxation peak is seen in Z'' vs. frequency plots. All the plots show linear behavior and they are fitted into Arrhenius equation given as [109]:

$$\tau = \tau_0 \exp[-\frac{E_a}{K_B T}] \tag{3.9}$$

here, K_B is the Boltzmann constant which has a magnitude of $1.38 \times 10^{-23}\ JK^{-1}$. For all the samples, we need two straight lines to fit all the data points as it is showing some deviation around $550\ K$. This is the transition temperature from FIM to PM state as per high temperature $M - T$ plots. This deviation around T_c indicates magneto-dielectric coupling in these samples. The activation energy of all the samples is estimated and tabulated in Table 3.3. These values of activation energy in FIM and PM region are comparable to singly ionized oxygen vacancies as reported by Wu *et al* [45].

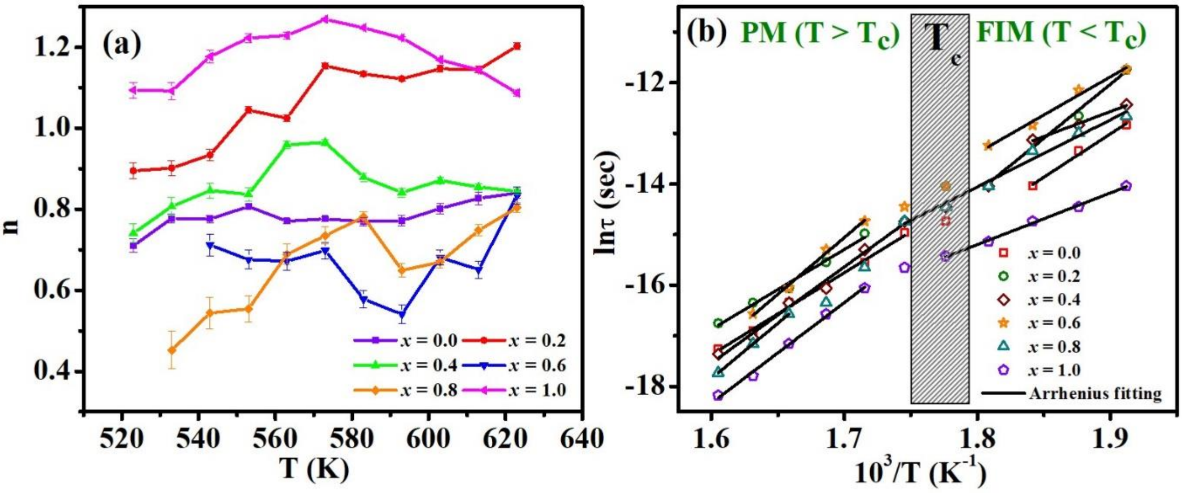

Fig. 3.17: (a) Temperature dependent exponent "n" along with the error bar and (b) fitting of Arrhenius law to relaxation time curves for $(Gd_{1-x}Ho_x)_3Fe_5O_{12}$ (x = 0.0 to 1.0) samples.

Table 3.3: Activation energy of both FIM and PM regions for all the concentrations of Ho-GdIG samples.

x	E_a	
	FIM (eV)	PM (eV)
0.0	0.33	0.31
0.2	0.41	0.31
0.4	0.19	0.36
0.6	0.29	0.43
0.8	0.25	0.42
1.0	0.19	0.38

प्रौद्योगिकी संस्थान गुवाहाटी • Indian Institute of Technology Guwahati •

3.2 Nd substituted Gadolinium iron garnet

We have prepared $(Gd_{1-x}Nd_x)_3Fe_5O_{12}$ with $x = 0.0, 0.1, 0.2, 0.3$ and 0.4 samples through solid-state reaction approach as discussed in Section 2.1. The precursors were took in oxide form such as Gd_2O_3, Nd_2O_3 and Fe_2O_3 with purity greater than 99%. These oxides were mixed uniformly in acetone medium and kept for calcination at $800°C$ for 12 hours. Finally, the pellets were formed with $10mm$ diameter and about $1mm$ thickness and were sintered at $1300°C$ 24 hours.

3.2.1 Structural characterization

The crystal structure of RIG comprises of three sublattices. Two of the sublattices are occupied by iron ions, with iron at the octahedral $(Fe1(\mathrm{a}))$ and tetrahedral $(Fe2(\mathrm{d}))$ sites and the dodecahedral position is lodged by the rare earth element. Now, to verify the purity of the garnet phase in Nd-GdIG series, the XRD patterns were recorded and they are shown in Fig. 3.18. All the diffracted planes in these XRD patterns correspond to the standard garnet phase without any heterogenous phase indicating the proper diffusion of Nd^{3+} ions into the sublattice of GdIG. These patterns are refined using the Rietveld refinement technique. The refined plots for the Nd-GdIG series are presented in Fig. 3.19 and Fig. 3.20. The Nd-GdIG samples have formed with cubic crystal structure and with a space group of $Ia\bar{3}d$. The quality of the fitting is assessed based on the reliability parameters $(R_p, R_{wp}, R_{Bragg}, R_F)$ and goodness of fit (χ^2) as listed in Table 3.4. Moreover, the most intense diffraction peak i.e., (420) shifts towards lower 2θ values with Nd substitution, which indicates an enhancement in the lattice constant values as per Bragg's law. After refinement, the lattice constant of the parent sample is found to be 12.4961 Å. We have noticed a monotonous increment in the lattice constant with Nd substitution and it reaches 12.5496 Å for $x = 0.4$ sample. This enlargement in lattice constant can be attributed to the expansion of net ionic radii of the lanthanides as we move from Gd^{3+} (1.07 Å) ions to Nd^{3+} ions (1.12 Å). A similar enhancement in unit cell volume is also observed with Nd substitution in YIG due to its larger ionic radii [111]. Moreover, the ocuupancy values of each cation in a specific composition sample is matching well with the expected one. All the lattice parameters as well as occupancy values are also listed in Table 3.4.

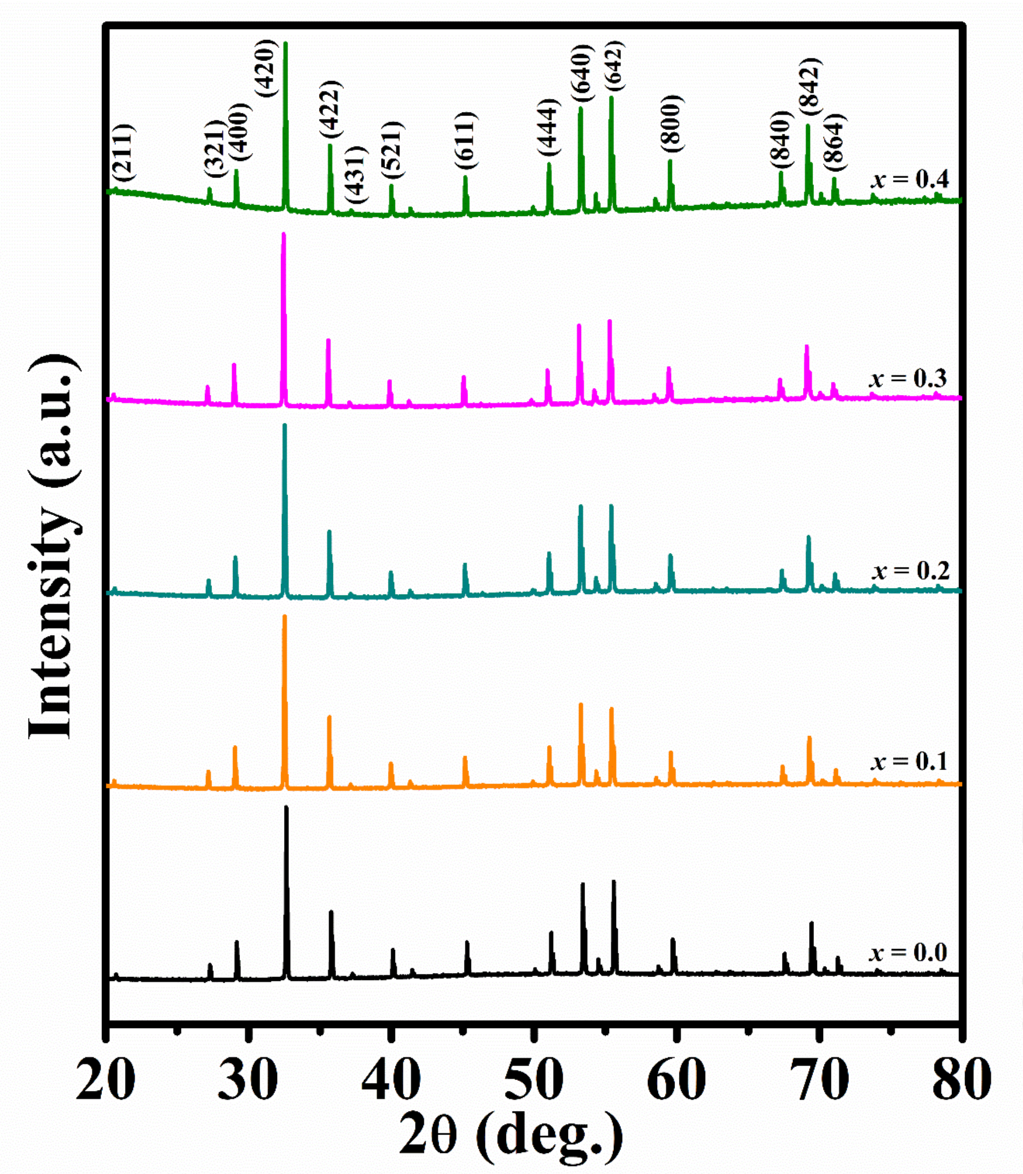

Fig. 3.18: XRD data patterns for $(Gd_{1-x}Nd_x)_3Fe_5O_{12}$ samples with $x = 0.0$ to 0.4.

Institute of Technology

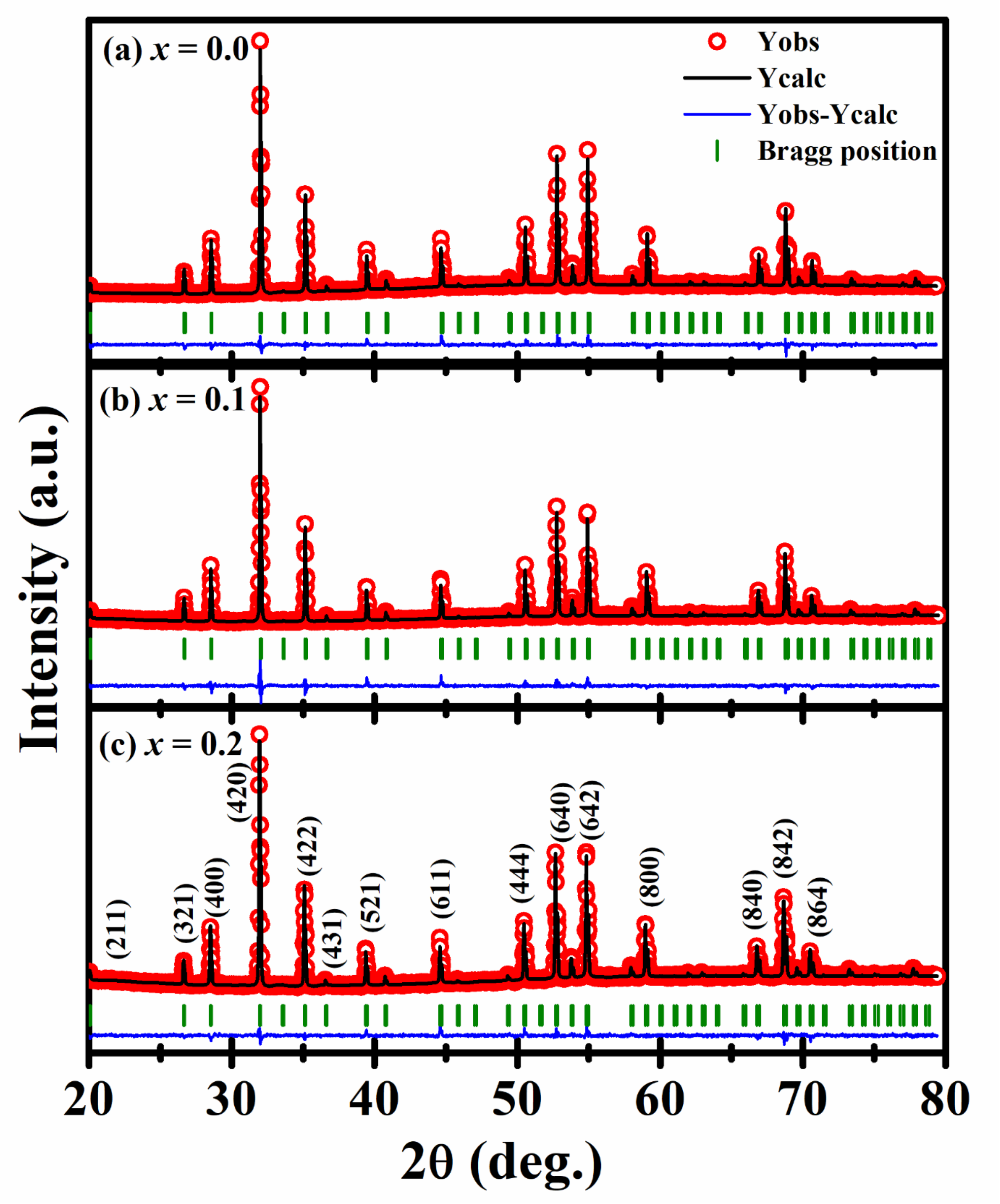

Fig. 3.19: Rietveld refined plots for $x = 0.0, 0.1$ and 0.2 samples of Nd-GdIG series.

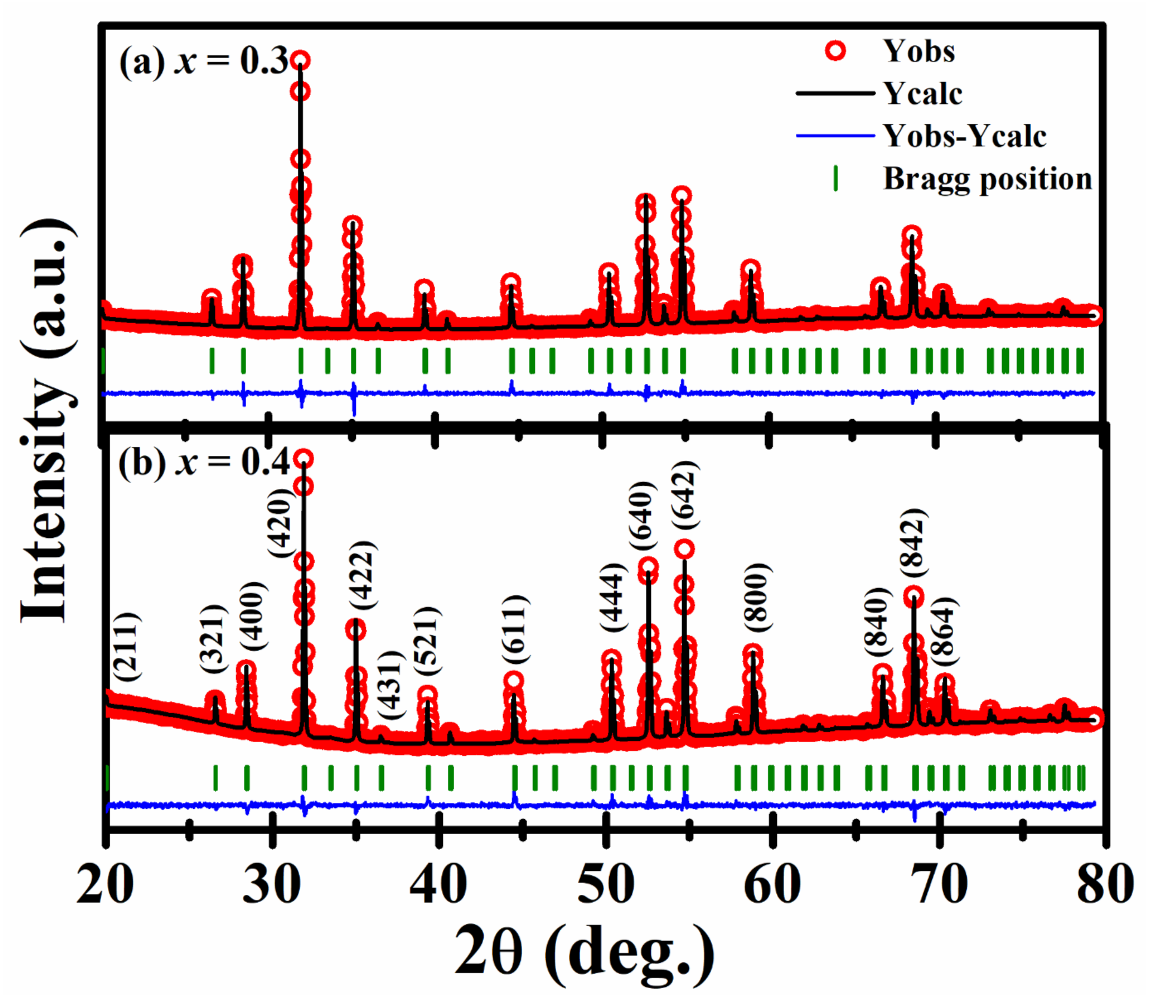

Fig. 3.20: Rietveld refined plots for $x = 0.3$ and 0.4 samples of Nd-GdIG series.

Table 3.4: Structural and refinement reliability parameters for different compositions of Nd-GdIG samples.

Sample → Parameters ↓	$x = 0.0$	$x = 0.1$	$x = 0.2$	$x = 0.3$	$x = 0.4$
Space group	$Ia\bar{3}d$	$Ia\bar{3}d$	$Ia\bar{3}d$	$Ia\bar{3}d$	$Ia\bar{3}d$
$a = b = c$ (Å)	12.4961 (1)	12.5024 (1)	12.5189 (1)	12.5303 (1)	12.5496 (1)
Volume (Å^3)	1945.9	1954.2	1962.0	1967.3	1976.4
R_p (%)	12.3	11.5	15.1	14.4	13.9
R_{wp} (%)	13.2	15.1	12.8	15.4	15.4
R_F (%)	5.2	5.2	4.4	5.1	6.3
R_{Bragg} (%)	5.1	5.7	4.3	4.8	6.2
χ^2	2.3	2.8	1.8	2.2	1.8
Occupancy					
Gd	2.97	2.66	2.38	2.09	1.75
Nd	0.0	0.28	0.55	0.89	1.17
Fe	4.96	4.98	4.97	4.92	4.98

Now, we have extracted XRD patterns by varying the temperature from $80K$ to $300K$ to further investigate the crystallographic interactions in different temperature conditions. The Rietveld refinement patterns from $80K$ to $300K$ have been demonstrated in Fig. 3.21 (a) for $x = 0.2$ sample. It is observed that the garnet phase without any impurity remains intact throughout the measured temperature range in all the XRD patterns. Moreover, the most intense peak corresponding to (420) plane is magnified and are shown in Fig. 3.21 (b). The peak is found to shift towards a lower 2θ value as we raise the temperature from $80K$ to $300K$. This shift suggests an increment in the lattice constant. This trend is verified by obtaining the lattice constant and bond length from the Rietveld refinement of the temperature-dependent XRD data. The dependence of both parameters is shown in Fig. 3.21 (c,d). The change in the lattice constant with temperature is consistent with the shift of the (420) Bragg peak towards lower 2θ values as the temperature increases. The lattice constant and bond length increase with temperature due to thermal expansion. As temperature rises, atoms vibrate more vigorously leading to greater interatomic distances. This causes the bond length to increase and as a result the lattice constant also expands. A similar type of lattice expansion with an increase in temperature is reported in $Pb_{1-x}La_xTi_{1-x}Al_xO_3$ $(0 \leq x \leq 0.25)$ ceramics [112]. However, they have observed a transformation of the tetragonal to cubic phase as the temperature is raised above room temperature. Moreover, Guillot *et al.* [113] have reported anomalies in SmIG single crystals at approximately $40\ K$ and $68\ K$ which is attributed to spin reorientation transitions. Although, in our study, these temperatures $(40\ K$ and $68\ K)$ fall outside the measured range, the rest of the temperature dependent lattice constant curve $(80\ K - 300\ K)$ exhibits a similar trend. Therefore, it can be reasonably assumed that Nd-GdIG samples may also display comparable anomalies near their spin reorientation transition temperatures.

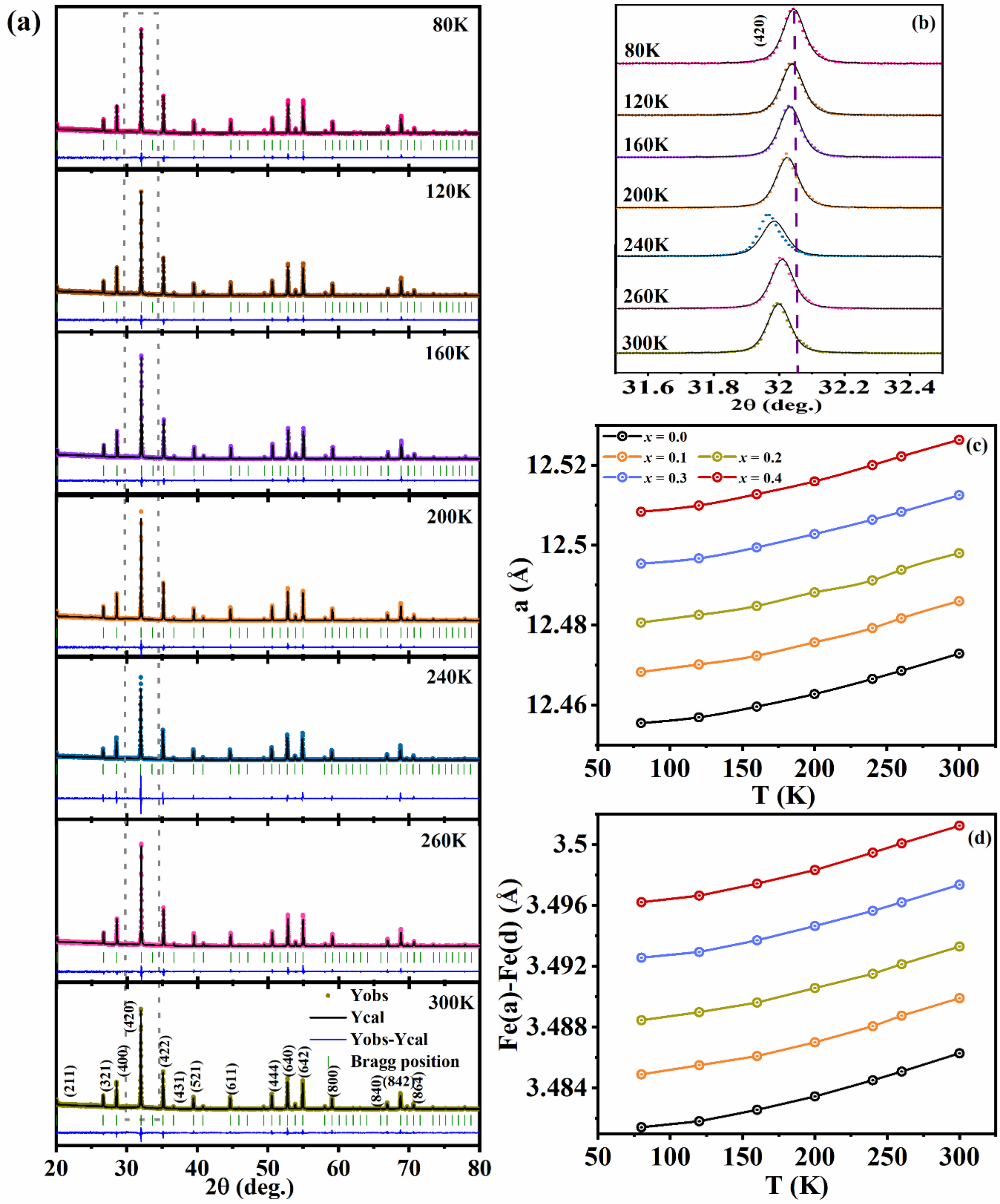

Fig. 3.21: (a) Temperature dependant XRD patterns for $x = 0.2$ sample, (b) magnified view of most significant peak i.e., (420) and variation of (c) lattice constant, and (d) bond length with temperature.

The FESEM micrographs are utilized to evaluate grain size of the samples by analyzing the histograms, which are fitted to log-normal distribution function. These micrographs, along with their corresponding frequency count histograms are illustrated in Fig. 3.22. A consistent morphology is observed across all the samples, characterized by well-defined grains separated by distinct grain boundaries. Notably, the analysis reveals that the average grain size for the $x = 0.0$ sample is $1.77\ \mu m$, which has been increased to $2.72\ \mu m$ for the $x = 0.4$ sample.

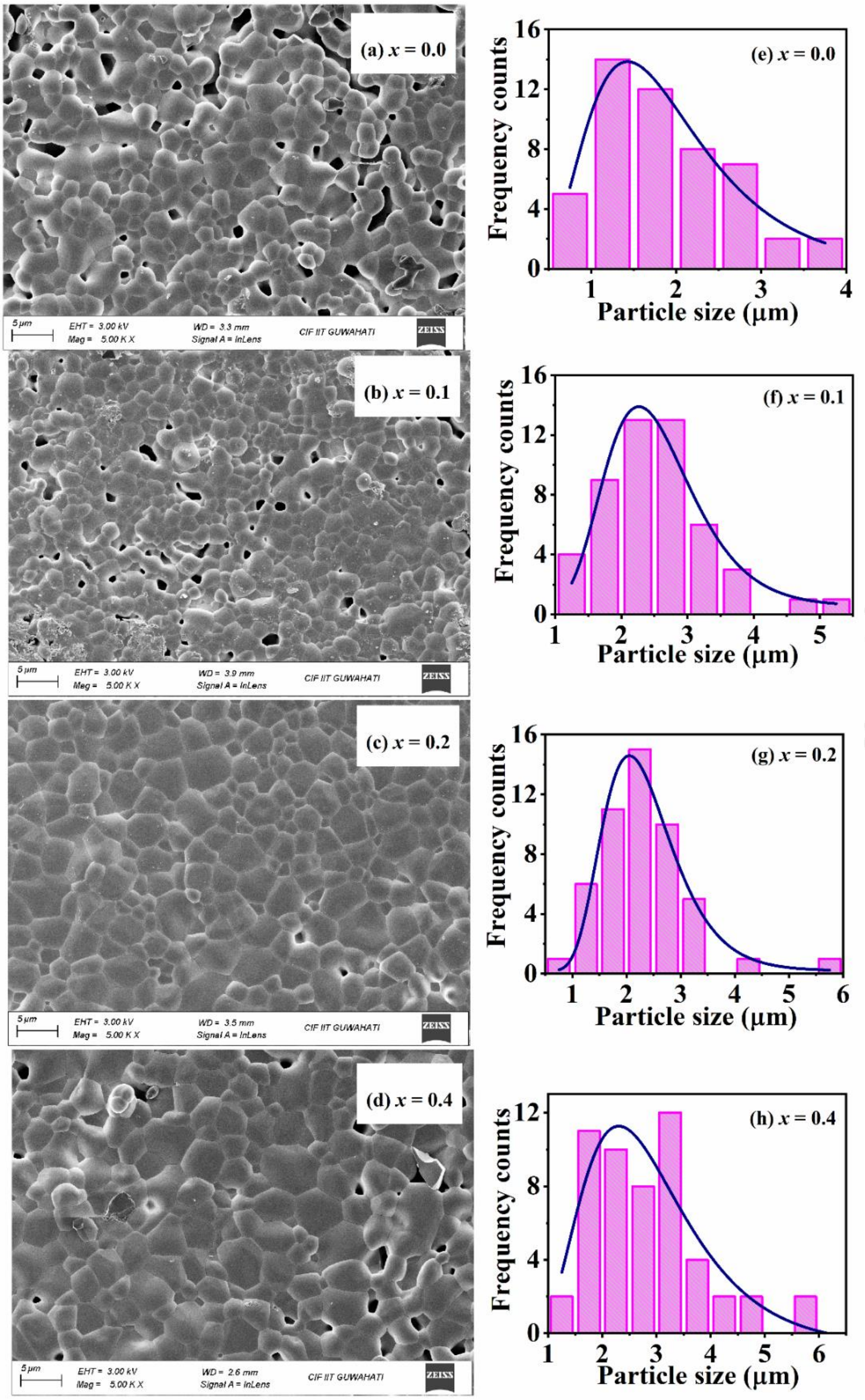

Fig. 3.22: FESEM images of Nd-GdIG samples with $x = 0.0, 0.1, 0.2$ and 0.4 and their inset are their respective particle size histograms to calculate the grain size.

Raman spectra at room temperature are studied in order to get insight into the crystal structure and the dynamic behaviour of atoms. These curves are fitted to Gaussian function to determine the various phonon excitation within our system and the same has been displayed in Fig. 3.23. According to Group theory, the garnet system has total 25 active Raman modes i.e., $3A_{1g}$ are internal modes, $8E_g$ are translational modes and $14F_{2g}$ corresponds to rotatory modes [96]. Fig. 3.23 provides the assignment of all observed Raman modes, demonstrating good agreement with the predicted number of active phonons. These Raman results resembles well with that of SmIG synthesized through hydrothermal process [114]. The most intense peak lies around $255\,cm^{-1}$ in all the compositions and it arises because of the translation motion of either Gd^{3+} or Nd^{3+} ions. Moreover, the modes above $300cm^{-1}$ results due to the stretching and bending of the bonding between $Fe-O$ situated at octahedral and tetrahedral sites [97]. Further, it has been observed that the intensity of the peak around $150cm^{-1}$ decreases with Nd substitution, likely due to the distortion in the crystal lattice. The $A_{1g}\ +\ E_g$ peak around 340 cm^{-1} shifts towards a lower wavenumber with Nd substitution, indicating a reduction in the force constant, consistent with the increase in lattice constant observed in the XRD results. The Raman spectroscopy also supports our previous results that states that the all the samples of Nd-GdIG series are formed in pure garnet phase.

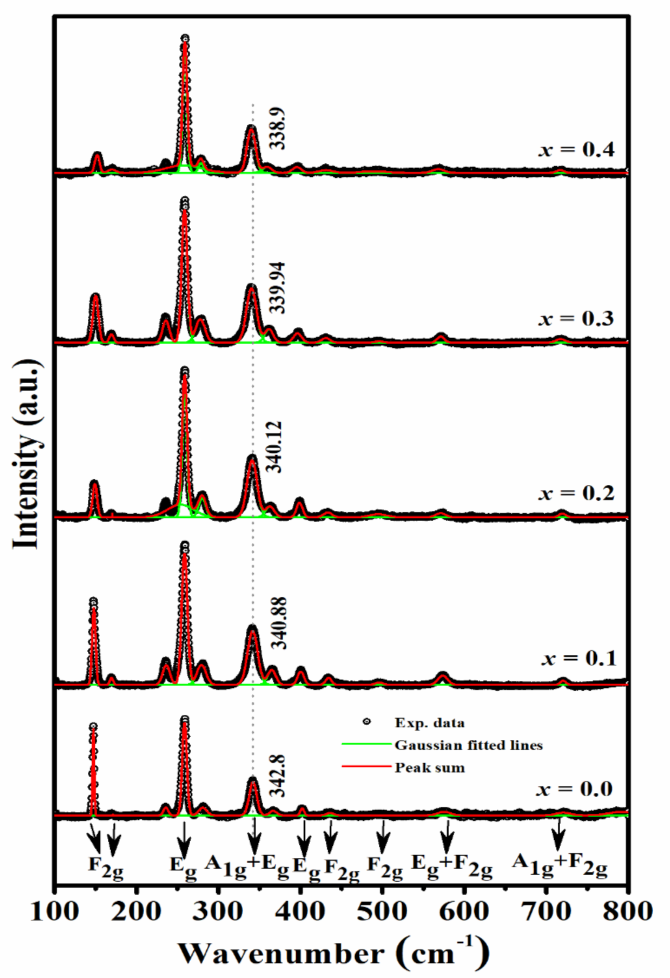

Fig. 3.23: Room temperature Raman spectrum fitted to Gaussian function and showing all the observed Raman active phonons for all the compositions of Nd-GdIG samples.

3.2.2 Magnetic characterization

The ZFC and FC variation in magnetization with temperature (M-T) are recorded and they are depicted in Fig. 3.24 (a-e). The magnetic interactions in Nd-GdIG samples lead to two types of transitions in the M-T plots; the first one is spin-reorientation transition and another is magnetic compensation. The net magnetization in RIGs arises from the weak ferromagnetic interaction between Fe^{3+} ions and the rare earth ion moment and can be empirically expressed as:

$$M_{net} = 3M_{Fe(d)} - 2M_{Fe(a)} - (3-x)M_{Gd(c)} - xM_{Nd(c)} \tag{3.10}$$

Since, the ordering temperature of rare earth spins in garnets is below $20K$, their contribution in net magnetization depends upon both internal and external magnetic fields. Therefore, at higher temperatures, the magnetic moment of Fe^{3+} ion spins predominate with minimal contributions from other sources. So, as the temperature rises from $5K$, a slight fluctuation at $\sim 11K$ is observed in the parent sample which gets more pronounced in the Nd-doped samples. This transition is named as spin reorientation transition and it lies around $\sim 50K$ in all the Nd doped GdIG samples as shown in Fig. 3.24 (f). Similar type of spin reorientation transition is also observed by Li *et al.* [115] during the study of magnetocaloric effect in Ho and Er iron garnet systems. The anisotropic exchange interaction between Fe^{3+} ions and rare earth ions generates an effective field at the tetrahedral and octahedral sites which helps the Fe^{3+} ions maintain their AFM ordering. As temperature decreases, the rare earth ions (Gd or Nd) become more magnetically ordered, strengthening their magnetization. This creates a stronger effective magnetic field that influences the Fe^{3+} ions in the material. Normally, Fe^{3+} ions prefer to align their spins in a specific direction due to magnetic anisotropy which resists changes in their orientation. However, when the effective field from the rare earth ions becomes strong enough, it can overcome the Fe^{3+} ion's anisotropy energy. At this point, the Fe^{3+} ions change the direction of their magnetization to align with the stronger field. This change is called spin reorientation and occurs at a characteristic temperature [31]. Since, the magnetic moment of Nd^{3+} $(3.62\mu B)$ ions is lower as compared to Gd^{3+} $(7.94\mu B)$ ions, which favours to relatively lower effective field production. As a result, the spin reorientation transition occurs at relatively higher temperatures in Nd-doped samples.

On further increasing the temperature beyond spin reorientation transition, the magnetic interaction between Fe^{3+} ions at octahedral site and the rare earth ions collectively suppress the moment of Fe^{3+} ions at tetrahedral site [116]. This results in the fall in net magnetization as per above empirical relation (eq. 3.8). After certain temperature, all the sublattices balance out the moment of each other and magnetic compensation arises. The T_{comp} of the parent compound is detected at $\sim 291K$ which is consistent with the reported literature [117]. The T_{comp} is found to be shift towards lower temperature with Nd substitution and it reaches almost $200K$ for $x = 0.2$ sample. This decrement in T_{comp} can be ascribed to the replacement of Gd^{3+} ions with Nd^{3+} ions, which have a lower magnetic moment, resulting in a decrease in the secondary terms of the empirical formula (refer to eqn. 3.10) and consequently lowering the T_{comp}. A similar reduction in T_{comp} is also observed by Aakansha *et al.* [86] when they have substituted Gd^{3+} by Sm^{3+} ions with a lower moment of $0.71\mu B$. However, it has been noticed that magnetic compensation disappears for $x = 0.3$ and 0.4 samples. For $T > T_{comp}$, magnetization increases due to domination of ferrimagnetic components in Nd-GdIG samples [86].

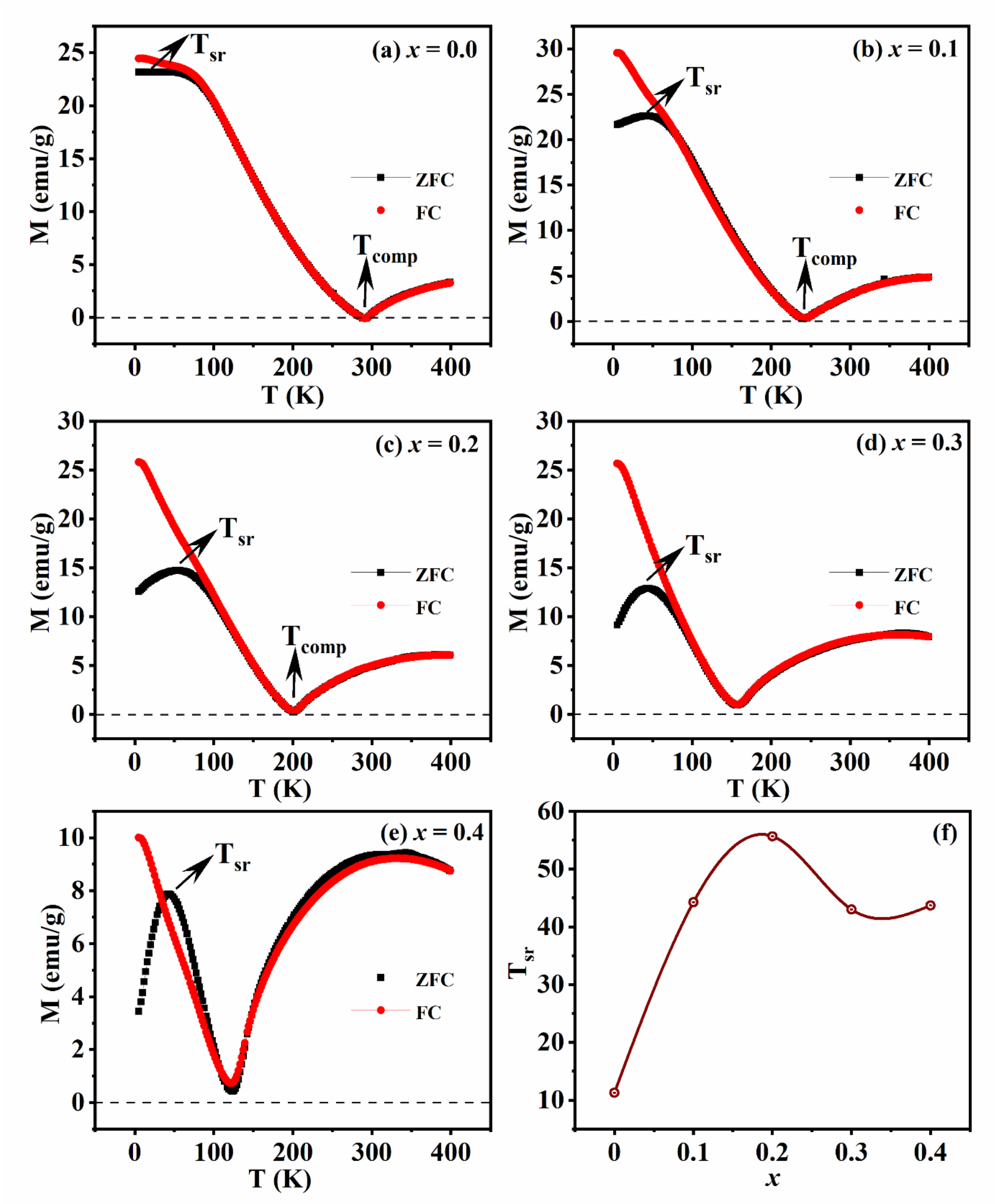

Fig. 3.24: (a-e) Record of magnetization with respect to temperature under ZFC and FC conditions by applying an external magnetic field of 200 Oe intensity for all the samples of $(Gd_{1-x}Nd_x)_3Fe_5O_{12}$ ($x = 0.0 - 0.4$) samples and (f) spin reorientation temperature as a function of x concentration.

Now, to further analyze the magnetic behaviour of Nd-GdIG samples, magnetic hysteresis curves are recorded at $5K$ and $300K$ as shown in Fig. 3.25 (a,b). The room temperature M-H loops are not completely saturated because the magnetically compensated region prevents the spins from aligning in an ordered pattern to show saturation. However, when the temperature is reduced to $5K$, which is far away from room and compensation temperature, the loops achieve saturation after applying a $1T$ magnetic field. We have deduced the saturation magnetization (M_s) and effective anisotropy constant (K_1) for these samples by fitting the initial M-H loops ($0 \rightarrow 5T$) to the Law of Approach to Saturation (LAS) equation as per eqn. (3.2) [98]. The room temperature saturation magnetization varies from 0.71 emu/g ($x = 0.0$) to 10.76 emu/g ($x = 0.4$). This increase in M_s can be attributed to the magnetic compensation temperature of the parent compound being close to room temperature. Upon doping with Nd, T_{comp} shifts to a lower temperature, resulting in a higher M_s value for these doped samples compared to the parent compound at RT. Similar increment in M_s is observed by Sharma *et al.* [111] with Nd substitution in Yttrium iron garnet. However, they have ascribed the improvement in magnetization to the exchange interaction among Fe^{2+} and Fe^{3+} ions. Moreover, the anisotropy constant is also calculated and tabulated in Table 3.5. It is interesting to note that the anisotropy constant increases from the order of 10^5 to 10^6 erg/cc as the temperature decreases from room temperature to $5K$, contributing to the magnetic compensation in these samples. The anisotropy constants obtained are comparable to those found in various garnet and hexaferrite systems [144,145].

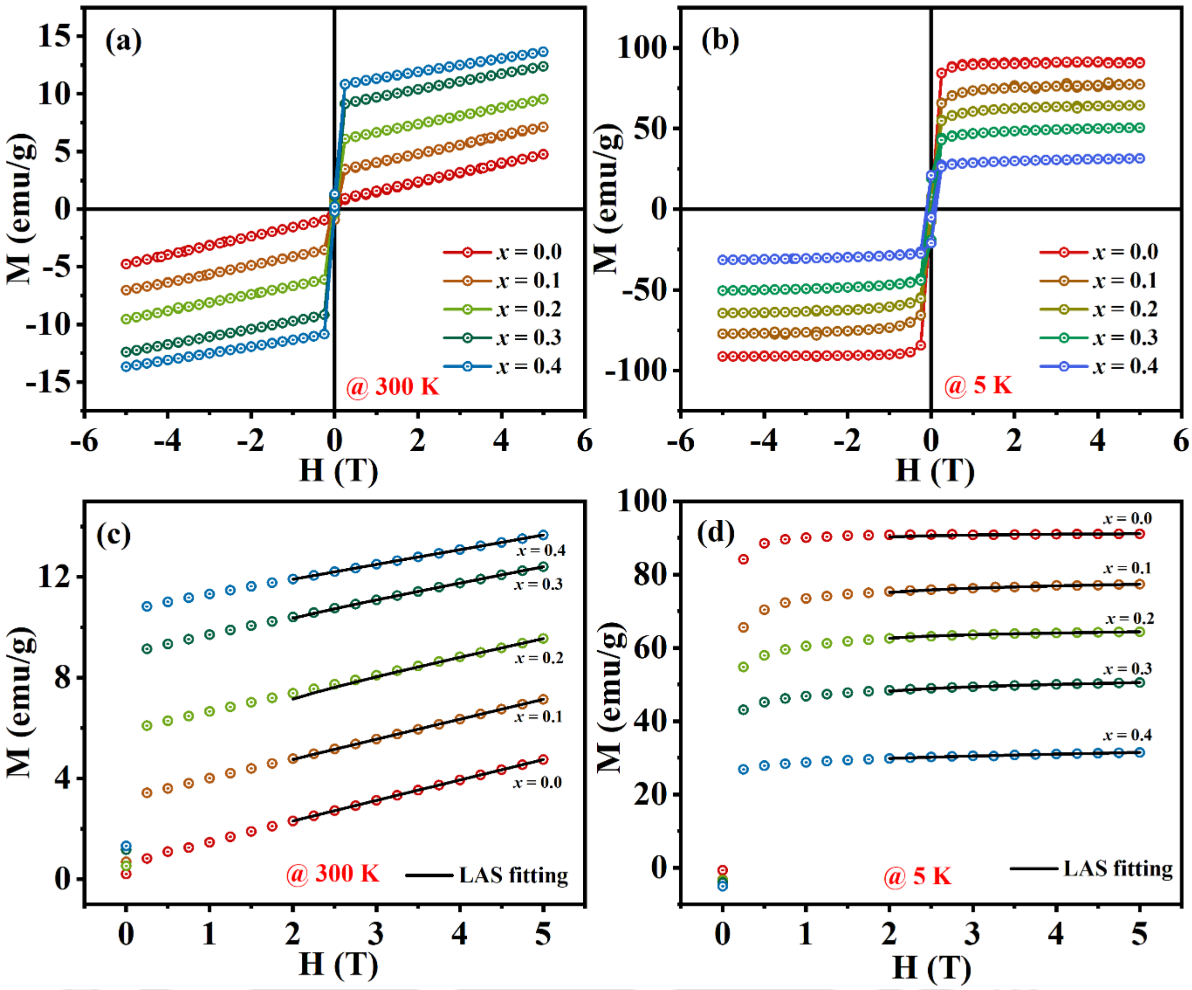

Fig. 3.25: (a,b) Magnetic hysteresis curves at $300K$ and $5K$ and (c,d) fitting of their initial M-H curves to LAS relation for all the samples of Nd substituted GdIG samples.

Table 3.5: List of fitting parameters of LAS equation for both the measured temperatures i.e., $300K$ and $5K$.

x	$300K$			$5K$		
	$M_s\ (emu/g)$	$K_1\ (10^5)$ (erg/cc)	$c\ (10^{-5})$ $(emu/g\ T)$	$M_s\ (emu/g)$	$K_1\ (10^6)$ (erg/cc)	$c\ (10^{-5})$ $(emu/g\ T)$
0.0	0.71	0.32	8.09	91.13	4.16	0.28
0.1	3.21	4.31	7.87	76.02	4.76	3.17
0.2	6.01	5.81	7.17	63.55	4.01	2.08
0.3	9.25	1.05	6.34	48.95	3.73	3.62
0.4	10.76	1.28	5.79	29.35	1.45	4.39

3.2.3 Dielectric characterization

The complex dielectric permittivity can be expressed as $\varepsilon^* = \varepsilon' - j\varepsilon''$ with ε' be the real component of dielectric permittivity that signifies the amount of electrical energy stored as potential energy, leading to polarization within the dielectric material. The imaginary component i.e., ε'' indicates energy dissipation which inevitably occurs alongside energy storage. The temperature dependence on dielectric permittivity (ε') by supplying 0 to $3T$ magnetic field at $10kHz$ frequency is analyzed and displayed in Fig. 3.26 for all the samples of Nd-GdIG series. We have measured ε' with geometrical capacitance (C_o) and the experimentally produced capacitance (C) as follows [48]:

$$\varepsilon' = \frac{C}{C_o} = \frac{Cd}{A\varepsilon_o} \tag{3.11}$$

where, A and d are the area and thickness of the used pellet, respectively and ε_o is the permittivity of free space. The dielectric constant value varies in between 6 to 9 in the entire temperature range for all the samples. These values of ε' are comparable to the dielectric constant of other garnet systems [146,147]. Additionally, we have observed a systematic increase in ε' values with the increase in temperature irrespective of the applied magnetic field. As the temperature rises, the thermal energy provided to the system allows more charge carriers to become mobile, contributing to the overall polarization of the dielectric material. This increased mobility and subsequent polarization lead to a higher ε' value. In $x = 0.0$ to 0.2 concentrations of Nd-GdIG series, a slight anomaly is observed in the T_{comp} region (denoted by cyan colour circle), which is independent of the applied magnetic field, indicating that this change is primarily driven by the internal magnetic field. As the temperature is further reduced, two distinct anomalies emerge: one around a secondary drop in the M-T curves around $\sim 150K$ (denoted by red colour circle) and another at very low temperatures near T_{sr} (denoted by black colour circle). Both transitions are dependent on the external magnetic field, showing slight variations with the application of a magnetic field from 0 to $3T$. However, for samples with $x = 0.3$ and 0.4, only two anomalies are detected, one near the T_{sr} region and another around the secondary drop. All the transitions observed in the ε' plots correspond to the magnetic transitions in the M-T curves, indicating the presence of magneto-dielectric properties in these samples. These materials have potential applications in sensors, tunable microwave components, and memory devices. Their ability to respond to external magnetic and electric fields makes them ideal for miniaturized and energy-efficient technologies in telecommunications, data storage, and sensing.

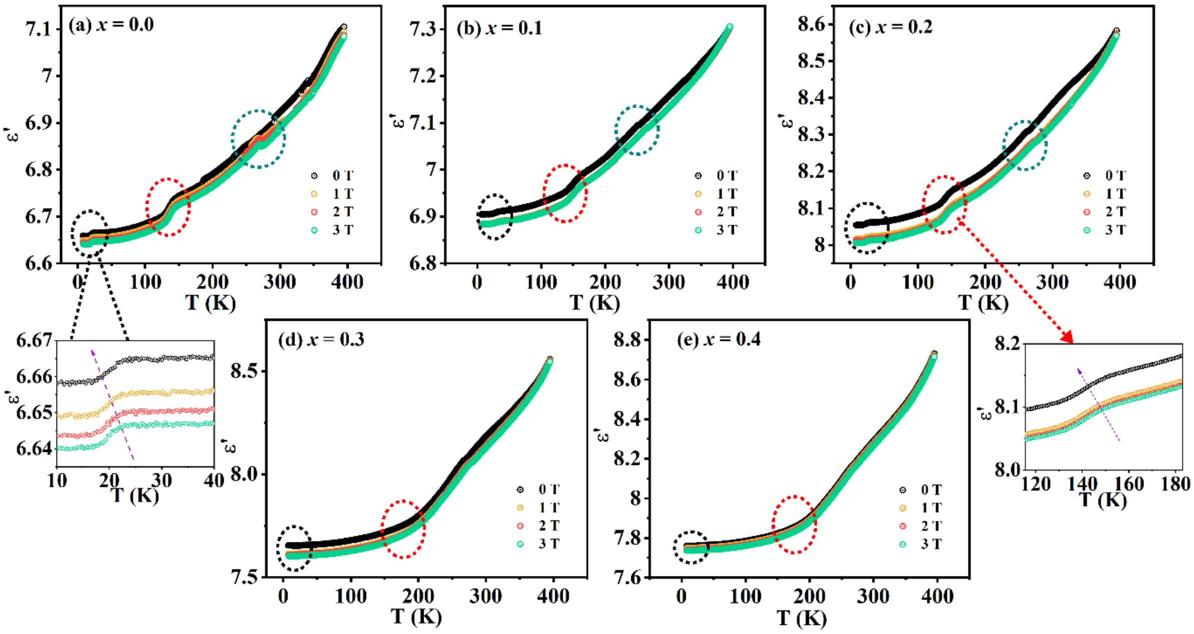

Fig. 3.26: (a-e) Temperature-dependent dielectric constant by applying magnetic field from 0 to $3T$ at $10kHz$ frequency for $(Gd_{1-x}Nd_x)_3Fe_5O_{12}$ samples with $x = 0.0$ to 0.4. Two small plots represents the magnified view of the peaks observed in dielectric constant curves.

The temperature-dependent dielectric curves are replotted with varying frequencies ranging from $5kHz$ to $100kHz$, and presented in Fig. 3.27. With the decrease in temperature, the Gd^{3+} and Nd^{3+} spins begin to align and the antiferromagnetic coupling between the rare earth spins and the net magnetization of the Fe^{3+} spins leads to a gradual decrease in magnetization until it reaches compensation. For $x = 0.0$ to 0.2 sample, while lowering the temperature from $400K$, a slight fluctuation is noticed around their corresponding to magnetic compensation transitions. As the temperature decreases further, a broad anomaly emerges around $125K - 200K$, which is also evident in the dielectric curves shown in the inset of Fig. 3.27 (b) and corresponds to the secondary drop in the magnetization curve. Further cooling reveals another anomaly around $45K$, which can be attributed to the spin-reorientation transition in the sample. For the $x = 0.3$ and 0.4 compositions, the last anomaly near magnetic compensation is absent, though the other two anomalies are still present. These findings closely align with the temperature dependence of the magnetization curves that supports the presence of magneto-dielectric coupling in these samples.

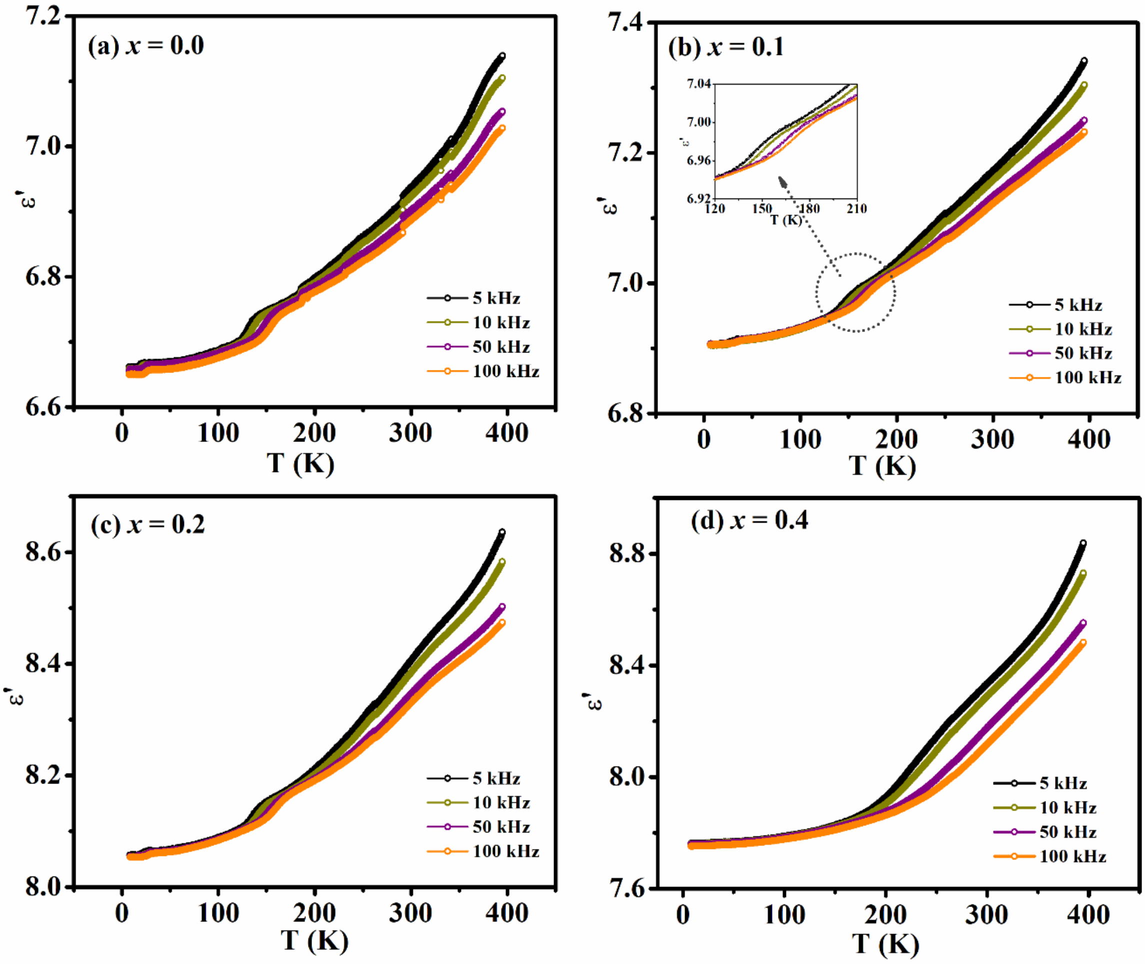

Fig. 3.27: Dependence of temperature on dielectric constant at different frequencies i.e., $5kHz$ to $100kHz$ for $x = 0.0, 0.1, 0.2$ and 0.4 compositions of Nd-GdIG samples.

The ability to store electric charge in any dielectric material is inherently accompanied by some energy dissipation as heat which is quantified as dielectric loss, denoted by $\tan\delta$. The ratio of ε'' to ε' stands for dielectric loss ($\tan\delta$) factor or energy loss [118]. The temperature dependance on $\tan\delta$ by varying magnetic field from 0 to $3T$ at $10kHz$ frequency is illustrated in Fig. 3.28. Notably, the peaks in the $tan\ \delta$ curves are more significant and broader compared to the ε' plots. All samples exhibit an increase in $tan\ \delta$ with rising temperature, suggesting enhanced conductivity due to the activation of mobile charge carriers [119]. For the parent sample, only two peaks are observed at lower temperatures in the absence of a magnetic field, as shown in the inset of Fig. 3.28 (a). However, the third peak around T_{comp} begins to emerge and becomes more pronounced with the application of a magnetic field, indicating an enhancement of the magneto-dielectric effect. Moreover, in $x = 0.1$ and 0.2 samples, all three peaks are present in the

$tan\delta$ curve, though the peak in the T_{comp} region is somewhat diminished. In contrast, for the $x = 0.3$ and 0.4 samples, only two peaks are observed: one in the T_{sr} region and another starting from the secondary fall zone. These observations suggest that the Nd-GdIG series exhibits magneto-dielectric properties, further highlighting the complex interplay between dielectric and magnetic behavior in these materials.

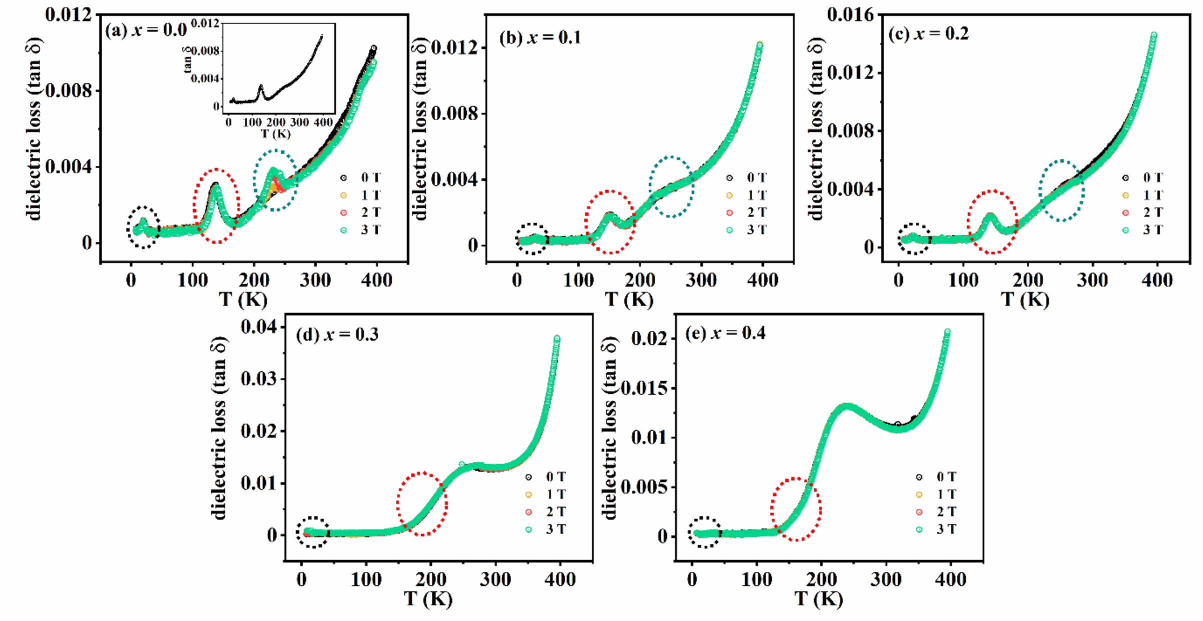

Fig. 3.28: Variation in dielectric loss ($\tan\delta$) with respect to temperature at different magnetic fields ($0 - 3\ T$) at $10\ kHz$ frequency for all the samples of Nd substituted GdIG series.

The isothermal magneto-dielectric (MD) curves are recorded over the temperature range of $10\ K$ to $60\ K$, as shown in Fig. 3.29 (a-e). Across all the samples, a consistent anomaly in the dielectric measurements was observed near the spin reorientation transition (refer to Fig. 3.24 (f)). This is the reason why we focused on conducting MD measurements within this specific temperature range. It is interesting to note that $x = 0.0$ and 0.1 samples show negative MD response up to $\sim 1\ T$ magnetic field for the entire measured temperature range. The effect becomes more pronounced with the increase in temperature. Further, for $x = 0.2$ sample, a negative MD effect is observed as well and it persists up to $5\ T$ magnetic field when the temperature is varied from $10\ K$ to $60\ K$. Conversely, for $x = 0.3$ and 0.4 samples, for the temperature range of 10 to $50\ K$, initially shows a positive MD effect followed by a negative MD response up to $1\ T$ magnetic field. However, this effect changes to negative MD at $60\ K$ for both samples. This combination of positive and negative MD effects can be attributed to the polycrystalline nature of the materials, where the contribution from different crystalline planes is averaged, leading to a complex dependence of the MD behavior on the applied magnetic field [120]. Moreover, the MD curves closely align with the magnetization M(H) measurements presented in Fig. 3.25. As observed in the M(H) loops at $5\ K$ (which is close to the measured temperature of MD curves), the magnetization increases rapidly up to $0.5\ T$, and then a small curvature is followed by a saturated curve after $1\ T$ field which is expected for typical ferrimagnetic materials. This trend is mirrored in the MD curves for all samples, where the positive or negative MD response is noticeable only up to $1\ T$. Beyond this field, the MD response stabilizes and remains constant, reflecting the same behavior observed in the magnetization data. Similar results are reported for Erbium iron garnet with a positive MD effect at $10\ K$ to that remains till $3\ T$ magnetic field and is further followed by a negative MD response [120].

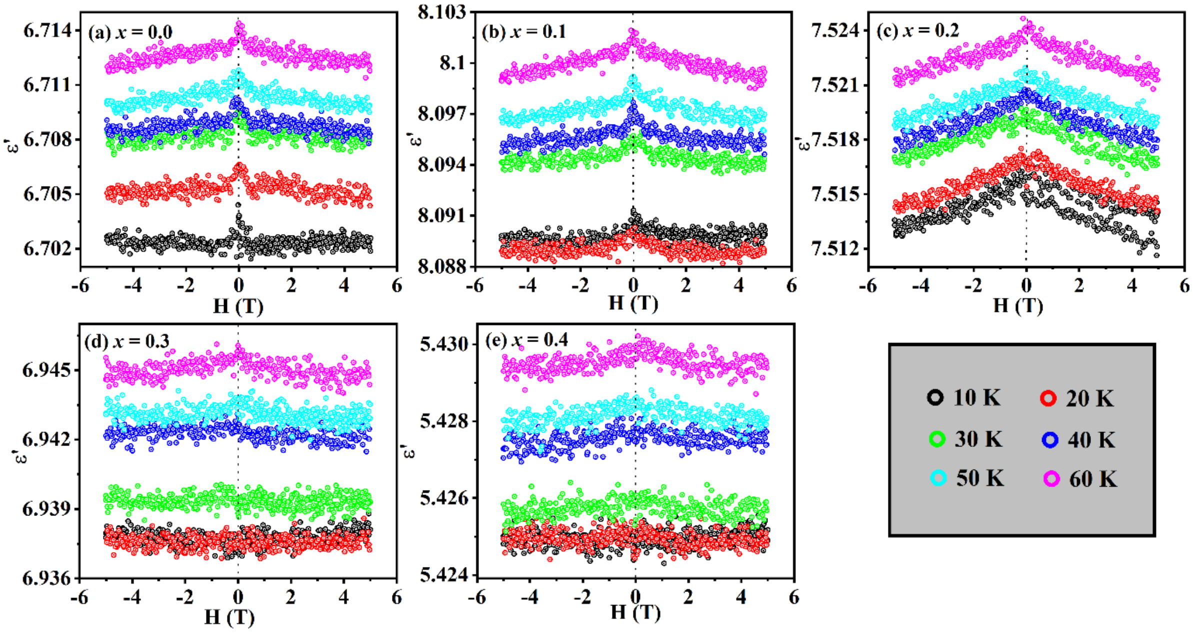

Fig. 3.29: Isothermal magneto-dielectric loops at $10kHz$ frequency in the temperature range of 10 to $60K$ for all the samples of the Nd-GdIG series.

3.3 Conclusion

We have successfully synthesized $(Gd_{1-x}Ho_x)_3Fe_5O_{12}$ $(x\ =\ 0.0$ to $1.0)$ samples using the conventional solid-state reaction method and confirmed the formation of the desired garnet phase through Rietveld refinement using FullProf software. The lattice constants for the samples exhibited a systematic decrease, ranging from 12.4841 Å for $x = 0.0$ to 12.3871 Å for $x = 1.0$, accompanied by decrease in bond lengths and bond angles at $Fe\ (a)$ and $Fe(d)$ sites due to Ho substitution. Analysis of FESEM micrographs revealed an increase in the volume density of grain boundaries with higher Ho doping. The

Raman spectra confirmed that the phonon modes are associated with the translational motion of rare-earth elements and the stretching and bending of the $Fe-O$ network. Further, XPS analysis validated the Gd^{3+} oxidation state and the presence of both Fe^{2+} and Fe^{3+} ions. All samples demonstrated a typical ferrimagnetic transition with T_c decreasing from $553K$ ($x = 0.0$) to $543K$ ($x = 1.0$). Furthermore, magnetic compensation was observed in all compositions where the net magnetic moment resulted from a complete cancellation of the contributions from all sublattices. Hysteresis loop measurements conducted at room temperature and $5K$ revealed significant enhancements in coercivity and the magnetocrystalline anisotropy constant with reducing the temperature from $300\ K$ to $5\ K$. Nyquist plots revealed depressed semicircles indicating a deviation from ideal Debye relaxation behavior. The dielectric constant exhibited a plateau region at low frequencies followed by a gradual decrease with increasing frequency which is consistent with Maxwell-Wagner type relaxation. Additionally, the ac conductivity is found to be more or less similar for all the concentrations of Ho-GdIG samples. The anomalies in the Arrhenius plots near the transition temperature range evidenced the magneto-dielectric coupling in all the samples of Ho-GdIG samples.

Besides Ho substitution in GdIG, we have also synthesized $(Gd_{1-x}Nd_x)_3Fe_5O_{12}$ ($x = 0.0$ to 0.4) ceramic samples using the solid-state reaction method. Rietveld refinement of the XRD patterns confirmed the pure garnet phase with a cubic crystal structure (space group $Ia\bar{3}d$) which remain stable in the temperature range of $80K$ to $300K$. The lattice parameter increased systematically from $12.4961(1)$ Å ($x = 0.0$) to $12.5496(1)$ Å ($x = 0.4$) that can be attributed to the larger ionic radius of Nd^{3+} compared to Gd^{3+} ions. The magnetic measurements revealed two transitions: a spin reorientation transition present in all samples and a magnetic compensation which is observed only up to $x = 0.2$ sample. This T_{comp} shifts from $291K$ to $200K$ as Nd content increased. This shift was linked to the lower magnetic moment of Nd^{3+} ions relative to Gd^{3+}. Moreover, the saturation magnetization increased significantly from room temperature to $5K$ which is accompanied by a notable improvement in anisotropy from the order of $10^5\ erg/cc$ to $10^6\ erg/cc$. Dielectric studies showed that the dielectric constant increased with temperature and is driven by thermally activated charge carriers enhancing polarization. Interestingly, the dielectric loss anomalies were correlated with magnetic transitions indicating magneto-dielectric coupling in these samples. This coupling was further validated through consistent correlation between isothermal magneto-dielectric and magnetic hysteresis curves which are getting saturated after few Tesla magnetic field, highlighting the strong interdependence of magnetic and dielectric properties in Nd-doped GdIG garnets.

Indian Institute of Technology Guwahati

Chapter 4

Magnetic and dielectric properties in Ho substituted Samarium and Dysprosium iron garnet

This chapter explores the magnetic and dielectric properties of Ho-substituted Samarium and Dysprosium iron garnets (SmIG and DyIG). SmIG is notable for its strong magneto-crystalline anisotropy at low temperatures, while HoIG exhibits magnetic compensation at $150K$ [121], [122]. Previous studies, such as those by Caffarena *et al.* [123] revealed that increasing the sintering temperature of $Sm_{0.6}Ho_{2.4}Fe_5O_{12}$ reduces coercive force due to grain growth, while Rivera *et al.* [124] confirmed the ferrimagnetic nature of $Sm_{3-x}Ho_xFe_5O_{12}$ samples with $x = 0.0$ to 1.0 and analyzed its structural and morphological changes. SmIG was chosen as the base material due to its high dielectric constant, low dielectric loss, and high Curie temperature, which makes it ideal for applications like microwave devices, magnetic storage, and sensors. Substituting Ho into SmIG introduces competing magnetic interactions due to the optimal ionic size and high magnetic moment of Ho^{3+} ions. To investigate these effects, the $(Sm_{1-x}Ho_x)_3Fe_5O_{12}$ with $x = 0.0 - 1.0$ were synthesized focusing on structural, magnetic, and dielectric properties to enhance understanding and explore potential applications.

Warburg was the first to discover the magnetocaloric effect (MCE) while studying the influence of temperature on iron in the presence of a magnetic field [125]. Many magnetic oxides exhibit significant MCE; however, they often undergo structural phase transitions that result in energy losses during the refrigeration cycle. In contrast, RIGs display MCE without structural phase transitions, offering a notable magnetic entropy change near the magnetic compensation point. For instance, Muniraju *et al.* [126] reported an exceptionally high entropy change $\Delta S_M = 45\, J/mol.K$ in a Cr- and Ga-doped GdIG sample at $2\ K$ under an $8\ T$ magnetic field. The substitution of Al in GdIG also known to enhance the MCE with the magnetic entropy value increasing from 1.92 to $3.08\, J/kgK$ [127]. Additionally, some RIGs exhibit both normal and inverse MCE. For example, GdIG demonstrates a reversal in the sign of ΔS_M which is close to room temperature (around 284 K), making it a promising candidate for air conditioning applications. Other examples include Er and Tb iron garnets which exhibit a sign change in ΔS_M at their respective magnetic transition temperatures [26,112]. Li *et al.* [85] reported that DyIG achieves a magnetic entropy change of 3.51 $J/kg \cdot K$ at 58 K under a 5 T magnetic field. Motivated by these findings, we aim to prepare $(Dy_{1-x}Ho_x)_3Fe_5O_{12}$ with $x = 0.0, 0.2, 0.4, 0.6, 0.8, 1.0$ (Ho-DyIG) samples to investigate their MCE and explore ways to enhance their magnetic entropy. Furthermore, we intend to analyze the type of magnetic phase transition in these materials using Arrott plots.

4.1 Ho substituted Samarium iron garnet

The samples of Ho-SmIG series were synthesized by solid-state reaction approach in which all the precursors are grinded in the acetone medium. The initial precursors were Sm_2O_3, Ho_2O_3 and Fe_2O_3 with purity better than 99%. The homogenous mixture was then proceeded for presintering at 800°C for 12 hours followed by pelettization. The pellets were finally sintered at 1400°C for 8 hours.

4.1.1 Structural characterization

The room temperature indexed XRD patterns of $(Sm_{1-x}Ho_x)_3Fe_5O_{12}$ samples for $x = 0.0$ to 1.0 are displayed in Fig. 4.1. The garnet phase formation with cubic crystal structure is verified with the Rietveld refinement of XRD patterns and $Ia\bar{3}d$ space group. The refined plots for all the samples of Ho-SmIG series are demonstrated in Fig. 4.2 and 4.3. The refined plots with red circles represent the experimental data points and black line shows the fitting. All the structural parameters including lattice constant, unit cell volume, space group and reliability parameters obtained from Rietveld refinement are listed in Table 4.1. The lattice constant along with its unit cell volume decreases on Ho substitution as Ho^{3+} ions (1.015Å) has smaller ionic radii as compared to Sm^{3+} (1.079Å) . The lattice parameters of the parent sample are in good agreement with the literature [59]. Ho^{3+} ions substitution may cause changes in the chemical bonding which results in lattice distortions and we observe a decrease in lattice parameters from 12.5375Å to 12.3936Å as x goes from 0.0 to 1.0. The $x = 0.2$ sample shows a relatively sharp drop in lattice constant due to the more pronounced chemical bonding alterations. The average bond lengths across $Fe\ (a) - Fe\ (d)$ network are found to decrease on Ho doping in accordance with smaller ion substitution at larger ion site. The bond angle between $Fe\ (a) - O - Fe\ (d)$ is getting reduced too on Ho substitution which affects the magnetic transition temperature. These bond length and bond angle for all the compositions of Ho-SmIG series are shown graphically in Fig. 4.4. We have also determined the occupancies (listed in Table 4.1) for different cations from the refinement and they are compatible with the initial stoichiometry ratio.

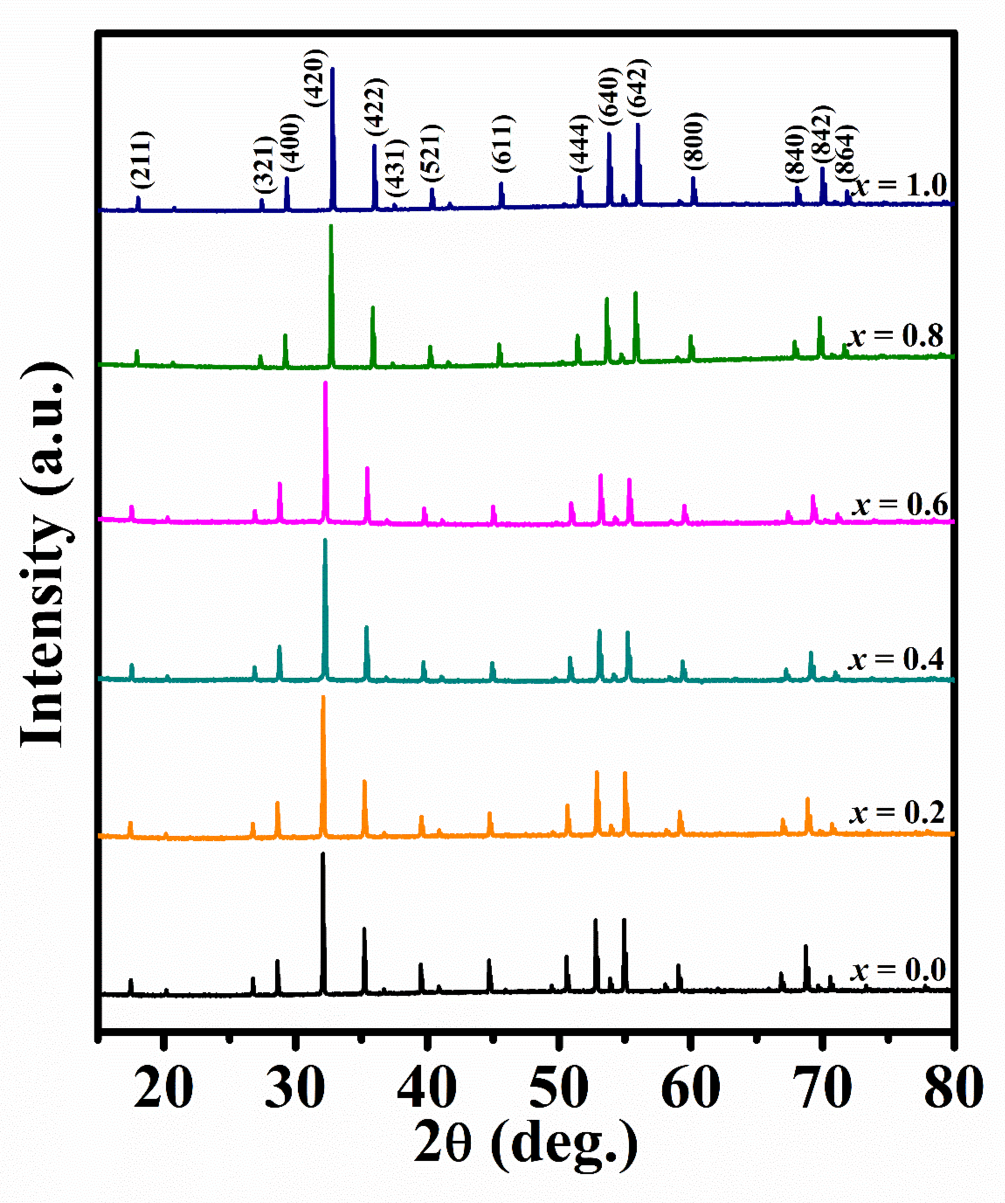

Fig. 4.1: The room temperature XRD patterns of $(Sm_{1-x}Ho_x)_3Fe_5O_{12}$ with $x = 0.0 - 1.0$ samples.

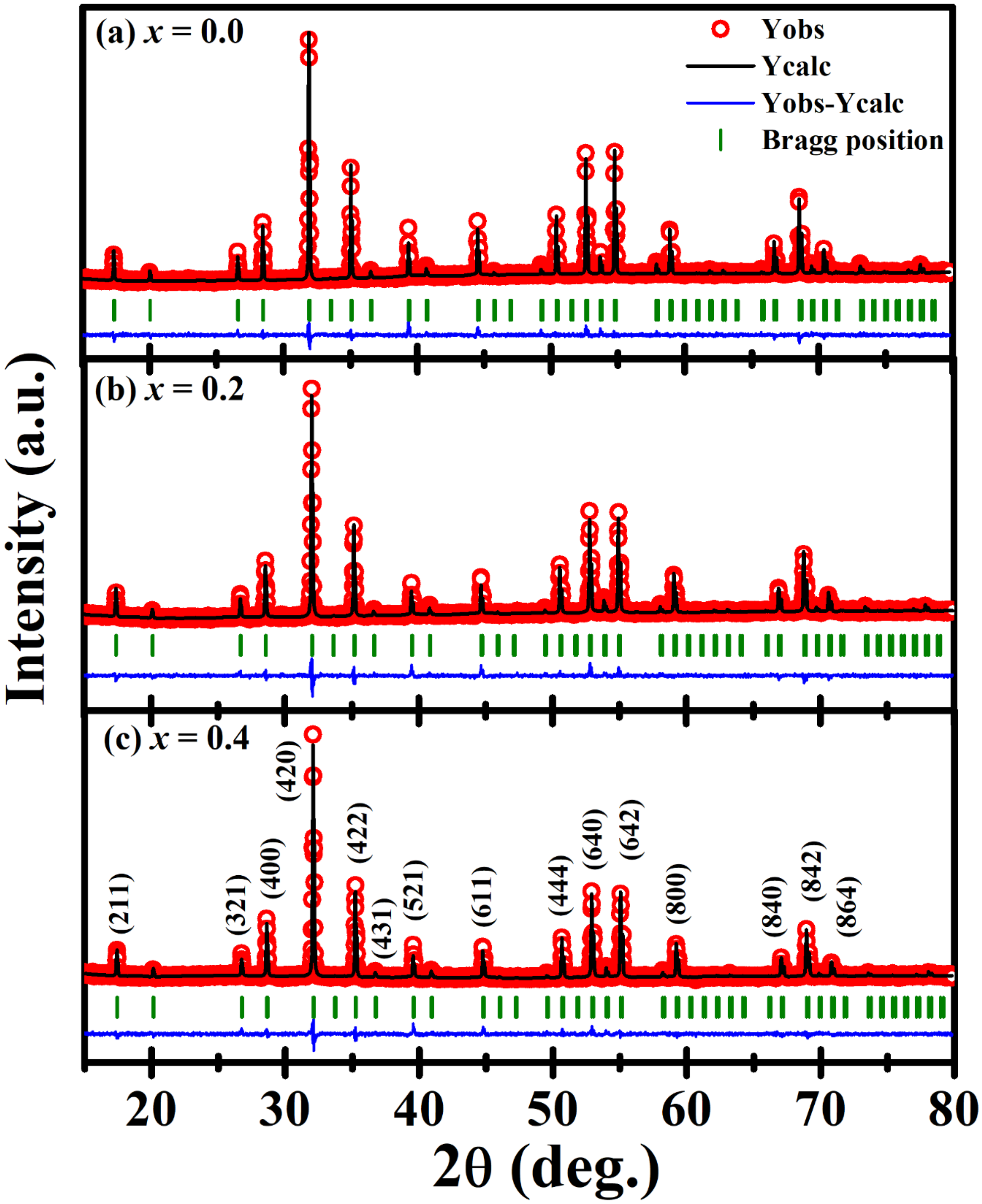

Fig. 4.2: The room temperature XRD data are Rietveld refined for $x = 0.0, 0.2$ and 0.4 sample.

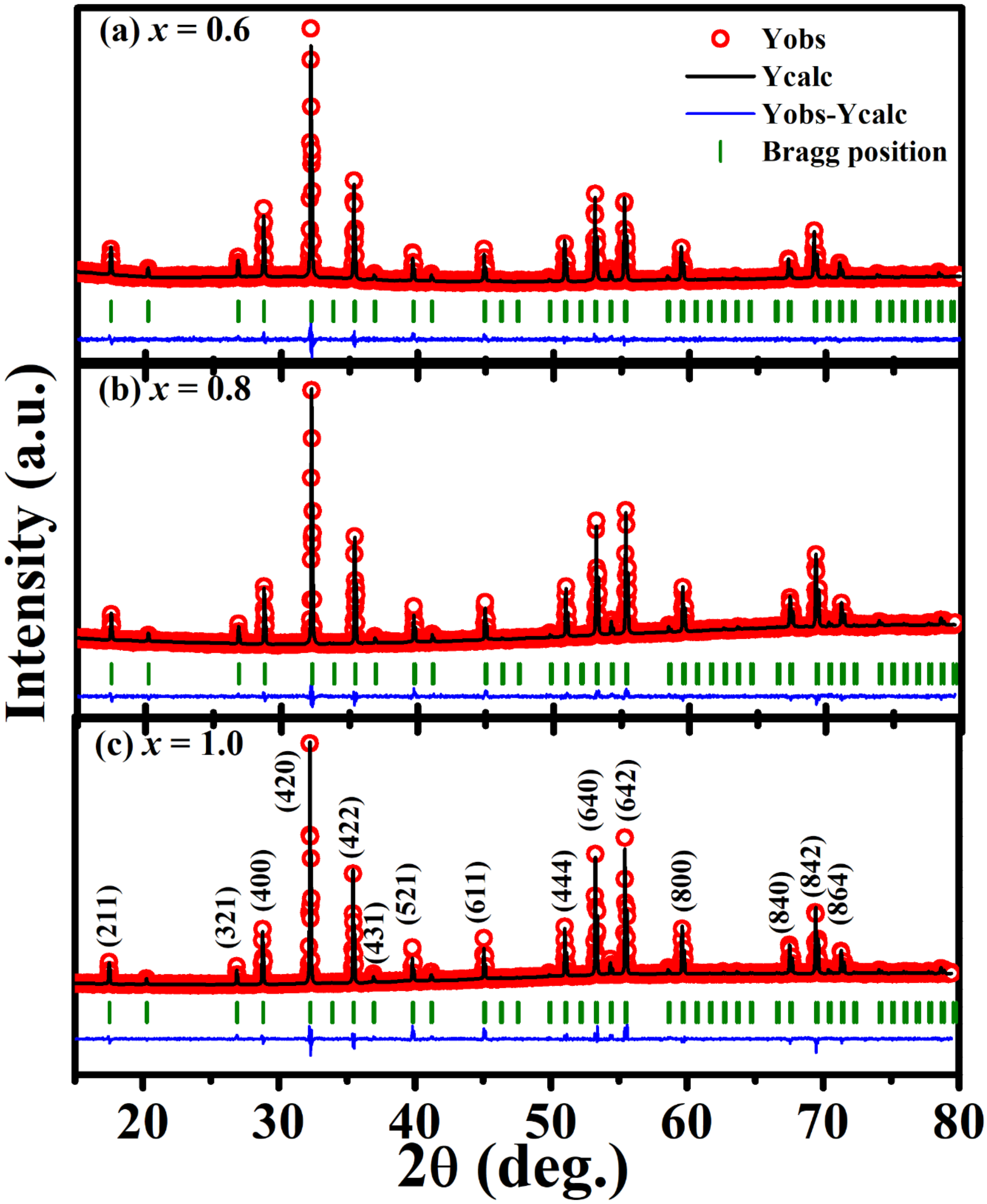

Fig. 4.3: The room temperature XRD data are Rietveld refined for $x = 0.6, 0.8$ and 1.0 sample.

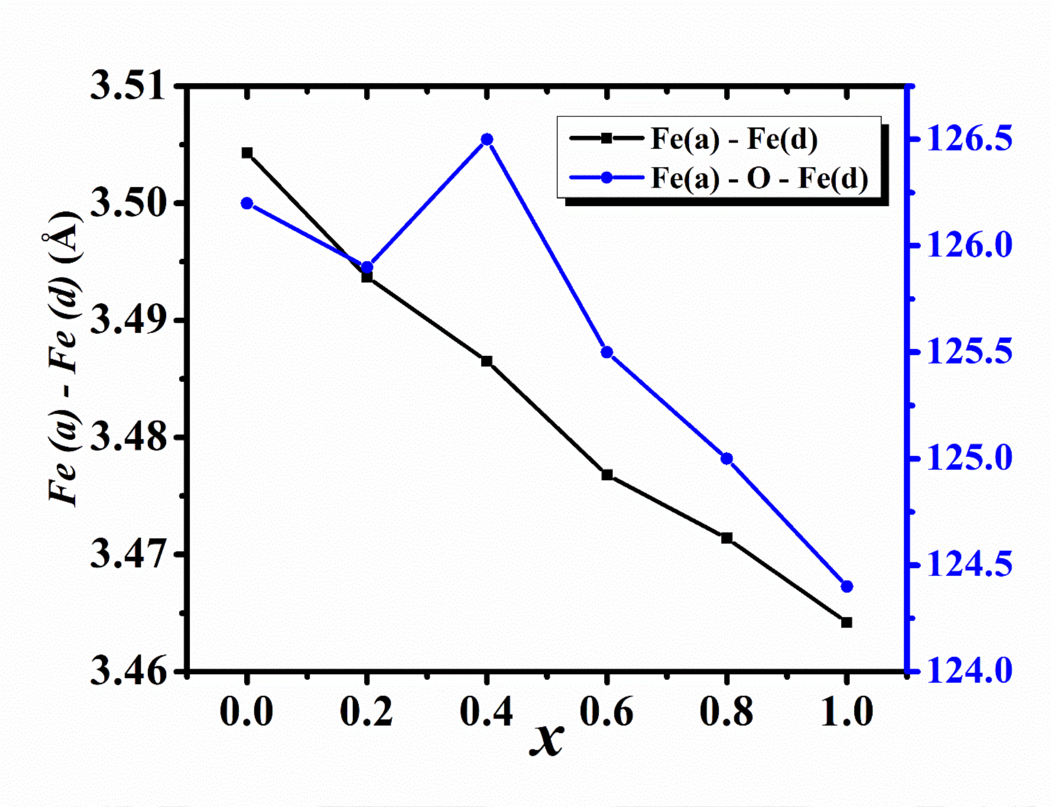

Fig. 4.4: The change in bond length and bond angle among $Fe\ (a)$ and $Fe(d)$ site for all the compositions of Ho-SmIG series.

Table 4.1: Structural and Rietveld refinement reliability parameters of $(Sm_{1-x}Ho_x)_3Fe_5O_{12}$ with $x = 0.0 - 1.0$ samples.

Sample → Parameters ↓	$x = 0.0$	$x = 0.2$	$x = 0.4$	$x = 0.6$	$x = 0.8$	$x = 1.0$
Space group	$Ia\bar{3}d$	$Ia\bar{3}d$	$Ia\bar{3}d$	$Ia\bar{3}d$	$Ia\bar{3}d$	$Ia\bar{3}d$
$a = b = c$ (Å)	12.5375 (1)	12.4996 (1)	12.4723 (1)	12.4390 (1)	12.4184 (1)	12.3936 (1)
Volume (Å^3)	1970.7	1952.9	1940.1	1924.6	1915.1	1903.6
R_p (%)	15.4	14.3	12.1	16.8	12.1	11.0
R_{wp} (%)	17.2	17.8	16.5	16.6	14.8	17.9
R_F (%)	6.9	6.3	6.1	5.5	7.1	8.7
R_{Bragg} (%)	6.9	6.0	5.4	5.1	5.9	8.7
χ^2	1.9	2.0	1.6	1.5	1.8	3.7
Occupancy						
Sm	2.97	2.37	1.77	1.18	0.59	0.0
Ho	0.0	0.56	1.19	1.78	2.36	2.98
Fe	4.95	4.98	4.96	4.92	4.98	4.99

Now, the FESEM micrographs are recorded to analyze the morphology of the samples and are shown in Fig. 4.5 (a-d). Densification of the samples is confirmed by these images as they show almost negligible pores on the surface. For dielectric measurements, we need highly dense pellets to reduce loss. The Archimedes principle was used to calculate the density of the synthesized pellets, and it was observed that the density was lying between 90% to 95% of the theoretical density. The histogram of particle size distribution (as shown in Fig. 4.5 (e-h)) is fitted to log-normal function and analyzed in order to determine the average grain size. We have obtained an increment in average grain size from $7.47\mu m$ to $8.56\mu m$ for $x = 0.0$ to 1.0 samples. As the ionic radii of Sm and Ho are somewhat comparable due to which the grain growth is not affected in our samples. Although, this increment in grain size is attributed to the enhancement in the mobility of the grain boundary which is introduced by smaller Ho^{3+} ion substitution at Sm^{3+} site [128].

Further, the elemental composition of all the cations are examined by EDS spectra as shown in Fig. 4.6 for $x = 0.0$ and 0.6 samples. The cationic ratio is obtained as Sm: Ho: Fe = $2.96: 0: 4.98$ for $x = 0.0$ and $1.18: 1.78: 4.97$ for $x = 0.6$ sample. These compositions are in good compatibility with the nominal starting compositions. Since we are using a gold coating to make the surface conductive for EDS analysis and mounting our sample on carbon tape, we observe peaks for gold and carbon which can be disregarded.

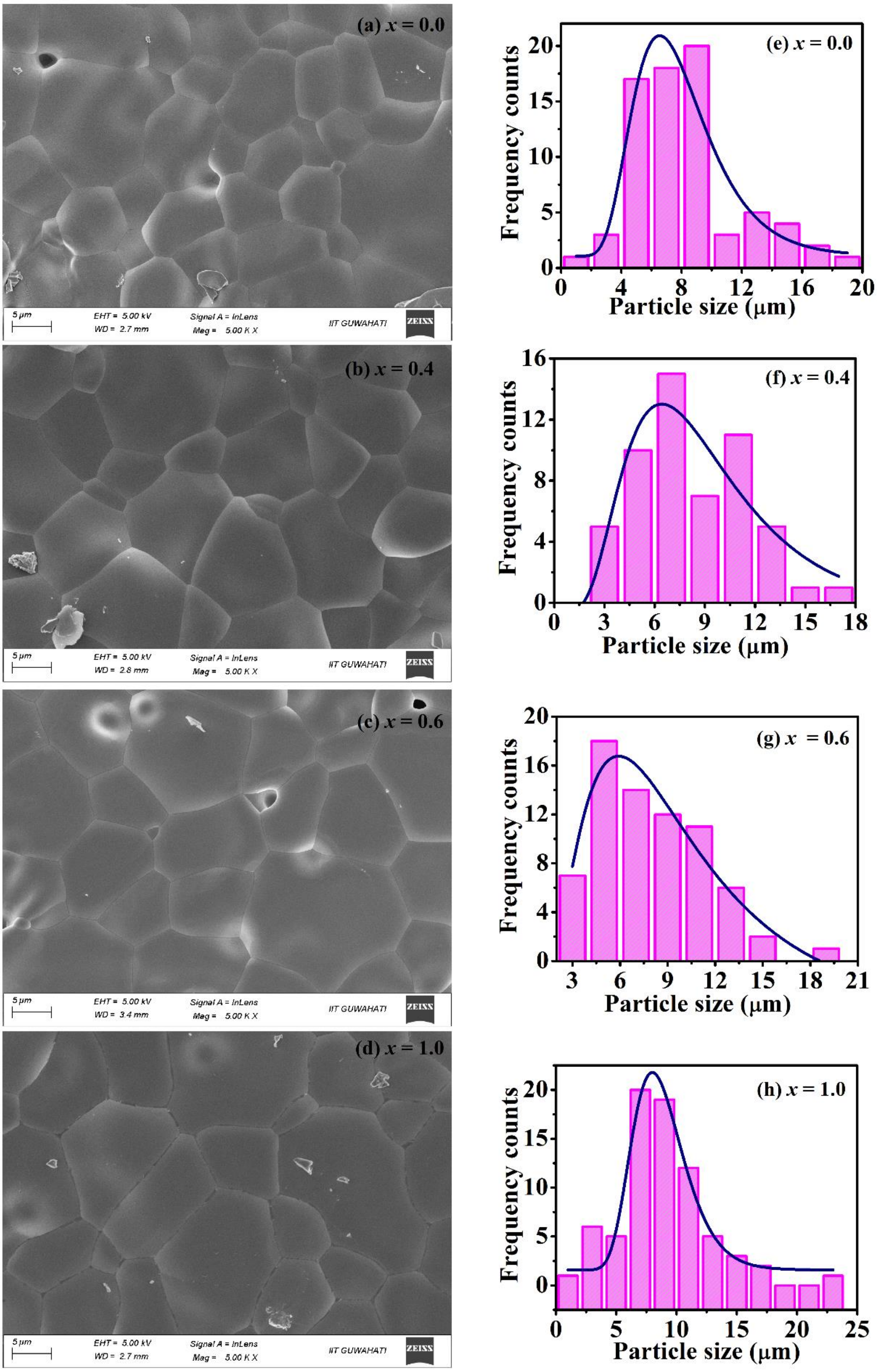

Fig. 4.5: (a-d) FESEM micrographs showing grains separated by grain boundaries and (e-h) Particle size distribution for $x = 0.0, 0.4, 0.6$ and 1.0 samples of Ho-SmIG series.

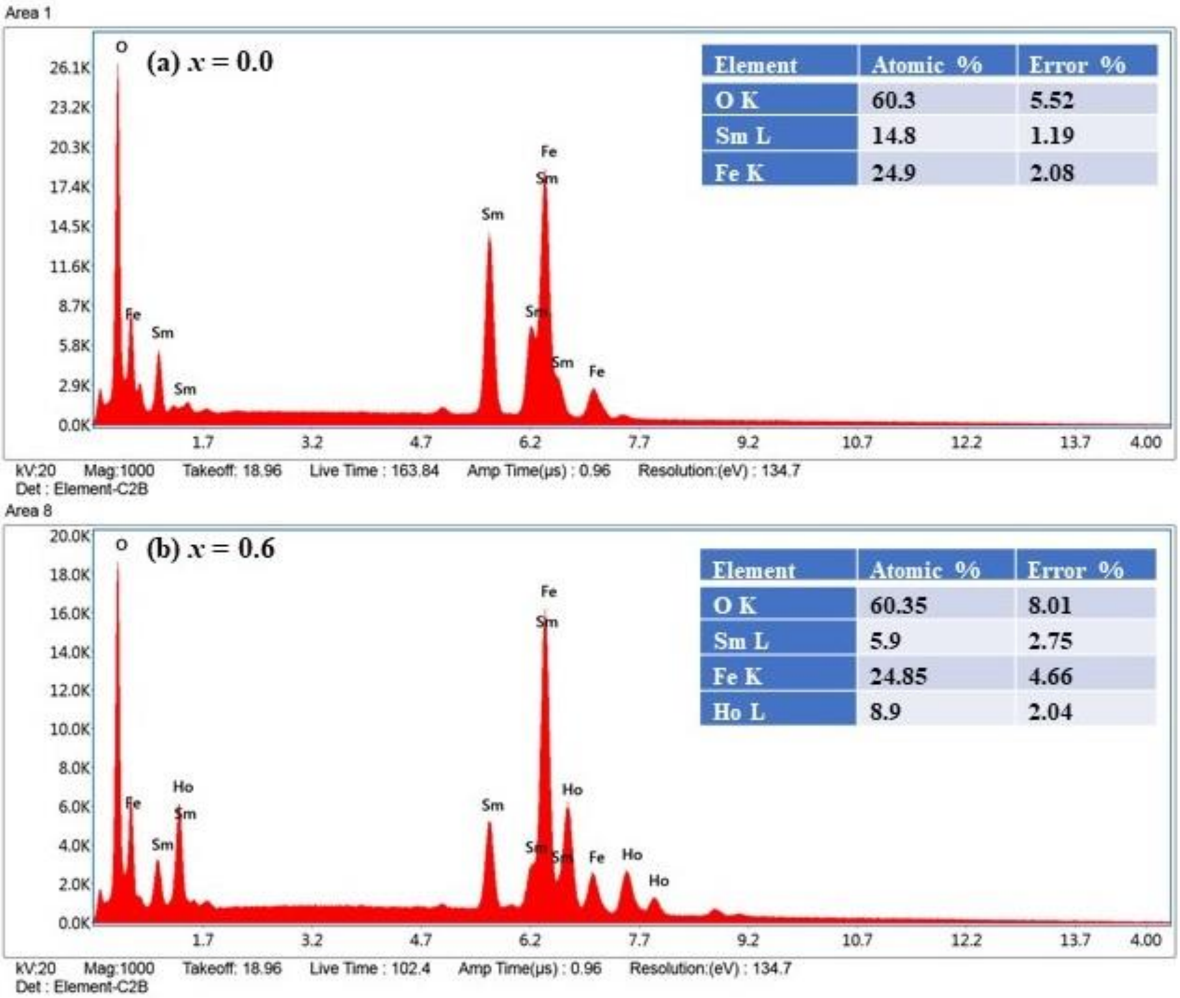

Element	Atomic %	Error %
O K	60.3	5.52
Sm L	14.8	1.19
Fe K	24.9	2.08

Element	Atomic %	Error %
O K	60.35	8.01
Sm L	5.9	2.75
Fe K	24.85	4.66
Ho L	8.9	2.04

Fig. 4.6: EDS spectrum for (a) $x = 0.0$ and (b) $x = 0.6$ samples of Ho-SmIG series.

To further verify the phase purity, we have carried out room temperature Raman spectra for Ho-SmIG samples (as shown in Fig. 4.7) in the range of $100 - 800\ cm^{-1}$. The used Raman laser is having a wavelength of $633nm$. Group theory says that there are total 25 active Raman modes i.e., $(3A_{1g} + 8E_g + 14F_{2g})$ which correspond to internal modes, translational modes and rotational modes, respectively [96]. The major Raman shift corresponding to Raman-active phonons for Ho-SmIG series are F_{2g}, E_g and $A_{1g} + E_g$. The peaks below 300 cm^{-1} are arising because of translational motion of either of the rare earth elements i.e., Sm^{3+} or Ho^{3+} cations. These peaks are shifting towards lower wavenumber as heavier Ho^{3+} ions substitute the Sm^{3+} ions site. While the peaks from $300 - 800\ cm^{-1}$ are originated from stretching and bending of FeO_4 tetrahedra and they are shifting towards higher wavenumber side [97]. The broadening of the band around 150 cm^{-1} with Ho substitution up to $x = 0.8$ could be due to the introduction of disorder in the crystal lattice. Substitution of Ho ions for the host ions can result in lattice distortions and changes the local symmetry which can broaden the phonon bands. This peak is getting sharper for $x = 1.0$ sample may be due to the less disordered crystal structure of the sample i.e., due to other end of the series where rare earth site is completely filled by Ho.

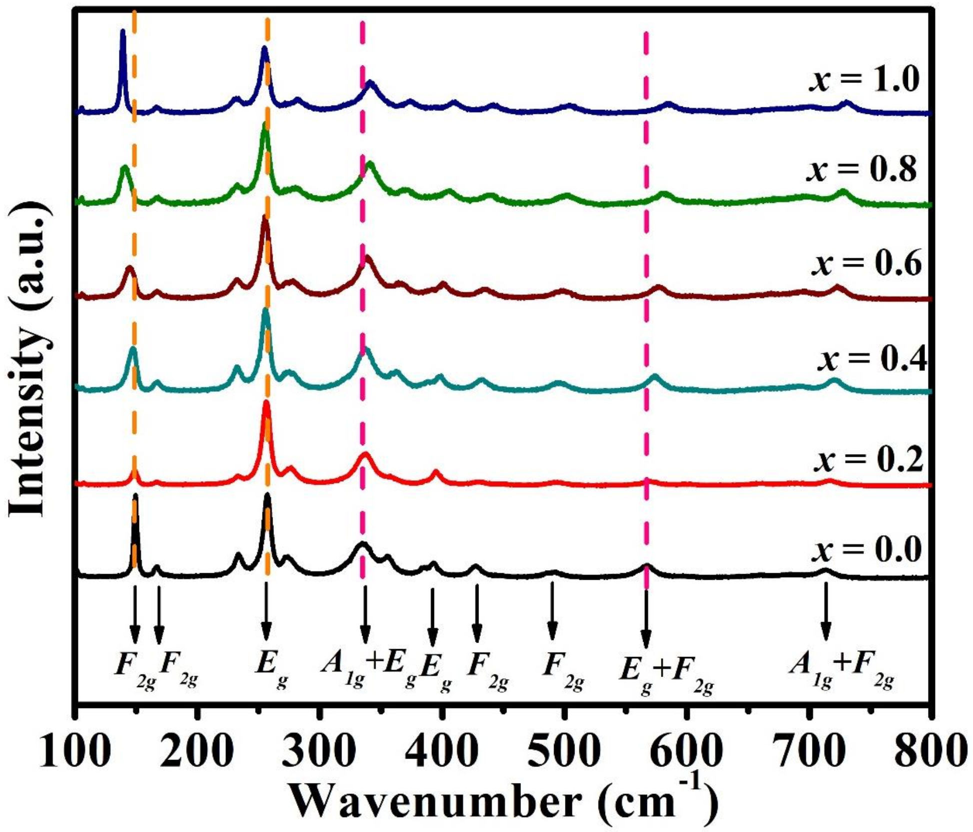

Fig. 4.7: Room temperature Raman spectra recorded for Ho-SmIG ($x = 0.0$ to $x = 1.0$) samples.

We have recorded XPS spectra to analyze the electronic states of all the individual elements in Ho-SmIG samples as shown in Fig. 4.8 for $x = 0.0$ and 0.4 samples. We can clearly see that $Sm3d$ is splitted into two energy levels i.e., $3d_{5/2}$ and $3d_{3/2}$ corresponding to binding energy 1082 eV and 1110 eV. This result is in good agreement with the XPS of SmIG reported by Rohith *et al* [129]. In addition to this, the energy doublet of Ho-doped sample is observed at 160 eV and 163 eV for $4d_{5/2}$ and $4d_{3/2}$ states, respectively (shown in Fig. 4.8 (g)) which confirms the presence of Ho in the $x = 0.4$ sample. We have also observed satellite peaks at around 169 eV and 176 eV in the $Ho4d$ spectrum signifying the shake ups in the spectra. Moreover, we have come to know about the oxidation states of Fe atom which are Fe^{2+} and Fe^{3+}. These two states of Fe collectively forms the energy doublet at 710 eV and 724 eV corresponding to $2p_{3/2}$ and $2p_{1/2}$ states. In most of the XPS studies, the behavior of $O1s$ spectra are somewhat different to rest of the cations. Generally, if $O1s$ spectra are formed because of more than two energy states, then this spectrum is attributed to the covalent or ionic bonding between oxygen and cation. Here we have observed two peaks for $O1s$ at $529\ eV$ and $531\ eV$ for both samples. The peak at $529\ eV$ is arising due to the ionic bonding between rare earth and oxygen ion. Whereas, the peak at $531\ eV$ is attributed to the covalent bonding among $Fe\ (a) - O - Fe(d)$ which confirms the formation of garnet structure [67].

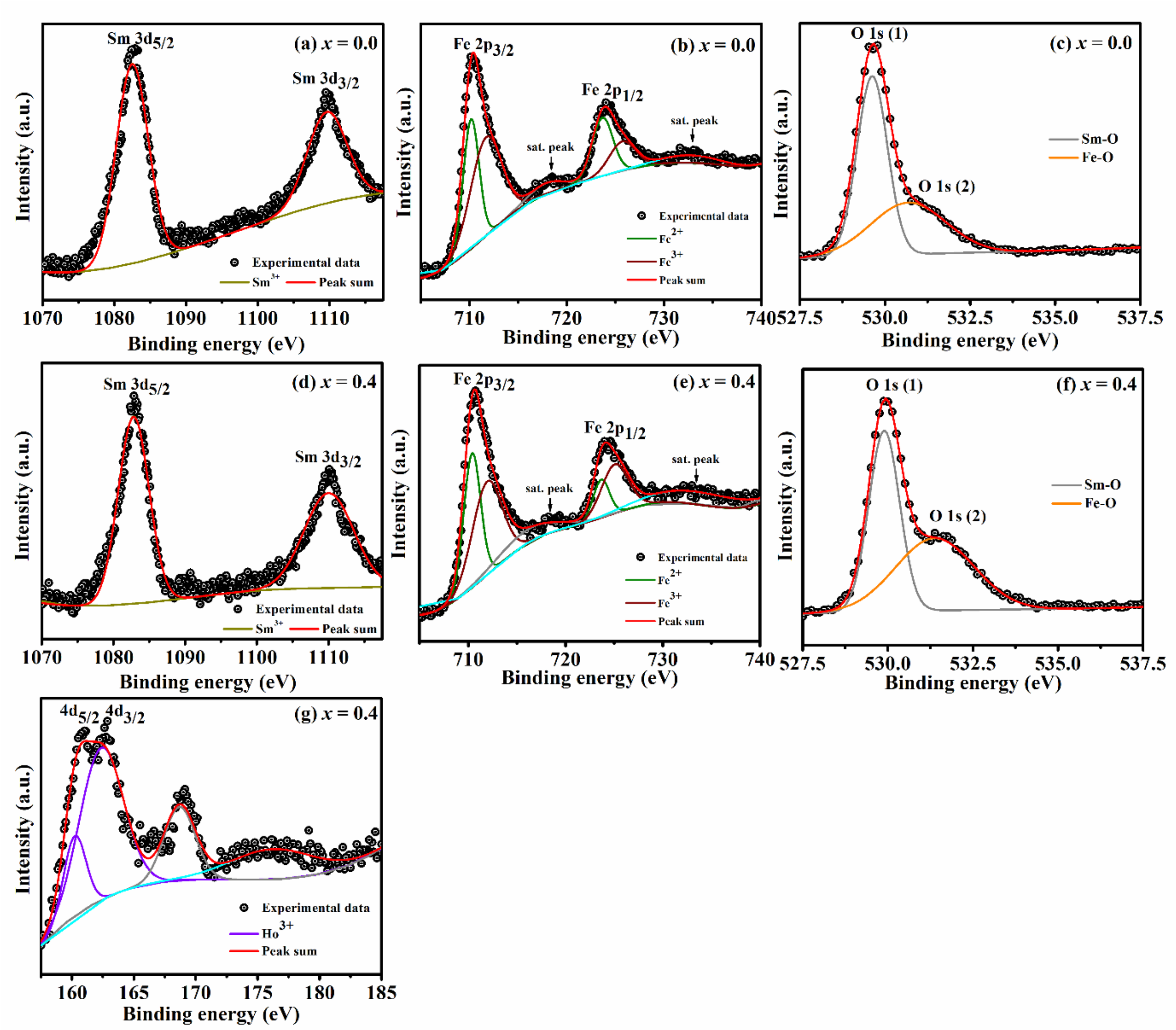

Fig. 4.8: Room temperature XPS spectrum for (a-c) $x = 0.0$ and (d-g) $x = 0.4$ sample for Sm3d, Fe2p, O1s and Ho4d levels.

4.1.2 Magnetic characterization

The temperature dependant zero field cooled (ZFC) magnetization curves are recorded by applying an external magnetic field of $500\ Oe$ as shown in Fig. 4.9 (a). These samples show similar trend and all of them undergoes a ferrimagnetic transition. The transition temperature (T_c) is estimated from the derivative of magnetization i.e., dM/dT vs. T plots and it is decreasing from $561\ K$ for $x = 0.0$ to $541\ K$ for $x = 1.0$ samples. These derivative plot of magnetization are shown in Fig. 4.9 (b). The T_c value for the parent sample is comparable to the literature [57]. This decrement in T_c can be arising because of the lattice distortion caused by the Ho substitution as a result of reduced super-exchange interaction among $Fe\ (a) - O -\ Fe\ (d)$ networks. This reduction is also consistent with the reduction in bond angle with Ho doping as shown in XRD data analysis (discussed in Section 4.1.1). Although the bond angles in the $x = 0.0$ and 0.4 samples are similar, there is still a noticeable decrease in T_c. We have just observed the drop in T_c from $561\ K$ to $552\ K$ from $x = 0.0$ to 0.4 sample. This decrement is not significant enough that it affects the bond angle much.

The temperature-dependence on magnetization by sweeping the temperature from $5K$ to $300K$ for $x = 0.0$ to $x = 1.0$ samples are shown in Fig. 4.10 (a-f) with black curve representing the ZFC condition and red curve for the field cooled (FC) case. In ZFC plots, all the samples exhibit spin reorientation transition (SRT) at low temperatures. The exchange coupling between the rare earth element and Fe^{3+} ion moments is responsible for this SRT [57]. Exchange coupling between transition metals is typically the strongest, followed by coupling between a transition metal and rare earth ion, while coupling among rare earth ions is usually quite weak [130]. The exchange interaction between rare earth and transition metal ions affects the effective magneto-crystalline anisotropy at low temperatures. For the parent sample, T_{SR} is found to be around $65K$ and it is decreasing with Ho doping. We have observed one more magnetic transition at $25K$ in the case of $x = 0.0$ and $x = 0.2$ samples in both ZFC as well as FC plots. Below the above transition temperature, the ZFC magnetization falls quite sharply. Similar type of transition is also observed for Ce doped $LaCrO_3$ samples [131]. This transition disappears after $x = 0.2$ concentration as it is shifting towards lower temperature and becomes out of measured temperature range for $x \geq 0.4$ samples.

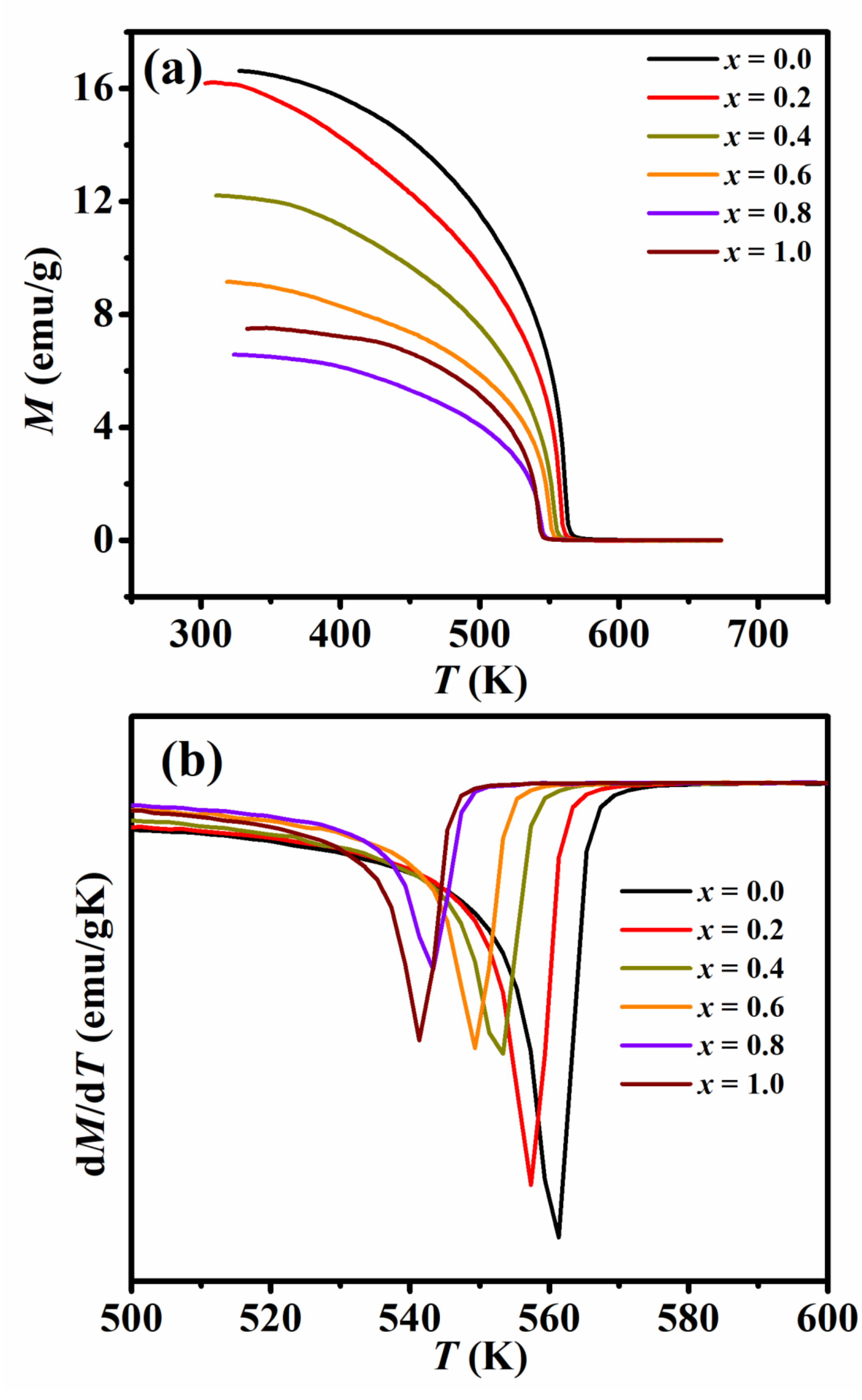

Fig. 4.9: (a) The variation in magnetization with temperature by providing an external field of 500 Oe and (b) corresponding dM/dT vs. T plots for all the samples of Ho-SmIG series.

Moreover, we have observed a novel magnetization reversal in FC condition in $x = 0.4$ sample for the first time in this series. The moment of the rare earth element in RIGs decreases significantly with the increment in temperature, while the moment of Fe at the octahedral and tetrahedral sites remains almost constant. At the ferrimagnetic transition temperature T_c, the moment of Fe becomes zero. Negative magnetization is an inherent property of some of the magnetic materials having multiple magnetic sublattices and considerable magnetocrystalline anisotropy. The magnetocrystalline anisotropy is prominent in bulk polycrystalline samples [132]. Therefore, the negative magnetization in $x = 0.4$ sample can be attributed to significant magnetocrystalline anisotropy caused by Ho ions. The magnetocrystalline anisotropy of Ho ions at low temperatures has been demonstrated by Pearson *et al* [133]. Similar type of magnetization reversal is also observed by many other researchers in different types of materials such as garnets, orthoferrites, spinels etc. [113,164,165]. The net moment in rare earth iron garnets is given by the empirical formula i.e., $M_{net} = 3M_{Fe}(d) - [2M_{Fe}(a) + (3-x)M_{Sm}(c) + xM_{Ho}(c)]$. Here, we can see that the resultant magnetic moment is mainly governed by the moment of Sm^{3+}/Ho^{3+} and Fe^{3+} ions at tetrahedral and octahedral sublattice. No negative magnetization can be seen for $x = 1.0$ sample, because the smaller magnetic moment of Fe^{3+} ions at octahedral site together with $Sm^{3+}/\,Ho^{3+}$ ions at dodecahedral site cannot suppress or overcome the moment due to Fe^{3+} ions at tetrahedral site. Ho substitution in SmIG reduces anisotropy (shown in Table 4.2), leading to a decrease in negative magnetization. The $x = 0.4$ sample exhibits a clear magnetization reversal, which decreases in $x = 0.6$ and $x = 0.8$ samples, eventually becoming entirely positive in the $x = 1.0$ sample. The compensation effect occurred twice for $x = 0.6$ and 0.8 samples and they are named as T_{comp1} and T_{comp2} as can be seen in the inset of Fig. 4.10 (e). Negative magnetization is very rare but two compensations are observed in a very few systems only. Canglong *et al.* [134] has also mentioned this kind of compensation in Mn substituted $NiCr_2O_4$ spinel chromite and Qiu *et al.* [135] has observed such effect in Fe substituted $CoCr_2O_4$ cobalt chromite spinel. The quantitative estimation of negative magnetization can be calculated as $(\frac{M_{min}}{M_{max}})$ and it is found to be 0.3 for $x = 0.4$ sample. This ratio lies in the range of 0.1 to 5 for some intermetallic alloys and spinels [30]. The relative magnetization irreversibility is calculated by using $\frac{\Delta M}{M_{ZFC}} = \frac{M_{FC}-M_{ZFC}}{M_{ZFC}}$ relation and it comes out to be -4 at $5K$ as displayed in the inset of Fig. 4.10 (c).

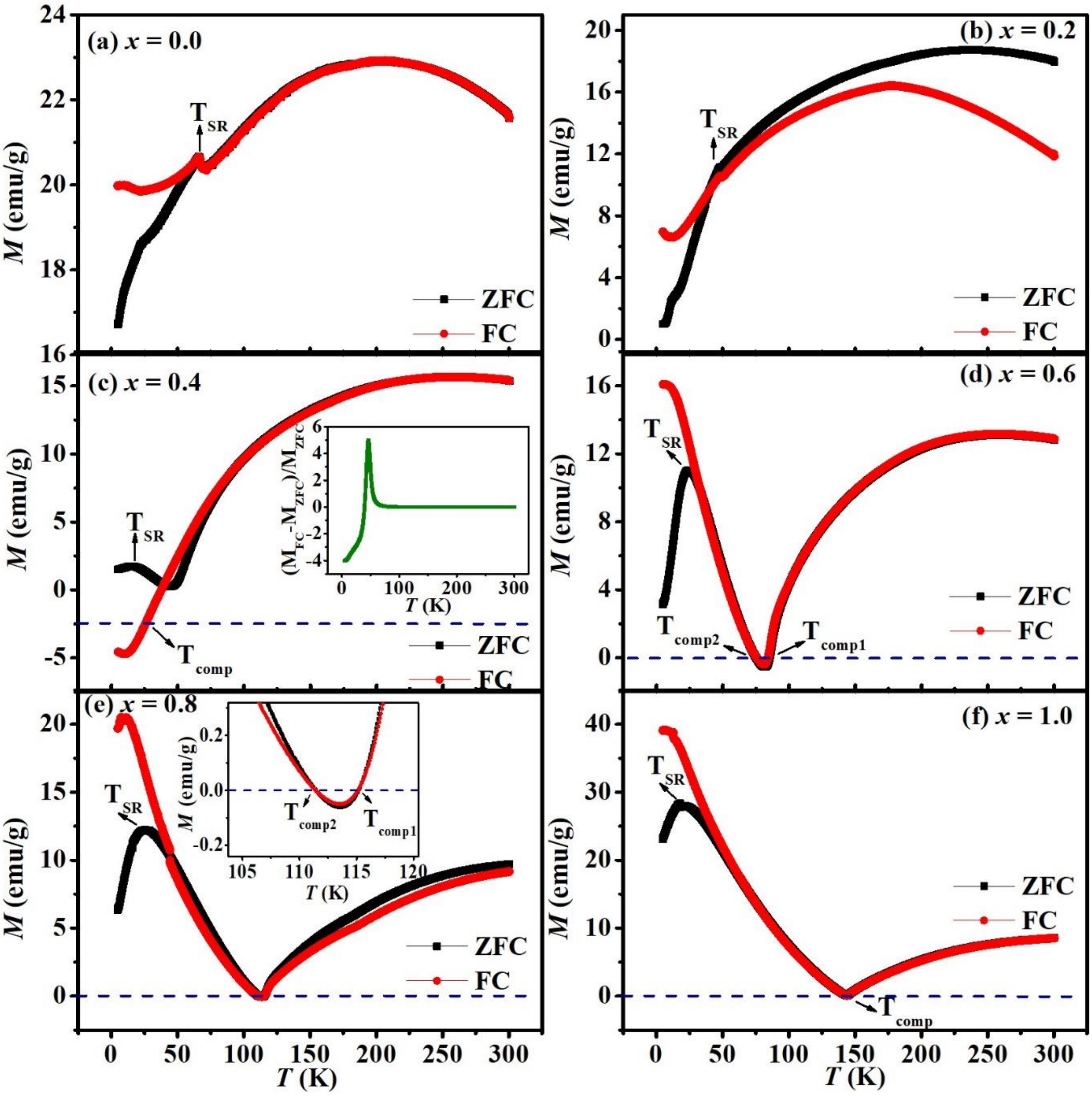

Fig. 4.10: (a-f) ZFC and FC $M-T$ plots for $(Sm_{1-x}Ho_x)_3Fe_5O_{12}$ $(x = 0.0 - 1.0)$ samples. The insets of (c) shows variation of irreversible magnetization with temperature for $x = 0.4$ sample and the inset of (e) represents the zoom out image of $x = 0.8$ sample around T_{comp}.

Now, we have carried out the $M-T$ plots at $+500\,Oe$ and $-500\,Oe$ from $5\,K$ to $300K$ to make sure that the negative magnetization in the $x = 0.4$ sample is not arising as a result of any artefact or stray field during the experiment. The $M-T$ plots at $\pm 500\,Oe$ are shown in Fig. 4.11 (a). We have observed magnetization reversal in both the cases and they are found to be mirror reflection of each other, which confirms that the negative magnetization is the inherent property of this sample. We have also performed FC $M-T$ measurements at different H_{FC} (demonstrated in Fig. 4.11 (b)) and found that the magnetic compensation is observed below 1000 Oe field only. No magnetization reversal is observed for $H_{FC} \geq 1000\ Oe$. So, from here, one can conclude that when $H_{FC} \geq 1000\ Oe$, the system gets free from anisotropy energy and the magnetic sublattice spins are flipped.

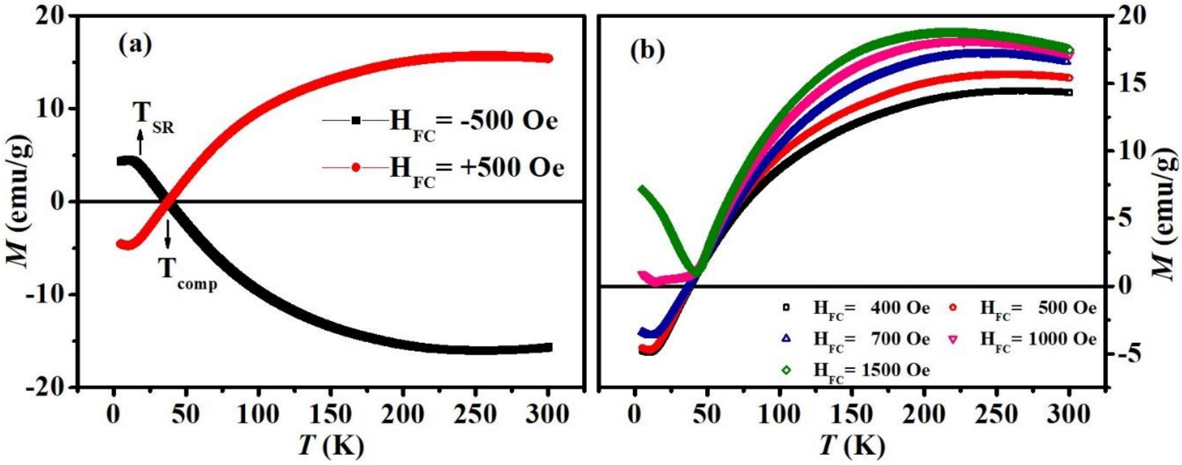

Fig. 4.11: $FC\ M-T$ plots at (a) $H_{FC} = \pm 500\ Oe$ and (b) by varying H_{FC} values from 400 to 1500 Oe for $x = 0.4$ sample.

The room temperature magnetic hysteresis loops $(M-H)$ for $(Sm_{1-x}Ho_x)_3Fe_5O_{12}$ $(x = 0.0, 0.2, 0.4, 0.6, 0.8, 1.0)$ samples are shown in Fig. 4.12 (a). They all are getting saturated after an applied field of about 2 kOe. The effective anisotropy constant (K_1) and saturation magnetization (M_s) are obtained by fitting these curves to Law of Approach to Saturation (LAS) relation (eqn. (3.2)) and are listed in Table 4.2. Saturation magnetization at RT is decreasing upon Ho substitution, i.e. from 19.83 emu/g $(x = 0.0)$ to 6.98 emu/g $(x = 1.0)$. The reason behind this decrement can be explained by the empirical formula for the net magnetic moment in rare earth iron garnets i.e., $M_{net} = 3M_{Fe}(d) - [2M_{Fe}(a) + (3-x)M_{Sm}(c) + xM_{Ho}(c)]$. As we replace Sm^{3+} $(0.71\ \mu B)$ with Ho^{3+} $(10.6\ \mu B)$, whose magnetic moment is larger, the net magnetization decreases. At room temperature, there is no significant change in effective anisotropy constant K_1 by Holmium substitution and it remains in the order of $10^4\ erg/cc$ for all the samples. Such an order of anisotropy constant is also observed for hexaferrites by Fu *et al.* [136]. The inset of Fig. 4.12 (a) displays the hysteresis curve for $x = 0.4$ sample at 5 K. Although rare earth iron garnets typically display soft ferrimagnetic behavior, they are known to exhibit low coercivity. In this study, however, we have found that the values of H_c for all samples are nearly identical, indicating only a minor change. Therefore, the observed difference in H_c values is too small to be significant.

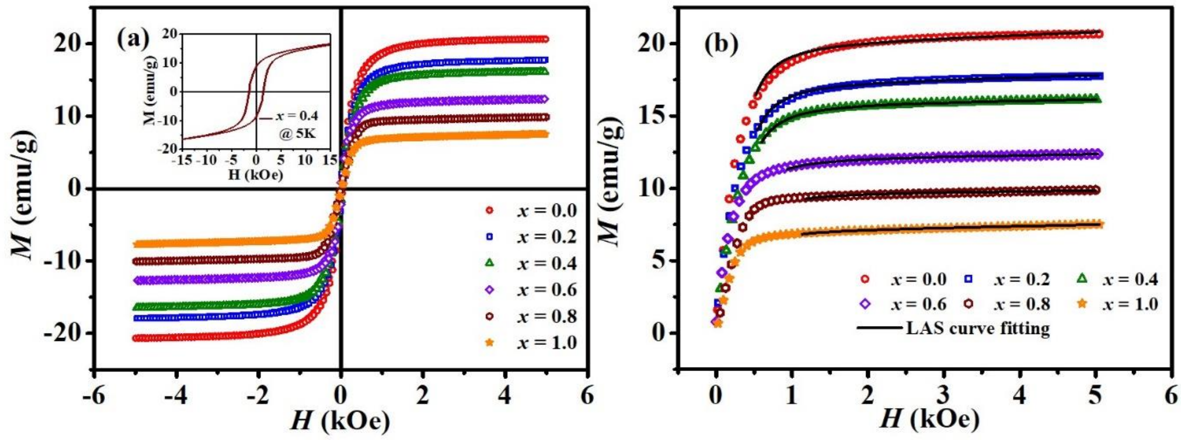

Fig. 4.12: (a) Hysteresis $(M - H)$ curves at room temperature for $(Sm_{1-x}Ho_x)_3Fe_5O_{12}$ $(x = 0.0 - 1.0)$ samples and inset shows the hysteresis loop for $x = 0.4$ sample at $5K$ and (b) fitting of initial $M - H$ plots to LAS equation.

Table 4.2: List of fitting parameters obtained from LAS equation.

x	*Ms* (emu/g)	*Hc* (Oe)	*K$_1$* (10^4) (erg/cc)
0.0	19.83	25.8	9.383
0.2	17.17	32.8	9.288
0.4	15.74	32.1	8.912
0.6	12.02	28.6	6.761
0.8	9.61	23.8	5.542
1.0	6.98	23.5	3.682

Indian Institute of Technology Guwahati

4.1.3 Complex impedance characterization

The real component of impedance (Z') with frequency variation at various temperatures ranging from $523\ K$ to $623\ K$ are displayed in Fig. 4.13 for $x = 0.0, 0.2, 0.6$ and 1.0 samples. These samples show plateau like behavior in Z' plots up to $10^4\ Hz$ frequency and then sharp fall can be seen in between 10^4 and $10^5\ Hz$ frequency. In the low frequency region, space charge polarization is responsible for this plateau-like characteristic. After $10^4\ Hz$ frequency, merger of all Z' indicates the release of space charge polarization. Moreover, Z' is decreasing with increase in Ho concentration for a specific temperature and frequency. The enhancement in grain size or reduction in grain boundary density offers less resistance for Ho doped samples that results in drop in Z' values. This decrease in resistivity also signifies an improvement in electrical conductivity values. Moreover, Z' is decreasing with the increase in temperature for a specific sample which indicates the negative temperature coefficient of resistance [50].

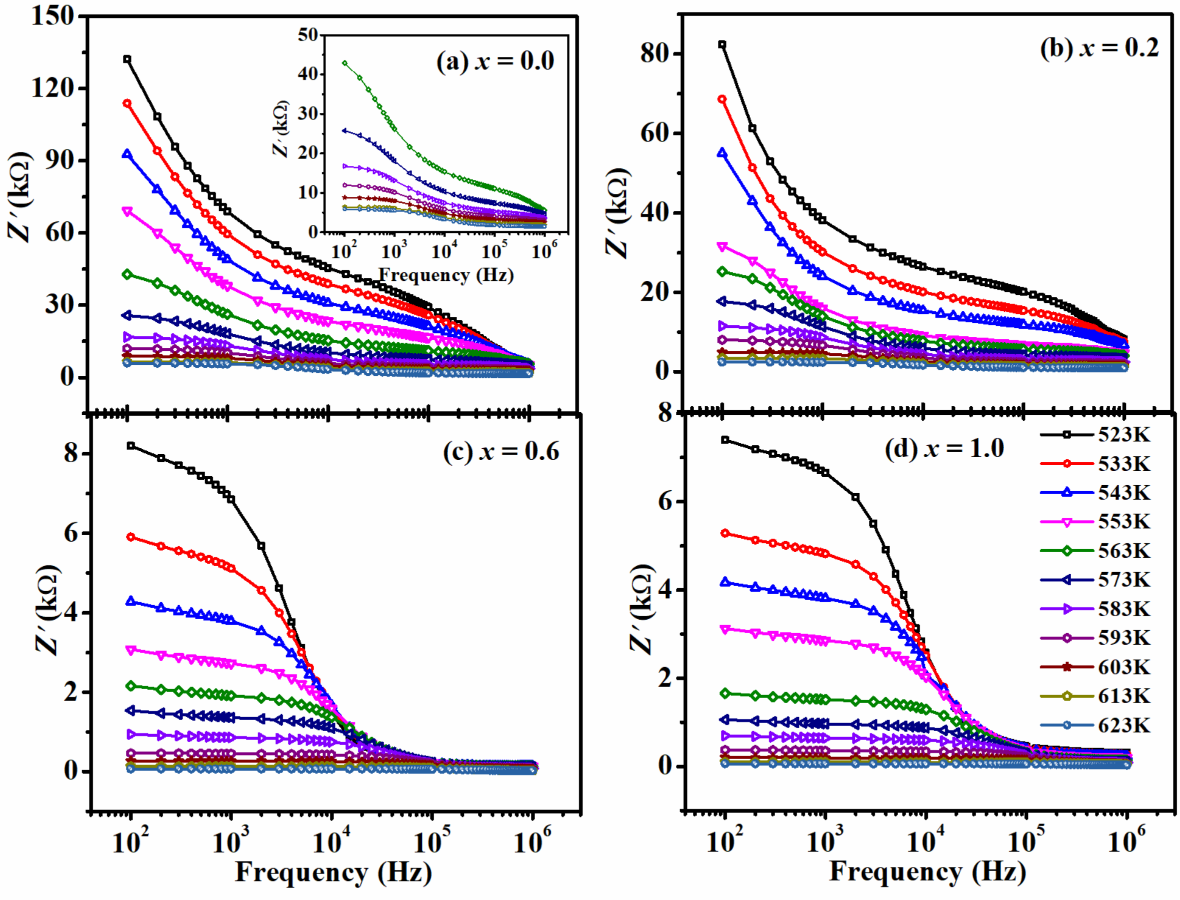

Fig. 4.13: Frequency dependent real part of impedance i.e., Z' with varying temperature from $523\ K - 623\ K$ for $x = 0.0, 0.2, 0.6$ and 1.0 samples of Ho-SmIG series. The inset of (a) shows the enlarged view of Z' at $563 - 623\ K$ temperature range in $x = 0.0$ sample.

Institute of Technology

In order to understand the relaxation dynamics in Ho-SmIG samples, we have gone through the variation of Z'' with respect to frequency at different temperatures varying from $523\ K$ to $623\ K$ and are shown in Fig. 4.14. The Z'' vs frequency plots are shown for $x = 0.0, 0.2, 0.6$ and 1.0 samples. All the plots show a characteristic peak which depicts the charge carrier's relaxation. The relaxation peaks are observed in lower frequency zone around $< 10^3\ Hz$ for lower doped samples. These relaxation peaks in the lower frequency range can be attributed to contributions from the grain boundaries [137]. However, for $x = 0.0$ and 0.2 concentrations, two peaks have been observed in low and high frequency regions and they are attributed to relaxation of charge carriers across grain boundaries and grains, respectively. Although the grain size increases with higher Ho concentration, the relaxation peak arising from grain boundary effect, shifts to higher frequencies indicating a reduction in relaxation time. This decrease in relaxation time in Ho-substituted samples can be attributed to the effective reduction in the bond length distance between Fe ions located at the ‘a’ and ‘d’ sites which enhance electron hopping between ‘a’ and ‘d’ sites. Also, the decrement in Z'' value with Ho doping is in parallel agreement with the Z' results. Moreover, the peaks are migrating towards higher frequency and they are broadening as the temperature rises which may result from thermally activated charge carriers [138].

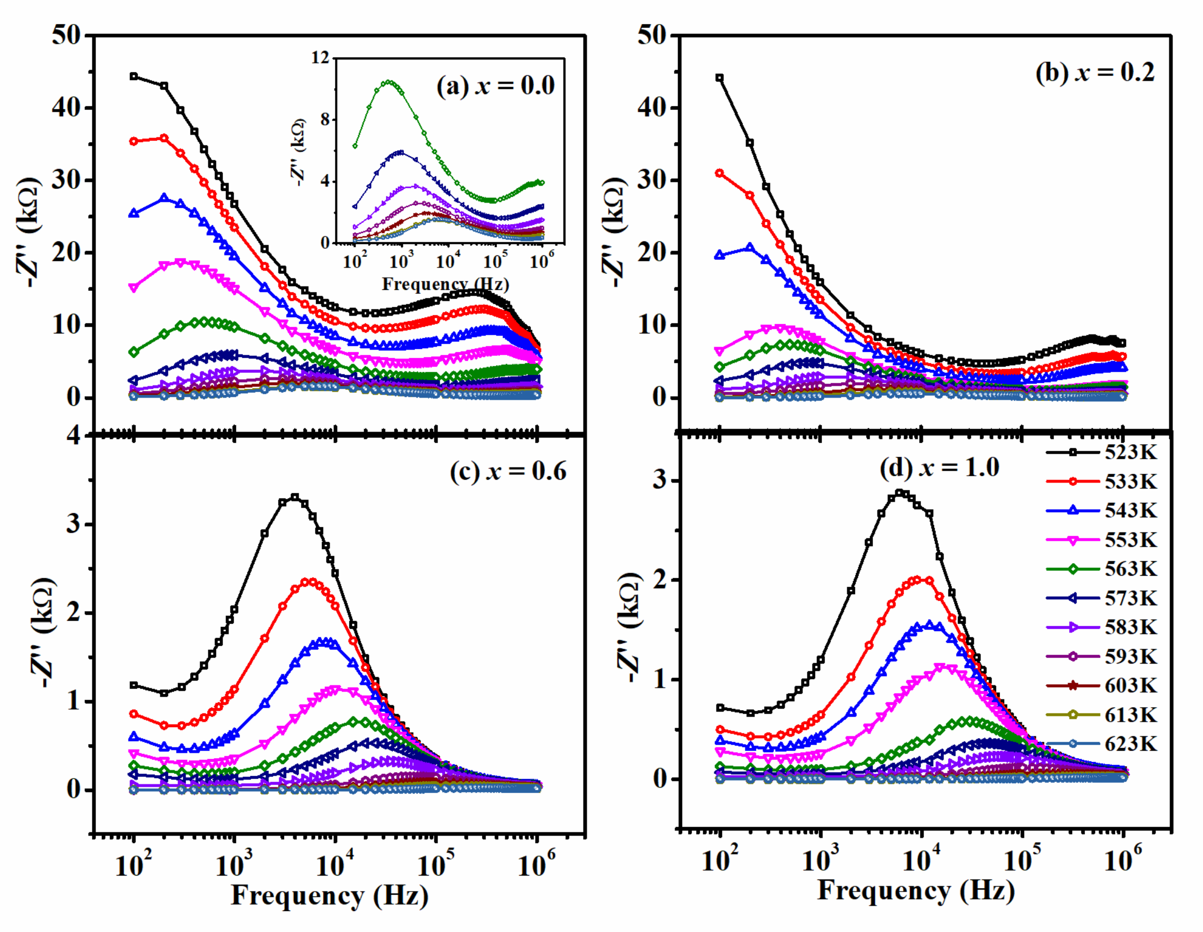

Fig. 4.14: Frequency dependent imaginary part of impedance i.e., Z'' with varying temperature from $523\ K - 623\ K$ for $x = 0.0, 0.2, 0.6$ and 1.0 samples of Ho-SmIG series. The inset of (a) shows the enlarged view of Z'' at $563 - 623\ K$ temperature range in $x = 0.0$ sample.

The Nyquist plots are plotted to understand the contribution of Gs and GBs in Ho-SmIG samples and are shown in Fig. 4.15 (a-c) for $x = 0.0, 0.6$ and 1.0 sample. Generally, we expect two semicircles in Nyquist plot with their center lying on Z' axis as discussed in section 1.9.1. Grain contributions account for one semicircle, whereas GBs account for another. Here, in Ho-SmIG series, we have observed two semicircles for $x = 0.0$ sample but only one semicircle for Ho-doped samples. The inset of Fig. 4.15 (a) indicates the contribution of Gs and GBs more evident. The short semi-circular arc in the high frequency (low Z') area is attributable to the contribution of Gs while the stretched semi-circular arc is attributed to the contribution of GBs. As the temperature rises, the contribution of the Gs diminishes and the Nyquist plots mostly show the contribution of the GBs. However, for Ho-doped samples, the main contribution is due to Gs only because of reduction in GBs as can be seen from FESEM images. Only a slight contribution of GBs is observed at lower frequency side (i.e., higher Z' axis side). On increasing temperature, the arcs are shifting towards lower Z' value suggesting the negative temperature coefficient [139]. Also, it represents the increment in conductivity with temperature. These Nyquist curves are fitted to the equivalent circuit (as shown in Fig. 4.15 (d)) using Zsimpwin software. $R_g, R_{gb}, R_{el}, C_{gb}$ represent the resistance due to Gs, GBs, electrode and grain boundary capacitance, respectively. The fact that the semicircles' centres do not lie on the Z' axis proves that system is deviating from the ideal Debye-type behavior. To describe such system, addition parameter known as constant phase element Q is used in the equivalent circuit with an impedance given by $Z_{CPE} = \frac{1}{A}(j\omega)^{-n}$. Here, A is a constant and n represents the distribution of relaxation times, ranging from $0 \leq n \leq 1$.

Indian Institute of Technology Guwahati

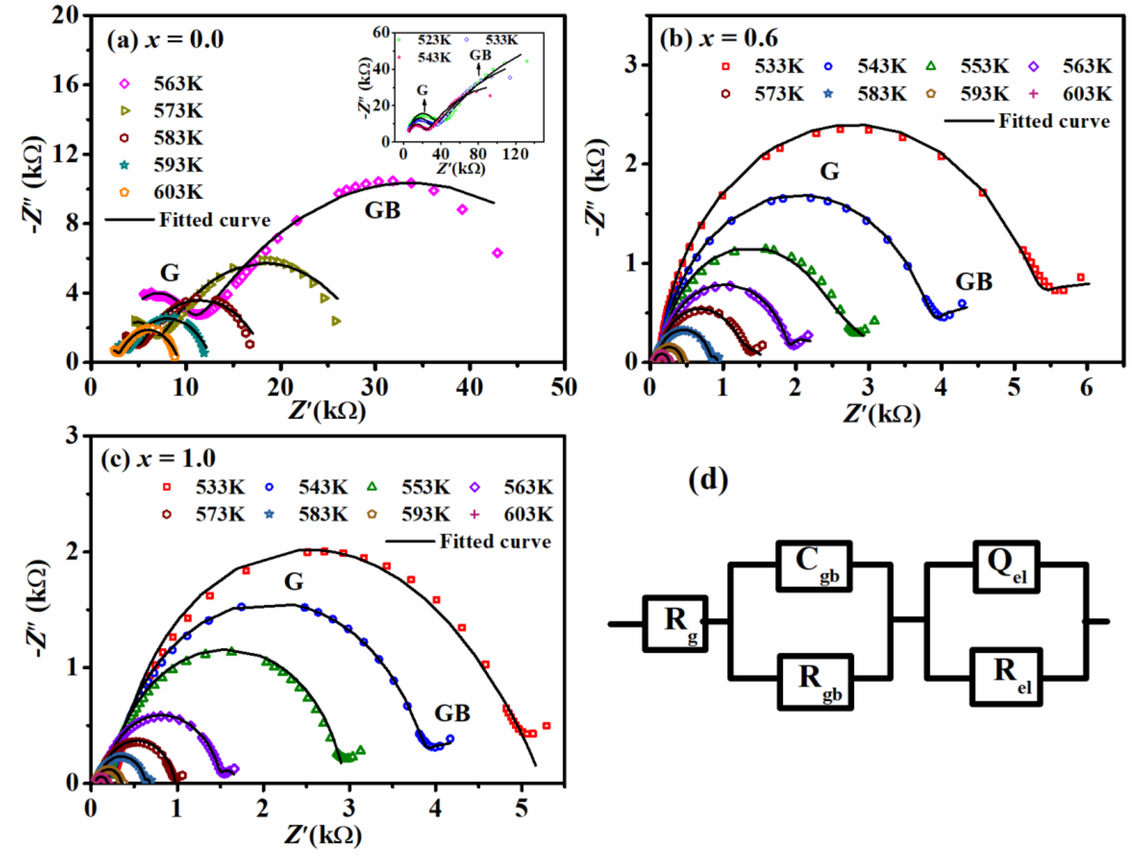

Fig. 4.15: (a-c) Nyquist plots for $(Sm_{1-x}Ho_x)_3Fe_5O_{12}$ $(x = 0.0, 0.6$ and $1.0)$ samples with inset of (a) showing the fitting of Nyquist plots for $523\ K - 543\ K$ and (d) equivalent circuit fitted to these Nyquist plots.

4.1.4 Complex dielectric characterization

The real and imaginary components of the complex dielectric constant can be calculated using eqn. (3.3) and (3.4). The dielectric constant is plotted against frequency by varying the temperature from $523\ K$ to $623K$ for $x = 0.0, 0.4, 0.6$ and 1.0 samples and the plots are shown in Fig. 4.16. The dielectric constant is found to be large at lower frequencies and they are in the order of 10^4 to 10^6 for $x = 0.0$ to $x = 1.0$ sample. But on increasing the frequency, the dielectric constant decreases to the order of 10^1 $(x = 0.0)$ to 10^3 $(x = 1.0)$ samples at $10^5\ Hz$ frequency. Maxwell-Wagner type relaxation is generally responsible for the high value of the dielectric constant in the lower frequency region. Typically, this form of relaxation is seen in heterogeneous systems where the conductivity of the Gs, GBs, and electrode effect all vary [50]. It is observed that the ε' is increasing with Ho substitution also. Ho^{3+} substitution in SmIG leads to increased oxygen vacancies due to the smaller ionic radius of Ho compared to Sm which causes lattice distortion. To

Indian Institute of Technology Guwahati

relieve this strain and maintain structural stability, the crystal forms oxygen vacancies. This results in an increase in the formation Fe^{2+} ions from Fe^{3+} ions. In turn, this will enhance the dielectric constant by producing a sufficient number of polarised electrons. However, we have not observed any significant change in ε' value for $x = 1.0$ sample and it is possibly due to the concentration of Fe^{2+} ions and oxygen vacancy may not be high enough to have a significant effect on ε'. In general, the dielectric properties correspond to four type of polarizations in different frequency zone i.e., ionic, electronic, orientational and space charge polarization. The space charge polarization depends on the purity of the material. According to the Debye's theory, the dielectric constant follows inverse proportionality with the temperature. Yet, we can see that ε' is increasing with the increment in temperature in our case. This increment is arising due to the space charge polarization caused by lattice defects [140].

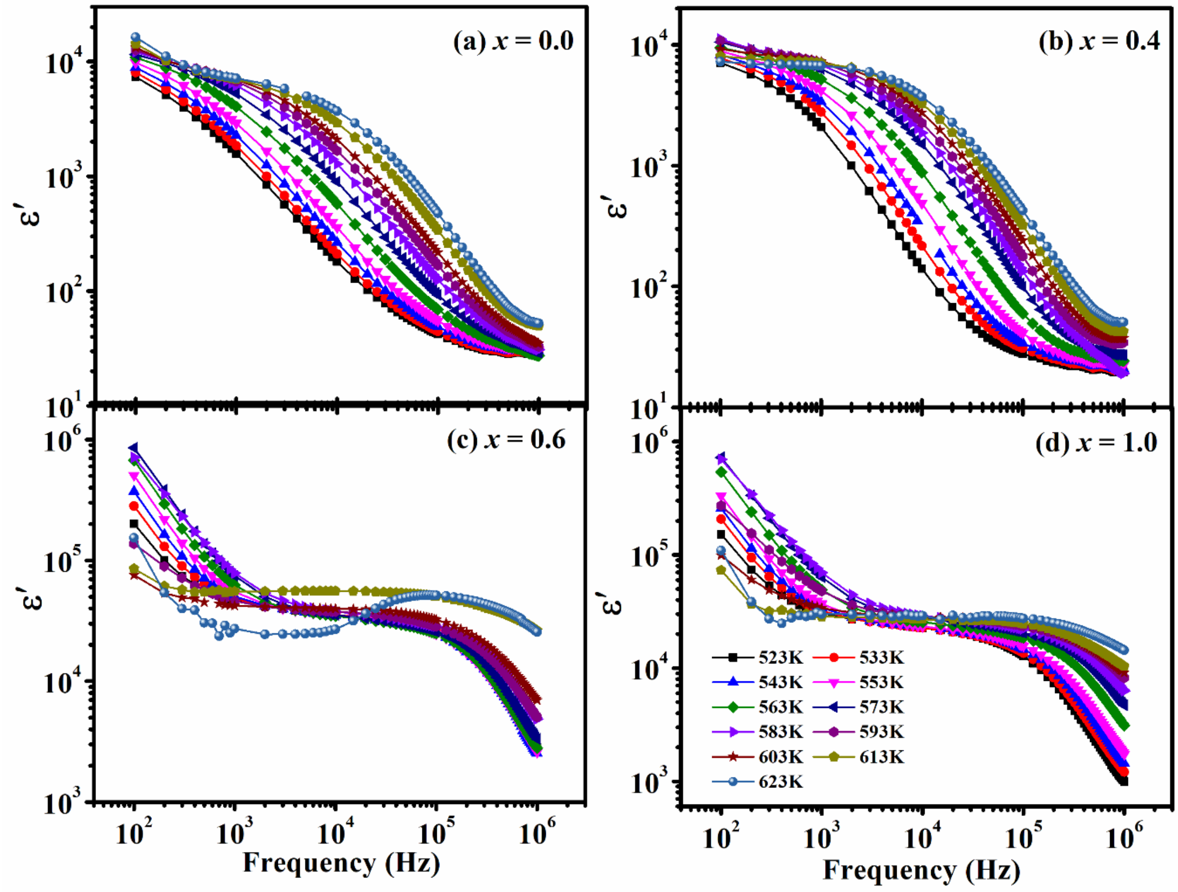

Fig. 4.16: The variation in real component of dielectric constant (ε') for $x = 0.0, 0.4, 0.6$ and 1.0 samples by varying temperature from $523K - 623K$.

The dielectric loss represents the energy decay within the garnet and is represented by the imaginary component of dielectric constant (ε'') which can be calculated from eqn.

(3.4). We have plotted ε'' with respect to frequency at different temperature from $523\ K$ to $623\ K$ as shown in Fig. 4.17 for $x = 0.0, 0.4, 0.6$ and 1.0 samples. The dielectric loss is high in the low frequency region because of the higher resistance offered by GBs. Since, it requires higher energy for transfer of electrons between Fe^{2+}/Fe^{3+} ions due to which high loss is observed. It has been noticed that the ε'' plots shows a linear behavior with a slope close to -1. This indicates that the conductivity contribution at higher temperatures follows the typical power law, commonly referred to as the Universal Dielectric Response [103].

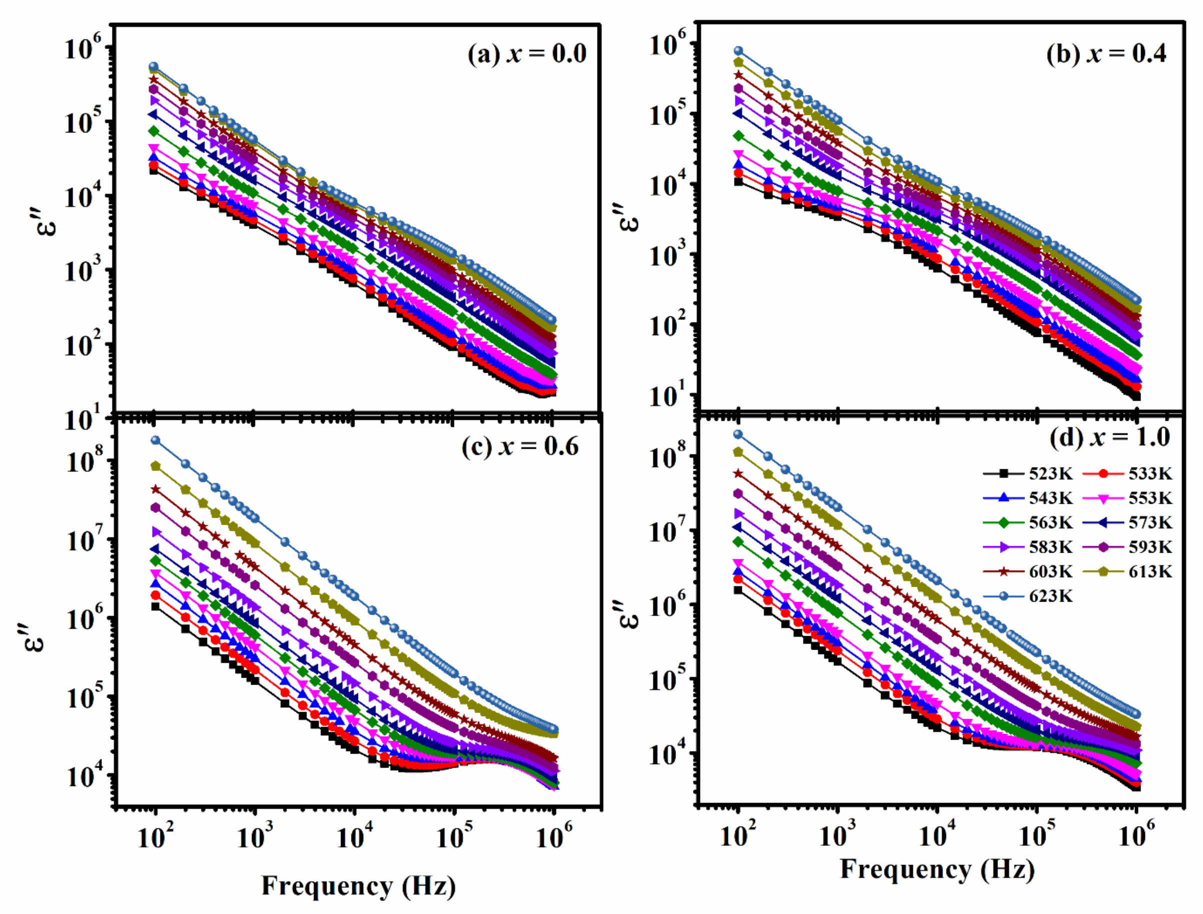

Fig. 4.17: The variation in imaginary component of dielectric constant (ε'') for $x = 0.0, 0.4, 0.6$ and 1.0 samples by varying temperature from $523K - 623K$.

4.2 Ho substituted Dysprosium iron garnet

The samples of $(Dy_{1-x}Ho_x)_3Fe_5O_{12}$ with $x = 0.0$ to 1.0 were prepared by solid-state reaction method. The stoichiometric ratio of all the oxides i.e., Dy_2O_3, Ho_2O_3 and Fe_2O_3 were grinded in acetone medium in agate mortar and pestle. The calcination is carried out at $800°C$ for 12 hours followed by pelettization using KBr press. The final sintering of pellets was held at $1200°C$ for 24 hours with multiple intermediate grinding and sintering. The samples is then procecessed for further characterizations.

4.2.1 Structural characterization

The indexed XRD patterns extracted at room temperature which are demonstrated in Fig. 4.18. The purity of the phase is tested with Rietveld refinement technique by using $Ia\bar{3}d$ space group with cubic crystal structure. The refined XRD plots for all the samples of Ho-DyIG series are shown in Fig. 4.19 and 4.20. Several structural and reliability parameters are extracted from the refinement which are listed collectively in Table 4.3. It is observed that the lattice constant and unit cell volume decreases gradually with Ho substitution. The obtained value of the lattice constant varies from 12.4181 Å for $x = 0.0$ to 12.3858 Å for $x = 1.0$ sample. So, we can predict that this lattice contraction is arising because of smaller ionic radii of Ho^{3+} ions (1.041 Å) compared to Dy^{3+} ions (1.052 Å). A similar value of the lattice parameter for the parent sample is reported in the literature [141]. Further, we have calculated the bond length and angles between all the ions using VESTA software. The bond length between $Fe\,(a) - Fe\,(d)$ and bond angle among $Fe\,(a) - O - Fe\,(d)$ are found to be decreased with Ho doping as shown in Fig. 4.21. In other words, we can say that the superexchange interaction among $Fe\,(a) - O - Fe\,(d)$ bond is getting weak with Ho substitution. The smaller Ho^{3+} ion replaces the larger Dy^{3+} ion, resulting in such contraction in bond angles.

The average crystallite size (D) of the samples is evaluated with the help of Williamson-Hall (W-H) approach which is given as [142]:

$$\beta cos\theta = \frac{k\lambda}{D} + 4\varepsilon sin\theta$$

(4.1)

here, k is the Scherer constant which is 0.89 for circular-shaped grains, β is the full-width half maximum (FWHM), ε is the micro-strain parameter, and θ is the Bragg angle for various XRD planes. The W-H plots for all the samples from $x = 0.0 - 1.0$ are shown in Fig. 4.22. The micro-strain and average crystallite size are calculated from the fitted parameters of eqn. (4.1). The crystallite size varies from 90 nm to 270 nm, while the order of strain remains in the order of 10^{-4} for all the compositions of Ho-DyIG series. Moreover, the site occupancy values of atoms have been refined and the results are tabulated in Table 4.3. These values are pretty compatible with nominal starting composition of the prepared samples.

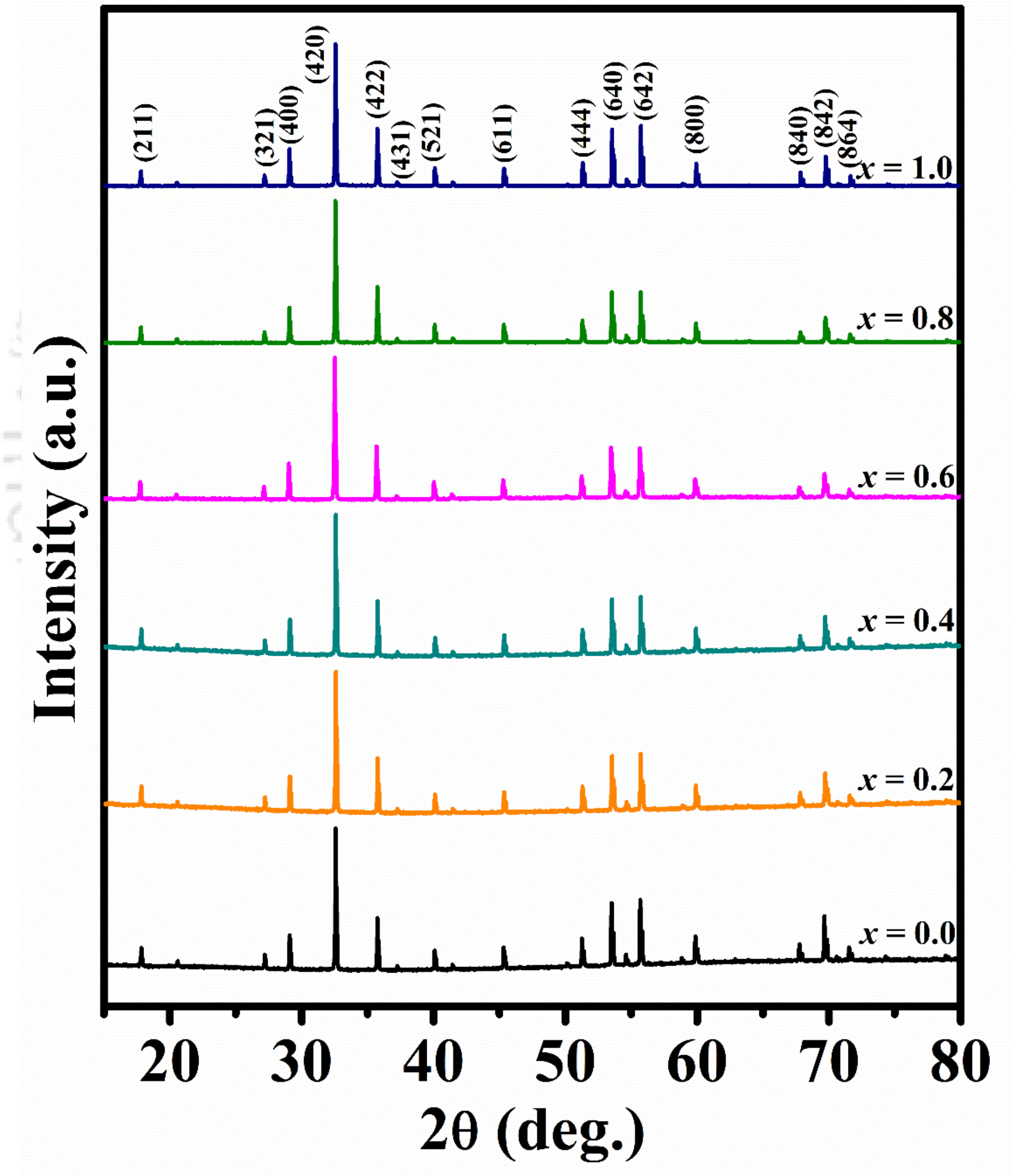

Fig. 4.18: The room temperature XRD plots of $(Dy_{1-x}Ho_x)_3Fe_5O_{12}$ with $x = 0.0$ to 1.0 samples with their indexed diffraction planes.

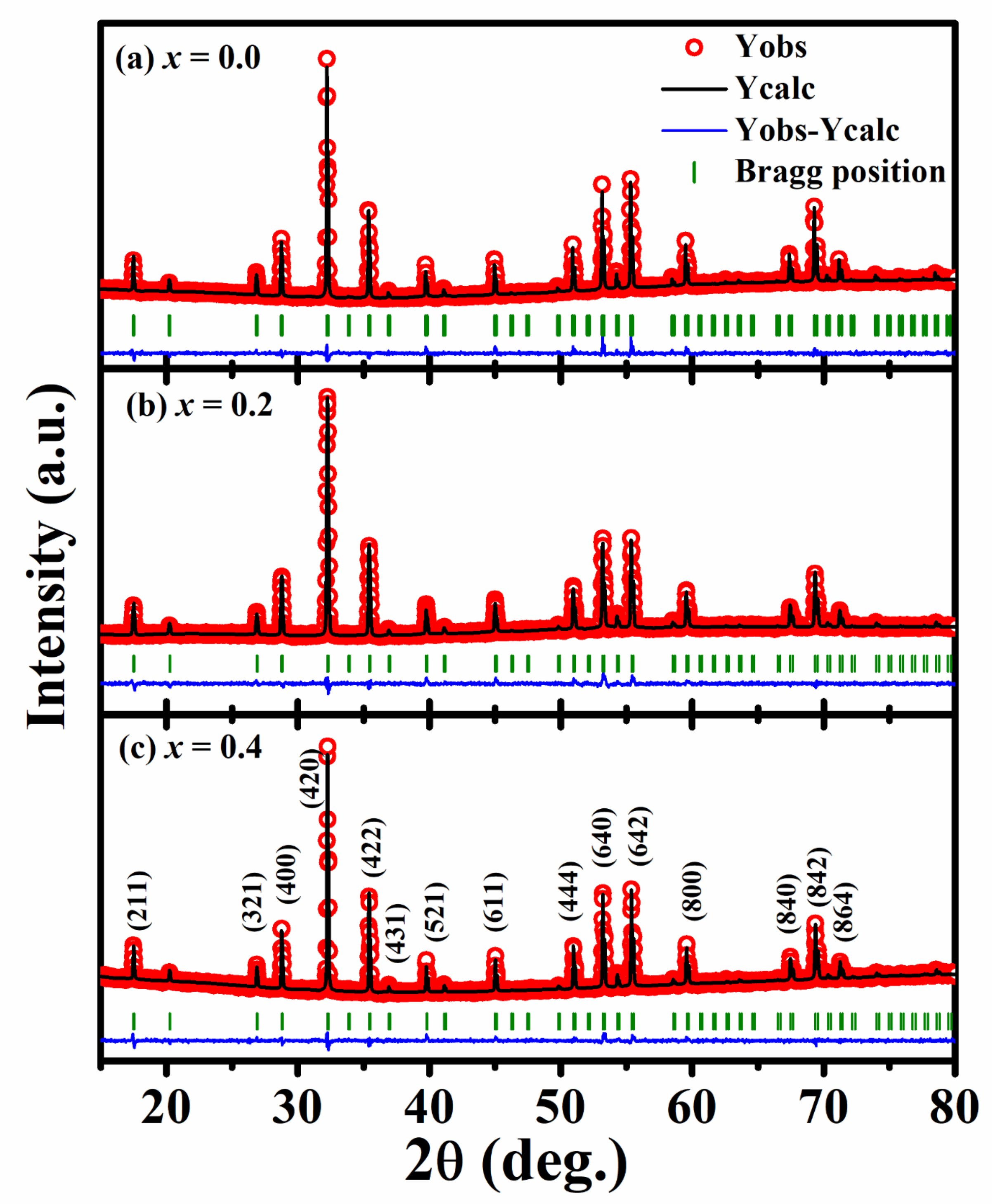

Fig. 4.19: Rietveld refined XRD patterns of $x = 0.0, 0.2$ and 0.4 concentrations of Ho-DyIG samples.

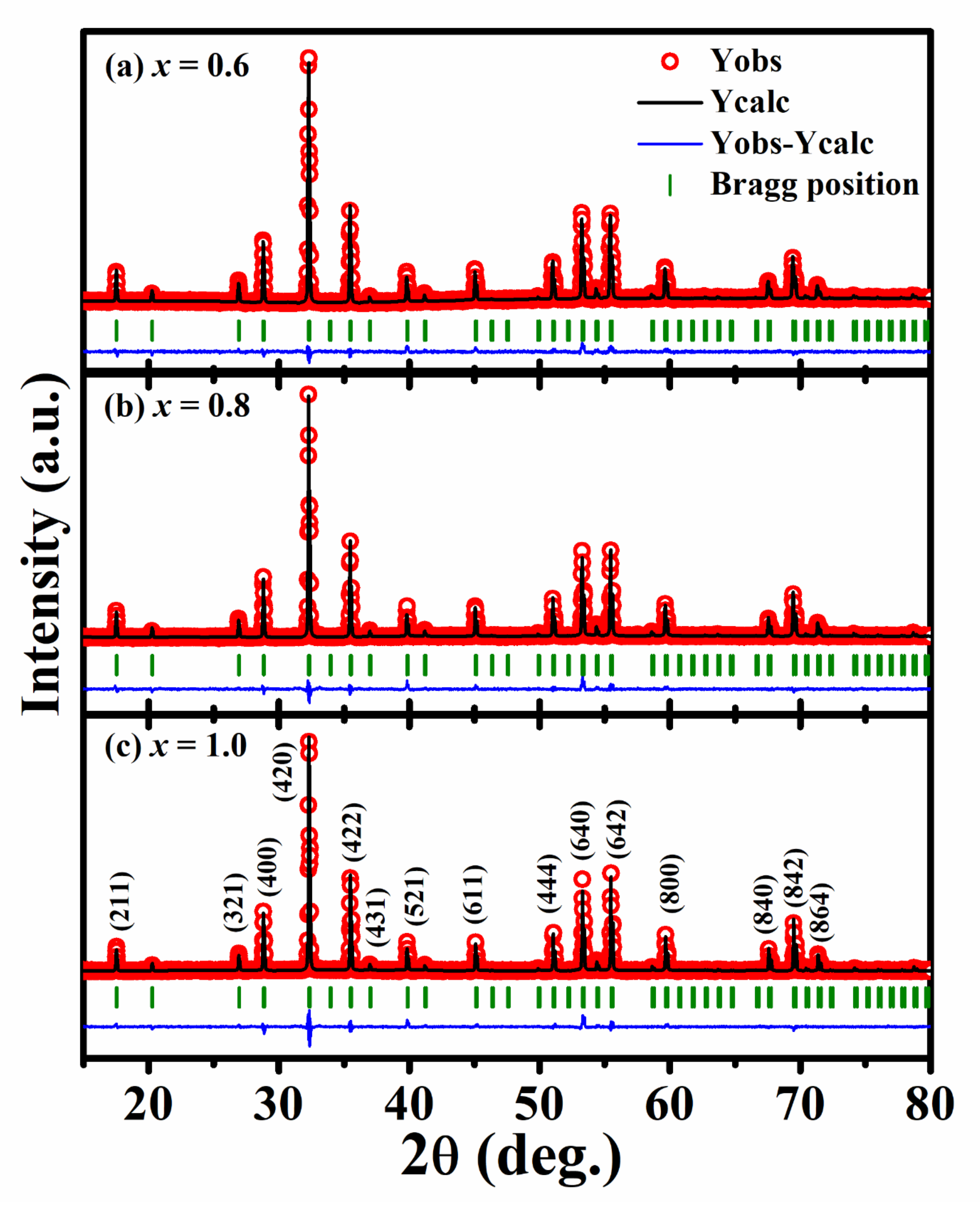

Fig. 4.20: Rietveld refined XRD patterns of $x = 0.6, 0.8$ and 1.0 concentrations of Ho-DyIG samples.

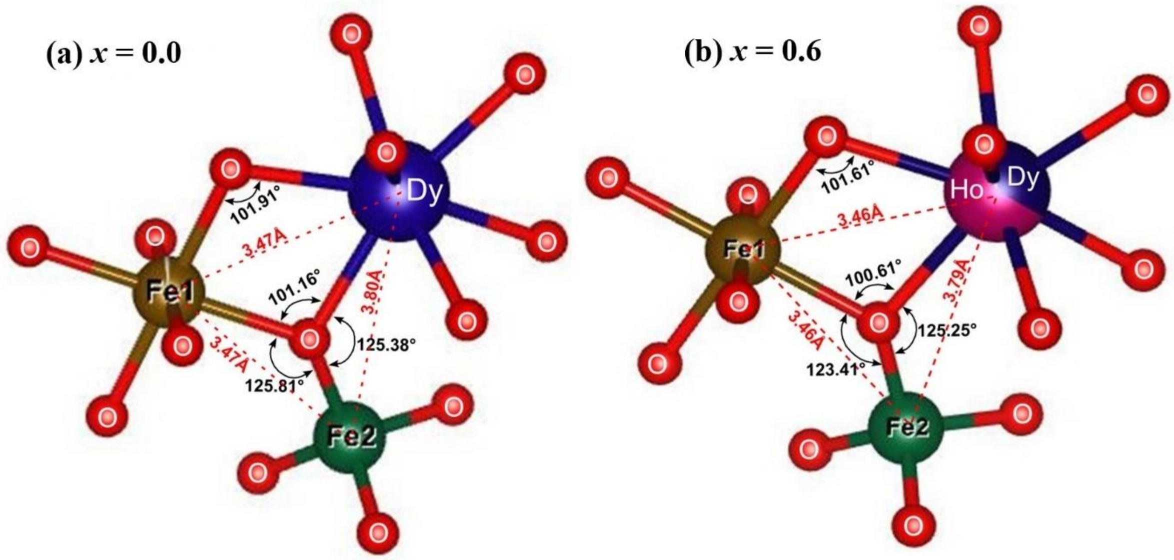

Fig. 4.21: Pictorial representation of bond length and bond angles among different cations of $x = 0.0$ and 0.6 samples of Ho-DyIG series.

Table 4.3: Structural parameters along with reliability factors obtained from Rietveld refinement for all the samples of Ho-DyIG series.

Sample → Parameters ↓	$x = 0.0$	$x = 0.2$	$x = 0.4$	$x = 0.6$	$x = 0.8$	$x = 1.0$
Space group	$Ia\bar{3}d$	$Ia\bar{3}d$	$Ia\bar{3}d$	$Ia\bar{3}d$	$Ia\bar{3}d$	$Ia\bar{3}d$
$a = b = c$ (Å)	12.4181 (1)	12.4090 (1)	12.4048 (1)	12.3957 (1)	12.3917 (1)	12.3858 (1)
Volume (Å^3)	1914.9	1910.7	1908.8	1904.6	1902.8	1900.0
R_p (%)	12.2	14.5	12.9	13.7	11.4	15.2
R_{wp} (%)	14.6	13.7	14.4	12.5	13.0	13.9
R_F (%)	6.8	4.5	5.4	5.0	5.6	5.8
R_{Bragg} (%)	7.1	4.8	5.5	4.9	6.1	6.5
χ^2	1.8	1.9	1.7	2.1	2.8	3.7
Occupancy						
Dy	2.98	2.39	1.78	1.16	0.57	0.0
Ho	0.0	0.58	1.17	1.79	2.35	2.95
Fe	4.99	4.98	4.98	4.95	4.97	4.98

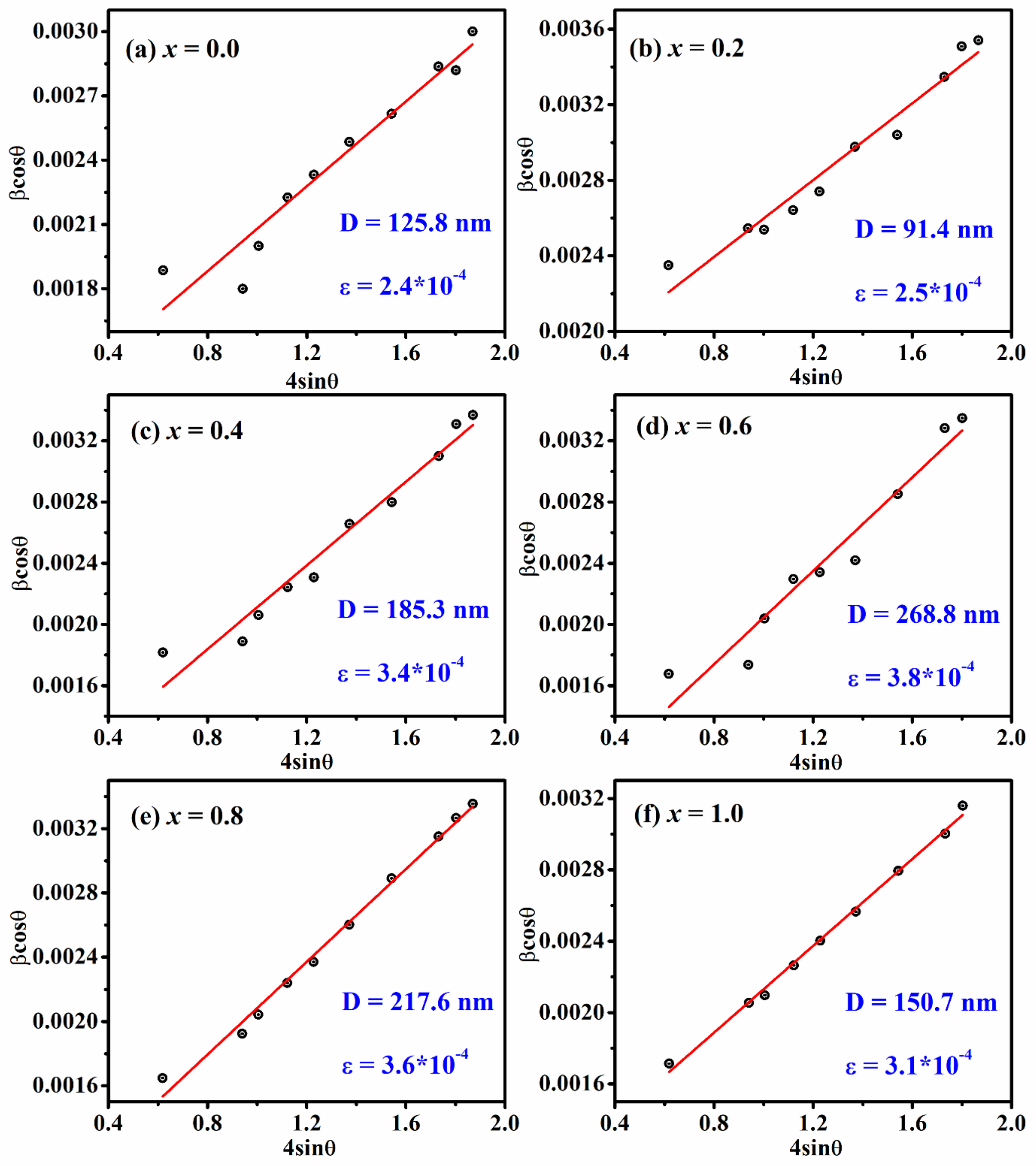

Fig. 4.22: Williamson-Hall plots with fitting for Ho-DyIG series ($x = 0.0 - 1.0$).

We have analyzed the surface morphology of these samples to investigate the average size of the grains in the samples. The FESEM micrographs are shown in Fig. 4.23 (a-d) along with their fitting of histograms to log-normal function (Fig. 4.23 (e-h)). The average grain size comes out to be $0.87 \pm 0.03\ \mu m$ for the parent sample and it goes to $1.13 \pm 0.09\ \mu m$ for $x = 1.0$ sample. So, we can see that we have attained a particle size in the order of μm with a low porosity in these samples of this series. The images show formation of clear grains separated by grain boundaries.

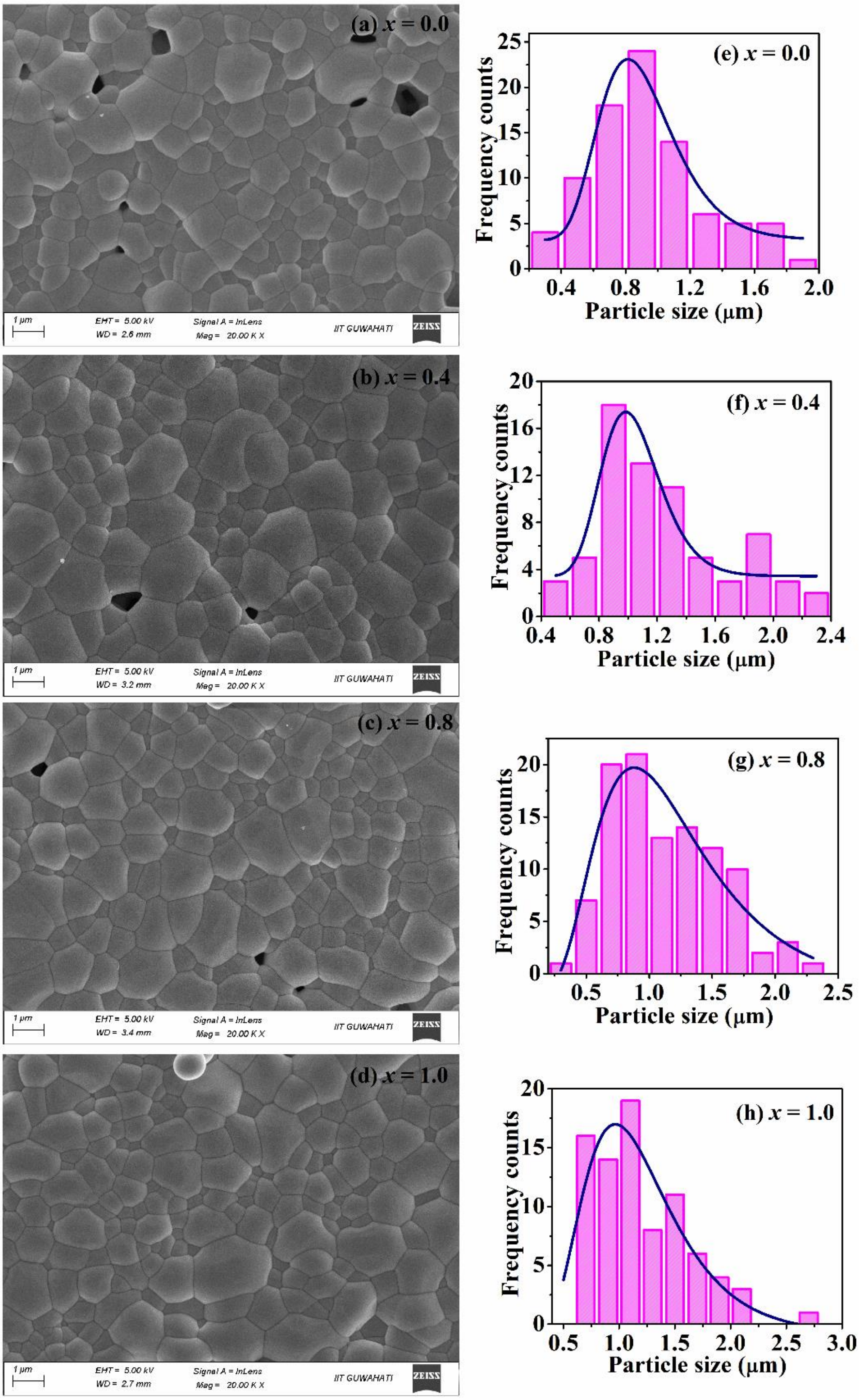

Fig. 4.23: (a-d) FESEM micrographs and (e-h) their corresponding fitting of particle size distributed histograms to the log-normal function for $x = 0.0, 0.4, 0.8$ and 1.0 compositions of Ho-DyIG series.

We have performed elemental composition study of this series with the help of Energy dispersive X-Ray spectroscopy. Fig. 4.24 (a,b) represents the area map of $x = 0.0$ and 0.6 samples and individual elements are shown by distinct colors at the bottom. We can see the increase in green colour intensity in the Ho doped sample, which ensures the presence of Ho in $x = 0.6$ sample. We have also attached the EDX spectrum for both samples in Fig. 4.24 (c,d). By considering the atomic percentage of all the elements, we have computed the composition of the corresponding element in the sample. We have obtained the composition as $Dy: Ho: Fe$ to be 2.95: 0.0: 5.0 and 1.18: 1.58: 5.0 for $x = 0.0$ and 0.6 samples, respectively. Some extra peaks are also detected, which are arising because of the coating of Gold to make the surface conducting.

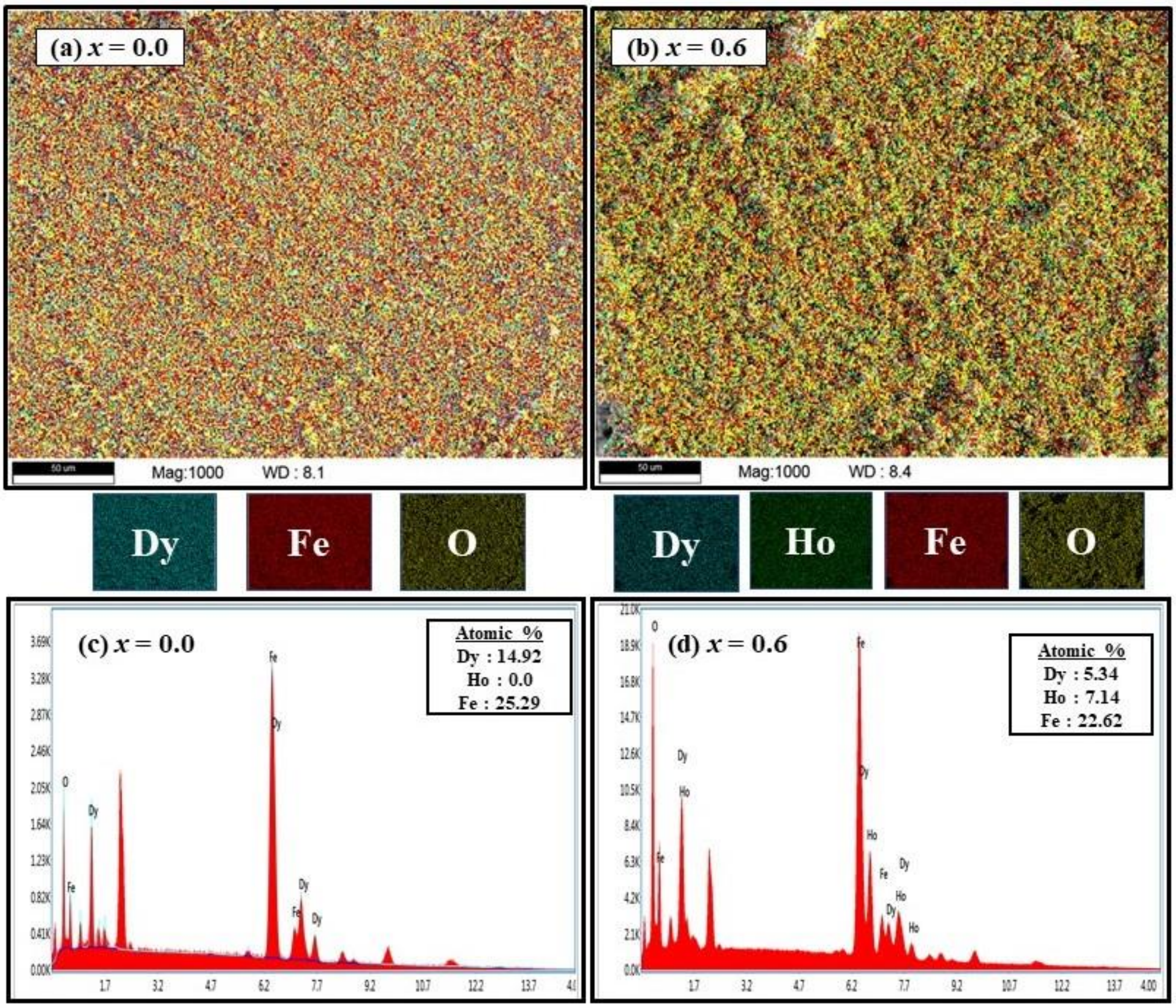

Fig. 4.24: Area mapping for (a) $x = 0.0$, (b) 0.6 samples and (c,d) their respective energy dispersion diagrams.

We have examined the XPS spectra for Ho-DyIG samples to determine the electronic state of each cation in our sample. The XPS plots with all the energy deconvolution of $x = 0.0, 0.2$ and 0.8 samples are shown in Fig. 4.25 (a-i). We have observed that the binding energy peaks for the parent sample corresponding to $4\,d_{5/2}$ and $4\,d_{3/2}$ energy doublets and they are deconvoluted into four lines at $152.1\,eV, 153.4\,eV, 155.8\,eV$ and $158.0\,eV$ binding energy. All these lines represent the standard oxidation state of Dy, i.e., Dy^{3+} [143]. For Ho-doped samples, similar energy doublets have been observed, i.e., $4\,d_{5/2}$ and $4\,d_{3/2}$ for both Dy as well as Ho but the difference is that now these energy doublets are deconvoluted into two lines. Further, the XPS spectra of $Fe2p$ are splitted into $2\,p_{3/2}$ and $2\,p_{1/2}$ energy doublet, which are fitted to the Gaussian-Lorentzian function to determine the oxidation state of Fe. For instance, for $x = 0.2$ sample, we have noticed the binding energy peaks at $710.1\,eV$ and $723.6\,eV$ which correspond to the Fe^{2+} state of iron, while the peaks at $711.6\,eV$ and $725.2\,eV$ are related to the Fe^{3+} ions. Additionally, two small satellite peaks are also observed at around $718.8\,eV$ and $732.9\,eV$. The high-resolution XPS spectra of $O\ 1s$ are also studied and the peak observed at $\sim 529\,eV$ in the XPS spectrum can be attributed to the presence metal-oxygen bond. Additionally, a shoulder peak at $\sim 531\,eV$ can be observed, which may indicate the presence of absorbed oxygen from the surface [144]. Moreover, we have observed some small shake ups next to $4\,d_{5/2}$ and $4\,d_{3/2}$ energy doublets in all the spectrums which are called as satellite peaks. Such satellite peaks are also observed for Fe spectra at around $718\,eV$ and $732\,eV$. These peaks are formed because of the excitation of electrons from the core level to higher energy levels or the ejection of an electron from the valence band, resulting in the emission of an X-ray photon with energy lower than that of the primary X-ray beam.

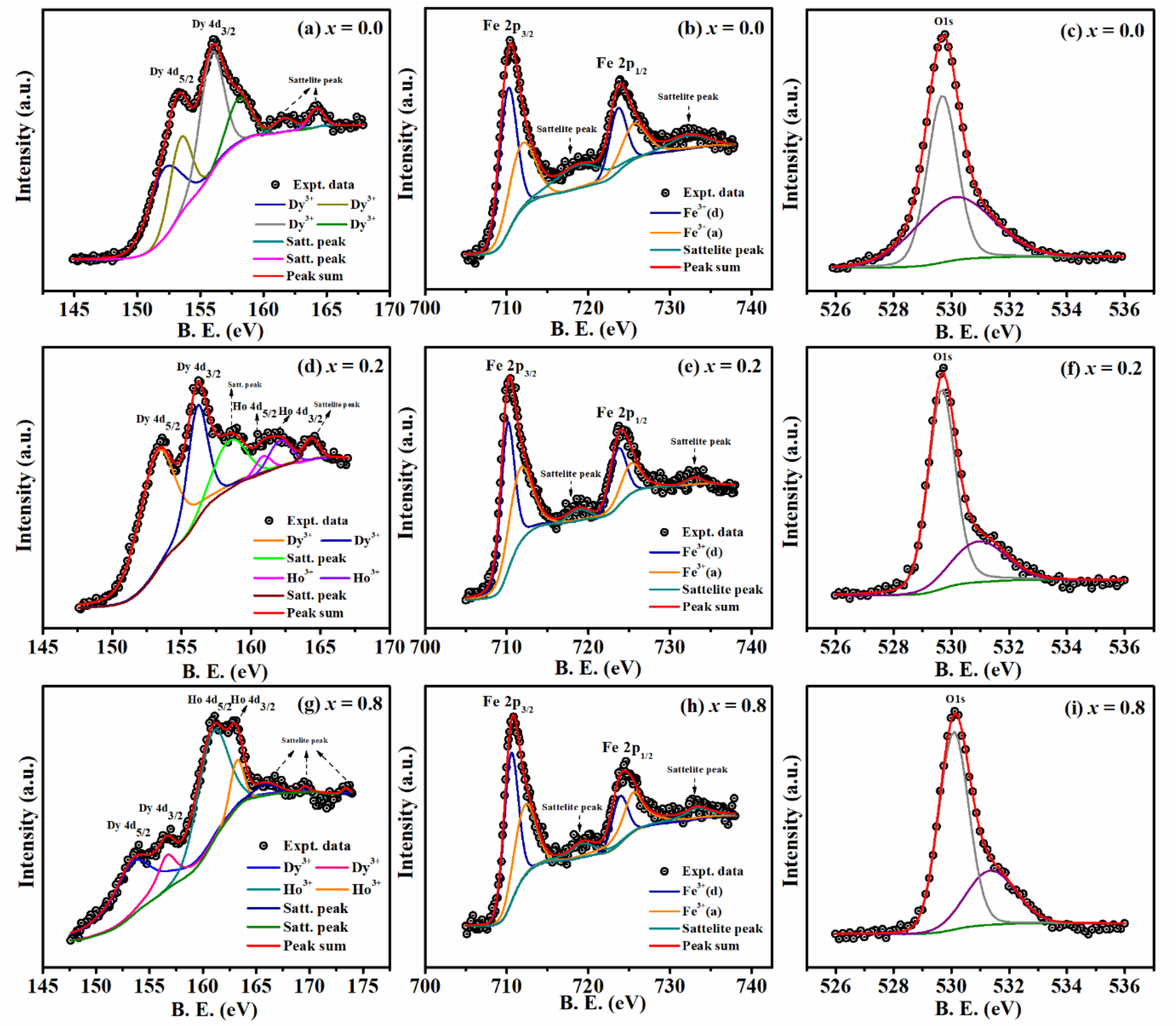

Fig. 4.25: XPS spectrum of $(Dy_{1-x}Ho_x)_3Fe_5O_{12}$ for (a,b,c) $x = 0.0$, (d,e,f) $x = 0.2$ and (g,h,i) $x = 0.8$ samples with fitting to Gaussian-Lorentzian function.

4.2.2 Magnetic characterizations

Since magnetization is a temperature-dependent property, we need to know that up to which temperature the ferrimagnetism holds in RIGs. In order to determine the transition temperature T_c from ferrimagnetic to paramagnetic state, we have carried out magnetization versus temperature data by applying an external field of 300 Oe as shown in Fig. 4.26 (a). All the M-T plots show typical ferrimagnetic nature. We have calculated T_c values from the derivative of magnetization with temperature and they are obtained as 555 K for $x = 0.0$ and 545 K for $x = 1.0$ sample. The possible reason for the drop in T_c is attributed to the distortion in superexchange interaction among $Fe\ (a) - O - Fe\ (d)$ networks due to the decrease of bond angle as can be seen in the crystal structure images of XRD data shown in Fig. 4.21.

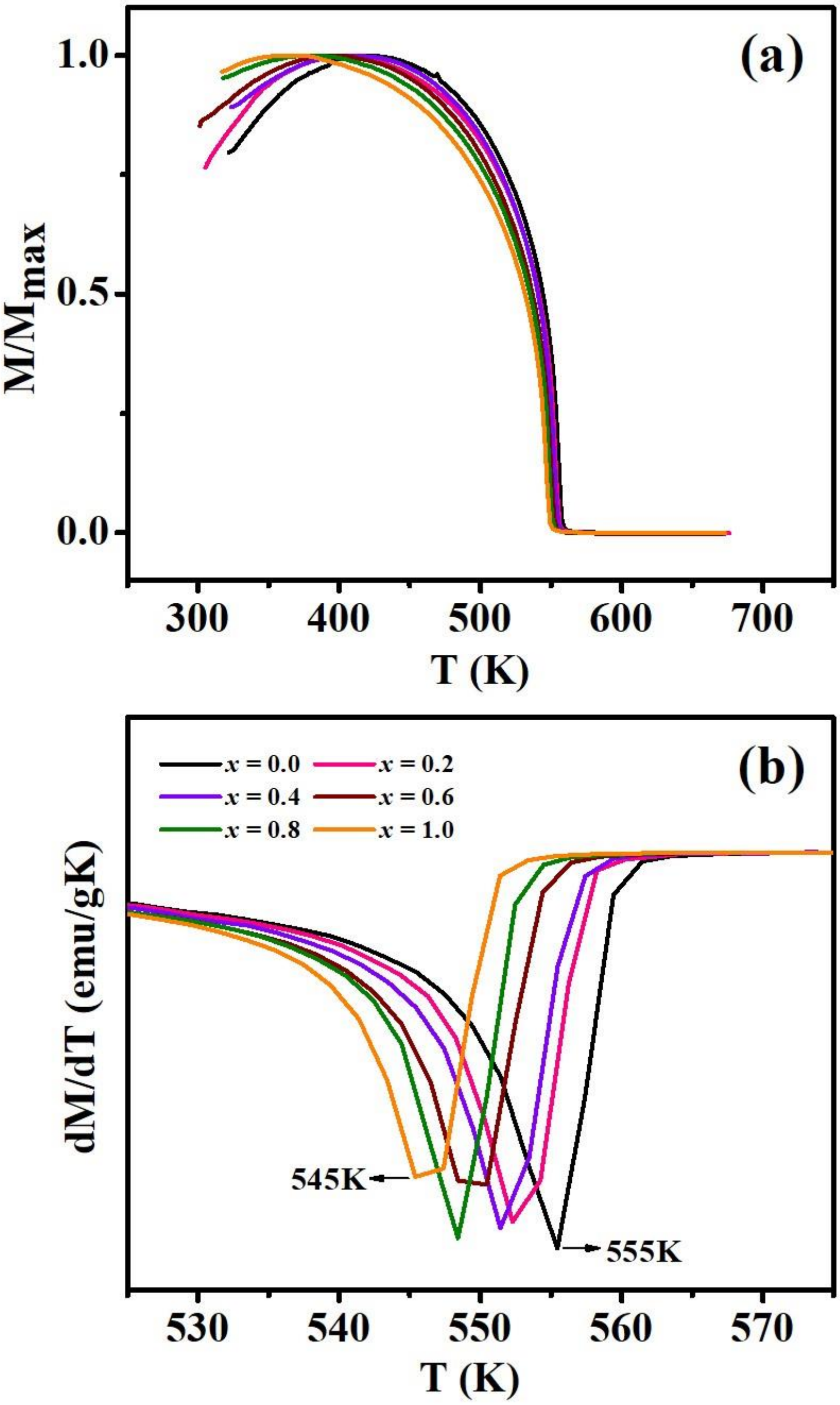

Fig. 4.26: (a) Temperature dependent magnetization in between $300K$ to $700K$ at $300Oe$ magnetic field for all the samples of Ho-DyIG series and (b) derivative of magnetization with temperature for $x = 0.0$ to 1.0 samples.

We have also performed low-temperature ZFC and FC magnetic measurements as shown in Fig. 4.27. It is very interesting to note different transitions in the parent as well as doped samples. After reducing the temperature below T_c, we have observed a compensation point (T_{comp}) at which all the sublattice moments align such that the net magnetization becomes zero. The following empirical relation gives the moment in Ho-DyIG:

$$M_{net} = 3M_{Fe(d)} - [2M_{Fe(a)} + 3(1-x)M_{Dy(c)} + 3xM_{Ho(c)}]$$

(4.2)

The antiferromagnetically coupled Fe^{3+} ions at octahedral and tetrahedral positions result in one Fe^{3+} ion moment, which is 5 μ_B. Since we are substituting smaller moment of Ho^{3+} (10.60 μ_B) at higher moment site, i.e., at Dy^{3+} (10.63 μ_B) and it results in a reduction in the net moment in the square bracket term. This process leads to an increment in net magnetization with Ho substitution as per above empirical formula. In order to achieve compensation, we must go towards lower temperatures and T_{comp} gets reduced. This decreasing trend in T_c and T_{comp} is shown in Fig. 4.28 (a). Moreover, a secondary rise in magnetization below this T_{comp} is observed due to weak magnetocrystalline anisotropy in the vicinity of T_{comp}.

When the temperature is further decreased below this T_{comp}, we have observed a transition which is named as T_B as discussed by Belov *et al* [145]. This transition is mainly attributed to the weakly ordered exchange coupling between rare earth ions and Fe^{3+} ions at octahedral site magnetic moments. According to Belov, this transition arises because of the paraprocess effect in ferrimagnets at lower temperatures. The impurities or defects can create local magnetic fields that interact with the external magnetic field and cause deviations from ideal paramagnetic behavior. The paraprocess effect can result in a broadening and shifting of the magnetic susceptibility peak. Some of the authors have observed a sharp change in susceptibility $\chi_p(T)$ curve in the vicinity of T_B and explained it by assuming that the thermal motion brings some partial but sharp changes in magnetic ordering of this weak sublattice at this temperature [146]. The value of T_B lies in the range of $34 - 44\ K$ for Ho-DyIG samples as can be seen from Fig. 4.28 (b). We have observed $T_B = 41.2\ K$ for the parent sample which is comparable to the literature [32]. However, the presence of impurities and defects in different concentrations can modify the value of T_B leading to an irregular trend in T_B with respect to x.

Further, we have seen the spin reorientation (T_{sr}) transition in all the samples upon continued cooling. The mechanism of spin reorientation is based upon the anisotropic exchange interaction of Fe^{3+} and rare earth ions. This anisotropic exchange interaction produces an effective field for Fe^{3+} ions at tetrahedral and octahedral site. These effective fields favor the rotation of Fe^{3+} ions in such a way that they retain their initial antiferromagnetic orientation. Therefore, the effective fields increase as temperature decreases due to the rise in rare earth magnetization. When the interaction energy of effective field with Fe^{3+} ions exceed the anisotropy energy of Fe^{3+} ions, spin reorientation takes place [31]. The spin reorientation is observed in the range of $10 - 18\ K$ for all the samples of Ho-DyIG series as shown in Fig. 4.28 (b). Lahoubi *et al.* [147] has observed a finite discontinuity in the specific heat i.e., $C_p\ (T)$ in the vicinity of spin reorientation transition indicating a second-order phase transition at the starting and ending of spin reorientation transition.

Indian Institute of Technology Guwahati

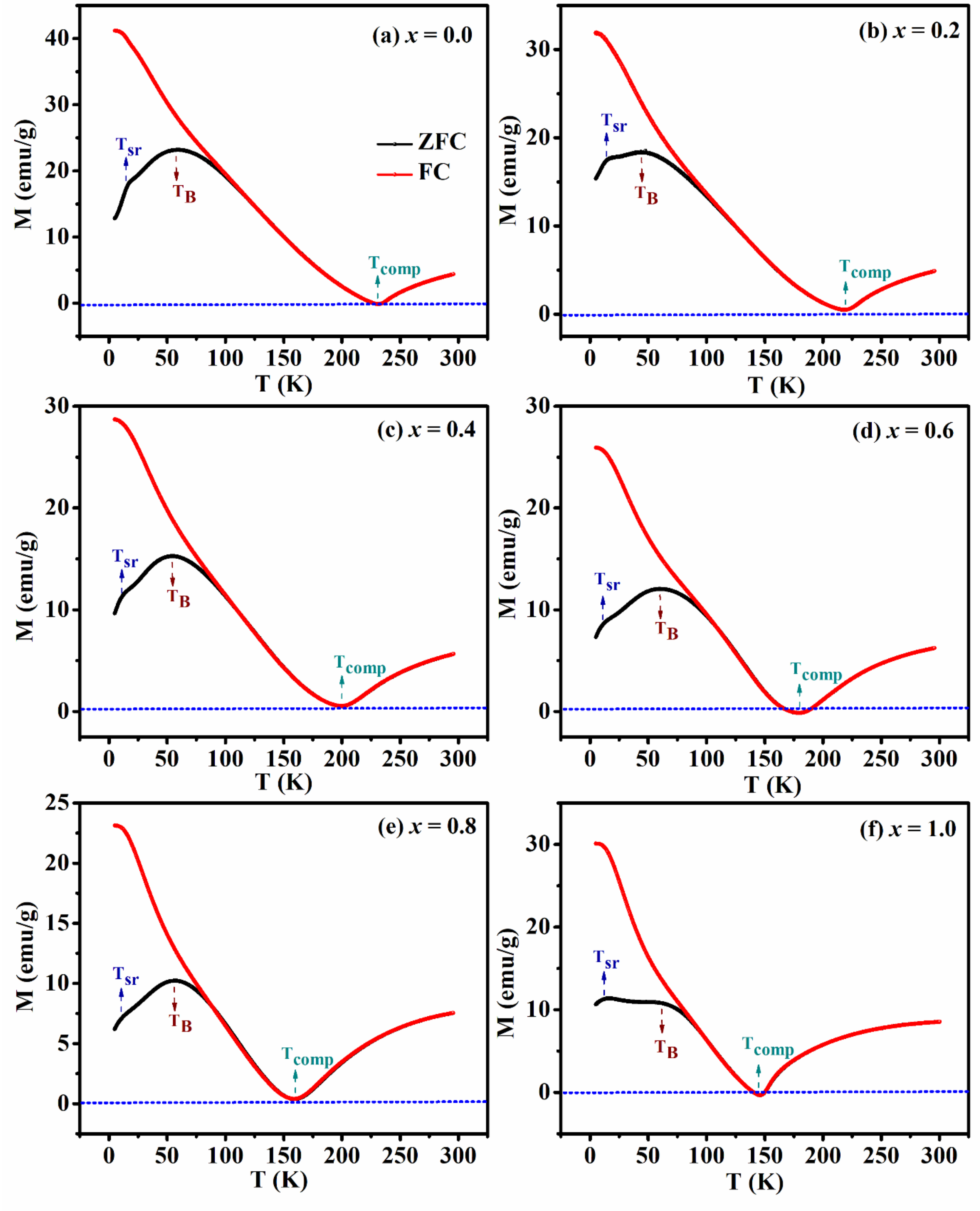

Fig. 4.27: Variation in magnetization with temperature from $5K$ to $300K$ by applying an external field of $300\ Oe$ for all the samples of Ho-DyIG series.

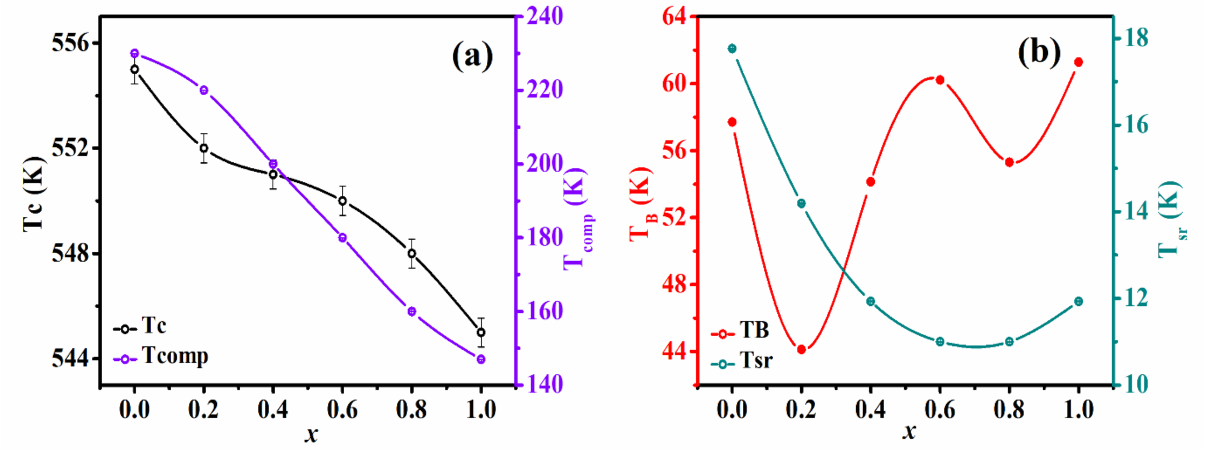

Fig. 4.28: Change in the value of different transition temperatures with Ho substitution.

In the continuity of magnetic studies, we have analyzed the hysteresis loops of Ho-DyIG samples at two temperatures, i.e., $5K$ and $300K$ by applying a maximum field of $5T$ in both cases as shown in Fig. 4.29 (a,b). We can see that the hysteresis curves are not getting adequately saturated at room temperature. At the same time, they show a very good saturation at the lower temperature because of the strengthening of the alignment of the magnetic spins in the direction of magnetic field at lower temperatures. Even though the moments of Ho^{3+} ($10.60\ \mu_B$) and Dy^{3+} ($10.63\ \mu_B$) are comparable, then also reduction in magnetization is observed at RT as Ho is doped in DyIG. One possibility is the non-colinear FIM interaction between Fe^{3+} ions at octahedral and tetrahedral site due to induced lattice defects. However, a reverse trend is observed in the saturation magnetization at $5K$, which can be attributed to the magnetic compensation effect. Specifically, the parent sample has a T_{comp} of $231K$, which is much higher than the measured temperature, i.e., $5K$ and results in a higher magnetic moment compared to $x = 1.0$ sample. This is because the $x = 1.0$ sample has a T_{comp} of $146K$, which is relatively closer to the temperature being measured and thus has a lower magnetic moment. Furthermore, these M-H curves are also fitted to the Law of Approach to Saturation (LAS) equation i.e., eqn. (3.2). The calculated values of M_s and K_1 are listed in Table 4.4. We have observed an increment in anisotropy constant as we go from room temperature to $5K$. Vinay *et al.* [111] have also observed a similar type of anisotropy constant for yttrium iron garnet at room temperature and improvement in anisotropy constant at low temperature is reported by Pearson *et al* [133].

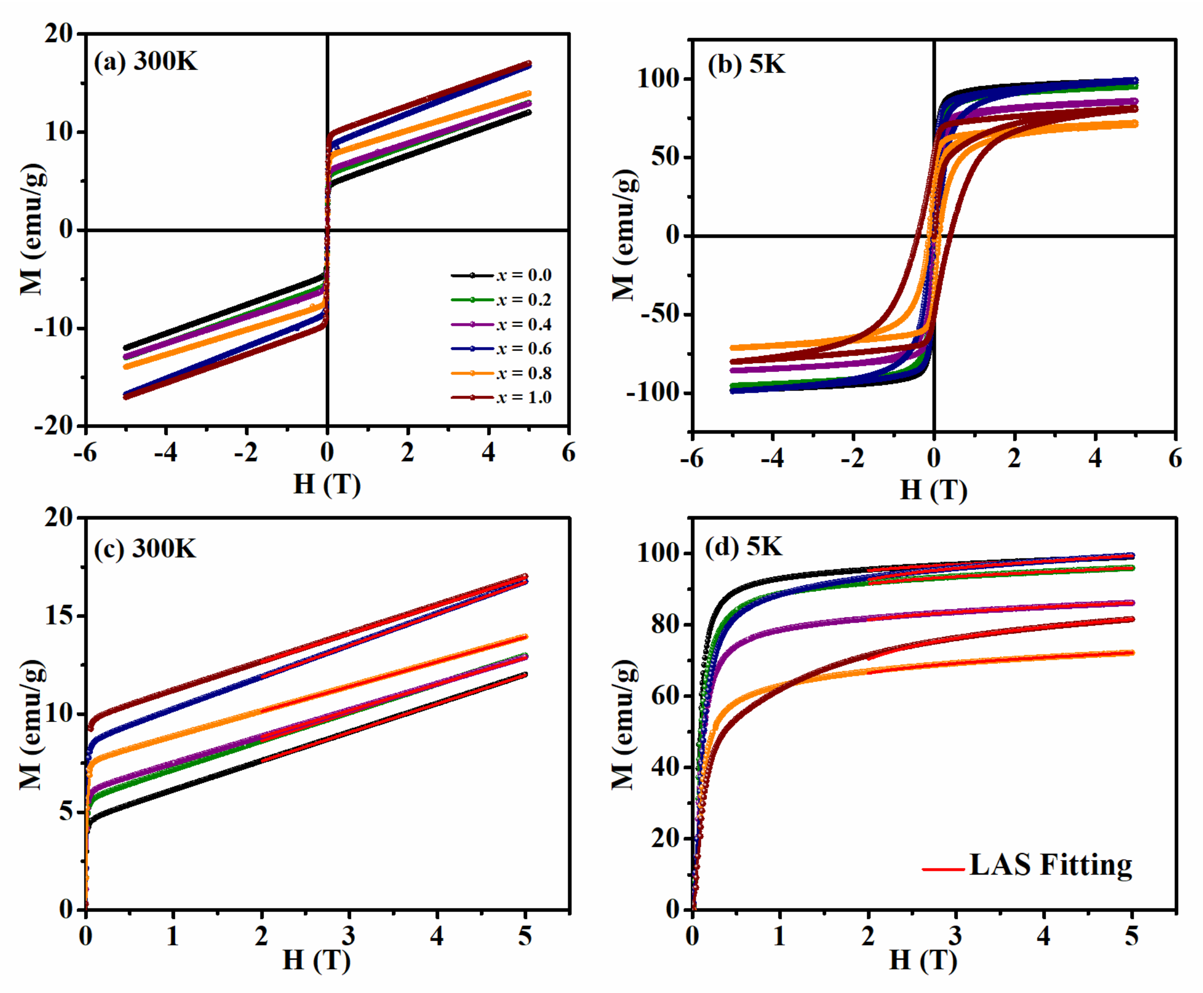

Fig. 4.29: (a,b) Magnetic hysteresis loops and (c,d) fitting of initial M-H curves to LAS equation at room temperature and 5 K for $(Dy_{1-x}Ho_x)_3Fe_5O_{12}$ samples with $x = 0.0$ to 1.0.

Table 4.4: List of saturation magnetization and effective anisotropy constant for all the samples of Ho-DyIG series obtained from the hysteresis curves at $300K$ and $5K$.

Sample name	$300K$		$5K$	
	$M_s\ (emu/g)$	$K_1 \times 10^4\ (erg/cc)$	$M_s\ (emu/g)$	$K_1 \times 10^6\ (erg/cc)$
$x = 0.0$	4.69	9.33	94.96	5.52
$x = 0.2$	5.73	8.06	91.56	6.30
$x = 0.4$	6.17	9.89	81.67	6.36
$x = 0.6$	8.67	15.59	93.64	8.63
$x = 0.8$	7.63	14.9	67.63	7.11
$x = 1.0$	9.82	23.55	75.32	11.83

4.2.3 Magnetocaloric effect (MCE)

After having an overview of hysteresis loops at $5K$ and $300K$, we are motivated to briefly study the MCE in the samples of this series. For this, we have carried out isothermal magnetization curves in the temperature range of $10 - 300\ K$ by applying a maximum field of $5\ T$ for $x = 0.4$ and 0.8 samples as shown in Fig. 4.30 (a-d). The $x = 0.4$ and 0.8 samples are so chosen for our analysis of MCE, as they represent an intermediate and higher concentration of Ho substitution in DyIG series. In addition, based on the similar transitions observed in the M-T plots of the other samples in the series, we can expect similar behavior from the entire series, although the transition temperatures may vary. We can see that the magnetization initially increases with the increment in magnetic field, but it becomes almost saturated after $3\ T$. Moreover, we have also observed that the saturation magnetization decreases on increasing the temperature up to compensation temperature and after that it starts rising further. This variation of magnetization is in good agreement with the $M - T$ plots discussed above.

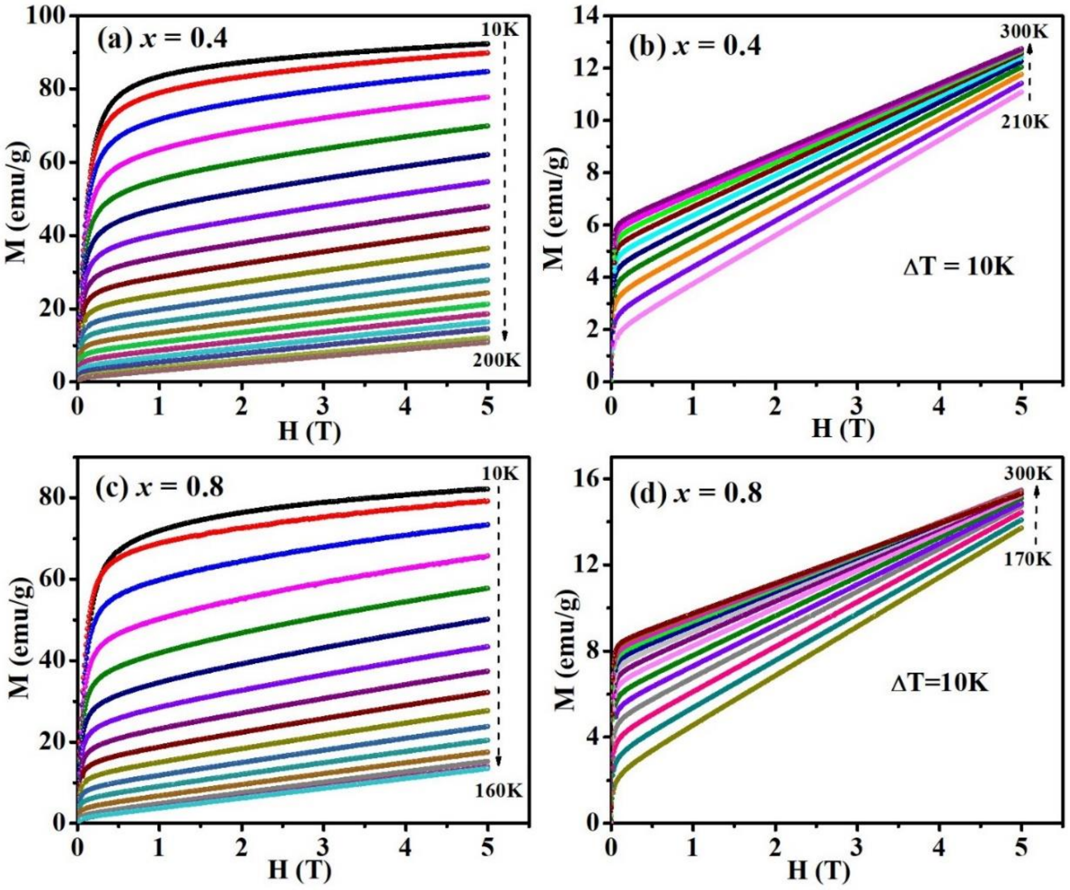

Fig. 4.30: Isothermal magnetization curves for (a,b) $x = 0.4$ and (c,d) $x = 0.8$ samples from $10\ K$ to $300\ K$.

We can calculate the magnetic entropy change with respect to temperature at different magnetic fields by using following Maxwell's equation [148]:

$$\Delta S_M(T,H) = \int_0^H \left(\frac{\partial M}{\partial T}\right)_H dH \tag{4.3}$$

This relation can also be written as:

$$\Delta S_M = \sum \frac{M_i - M_{i+1}}{T_{i+1} - T_i} \Delta H_i \tag{4.4}$$

here, M_i and M_{i+1} are the value of magnetization at temperature T_i and T_{i+1}, respectively and ΔH_i is the change in the applied magnetic field which is taken as $100\ Oe$. We have calculated the magnetic entropy for $x = 0.4$ and 0.8 samples at different temperatures as shown in Fig. 4.31 (a,b). It is observed that $-\Delta S_M$ is increasing with the increment in magnetic field from $1 - 5T$ for both samples. We can clearly see a peak around T_B (shown in $M - T$ plots) which confirms the existence of this transition temperature. Also, this peak is almost independent of the applied field. It is very interesting to note that the maximum value of $-\Delta S_M$ is enhanced from 3.92 to $4.30\,J/kgK$ for $x = 0.4$ to 0.8 samples, respectively at an applied field of $5T$. The estimated values of $-\Delta S_M$ at different applied magnetic fields are tabulated in Table 4.5. Moreover, a change in the sign of $-\Delta S_M$ from positive to negative is also observed in both samples. This sign reversal in magnetic entropy is observed at $200K$ and $160K$ for $x = 0.4$ and 0.8 samples, respectively which are also the magnetic compensation temperature of these samples. So, we have observed both normal as well as inverse magnetocaloric effect (IMCE) in our samples. The well-known application of normal MCE is in magnetic refrigeration and IMCE is in magnetic heating [149].

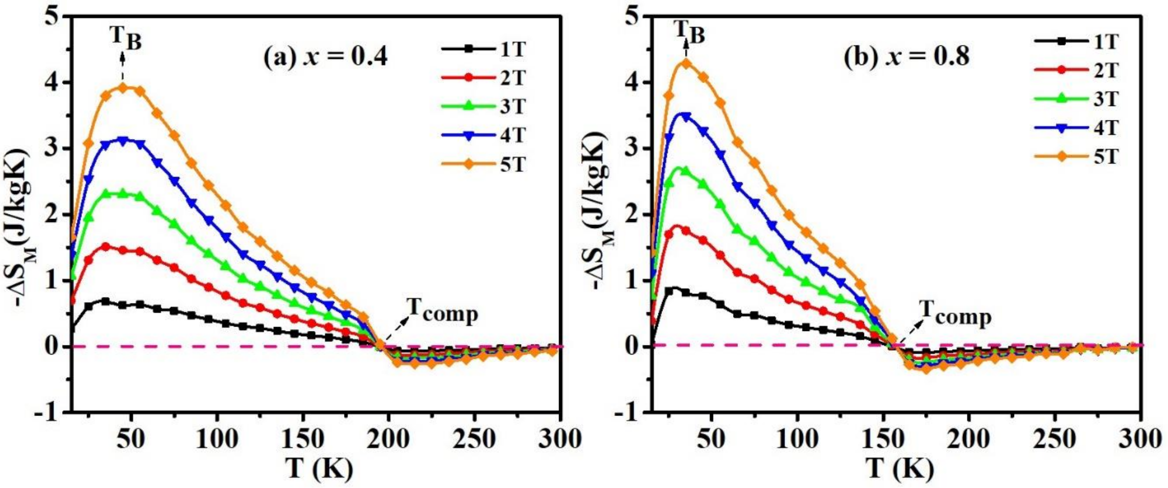

Fig. 4.31: The change in $-\Delta S_M$ with temperature $(5\ K - 300\ K)$ by varying magnetic field from $1\ T$ to $5\ T$ for (a) $x = 0.4$ and (b) $x = 0.8$ samples.

Three types of entropies are present in any magnetic material: electron entropy, lattice entropy and magnetic entropy [150]. Out of these three entropies, only magnetic entropy takes part in the magnetic refrigeration and rest of the two entropies do not contribute because they are magnetic field independent. Now, to clearly visualize the variation of magnetic entropy $(-\Delta S_M)$ with temperature, we have plotted the contour plots for $x = 0.4$ and $x = 0.8$ samples as shown in Fig. 4.32 (a,b). We can see the cone shape peak in these plots in the lower temperature region which is T_B temperature zone. As we move towards higher temperature, the sign reversal of $-\Delta S_M$ is observed at T_{comp} and this region is shown by dark yellow colour in the contour plots. According to $M - T$ data, RIG has cubic structure with collinear FIM ordering at room temperature. However, when the temperature is reduced, this cubic structure undergoes rhombohedral distortion which makes the spin of R^{3+} to be non-collinear [151]. This newly formed structure is generally named as double-umbrella structure. As we know, the entropy of ordered collinear state is lower as compared to non-collinear state resulting in the sign reversal of $-\Delta S_M$ at T_{comp} due to the spin-reorientation of R^{3+} ions.

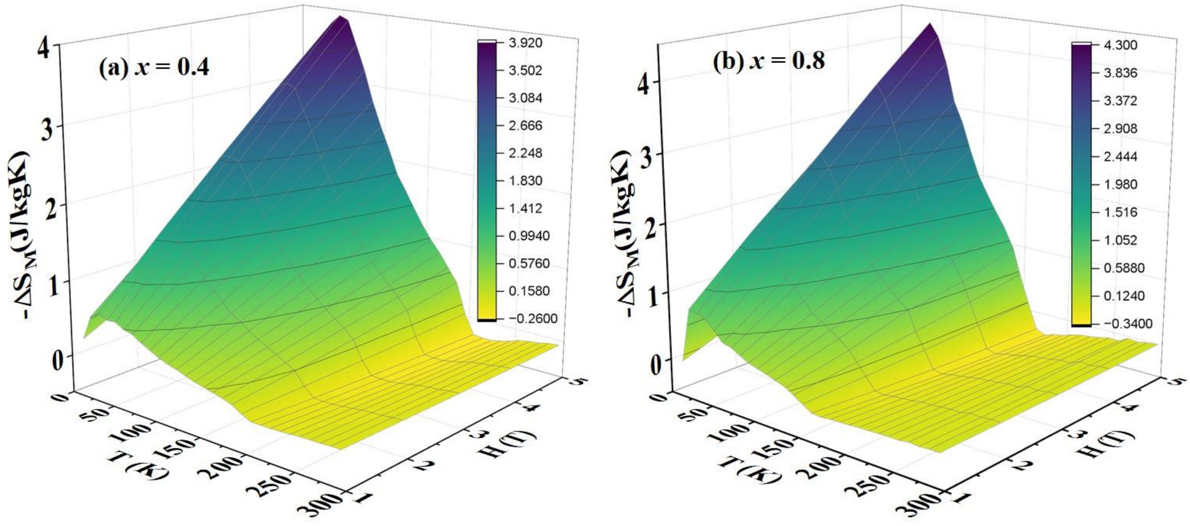

Fig. 4.32: Contour plots for $-\Delta S_M$ with temperature and magnetic field for (a) $x = 0.4$ and (b) $x = 0.8$ samples.

Relative cooling power (RCP) represents the efficiency of any magnetocaloric material for the refrigeration process and it is calculated by the following relation [36]:

$$RCP = |\Delta S_M^{max}| \times \delta T_{FWHM}$$
(4.5)

here, δT_{FWHM} is the full-width half maxima of magnetic entropy variation with temperature plot. It is obtained in the range of $60 - 90K$ for all the applied magnetic fields from $1 - 5\,T$ as listed in Table 4.5. Then RCP is calculated and is represented in Fig. 4.33. RCP is found to be in increasing trend with the increment in the applied magnetic field. The RCP values are obtained as $364.6\,J/kg$ and $313.0\,J/kg$ at $5\,T$ for $x = 0.4$ and 0.8 samples, respectively. Hence, we can say that our material is preferable for the magnetic refrigeration application, but to achieve that low temperature and high magnetic field is quite challenging. Therefore, although the material is promising, further research and development may be necessary to optimize its performance for practical magnetic refrigeration applications.

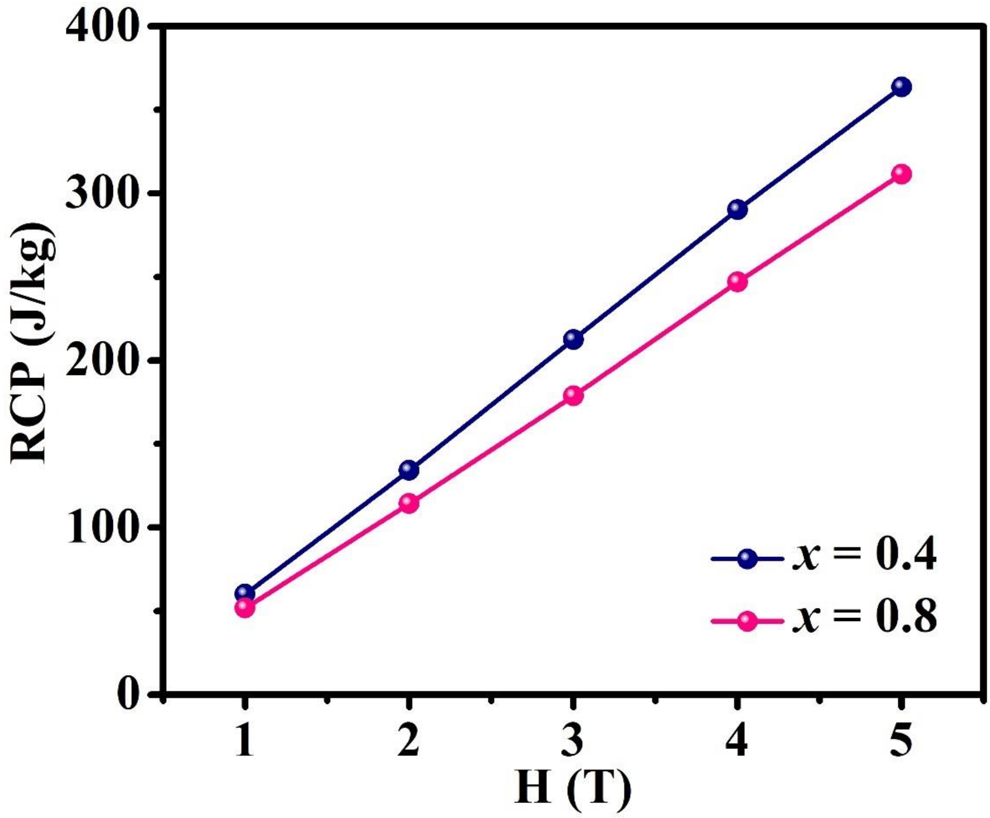

Fig. 4.33: Relative cooling power with change in magnetic field for $x = 0.4$ and 0.8 samples Ho-DyIG series.

Table 4.5: Listing the magnetocaloric parameters for $x = 0.4$ and 0.8 samples.

H (T)	$x = 0.4$			$x = 0.8$		
	$-\Delta S_{max}$ (J/kgK)	δT_{FWHM} (K)	RCP (J/kg)	$-\Delta S_{max}$ (J/kgK)	δT_{FWHM} (K)	RCP (J/kg)
1	0.68	87.95	60.1	0.83	61.67	51.7
2	1.51	88.96	134.1	1.73	65.71	114.3
3	2.31	91.99	212.5	2.63	67.72	178.8
4	3.11	93.11	290.1	3.48	70.77	246.9
5	3.92	93.01	364.6	4.30	72.79	313.0

To determine the order of magnetic transitions, we have analyzed the magnetic isotherms in the form of M^2 vs. H/M plots better known as Arrott plots as shown in Fig. 4.34 (a,b). According to Banerjee criteria [37], the slope of the Arrott plot will decide the order of magnetic transition, i.e., the negative slope of the Arrott plot stands for first-order phase transition (FOPT) whereas, the positive slope indicates the second-order phase transition (SOPT). For our case, we have observed positive slope for both the samples suggesting the presence of SOPT in our samples. Furthermore, we have estimated the magnetic entropy change with respect to magnetic field in the form of the following power law:

$$\Delta S_M^{max} \ \alpha \ H^n \tag{4.6}$$

For a magnetic system having a single transition temperature, the value of n should be close to 1 in the low-temperature region (far away from T_c), $2/3$ at critical temperature and become 2 in the paramagnetic region [38]. Additionally, as per the reported literature if $0 < n < 1$ implies SOPT and $n > 1$ represents FOPT [183,184]. So, we have calculated the maximum magnetic entropy at every field from $1 - 5\ T$ and fitted these data points to eqn. (4.6) as represented in Fig. 4.34 (c,d). After fitting, the value of n comes out to be 1.055 ± 0.014 and 0.984 ± 0.019 for $x = 0.4$ and 0.8 samples, respectively. These values are close to 1 which confirms the presence of SOPT in the samples of Ho-DyIG series.

Indian Institute of Technology Guwahati

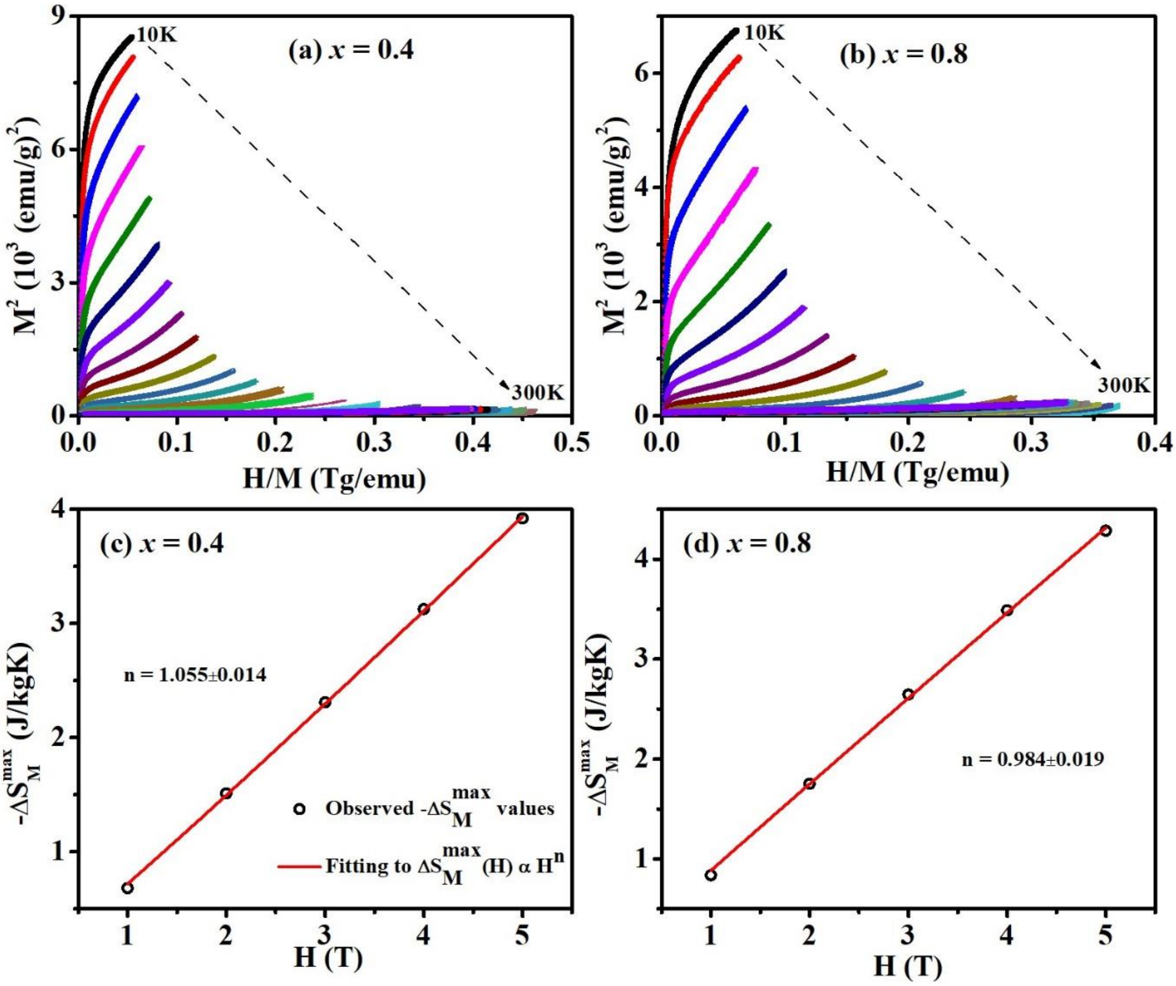

Fig. 4.34: (a,b) Arrott plots ($M^2\ vs. H/M$) from 10 K to 300 K and (c,d) variation of maximum $-\Delta S_M$ at different magnetic fields for $x = 0.4$ and 0.8 samples.

4.3 Conclusion

We have synthesized $(Sm_{1-x}Ho_x)_3Fe_5O_{12}$ $(x = 0.0 - 1.0)$ series using the conventional solid-state route and phase formation for each composition was confirmed through Rietveld refinement of XRD patterns. The lattice constant decreased from 12.5375 Å to 12.3936 Å as x increased from 0.0 to 1.0, accompanied by a reduction in bond length and bond angle among Fe ions at octahedral and tetrahedral sites due to Ho substitution. The average grain size increased from 7.47 μm to 8.56 μm with higher x values. XPS analysis confirmed the $+3$ oxidation state of the rare-earth elements and the mixed valence state of Fe existing as both $+2$ and $+3$. Room-temperature saturation magnetization declined from 19.83 emu/g $(x = 0.0)$ to 6.98 emu/g $(x = 1.0)$, while the FIM transition temperature reduced from 561 K $(x = 0.0)$ to 541 K $(x = 1.0)$. All samples exhibited a spin reorientation transition, with the transition temperature decreasing upon Ho substitution. Samples with $x \geq 0.4$ exhibited magnetic compensation and for the $x = 0.4$ composition, a negative magnetization was observed under field-cooled conditions below T_{comp} $(25\ K)$. This magnetization reversal is attributed to the magnetocrystalline anisotropy induced by Ho substitution. The complex impedance spectra were analyzed using Nyquist plots and fitted to equivalent circuits comprising resistance from grains and grain boundaries along with the capacitance due to grain boundary. The asymmetric Nyquist plots indicate a deviation from ideal Debye-type relaxation. Furthermore, the dielectric constant increased with both temperature and Ho substitution at the Sm site and the energy loss ε'' is in correspondence with Universal Dielectric Response.

Apart from this, the single-phase $(Dy_{1-x}Ho_x)_3Fe_5O_{12}$ where $x = 0.0$ to 1.0 samples were synthesized using the solid-state reaction method. A systematic decrease in lattice constant was observed ranging from 12.4181 Å for $x = 0.0$ to 12.3858 Å for $x = 1.0$. Also, the average crystallite size ranges in between $90\ nm$ to $270\ nm$ for all the samples of Ho-DyIG series. The grain size is not affected much with Ho substitution; however, a slight increment has been observed. XPS studies revealed the oxidation state of rare earth ions to be $+3$ and Fe holds mixed valanced state i.e., $+2$ and $+3$. Further, the substitution of Ho lead to a reduction in the FIM transition temperature from $555\ K$ to $545\ K$ attributed to the lowering of the superexchange interaction in the $Fe(a) - O - Fe(d)$ bond. Low-temperature magnetic studies revealed multiple transitions, including magnetic compensation, blocking temperature, and spin reorientation across all samples in the Ho-DyIG series. A notable enhancement in effective anisotropy was observed increasing from 10^4 to $10^6 erg/cc$ as the temperature decreased from room temperature to $5\ K$. The magnetocaloric effect was investigated for the $x = 0.4$ and $x = 0.8$ samples, showing an increase in magnetic entropy change $(-\Delta S_M)$ from 3.92 to 4.30 J/kgK under a maximum applied magnetic field of $5\ T$. Both normal and inverse magnetocaloric effects were identified in these samples with relative cooling power calculated as $364.6\ J/kg$ for $x = 0.4$ and $313.0\ J/kg$ for $x = 0.8$ at $5\ T$. Additionally, the Arrott plots displayed a positive slope indicating the presence of a second-order phase transition. The considerable rise in $-\Delta S_M$ and RCP value with Ho doping in DyIG highlights the potential applications in magnetic refrigeration and heating.

भारतीय प्रौद्योगिकी संस्थान गुवाहाटी • Indian Institute of Technology Guwahati •

Chapter 5

Magnetic and dielectric investigations in $(Gd_{0.2}Y_{0.2}Nd_{0.2}Dy_{0.2}R_{0.2})_3Fe_5O_{12}$ $(R = Er, Sm, \mathrm{Pr})$ high entropy garnet

High-entropy oxide ceramics stand out from traditional materials due to their diverse range of functional properties including a high dielectric constant, low thermal conductivity, electrocatalytic activity, and strong mechanical strength [76]. Among these, high-entropy garnet ferrites have gained significant attention in recent years, particularly in the field of quantum materials. For example, Liu *et al.* [77] explored the dielectric properties of the high-entropy garnet ceramics $(Y_{0.2}Eu_{0.2}Er_{0.2}Dy_{0.2}Lu_{0.2})_3(Al_xFe_{1-x})_5O_{12}$ and observed a significant reduction in the dielectric constant from 10^4 to 10^2 at $100Hz$ with Al substitution. Similarly, Dąbrowa *et al.* [78] investigated the transport properties of $(Dy, Er, Gd, Ho, Y)_3Fe_5O_{12}$ and found that electrical conductivity was minimal at lower temperatures primarily due to the presence of Fe^{3+} ions in distorted octahedral and tetrahedral sites. In another study, Chen *et al.* [79] examined the structural and magnetic properties of $(Gd_{0.2}Dy_{0.2}Er_{0.2}Y_{0.2}RE_{0.2})_3Fe_5O_{12}$ $(RE = Sm, Eu, Tm, Yb)$ garnet ferrites and found that the saturation magnetization values were around $13emu/g$. In this chapter, we focus on the synthesis and characterization of a new series of high-entropy garnet oxides, namely $(Gd_{0.2}Y_{0.2}Nd_{0.2}Dy_{0.2}R_{0.2})_3Fe_5O_{12}$ (GYNDR) $(R = Er, Sm$ and Pr).

5.1 $(Gd_{0.2}Y_{0.2}Nd_{0.2}Dy_{0.2}R_{0.2})_3Fe_5O_{12}$ with $R = Er, Sm$ and Pr high entropy garnets

The high entropy ceramics were obtained by synthesizing them from solid-state reaction method in which Gd_2O_3, Y_2O_3, Nd_2O_3, Dy_2O_3, Er_2O_3, Sm_2O_3, Pr_6O_{11} and Fe_2O_3 were weighed and grinded in acetone medium (details are provided in section 2.1). Once the powder is uniformly grinded, calcination was carried out at $800°C$ for 12 hours. The powder was then moulded into pellets and final sintering held at $1200°C$ for 24 hours. The structural, magnetic and dielectric characterizations are discussed below:

5.1.1 Structural characterization

First of all, all the samples are characterized through X-ray diffractometer and these XRD patterns are shown in Fig. 5.1. All the peaks in these plots are in good correspondence with that of pure garnet phase. The purity of this garnet phase is verified by the Rietveld refinement of the XRD patterns of $(Gd_{0.2}Y_{0.2}Nd_{0.2}Dy_{0.2}R_{0.2})_3Fe_5O_{12}$ with $R = Er, Sm$ and Pr samples as demonstrated in Fig. 5.2. All the high entropy garnet ferrites possess cubic crystal structure along with $Ia\overline{3}d$ space group. The fitting of the refined patterns is carried out by varying various parameters and goodness of fit i.e., χ^2 value which are displayed in Table 5.1. Further, we have extracted the lattice constant values and they are found to be $12.4458(2)$ Å, $12.4834(4)$ Å and $12.5062(2)$ Å for GYNDE, GYNDS and GYNDP samples, respectively. In addition, their corresponding unit cell volume is also following a similar trend as that of lattice constant. This trend for lattice constant and volume is attributed to the ionic radii order of the substituent i.e., Er^{3+} $(0.86\text{Å}) < Sm^{3+}$ $(1.07\text{Å}) < Pr^{3+}(1.13\text{Å})$. Both the lattice parameter and unit cell volume variation for different compositions are shown in Fig. 5.3. Additionally, we have estimated the densities (ρ) of the formed high entropy samples by Archimedes' principle and they are obtained as $91\%, 89\%$ and 93% of their theoretical densities for GYNDE, GYNDS and GYNDP samples, respectively. We have listed different lattice parameters and unit cell volume obtained based on the analysis of XRD data in Table 5.1.

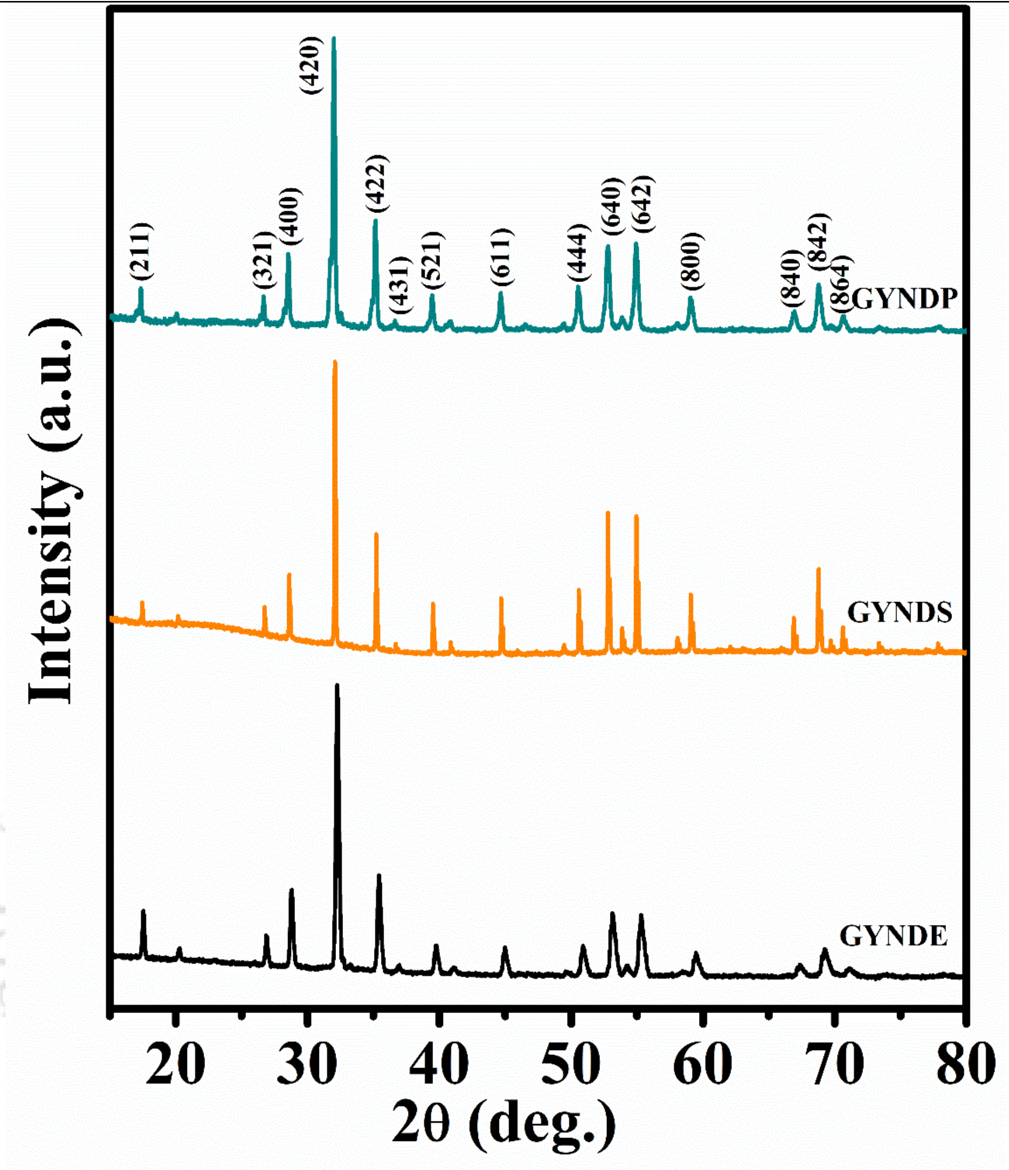

Fig. 5.1: The indexed XRD patterns of GYNDE, GYNDS and GYNDP samples at room temperature.

stitute of Technology

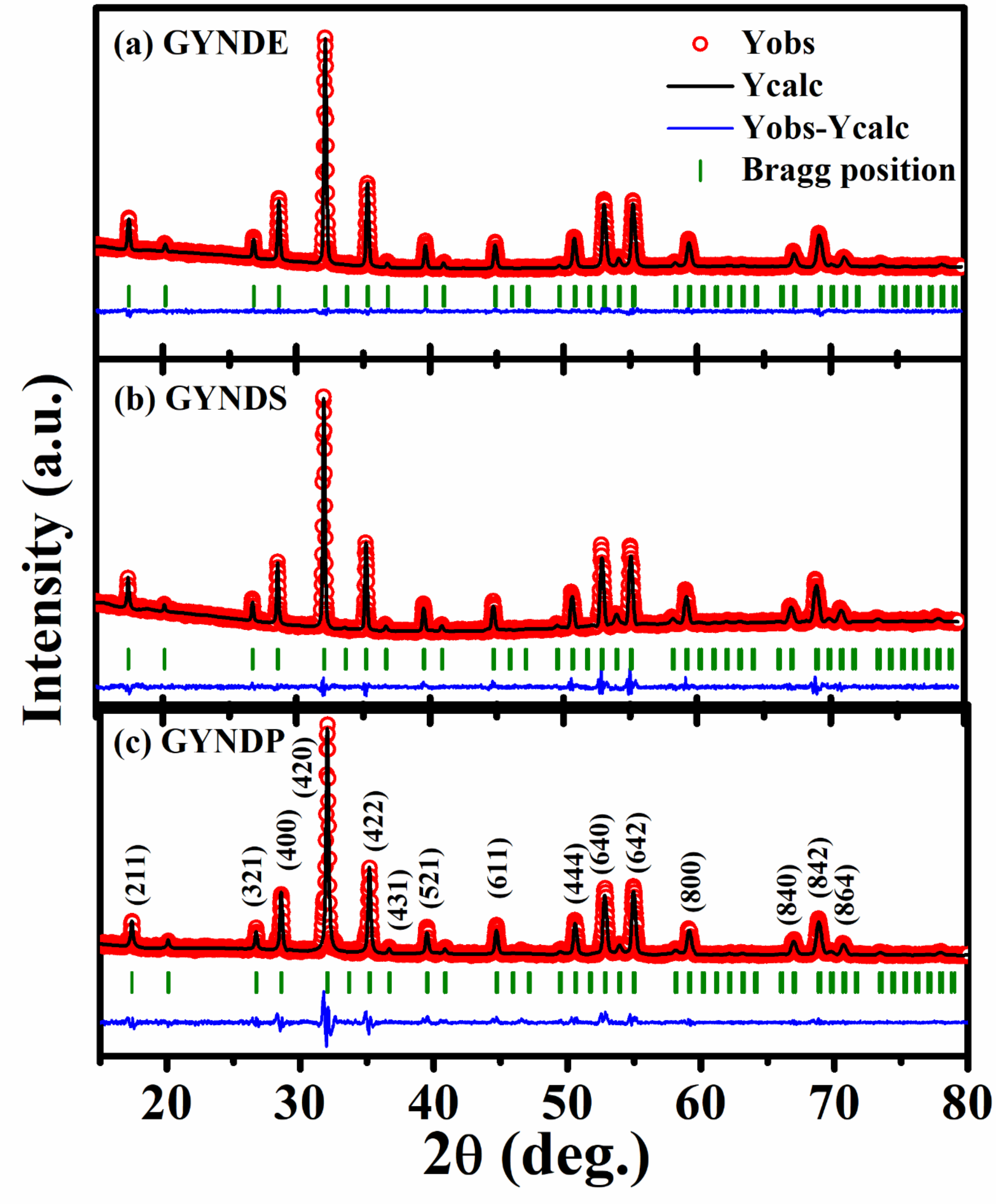

Fig. 5.2: The Rietveld refined XRD patterns for all the compositions of high entropy garnets.

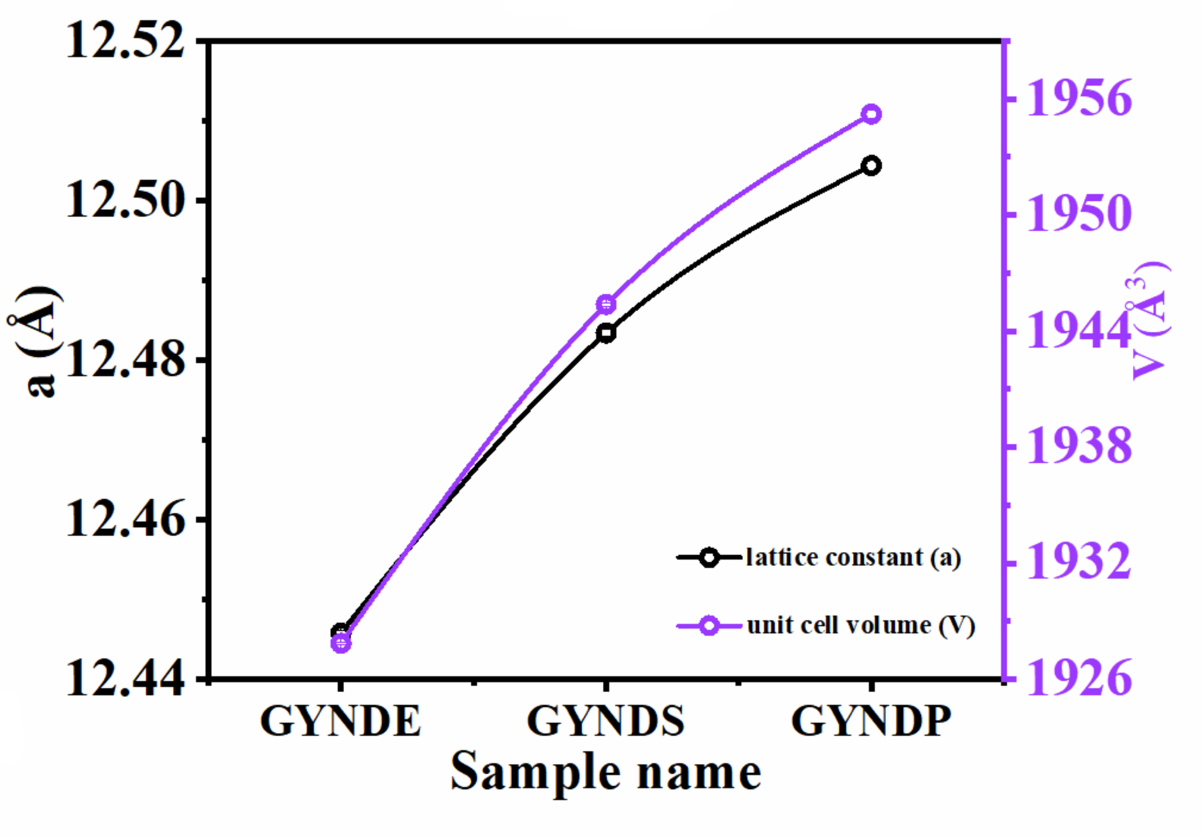

Fig. 5.3: The trend of lattice constant and unit cell volume for different $(Gd_{0.2}Y_{0.2}Nd_{0.2}Dy_{0.2}R_{0.2})_3Fe_5O_{12}$ $(R = Er, Sm$ and Pr) samples.

Table 5.1: Structural and Rietveld refinement reliability parameters for $(Gd_{0.2}Y_{0.2}Nd_{0.2}Dy_{0.2}R_{0.2})_3Fe_5O_{12}$ $(R = Er, Sm$ and Pr) samples.

Sample → Parameters ↓	GYNDE	GYNDS	GYNDP
Space group	$Ia\bar{3}d$	$Ia\bar{3}d$	$Ia\bar{3}d$
$a = b = c$ (Å)	12.4458(2)	12.4834 (4)	12.5062(2)
Volume (Å^3)	1927.8	1945.3	1956.0
R_p (%)	10.5	13.8	8.5
R_{wp} (%)	10.6	16.5	19.4
R_F (%)	15.3	9.3	9.0
R_{Bragg} (%)	3.8	5.3	8.9
χ^2	1.6	2.6	5.7

To further analyze the particle size distribution within the sample, we applied log-normal function fitting to the histograms obtained from the FESEM micrographs presented in Fig. 5.4. All the micrographs represent a uniform distribution of compactly formed grains that are separated by grain boundaries. The average grain size is calculated by fitting the distribution of particle size to log-normal function. A per the fitting, the particle size is quantified as $1.29 \pm 0.04, 1.14 \pm 0.15$ and $1.28 \pm 0.06\ \mu m$ for GYNDE, GYNDS and GYNDP samples, respectively. The average particle size is almost same for all the high entropy garnet ceramics compounds because the doping element concentration is too low to affect the grain boundary mobility. However, several other factors affect the particle size such as sintering temperature, rate of heating and duration of sintering, impurities, nucleation and growth, and many more [128].

Then, we employed FETEM analysis to investigate the distinct planes within the crystalline structure of high entropy garnet samples. Fig. 5.4 (a-c) displays the HRTEM graphs and their respective Selected Area Electron Diffraction (SAED) patterns for GYNDE, GYNDS and GYNDP samples are displayed in Fig. 5.4 (d-f). These HRTEM patterns comprise the different crystalline planes which gives us insights into the crystallinity of the samples. The interplanar spacing (d) values of GYNDE, GYNDS and GYNDP samples are estimated to be $0.26\ nm, 0.31\ nm$ and $0.29\ nm$, respectively. These values of d stand for the (420) peak of GYNDE and (400) plane for GYNDS and GYNDP samples which are consistent with XRD miller planes. Moreover, the co-centric circles are also obtained in the SAED patterns of all three samples which signify the polycrystalline behavior of the samples. The $(h\ k\ l)$ planes obtained in SAED patterns i.e., $(420), (642), (842)$ and (864) are matching with the Miller indices of XRD data. These diffracted planes correspond to a cubic structure with a body-centered Bravais lattice, thereby confirming the garnet phase and its characteristic crystallographic symmetry.

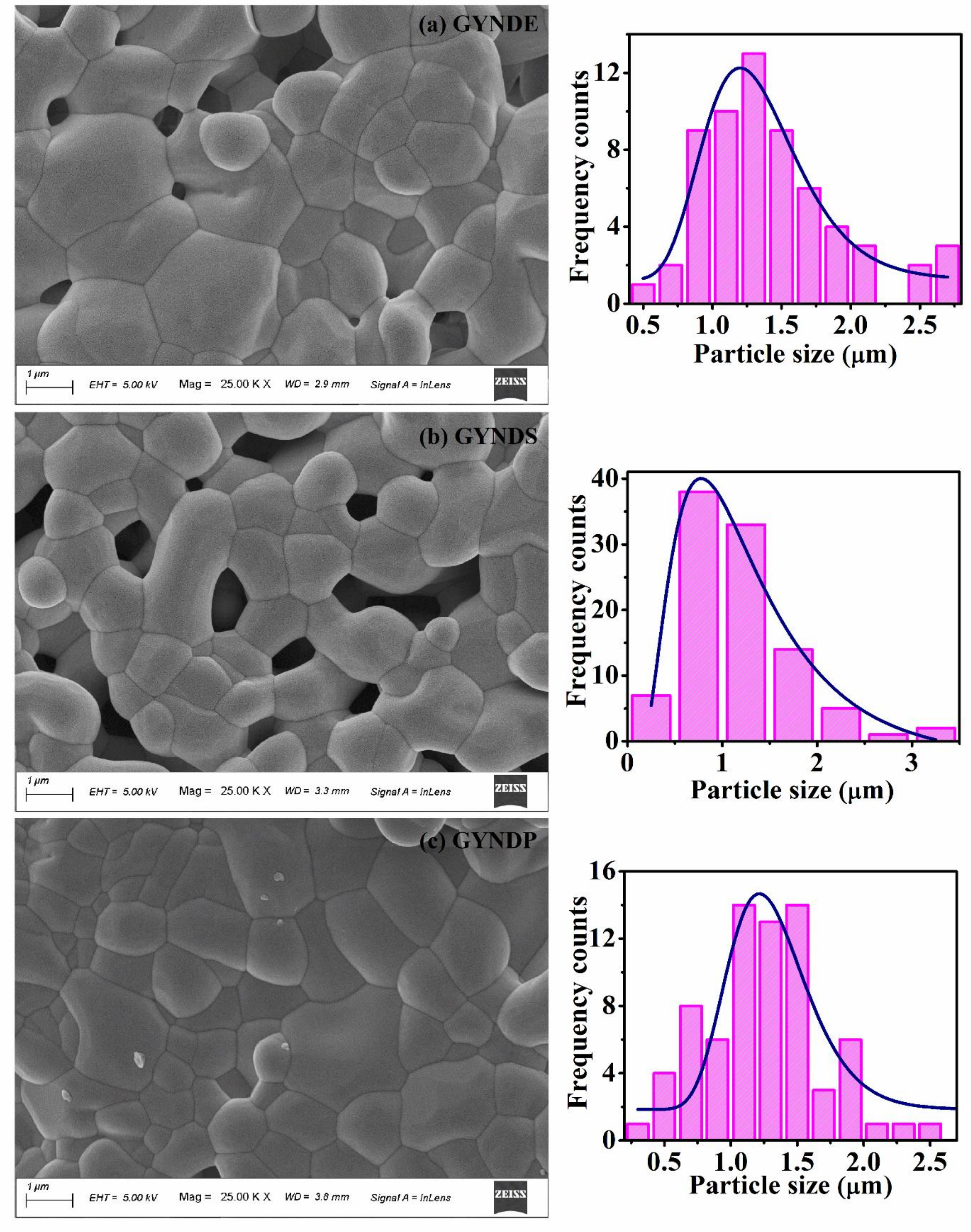

Fig. 5.4: (a-c) The FESEM micrographs and (d-f) showing their corresponding fitting of particle size distribution to log-normal function.

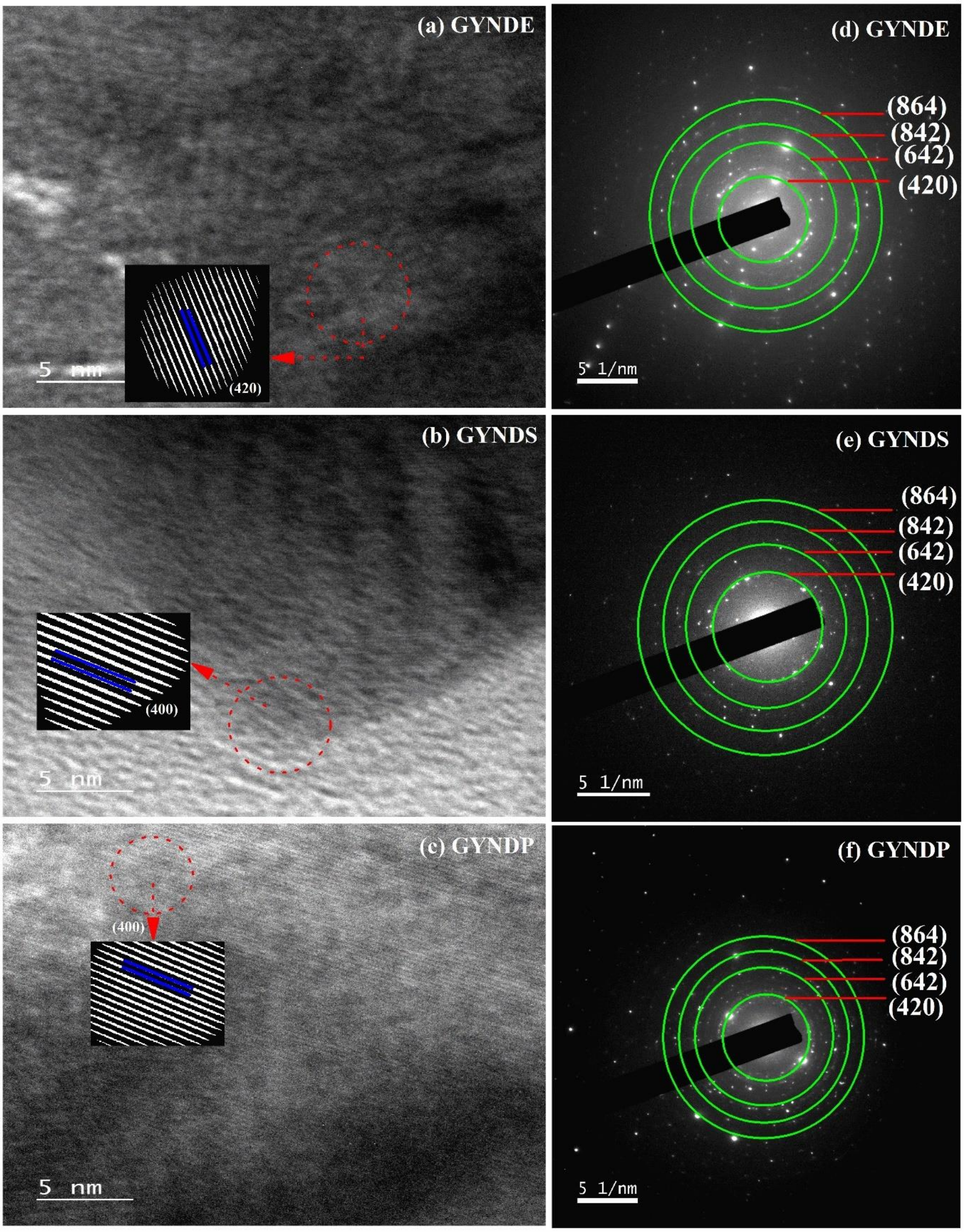

Fig. 5.5: (a-c) HRTEM images with their magnified view of planes and (d-f) the SAED images for GYNDE, GYNDS and GYNDP samples.

The elemental distribution is analyzed with the EDS area mapping of high entropy ceramics which are attached with the area maps of the individual five rare earth elements along with iron and oxygen (demonstrated in Fig. 5.6). The rare-earth elements are evenly distributed within the grains and there is no indication of element segregation based on the EDS mappings. This confirmation affirms the formation of a solid solution in the sintered samples. These findings reinforce the structural integrity and chemical uniformity of the high-entropy ceramic material.

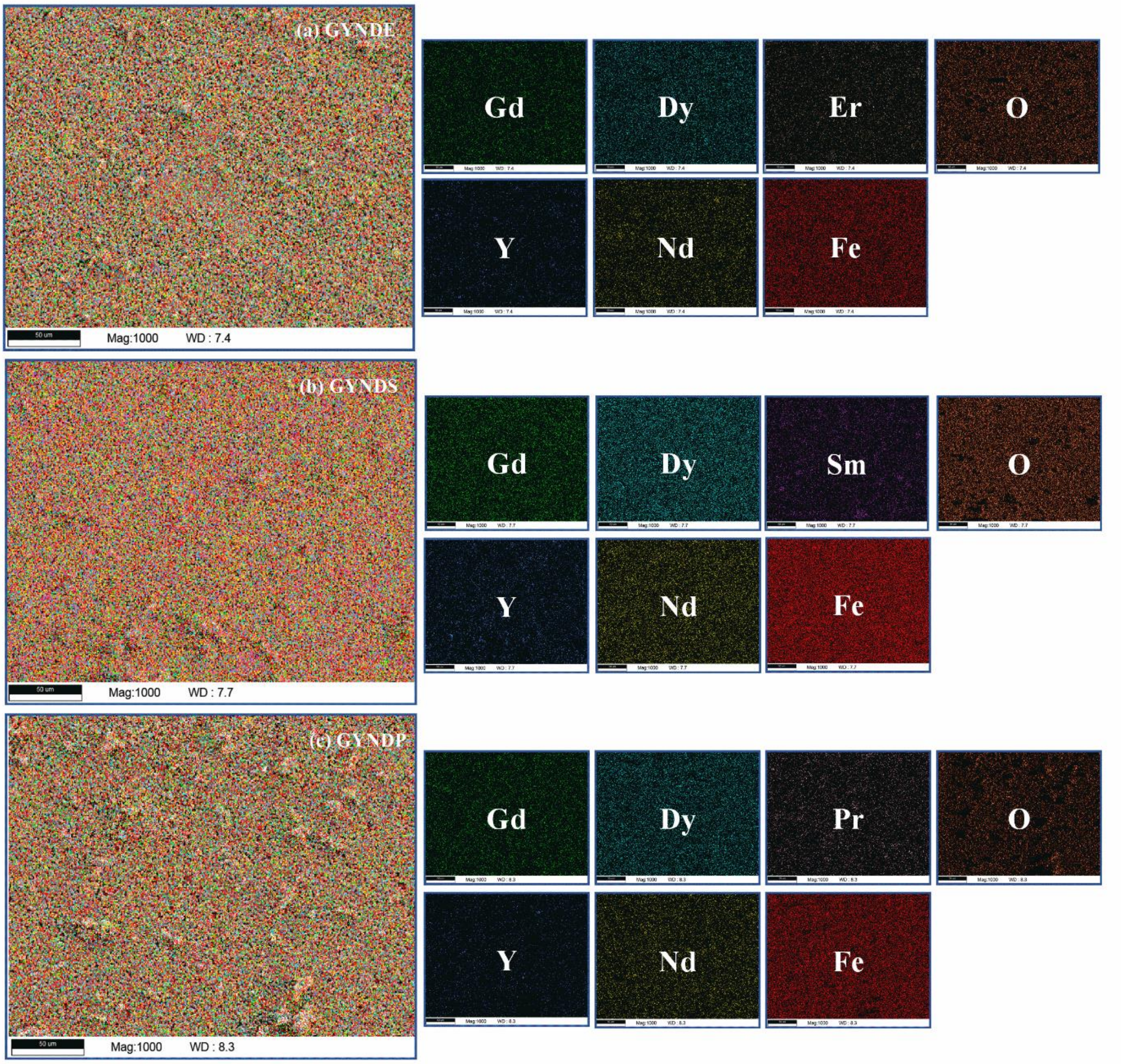

Fig. 5.6: The overall area mapping of EDS along with the area mapping of individual elements (right side) present in that particular composition.

Further, we have analyzed the Raman spectrum of all the high entropy garnet samples by fitting the peaks to the Gaussian function as represented in Fig. 5.7. The laser having an excitation wavelength of 514 nm has been used for this detection. Group theory indicates that within a RIG system, there are a total of 25 active Raman modes comprising $3A_{1g}$ internal modes, $8E_g$ translational modes and 14 F_{2g} rotatory modes [96]. Any mode observed in addition to these signifies impurities in the garnet structure. The modes below 300 cm^{-1} arise primarily due to the translation motion of different rare earth elements such as $Gd^{3+}, Y^{3+}, Nd^{3+}, Dy^{3+}, Er^{3+}, Sm^{3+}$ and Pr^{3+} at the dodecahedral site. Whereas, the modes from 300 to 800 cm^{-1} originate from the stretching and bending of $Fe - O$ bond at tetrahedral and octahedral sites [97]. Moreover, the increase in lattice constant observed from GYNDE to GYNDP suggests a decrease in the force constant, leading to a reduction in the frequency of vibration modes. This shift is referred to as a red shift in Raman spectroscopy.

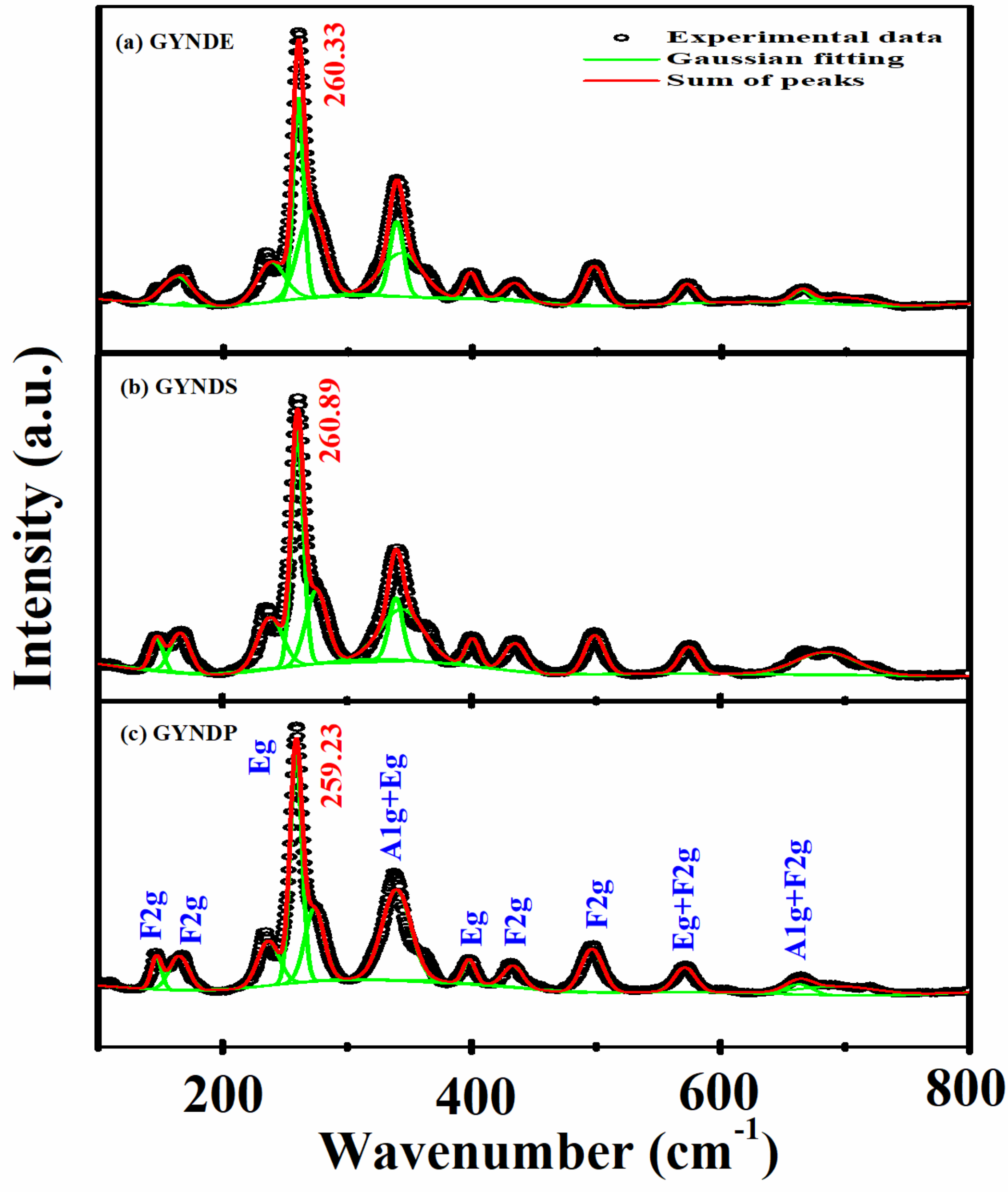

Fig. 5.7: The room temperature Raman spectrum of GYNDR (R = Er, Sm, Pr) samples with their peaks fitted to the Gaussian function.

ute of Technology

5.1.2 Magnetic characterization

The magnetic hysteresis loops for $(Gd_{0.2}Y_{0.2}Nd_{0.2}Dy_{0.2}R_{0.2})_3Fe_5O_{12}$ with $R = Er, Sm$ and Pr samples are displayed in Fig. 5.8 (a). The measurement is carried out up to $\pm 15\ kOe$ magnetic field and it is observed that all the curves show complete saturation after $\sim 5\ kOe$ magnetic field. All the synthesized garnet ceramics represent a typical ferrimagnetic nature by having very low coercivity. Further, we have utilized the LAS equation which is discussed earlier in eqn. (3.2). The fitting of LAS equation to initial $M -$

H curves are shown in Fig. 5.8 (b). The M_s value for $(Gd_{0.2}Y_{0.2}Nd_{0.2}Dy_{0.2}Er_{0.2})_3Fe_5O_{12}$ sample is obtained as 13.67 emu/g, whereas rest of the two samples exhibit comparable M_s value i.e., 16.32 emu/g for $(Gd_{0.2}Y_{0.2}Nd_{0.2}Dy_{0.2}Sm_{0.2})_3Fe_5O_{12}$ and 16.05 emu/g for $(Gd_{0.2}Y_{0.2}Nd_{0.2}Dy_{0.2}Pr_{0.2})_3Fe_5O_{12}$. The coercivity of these two samples also aligns with each other and for GYNDE it is slightly high. We have tabulated the M_s and H_c values for all the synthesized samples in Table 5.2. Along with the saturation magnetization, we have also estimated the effective anisotropy constant i.e., K_1 for all the samples which are obtained in the order of 10^5 erg/cc. These values of K_1 resemble with other garnet systems such as Bi substituted Yttrium iron garnet reported by Gouéré *et al* [152].

Table 5.2: Magnetic fitting parameters extracted from LAS equation and the coercivity of different samples of high entropy garnet ceramics at RT.

Sample	M_s (emu/g)	H_c (Oe)	K_1 $\times 10^5$ (erg/cc)
GYNDE	13.67	57.65	5.16
GYNDS	16.32	49.25	3.36
GYNDP	16.05	47.01	5.11

The magnetic structure of garnets can be comprehended with the help of Dionne's sublattice magnetization model [153]. According to this model, substituting the Y^{3+} ion in Yttrium iron garnet with a lighter rare earth element $(Sm, Ce, Nd, Pr, Eu\ La)$ is expected to result in an overall increase in molecular magnetic moment. Additionally, the magnetic moment of this lighter element aligns parallelly with the resultant moment originating from the octahedral and tetrahedral Fe^{3+} ions. In other words, we can say that the magnetic moment of d and c sublattices are in opposite directions to that of a sublattice [79]. Consequently, the net magnetic moment can be expressed as follows:

$$M_{net} = M_{Fe\,(d)} - M_{Fe\,(a)} + M_{R\,(c)} \tag{5.1}$$

On the other hand, when the Y^{3+} ions are replaced by the heavier elements such as $Gd, Y, Tb, Dy, Er, Lu, Sc$ etc., the net molecular magnetic moment should increase. Moreover, the magnetic moment of this heavier ion aligns antiparallel with the moment arising from the magnetic moment of Fe^{3+} ions at octahedral and tetrahedral sites. Therefore, the resultant magnetic moment can be expressed as follows:

$$M_{net} = M_{Fe\,(d)} - M_{Fe\,(a)} - M_{R\,(c)} \tag{5.2}$$

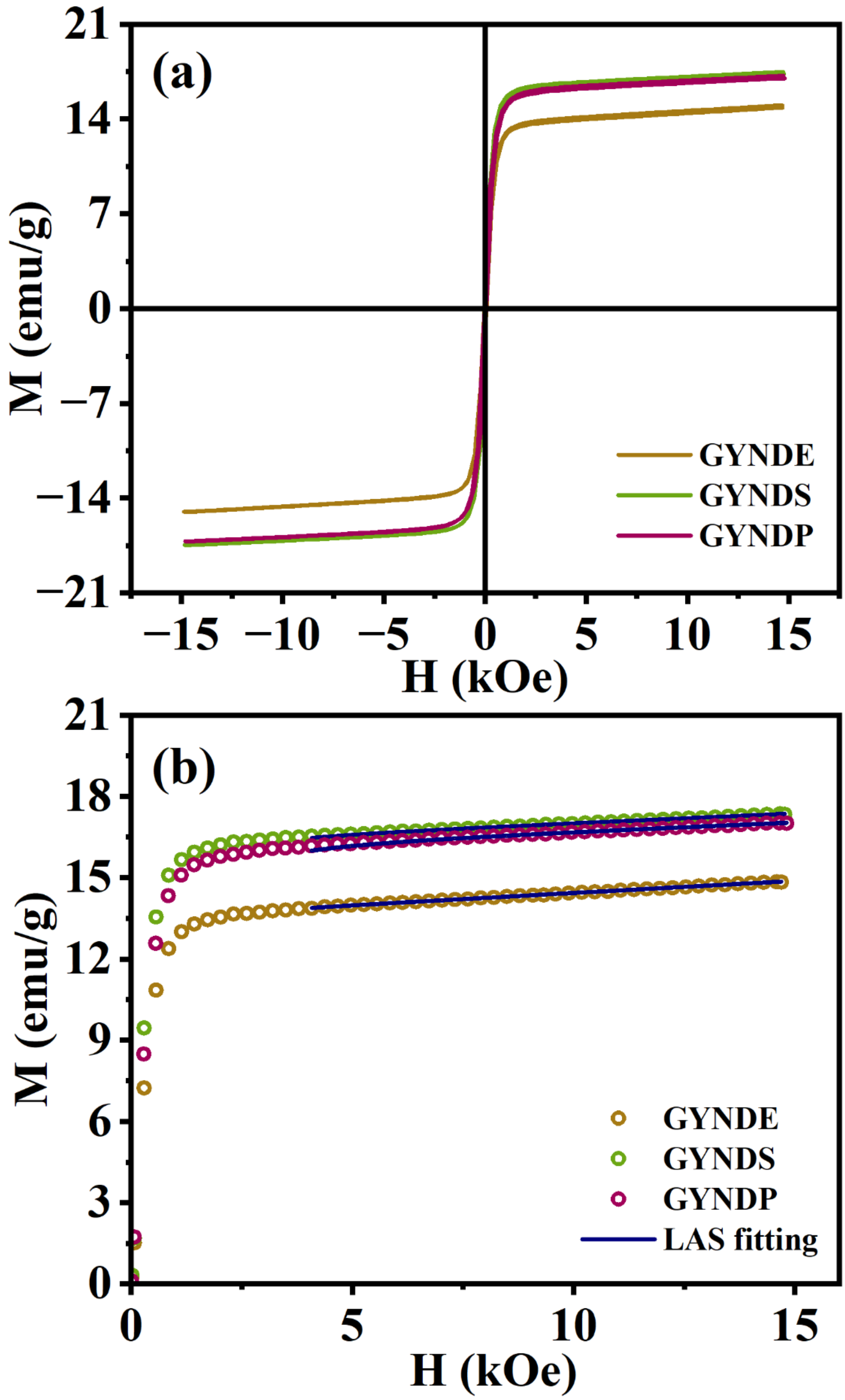

Fig. 5.8: (a) The room temperature hystersis loops and (b) fitting of initial $M - H$ curve to LAS relation for GYNDE, GYNDS and GYNDP samples.

Hence, it is clear that the magnetic moment of the GYNDE sample is governed by eqn. (5.2), where the presence of Er^{3+} ions reduces the overall moment and yields a lower net moment in comparison to the other two samples. Conversely, the magnetic moments of GYNDS and GYNDP samples are relatively higher and can be interpreted through eqn. (5.1). The magnetic moments of Sm^{3+} and Pr^{3+} ions contribute to supporting the resultant magnetic moment of Fe^{3+} ions at octahedral and tetrahedral sites, leading to a comparatively higher net magnetization. Moreover, the magnetic properties of high-entropy garnet ceramics are closely tied to lattice distortion within their crystal structure. A key factor contributing to this distortion is the superexchange interaction between Fe^{3+} ions through non-magnetic oxygen anions, which influences the macroscopic magnetic characteristics of garnet ceramics. Additionally, the ionic radii of various rare earth elements closely resemble with that of Y^{3+} ions. Substituting Y^{3+} ions with another rare earth ions at the dodecahedral site induces lattice distortion, thereby impacting both the crystal structure and magnetic moment of the material [79]. Furthermore, the magnetic arrangement of garnet involves an antiferromagnetic alignment between the Fe^{3+} ions at octahedral and tetrahedral sites. Consequently, their combined magnetic moment is also antiferromagnetically oriented with the moment of the rare earth element. At absolute zero $(0\ K)$, the iron magnetic moments within the lattice align completely in an antiparallel manner. With increasing temperature, this antiparallel alignment gradually deviates, resulting in a departure from the initial arrangement [154]. Hence, the room temperature M_s values are different from the theoretical values.

5.1.3 Dielectric characterization

The impedance of a material reflects the combined effects of resistance and reactance encountered by charge carriers as they move through intergranular and intragranular regions, and electrodes. The electrical properties of these components are analyzed using room-temperature Nyquist plots (complex impedance spectra) as shown in Fig. 5.9 (a-c). As we can see complete semicircles are not formed in the Nyquist plots which could be attributed to the absence of relaxation phenomenon at room temperature. This observation suggests that the relaxation species present are either immobile charge carriers or defects within the material. Rather, these Nyquist plots exhibit a slightly short semi-circle in the higher frequency region, originating from the contribution of the grains and a linear trend in the lower frequency regime, attributed to the effect of grain boundaries.

However, precise determination of the resistance and capacitance of both grains and grain boundaries from these plots is challenging. To address this, we have employed the $(RQ1)Q2$ equivalent circuit, as depicted in Fig. 5.9 (d (i)) to fit the Nyquist plot of the GYNDS sample. Additionally, for the other two high-entropy garnet ceramics i.e., GYNDE and GYNDP samples, an extra capacitor is introduced in parallel to this circuit which is denoted as $[(RQ1C)Q2]$ (see Fig. 5.9 (d (ii))). Here, R and C stand for the resistance and capacitance of the charge carriers, respectively. A similar type of equivalent electronic circuit is also utilized by Fu *et al.* [155] for fitting the room temperature Nyquist plots of $Li_7La_3Zr_{0.5}Nb_{0.5}Ta_{0.5}Hf_{0.5}O_{12}$ high-entropy Li–garnet ceramics. Notably, we observed depressed semicircles indicating a departure from the ideal Debye-type relaxation, where the center of the semicircles deviates from the Z' axis. This deviation from ideal Debye-type behavior can be elucidated by introducing a constant phase element (Q) with impedance $Z_Q = 1/A(j\omega)^{-n}$, where A is a constant and n represents the distribution of relaxation time. In the context of a perfect capacitor $n = 1$, while for a perfect resistor $n = 0$.

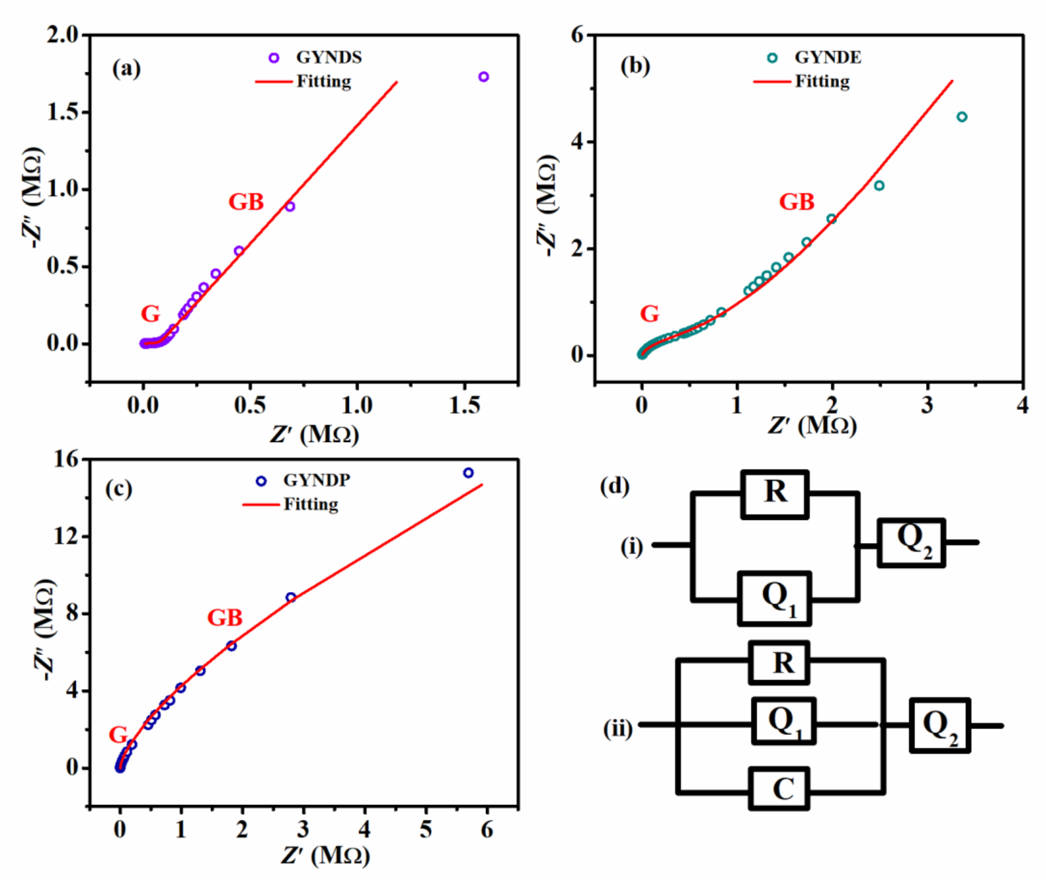

Fig. 5.9: (a-c) The Nyquist plots of GYNDS, GYNDE and GYNDP samples and (d) equivalent electronic circuits used for fitting: (i) the Nyquist plot of the GYNDS sample and (ii) the Nyquist plots of GYNDE and GYNDP samples.

The dielectric constant (ε') demonstrates the amount of electrical charges that can be stored within the material. The quantity of such an entity can be measured with the help of eqn. (3.3). In Fig. 5.10, we've depicted the change in ε' over a temperature range of $303\ K$ to $623\ K$, across various applied frequencies ranging from $15\ kHz$ to $1.0\ MHz$. The trend observed reveals a decrease in the dielectric constant with increasing frequency. This phenomenon is associated with the release of space charge polarization at higher frequencies [156]. In the lower frequency range, there is a notable accumulation of charge carriers along grain boundaries, leading to higher ε' values for all three samples. Additionally, among all the synthesized high entropy samples, the dielectric constant is highest for the GYNDP sample. This enhancement in the dielectric constant could be attributed to a reduction in oxygen vacancies. According to Kalpakli *et al.* [157], Pr exists in both Pr^{3+} and Pr^{4+} states in Pr_6O_{11}. The presence of Pr^{4+} is likely a contributing factor to the reduction in oxygen vacancies, thereby enhancing the dielectric constant of the GYNDP sample. Also, the ionization of these oxygen vacancies results in the reduction of some Fe^{3+} ions to Fe^{2+}. The released electrons then hop between Fe^{2+} and Fe^{3+} sites, contributing to the conduction mechanism within the grains. Moreover, we have observed an enhancement in ε' with temperature increment for all three high entropy garnets which is due to the thermal activation of charge carriers [158]. Interestingly, ε' versus temperature plots exhibit a broad peak and they are found to be in the vicinity of the ferrimagnetic transition temperature (T_c). Based on results in our prior chapters, the T_c for Samarium, Gadolinium, and Dysprosium ion garnets typically falls within the range of $550\ K$ to $580\ K$. Additionally, the transition temperature from the ferrimagnetic to paramagnetic region for other rare earth iron garnets is around $550\ K$. This T_c is mainly attributed to the superexchange interaction between $Fe(a) - O - Fe(d)$ networks and we are substituting at the rare earth site which does not affect the transition temperature much. Hence, it is reasonable to assume that the ferrimagnetic transition temperature T_c for the synthesized high entropy ceramics will also fall within this range. The detected broad peak in the dielectric plots around the ferrimagnetic T_c is attributed to magneto-dielectric coupling in the synthesized $(Gd_{0.2}Y_{0.2}Nd_{0.2}Dy_{0.2}R_{0.2})_3Fe_5O_{12}$ with $R = Er, Sm$ and Pr samples. This magneto-dielectric behavior is characterized by the coexistence of dielectric and magnetic properties that holds significant promise for diverse applications. This phenomenon opens avenues for advancements in memory devices, sensors, spintronics, tunable microwave devices, energy harvesting, logic devices, medical imaging, and other technologies where the coupling of these properties can be harnessed for enhanced functionality and performance [30,192-194].

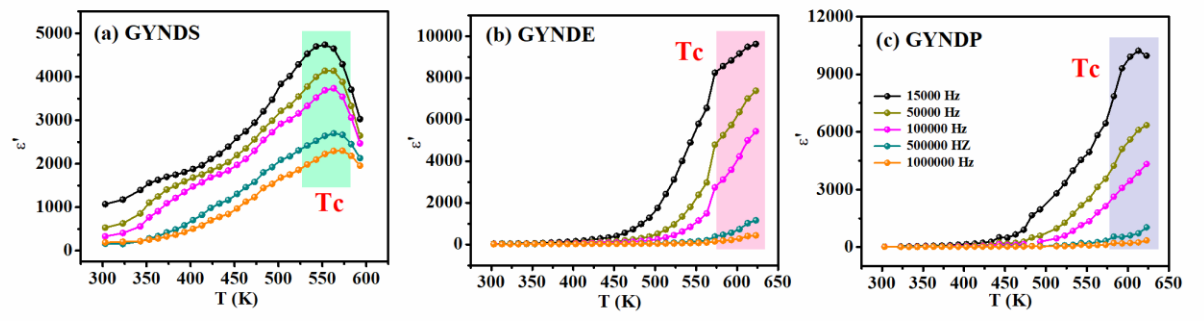

Fig. 5.10: The temperature dependant dielectric constant by varying the frequency from $15000\ Hz$ to $1000000\ Hz$ for GYNDS, GYNDE and GYNDP samples.

5.2 Conclusion

High-entropy garnet ceramics of the composition $(Gd_{0.2}Y_{0.2}Nd_{0.2}Dy_{0.2}R_{0.2})_3Fe_5O_{12}$ where $R = Er, Sm$ and Pr were successfully synthesized using the solid-state reaction method. The samples exhibited a single-phase garnet structure with a uniform cubic symmetry corresponding to the $Ia\bar{3}d$ space group. The lattice parameters varied between 12.4458 Å and 12.5062 Å, showing a consistent correlation with the ionic radii of the substituent elements. Grain size analysis indicated no significant differences among the samples with an average size of approximately $1\ \mu m$ across all compositions. TEM analysis unfolds the possible diffracted planes which resembles well with the XRD Miller indices hence confirms the formation of single phase and cubic crystal structure. Magnetic characterization revealed saturation magnetization values of $13.67, 16.32,$ and $16.05\ emu/g$ for the GYNDE, GYNDS, and GYNDP samples, respectively and the observed trend was explained using Dionne's model. Impedance analysis based on Nyquist plots were fitted to equivalent electronic circuits that highlighted deviations from ideal Debye relaxation behavior as the plot centre's did not coincide with the Z' axis. Additionally, dielectric studies revealed broad peaks near the ferrimagnetic Curie temperature, suggesting magneto-electric coupling in these materials. This combination of magnetic and dielectric properties makes these high-entropy garnet ceramics highly promising for diverse technological applications, including memory storage devices, sensors, spintronics, tunable microwave components, energy harvesters, logic circuits, and medical imaging systems. These findings open new possibilities for advancing next-generation multifunctional materials and devices.

भारतीय प्रौद्योगिकी संस्थान गुवाहाटी • Indian Institute of Technology Guwahati •

Chapter 6

Conclusions

The substitution plays a crucial role in modifying the physical properties and driving the way for technological advancements. This chapter summarizes the structural, magnetic, and dielectric characterizations influenced by the substitution of Ho and Nd at the rare-earth sites in Gd iron garnet. It also explores the effect of Ho substitution in Sm and Dy iron garnets. Additionally, these properties are studied in high-entropy garnet ceramics.

We successfully synthesized $\boldsymbol{(Gd_{1-x}Ho_x)_3Fe_5O_{12}}$ $\boldsymbol{(x = 0.0 - 1.0)}$ **(Ho-GdIG)** samples using the solid-state reaction method and confirmed the formation of the garnet phase through Rietveld refinement performed with FullProf software. The lattice constants systematically decreased with increasing Ho content ranging from 12.4841 Å for $x = 0.0$ to 12.3871 Å for $x = 1.0$, reflecting structural contraction caused by the smaller ionic radius of Ho compared to Gd. This decrease is also accompanied by distortion in bond lengths and bond angles at $Fe(a)$ and $Fe(d)$ sites with Ho substitution. The FESEM micrographs revealed microstructural changes with an increase in the volume density of grain boundaries as Ho doping increased. The average grain size has reduced from $4.88\ \mu m$ $(x = 0.0)$ to $2.59\ \mu m$ for the maximum doped sample. Raman spectroscopy confirmed that the phonon modes were associated with the translational motion of rare-earth elements and the stretching and bending vibrations of the $Fe - O$ network. The XPS analysis verified the Gd^{3+} oxidation state and the coexistence of Fe^{2+} and Fe^{3+} ions suggesting mixed-valence states that influence the electronic properties of the material.

Magnetic measurements showed a typical ferrimagnetic transition for all compositions with the transition temperature (T_c) decreasing from $553\ K$ $(x = 0.0)$ to $543\ K$ $(x = 1.0)$ which can be attributed to the dilution of magnetic interactions $(Fe(a) - O - Fe(d))$ with increasing Ho substitution. Remarkably, magnetic compensation was observed across all compositions of Ho-GdIG series where the net magnetic moment was nullified by the complete cancellation of contributions from all magnetic sublattices. The hysteresis loop measurements at both room temperature and $5\ K$

revealed notable enhancements in coercivity and the magnetocrystalline anisotropy constant while moving from 300 K to 5 K, that shows the potential of these materials for magnetic storage applications.

Electrical characterizations further elucidated the impact of Ho substitution. The $-Z''$ plots consist of a relaxation peak that shifts to higher frequency side with temperature due to thermal activation of charge carriers. Nyquist plots displayed depressed semicircles indicating deviations from ideal Debye relaxation behavior. These plots were analyzed by fitting them to equivalent electronic circuits. For $T < 523\ K$, the plots revealed contributions solely from grain boundaries and electrode effects. However, at temperatures of 523 K and above, the grains contribution was also included in the analysis. The dielectric constant showed a distinct plateau at low frequencies followed by a gradual decrease at higher frequencies which is consistent with the Maxwell-Wagner relaxation. The ε' value dropped from the order of 10^5 to 10^4 in the lower frequency region ($\sim 100\ Hz$) with Ho substitution because of the reduction in oxygen vacancies. Further, a slight reduction in ac conductivity with increasing Ho content suggested a decrease in charge carrier concentration that enhances the insulating nature of the material. Notably, anomalies in the Arrhenius plots near the magnetic transition temperature indicated the presence of magneto-dielectric coupling in all Ho-GdIG samples.

In addition to Ho substitution in GdIG, we also synthesized $\boldsymbol{(Gd_{1-x}Nd_x)_3Fe_5O_{12}\ (x = 0.0 - 0.4)}$ **(Nd-GdIG)** ceramic samples using the same solid-state reaction method. Rietveld refinement of the XRD patterns confirmed the formation of a pure garnet phase with a cubic crystal structure and space group $Ia\bar{3}d$ which remained stable across the temperature range of 80 K to 300 K. We have noticed an increment in lattice constant with temperature due to more rigorous vibrations generated with thermal energy that leads to lattice expansion. Also, the lattice parameter systematically increased from 12.4961 Å ($x = 0.0$) to 12.5496 Å ($x = 0.4$) that can be attributed to the larger ionic radius of Nd^{3+} ions as compared to Gd^{3+}. The occupancies of all the cations obtained after refinement are in good comparison with their initial starting compositions. Moreover, the average grain size of Nd-GdIG samples has increased from 1.77 μm ($x = 0.0$) to 2.72 ($x = 0.4$). Raman spectroscopy provided additional insights into lattice dynamics, showing shifts in phonon modes associated with the $Fe - O$ network.

Further, the magnetic measurements revealed two distinct transitions: a spin reorientation transition observed in all samples and a magnetic compensation phenomenon which is present only up to $x = 0.2$ concentration. The spin reorientation transition occurs due to the ordering of rare earth ions in the low temperature region that influences the generated effective field of individual cations. When this effective field overcomes the anisotropy of the Fe^{3+} ions, spin reorientation arises. Further, the magnetic compensation temperature (T_{comp}) gets shifted from 291 K to 200 K as Nd content increased because of the lower magnetic moment of Nd^{3+} compared to Gd^{3+} ions. The saturation magnetization exhibited a substantial increased value at 5 K as compared to room temperature values and it is accompanied by a significant enhancement in magnetic anisotropy from the order of 10^5 erg/cc to 10^6 erg/cc.

The dielectric studies revealed that the dielectric constant increased with temperature which is driven by thermally activated charge carriers enhancing polarization. Notably, dielectric loss anomalies were strongly correlated with all the magnetic transitions, suggesting the presence of magneto-dielectric coupling. This coupling was further substantiated by consistent findings from isothermal magneto-dielectric measurements and magnetic hysteresis curves, underscoring the strong interplay between magnetic and dielectric properties in Nd-doped GdIG garnets. This type of multifunctional properties makes the Nd-GdIG series useful in various technological applications such as antenna miniaturization, EMI shielding, RF devices, energy harvesting, metamaterials, high-frequency transformers, and wireless power transfer to enhance efficiency and performance.

We have prepared the $\boldsymbol{(Sm_{1-x}Ho_x)_3Fe_5O_{12}}$ $\boldsymbol{(x = 0.0 - 1.0)}$ **(Ho-SmIG)** series using the conventional solid-state route and phase formation for each composition was confirmed through Rietveld refinement of XRD patterns. The lattice constant decreased systematically from 12.5375 Å ($x = 0.0$) to 12.3936 Å ($x = 1.0$) that can be attributed to the smaller ionic radius of Ho compared to Sm. This was accompanied by a reduction in bond length and bond angle among Fe^{3+} ions at octahedral and tetrahedral sites with Ho substitution. The average grain size showed a notable increase from 7.47 μm to 8.56 μm with higher x values, reflecting the impact of Ho incorporation on microstructural evolution. Further, the Raman spectra revealed the presence of different translation, vibrational and rotatory phonon active modes belonging to the garnet system which parallelly confirms the formation of pure garnet phase. XPS analysis confirmed the $+3$ oxidation state of the rare-earth elements and revealed the mixed valence state of Fe, i.e., in both $+2$ and $+3$ states.

The magnetic characterization demonstrated a reduction in the ferrimagnetic transition temperature from $561\ K$ to $541\ K$ as x increased and it can be linked to the lowering of bond angle among $Fe(a) - O - Fe(d)$ site. All the samples exhibited a spin reorientation transition with the transition temperature systematically decreasing with Ho substitution. An additional magnetic transition is observed around $25\ K$ in the parent and $x = 0.2$ samples. However, this transition shifts to lower temperatures for higher Ho substitutions, moving beyond the measured temperature range for the rest of the samples. We have noticed a magnetic compensation for samples with $x \geq 0.4$ compositions. Interestingly, the $x = 0.4$ composition exhibited a negative magnetization under field-cooled conditions below T_{comp} $(25\ K)$. This magnetization reversal is attributed to the magnetocrystalline anisotropy introduced by Ho substitution. The obtained mirror image of magnetization by applying $\pm 500\ Oe$ field verifies that the negative magnetization is an inherent property of $x = 0.4$ sample. Moreover, the room-temperature saturation magnetization decreased significantly from $19.83\ emu/g$ $(x = 0.0)$ to $6.98\ emu/g$ $(x = 1.0)$ because of the large magnetic moment of Ho^{3+} $(10.6\ \mu B)$ compared to Sm^{3+} $(0.71\ \mu B)$ ions.

The impedance spectra (Z'') consist of relaxation peak at particular frequency that arises due to the grain boundaries contribution. Further, the complex impedance spectra were analyzed using Nyquist plots which were fitted to equivalent circuits comprising resistances from grains and grain boundaries along with capacitance contributions from grain boundaries. Also, the electrode effects are considered for the fitting of equivalent circuits. The asymmetric nature of the Nyquist plots indicates a deviation from ideal Debye-type relaxation behavior. Furthermore, the dielectric constant increased with both temperature and Ho substitution at the Sm site, demonstrating enhanced polarizability. The dielectric constant improves from 10^1 $(x = 0.0)$ to 10^3 $(x = 1.0)$ at $10^5\ Hz$ frequency due to the presence of Maxwell Wagener type relaxation. Additionally, the energy loss factor ε'' followed the Universal Dielectric Response model providing insights into charge transport and relaxation dynamics.

The single-phase $(Dy_{1-x}Ho_x)_3Fe_5O_{12}$ $(x = 0.0 - 1.0)$ **(Ho-DyIG)** samples were successfully synthesized using the solid-state reaction method. The phase purity was tested with Rietveld refinement of room temperature XRD patterns. A continuous decrease in the lattice constant was observed that ranges from 12.4181 Å at $x = 0.0$ to 12.3858 Å at $x = 1.0$. This reduction in lattice constant is attributed to the substitution of Ho^{3+} ions with smaller ionic radii than that of Dy^{3+} ions. Additionally, average crystallite size lies in the range of $90\,nm$ to $270\,nm$ and strain remains in the order of 10^{-4} for all the compositions of Ho-DyIG series. The estimated grain size from the FESEM images was not showing significant change in the size of the grains with Ho substitution which is accompanied by EDX spectrum showing comparable compositions of cations to the expected one. XPS results confirms the $+3$ oxidation states of rare earth components, while mixed valance state of $+2$ and $+3$ iron sublattice is observed.

The ferrimagnetic transition temperature varies from $555\,K$ $(x = 0.0)$ to $545\,K$ $(x = 1.0)$ due to the distortion in the superexchange interaction in the $Fe(a) - O - Fe(d)$ bond. Low-temperature magnetic studies revealed multiple intriguing transitions, including magnetic compensation, blocking temperature, and spin reorientation across the entire Ho-DyIG series. The blocking temperature is described as Belov transition that arises due to the paraprocess effect at low temperatures. Notably, the effective magnetic anisotropy exhibited a significant enhancement, increasing from 10^4 to $10^6 erg/cc$ as the temperature decreased from room temperature to $5\,K$. Similarly, the saturation magnetization also improved drastically by lowering the temperature from $300\,K$ to $5\,K$.

The MCE was thoroughly examined for the $x = 0.4$ and $x = 0.8$ samples, and it reveals a magnetic entropy change $(-\Delta S_M)$ of $3.92\,J/kg \cdot K$ and $4.30\,J/kg \cdot K$, respectively under a maximum applied magnetic field of $5\,T$. Both normal and inverse magnetocaloric effects were observed that highlights the versatility of these materials. The relative cooling power was calculated to be $364.6\,J/kg$ for $x = 0.4$ and $313.0\,J/kg$ for $x = 0.8$ at $5\,T$, showcasing their potential for efficient thermal management. Furthermore, the Arrott plots exhibited a positive slope which confirms the presence of a second-order phase transition. These findings underscore the potential of the synthesized Ho-DyIG samples for advanced applications in magnetic refrigeration and heating.

High-entropy garnet ceramics with the composition $(Gd_{0.2}Y_{0.2}Nd_{0.2}Dy_{0.2}R_{0.2})_3Fe_5O_{12}$ **where** $R = Er, Sm$ **and** Pr **(GYNDR)**, were successfully synthesized using the solid-state reaction method. All samples exhibited a single-phase garnet structure with uniform cubic symmetry corresponding to the $Ia\bar{3}d$ space group. The lattice parameters ranged from 12.4458 Å to 12.5062 Å which is correlated consistently with the ionic radii of the substituted elements. Grain size analysis revealed an average grain size of approximately 1 μm with no significant variation across all compositions. TEM analysis confirmed the presence of diffraction planes that closely matched the XRD Miller indices, and it further validates the formation of a single-phase, cubic crystal structure. Further, the Raman analysis confirmed the presence of only Raman active phonon bands in the GYNDR samples.

Magnetic characterization showed saturation magnetization values of 13.67, 16.32 and 16.05 emu/g for the GYNDE, GYNDS, and GYNDP samples, respectively. The observed trend was explained using Dionne's model, highlighting the role of cationic substitution in tuning the magnetic interactions. The magnetocrystalline anisotropy, determined using the LAS equation was found to be in the order of 10^5 erg/cc for all the high entropy samples. Impedance analysis using Nyquist plots indicated deviations from ideal Debye relaxation behavior, as the plot centre's did not align with the Z' axis, suggesting complex electronic transport mechanisms. Dielectric studies revealed broad peaks near the ferrimagnetic Curie temperature, indicative of magneto-electric coupling of these ceramics. These properties suggest that the materials exhibit strong interactions between magnetic and dielectric order parameters.

Future scope of studies:

The following studies can be pursued as a continuation of the previous work:

1. Investigate the phenomena of negative magnetization, bipolar switching of magnetization, and the exchange bias effect in Ho-substituted GdIG, SmIG, and DyIG thin films that hold significant potential for applications in memory storage devices.
2. Examine the impact of substituting divalent or trivalent cations at the rare earth or Fe site on magnetic and dielectric properties. Such substitutions may induce non-centrosymmetric crystal structures, potentially leading to multiferroicity.

3. Study the magneto-caloric effect in Ho-substituted SmIG or GdIG samples to explore their suitability for magnetic cooling applications.
4. Conduct investigations on magneto-electric and magneto-dielectric effects, including the influence of an electric field on polarization. These studies could pave the way for developing advanced energy storage capacitors.
5. Synthesize the above materials using alternative techniques to produce nanocrystalline forms and evaluate the effect of particle size on their magnetic and dielectric properties.
6. Utilize UV-Vis and photoluminescence (PL) spectroscopy to study the band gap and lattice distortions in the above samples, gaining insights into their structural and electronic properties.

भारतीय प्रौद्योगिकी संस्थान गुवाहाटी • Indian Institute of Technology Guwahati •

References

1. H. Shen, Y. Zhao, L. Li, Q. Li, H. Geng, Y. Li, X. Shen, J. Xu, D. Zhou, T. Tian, Y. Ma, J. Shang, and A. Wu, J. Cryst. Growth **631**, 127626 (2024).

2. D. Cruickshank, J. Eur. Ceram. Soc. **23**, 2721 (2003).

3. J. D. Adam, L. E. Davis, G. F. Dionne, E. F. Schloemann, and S. N. Stitzer, IEEE Trans. Microw. Theory Tech. **50**, 721 (2002).

4. A. Priyanshu, M. Nath, and A. Bandyopadhyay, IOP Conf. Ser. Mater. Sci. Eng. **1291**, 012028 (2023).

5. C. Song, R. Zhang, L. Liao, Y. Zhou, X. Zhou, R. Chen, Y. You, X. Chen, and F. Pan, Prog. Mater. Sci. **118**, 100761 (2021).

6. K. Matsumoto, A. Matsuzaki, K. Kamiya, and T. Numazawa, Jpn. J. Appl. Phys. **48**, 113002 (2009).

7. M. L. Néel, Ann. Phys. (Paris). **12**, 137 (1948).

8. G. Menzer and Berlin, **69**, 301 (1928).

9. S. C. Parida, S. K. Rakshit, and Z. Singh, J. Solid State Chem. **181**, 101 (2008).

10. K. E. Sickafus, C. L. Melcher, M. I. Flynn-Hepford, Y. Wang, G. Jaroslaw, J. P. Smith, S. M. Drewry, and M. Zhuravleva, J. Solid State Chem. **310**, 122997 (2022).

11. M. Lahoubi, J. Phys. Conf. Ser. **574**, 012099 (2014).

12. L. Kumar, P. Kumar, V. Kuncser, S. Greculeasa, B. Sahoo, and M. Kar, Mater. Chem. Phys. **211**, 54 (2018).

13. C. Simserides, J. A. Majewski, K. N. Trohidou, and T. Dietl, EPJ Web Conf. **75**, 4 (2014).

14. S. Blundell, *Magnetism in Condensed Matter* (2001).

15. R. Adolph, Phys. Rev. **177**, 1 (2016).

16. J. L. García-Palacios and F. J. Lázaro, Phys. Rev. B - Condens. Matter Mater. Phys. **58**, 14937 (1998).

17. I. Bertini, C. Luchinat, and G. Parigi, Prog. Nucl. Magn. Reson. Spectrosc. **40**, 249 (2002).

18. M. S. Seehra and A. Punnoose, Phys. Rev. B - Condens. Matter Mater. Phys. **64**, 4 (2001).

19. N. S. Akulov, Zeitschrift Für Phys. **57**, 249 (1929).

20. E. Schlömann, J. Appl. Phys. **33**, 2825 (1962).

21. T. I. Baskin and O. E. Jensen, J. Exp. Bot. **64**, 4697 (2013).

22. L. Néel, Phys. Chem. Earth Sci. **31**, 18 (1984).

23. K. Yoshii, J. Solid State Chem. **159**, 204 (2001).

24. E. Technique, Phys. Status Solidi **173**, 459 (1999).

25. Y. J. Hong, J. S. Kum, I. B. Shim, and C. S. Kim, IEEE Trans. Magn. **40**, 2808 (2004).

26. I. J. Park, K. U. Kang, and C. S. Kim, IEEE Trans. Magn. **42**, 2882 (2006).

27. I. J. Park and C. S. Kim, Phys. Status Solidi **244**, 4562 (2007).

28. S. Kazan, E. E. Tanrıverdi, R. Topkaya, Demirci, Akman, A. Baykal, and B. Aktaş, Arab. J. Chem. **9**, S1131 (2016).

29. V. A. Khomchenko, I. O. Troyanchuk, R. Szymczak, and H. Szymczak, J. Mater. Sci. **43**, 5662 (2008).

30. X. H. Chen, K. Q. Wang, P. H. Hor, Y. Y. Xue, and C. W. Chu, Phys. Rev. B - Condens. Matter Mater. Phys. **72**, 1 (2005).

31. T. Yamaguchi, J. Phys. Chem. Solids **35**, 479 (1974).

32. A. Boutaba, M. Lahoubi, V. Varazashvili, and S. Pu, J. Supercond. Nov. Magn. **32**, 3087 (2019).

33. R. Pal, B. Pal, S. Mondal, R. O. Sharma, T. Das, P. Mandal, and A. N. Pal, Npj 2D Mater. Appl. **8**, (2024).

34. S. Y. Bodnar, L. Šmejkal, I. Turek, T. Jungwirth, O. Gomonay, J. Sinova, A. A. Sapozhnik, H. J. Elmers, M. Klaüi, and M. Jourdan, Nat. Commun. **9**, 1 (2018).

35. L. M. Moreno-Ramírez, J. Y. Law, S. S. Pramana, A. K. Giri, and V. Franco, Results Phys. **22**, 103933 (2021).

36. R. Selmi, W. Cherif, A. R. Sarabando, N. M. Ferreira, and L. Ktari, J. Mater. Sci. Mater. Electron. **33**, 1703 (2022).

37. B. K. Banerjee, Phys. Lett. **12**, 16 (1964).

38. M. C. Silva-Santana, C. A. Dasilva, P. Barrozo, E. J. R. Plaza, L. De Los Santos Valladares, and N. O. Moreno, J. Magn. Magn. Mater. **401**, 612 (2016).

39. L. A. Melnikovsky, J. Low Temp. Phys. **148**, 559 (2007).

40. A. M. Enders and M. T. Armaly, Polit. Behav. **41**, 815 (2019).

41. C. Guo, F. Liu, S. Chen, C. Feng, and Z. Zeng, IEEE Commun. Surv. Tutorials **19**, 125 (2017).

42. V. Komarov, S. Wang, and J. Tang, Encycl. RF Microw. Eng. (2005).

43. B. Ulriksson, Proc. IEEE **74**, 74 (1986).

44. J. E. Brittain, Proc. IEEE **72**, 462 (1984).

45. B. F. García and S. Saraji, J. Colloid Interface Sci. **517**, 265 (2018).

46. L. M. Wang and R. Richert, J. Phys. Chem. B **109**, 11091 (2005).

47. M. R. Shoar Abouzari, F. Berkemeier, G. Schmitz, and D. Wilmer, Solid State Ionics **180**, 922 (2009).

48. S. Y. Wu, Q. Y. Zhou, G. Wang, L. Yang, and C. P. Ling, Environ. Earth Sci. **62**, 999 (2011).

49. J. H. Park, C. S. Kim, B. C. Choi, and K. Y. Ham, Biosens. Bioelectron. **19**, 321 (2003).

50. H. Li, Ceram. Int. **46**, 15408 (2020).

51. J. Lee, Y. K. Hong, W. Lee, G. S. Abo, J. Park, W. M. Seong, and W. K. Ahn, J. Appl. Phys. **113**, 073909 (2013).

52. S. Havriliak and S. Negami, Polymer (Guildf). **8**, 161 (1967).

53. A. El-ghandour, N. A. El-Ghamaz, M. M. El-Nahass, and H. M. Zeyada, Phys. E Low-Dimensional Syst. Nanostructures **105**, 13 (2019).

54. A. A. Lukichev, J. Non. Cryst. Solids **442**, 17 (2016).

55. B. M. Greenhoe, M. K. Hassan, J. S. Wiggins, and K. A. Mauritz, J. Polym. Sci. Part B Polym. Phys. **54**, 1918 (2016).

56. S. Geller and M. A. Gilleo, J. Phys. Chem. Solids **3**, 30 (1957).

57. M. Brahma, Aakansha, V. M. Gaikwad, and S. Ravi, Appl. Phys. A **125**, 1 (2019).

58. A. M. M. Rivera, J. E. R. López, J. Munevar, E. B. Saitovitch, L. C. M. Aldana, and C. A. P. Vargas, J. Alloys Compd. **859**, 157883 (2021).

59. S. Huang, L. R. Shi, H. G. Sun, C. L. Li, L. Chen, and S. L. Yuan, J. Alloys Compd. **674**, 341 (2016).

60. J. S. McCloy and B. Walsh, IEEE Trans. Magn. **49**, 4253 (2013).

61. D. T. T. Nguyet, N. P. Duong, T. Satoh, L. N. Anh, and T. D. Hien, J. Magn. Magn. Mater. **332**, 180 (2013).

62. K. Jawahar and R. N. P. Choudhary, Mater. Lett. **62**, 911 (2008).

63. R. Pauthenet, J. Appl. Phys. **29**, 253 (1958).

64. A. Rajan, S. L. Das, K. S. Sibi, and G. Subodh, J. Electron. Mater. **48**, 1133 (2019).

65. M. R. Khalifeh, H. Shokrollahi, S. M. Arab, and H. Yang, Mater. Chem. Phys. **247**, 122838 (2020).

66. M. A. Ahmed, S. T. Bishay, and S. I. El-Dek, Mater. Chem. Phys. **126**, 780 (2011).

67. R. Tholkappiyan and K. Vishista, Appl. Surf. Sci. **351**, 1016 (2015).

68. M. Lahoubi, W. Younsi, M. L. Soltani, J. Voiron, and D. Schmitt, J. Phys. Conf. Ser. **150**, 3 (2009).

69. C. M. Rost, E. Sachet, T. Borman, A. Moballegh, E. C. Dickey, D. Hou, J. L. Jones, S. Curtarolo, and J. P. Maria, Nat. Commun. **6**, 8485 (2015).

70. G. H. J. Johnstone, M. U. González-Rivas, K. M. Taddei, R. Sutarto, G. A. Sawatzky, R. J. Green, M. Oudah, and A. M. Hallas, J. Am. Chem. Soc. **144**, 20590 (2022).

71. S. Zhou, Y. Pu, Q. Zhang, R. Shi, X. Guo, W. Wang, J. Ji, T. Wei, and T. Ouyang, Ceram. Int. **46**, 7430 (2020).

72. L. Spiridigliozzi, C. Ferone, R. Cioffi, and G. Dell'Agli, Acta Mater. **202**, 181 (2021).

73. Z. Teng, L. Zhu, Y. Tan, S. Zeng, Y. Xia, Y. Wang, and H. Zhang, J. Eur. Ceram. Soc. **40**, 1639 (2020).

74. D. A. Vinnik, E. A. Trofimov, V. E. Zhivulin, O. V. Zaitseva, D. A. Zherebtsov, A. Y. Starikov, D. P. Sherstyuk, S. A. Gudkova, and S. V. Taskaev, Ceram. Int. **46**, 9656 (2020).

75. N. Hirosaki, S. Ogata, and C. Kocer, J. Alloys Compd. **351**, 31 (2003).

76. D. Bérardan, S. Franger, A. K. Meena, and N. Dragoe, J. Mater. Chem. A **4**, 9536 (2016).

77. H. Liu, A. Bao, J. Zhang, Y. Gu, X. Zhang, and X. Qi, Ceram. Int. **49**, 7208 (2023).

78. J. Dąbrowa, J. Cieślak, M. Zajusz, M. Moździerz, K. Berent, A. Mikuła, A. Stępień, and K. Świerczek, J. Eur. Ceram. Soc. **41**, 3844 (2021).

79. D. Chen, Y. Yang, C. Chen, Y. Meng, Y. Zhang, and C. Zhang, Ceram. Int. **49**, 9862 (2023).

80. C. J. Humphreys, Acta Crystallogr. Sect. A Found. Crystallogr. **69**, 45 (2013).

81. X. Cui, Z. Feng, Y. Jin, Y. Cao, D. Deng, H. Chu, S. Cao, C. Dong, and J. Zhang, J. Appl. Crystallogr. **48**, 1581 (2015).

82. D. E. Cox, J. Appl. Crystallogr. **27**, 440 (1994).

83. S. Hűfner, *Photoelectron Spectroscopy: Principles and Applications* (Springer Berlin Heidelberg, 2003).

84. S. Foner, Rev. Sci. Instrum. **30**, 548 (1959).

85. C. Li, G. O. Barasa, Y. Qiu, and S. Yuan, J. Alloys Compd. **820**, 153138 (2020).

86. Aakansha and S. Ravi, Mater. Res. Express **6**, 126113 (2019).

87. P. Ilanchezhiyan, G. Mohan Kumar, C. Siva, A. Madhan Kumar, S. U. Yuldashev, Y. H. Kwon, and T. W. Kang, CrystEngComm **20**, 2806 (2018).

88. M. Deb, P. Molho, and B. Barbara, Phys. Rev. B **105**, 014432 (2022).

89. Aakansha and S. Ravi, Appl. Phys. A Mater. Sci. Process. **125**, 1 (2019).

90. P. B. A. Fechine, F. M. M. Pereira, M. R. P. Santos, F. P. Filho, A. S. de Menezes, R. S. de Oliveira, J. C. Góes, L. P. Cardoso, and A. S. B. Sombra, J. Phys. Chem. Solids **70**, 804 (2009).

91. S. S. Aplesnin, A. N. Masyugin, M. N. Sitnikov, and T. Ishibashi, JETP Lett. **110**, 223 (2019).

92. M. Kumar, S. Shankar, G. D. Dwivedi, A. Anshul, O. P. Thakur, and A. K. Ghosh, Appl. Phys. Lett. **106**, 072903 (2015).

93. P. Manimuthu, R. Vidya, P. Ravindran, H. Fjellvåg, and C. Venkateswaran, Phys. Chem. Chem. Phys. **17**, 17688 (2015).

94. N. Aparnadevi, K. Saravana Kumar, M. Manikandan, B. Santhosh Kumar, J. Stella Punitha, and C. Venkateswaran, J. Mater. Sci. Mater. Electron. **31**, 2081 (2020).

95. E.A. Odo, Nanosci. Nanotechnol. Lett. Nanotechnol **5**, 57 (2015).

96. K. Rohith Vinod, N. K. Mathew, G. Theertharaman, R. Radha, K. Sethupathi, P. Saravanan, and S. Balakumar, Mater. Sci. Eng. B Solid-State Mater. Adv. Technol. **276**, 115521 (2022).

97. E. J. J. Mallmann, A. S. B. Sombra, J. C. Goes, and P. B. A. Fechine, Solid State Phenom. **202**, 65 (2013).

98. E. C. Devi and I. Soibam, J. Alloys Compd. **772**, 920 (2019).

99. B. A. Calhoun and M. J. Freiser, J. Appl. Phys. **34**, 1140 (1963).

100. S. Huang, K. P. Su, H. O. Wang, S. L. Yuan, and D. X. Huo, Mater. Chem. Phys. **197**, 11 (2017).

101. B. Deka, S. Ravi, A. Perumal, and D. Pamu, Ceram. Int. **43**, 1323 (2017).

102. Y. J. Siao and X. Qi, J. Alloys Compd. **691**, 672 (2017).

103. M. Kamran and M. Anis-ur-Rehman, Mater. Sci. Semicond. Process. **153**, 107111 (2023).

104. Y. J. Wu, Y. Gao, and X. M. Chen, Appl. Phys. Lett. **91**, 092912 (2007).

105. M. A. Elkestawy, J. Alloys Compd. **492**, 616 (2010).

106. R. C. Pullar, S. J. Penn, X. Wang, I. M. Reaney, and N. M. N. Alford, J. Eur. Ceram. Soc. **29**, 419 (2009).

107. A. S. Nowick and B. S. Lim, J. Non. Cryst. Solids **172–174**, 1389 (1994).

108. R. Gangopadhyay, A. De, and S. Das, J. Appl. Phys. **87**, 2363 (2000).

109. J. G. Paik, M. J. Lee, and S. H. Hyun, Thermochim. Acta **425**, 131 (2005).

110. J. Wu and J. Wang, J. Am. Ceram. Soc. **93**, 2795 (2010).

111. V. Sharma and B. K. Kuanr, J. Alloys Compd. **748**, 591 (2018).

112. A. Verma, A. K. Yadav, S. Kumar, V. Srihari, P. Rajput, V. R. Reddy, R. Jangir, H. K. Poshwal, S. W. Liu, S. Biring, and S. Sen, J. Appl. Phys. **123**, 224101 (2018).

113. M. M. M. Guillot, D. Rodic, J. Appl. Phys. **73**, 210502 (1993).

114. H. Liu, L. Yuan, S. Wang, H. Fang, Y. Zhang, C. Hou, and S. Feng, J. Mater. Chem.

C **4**, 10529 (2016).

115. C. Li, Y. Qiu, G. O. Barasa, and S. Yuan, Ceram. Int. **46**, 18758 (2020).

116. D. Thi, T. Nguyet, N. Phuc, T. Satoh, L. Ngoc, and T. Duc, J. Magn. Magn. Mater. **332**, 180 (2013).

117. M. Kuila, Z. Hussain, and V. R. Reddy, J. Magn. Magn. Mater. **473**, 458 (2019).

118. R. D. R. Kahmei, S. Arackal, S. A. Shivashankar, N. Bhat, and R. Sai, AIP Adv. **11**, 025003 (2021).

119. E. Suna, X. Qib, Z. Yuanb, S. Sangb, R. Zhangb, B. Yangb, Wenwu Caob, and L. Zhaoa, Ceram. Int. **42**, 4893 (2016).

120. A. Maignan, K. Singh, C. Simon, O. I. Lebedev, C. Martin, H. Tan, J. Verbeeck, and G. Van Tendeloo, J. Appl. Phys. **113**, 2 (2013).

121. V. Nekvasil, Czechoslov. J. Phys. **34**, 1052 (1984).

122. M. Malar Selvi, D. Chakraborty, and C. Venkateswaran, J. Magn. Magn. Mater. **423**, 39 (2017).

123. V. da R. Caffarena and T. Ogasawara, Mater. Res. **6**, 569 (2003).

124. A. M. M. Rivera, J. M. Araque, and C. A. P. Vargas, Mater. Res. Bull. **160**, 112127 (2023).

125. G. Wiedemann, Ann. Phys. **202**, 1 (1865).

126. N. K. Chogondahalli Muniraju, R. Baral, Y. Tian, R. Li, N. Poudel, K. Gofryk, N. Barišić, B. Kiefer, J. H. Ross, and H. S. Nair, Inorg. Chem. **59**, 15144 (2020).

127. D. Neupane, L. Hulsebosch, K. S. S. Ali, R. Bhattarai, X. Shen, A. K. Pathak, and S. R. Mishra, Materialia **21**, 101301 (2022).

128. P. L. Chen and I. W. Chen, J. Am. Ceram. Soc. **79**, 1793 (1996).

129. K. Rohith Vinod, N. K. Mathew, G. Theertharaman, R. Radha, K. Sethupathi, P. Saravanan, and S. Balakumar, Mater. Sci. Eng. B Solid-State Mater. Adv. Technol. **276**, 115521 (2022).

130. A. Sarkis and E. Callen, Phys. Rev. B **26**, 3870 (1982).

131. T. Bora and S. Ravi, Phys. B Condens. Matter **448**, 233 (2014).

132. A. Kumar and S. M. Yusuf, Phys. Rep. **556**, 1 (2015).

133. R. F. Pearson, J. Appl. Phys. **33**, 1236 (1962).

134. C. Li, T. Yan, G. Zerihun, Q. Fu, R. Zhang, X. Chen, S. Huang, and S. Yuan, J. Am. Ceram. Soc. **101**, 5571 (2018).

135. Y. Qiu, S. S. Zheng, C. L. Li, G. O. Barasa, M. L. Chen, L. Wang, Y. F. Zhao, Y. Lu, and Y. S. Luo, J. Alloys Compd. **901**, 163692 (2022).

136. H. Fu, H. R. Zhai, Y. C. Zhang, B. X. Gu, and J. Y. Li, J. Magn. Magn. Mater. **54**, 905 (1986).

137. K. P. Patra and S. Ravi, Appl. Phys. A Mater. Sci. Process. **128**, 289 (2022).

138. S. Pattanayak, B. N. Parida, P. R. Das, and R. N. P. Choudhary, Appl. Phys. A Mater. Sci. Process. **112**, 387 (2013).

139. R. N. P. Choudhary, D. K. Pradhan, C. M. Tirado, G. E. Bonilla, and R. S. Katiyar, J. Mater. Sci. **42**, 7423 (2007).

140. D. M. Hemeda, A. Tawfik, O. M. Hemeda, and S. M. Dewidar, Solid State Sci. **11**, 1350 (2009).

141. M. Stan, R. Lach, P. A. Krawczyk, W. Salamon, J. Haberko, J. Nizioł, A. Trenczek-Zając, Ł. Gondek, B. Kowalski, and A. Żywczak, Materials (Basel). **15**, 2356 (2022).

142. J. Pelleg, E. Elish, and D. Mogilyanski, Metall. Mater. Trans. A Phys. Metall. Mater. Sci. **36**, 3187 (2005).

143. R. Tholkappiyan and K. Vishista, Nanosci. Nanotechnol. Lett. **7**, 469 (2015).

144. S. Chanda, R. Maity, S. Saha, A. Dutta, and T. P. Sinha, J. Sol-Gel Sci. Technol. **99**, 600 (2021).

145. K. P. Belov, Uspekhi Fiz. Nauk **166**, 681 (1996).

146. K. . Belov, R. Z. Levitin, S. A. Nikitin, and A. V. Ped’ko, Sov. Phys. JETP **13**, 1096 (1961).

147. M. Lahoubi, W. Younsi, M. L. Soltani, J. Voiron, and D. Schmitt, J. Phys. Conf. Ser. **150**, 10 (2009).

148. J. Hu, C. Liu, M. Wang, M. Wang, S. Wang, G. Zheng, and Y. Ma, J. Solid State Chem. **314**, 123369 (2022).

149. V. K. Pecharsky and K. A. Gschneidner, J. Magn. Magn. Mater. **200**, 44 (1999).

150. A. Gschneidner, V. K. Pecharsky, and A. O. Tsokol, Reports Prog. Phys. **68**, 1479 (2005).

151. T. N. Stanislavchuk, T. D. Kang, P. D. Rogers, E. C. Standard, R. Basistyy, A. M. Kotelyanskii, G. Nita, T. Zhou, G. L. Carr, M. Kotelyanskii, and A. A. Sirenko, Rev. Sci. Instrum. **84**, 023901 (2013).

152. D. Gouéré, H. Merbouche, A. El Kanj, F. Kohl, C. Carrétéro, I. Boventer, R. Lebrun, P. Bortolotti, V. Cros, J. Ben Youssef, and A. Anane, Phys. Rev. Mater. **6**, 1 (2022).

153. G. F. Dionne, J. Appl. Phys. **41**, 4874 (1970).

154. B. Dong, Y. Cui, H. Yang, L. Yu, W. Jin, and S. Feng, Mater. Lett. **60**, 2094 (2006).

155. Z. Fu and J. Ferguson, J. Am. Ceram. Soc. **105**, 6175 (2022).

156. Y. Wang, J. Duan, X. Yang, L. Liu, L. Zhao, and Q. Tang, Nano Energy **69**, 104418 (2020).

157. Y. Kalpaklı, Inorg. Chem. Commun. **159**, 111788 (2024).

158. A. M. Abdeen, O. M. Hemeda, E. E. Assem, and M. M. El-Sehly, J. Magn. Magn. Mater. **238**, 75 (2002).

भारतीय प्रौद्योगिकी संस्थान गुवाहाटी • Indian Institute of Technology Guwahati •

I. List of publications from the present work

(a) International journals from thesis work

1. **Shalini Verma and S. Ravi**

   Analysis of negative magnetization and dielectric studies in holmium substituted samarium iron garnet

   Solid State Sciences 139 (2023) 107189.

2. **Shalini Verma and S. Ravi**

   Phenomenological investigation of structural, magnetic, and dielectric properties of holmium substituted gadolinium iron garnet

   Journal of Material Science: Material in Electronics 34 (2023) 1011.

3. **Shalini Verma and S. Ravi**

   Investigation of magnetocaloric effect in Holmium substituted Dysprosium iron garnet for magnetic refrigeration applications

   Journal of Magnetism and Magnetic Materials 589 (2024) 171512.

4. **Shalini Verma and S. Ravi**

   Structural, Magnetic and Impedance Dynamics of Multiferroic High Entropy Garnet Ceramics

   Ceramics International 50 (2024) 35449-35456.

5. **Shalini Verma and S. Ravi**

   Tailoring structural, magnetic and magneto-dielectric features of $(Gd_{1-x}Nd_x)_3Fe_5O_{12}$ $(x = 0.0 - 0.4)$ garnet ceramics

   Journal of Applied Physics 137 (2025).

(b) International journals outside thesis work

6. **Shalini Verma and S. Ravi**

   Altering the magnetic and dielectric responses of polycrystalline Gadolinium iron garnet by Al substitution

   Ceramics International 50 (2024) 13022-13033.

7. **Shalini Verma and S. Ravi**

   Insights into crystal structure, temperature-dependent magnetization and dielectric relaxation mechanism in Bi substituted Samarium iron garnet

   Solid State Sciences 154 (2024) 107629.

8. **Shalini Verma and S. Ravi**

   Cr Induced Modifications in $Dy_3Fe_5O_{12}$: Structural, Magnetic, and Electrical Perspectives

   Journal of Material Science: Material in Electronics 35 (2024) 1937.

9. **Junmoni Barman, Shalini Verma and S. Ravi**

   Exploring the Structural, Magnetic, and Dielectric Properties of Fe^{3+} and rare earth Y^{3+} ion substituted $NiCr_2O_4$

   Journal of Alloys and Compounds 1003 (2024) 175680.

II. Conferences/Workshops attended

1. **Symposium on Magnetism and Spintronics (SMS)** held at NISER Bhuvneshwar, India on 25-27 November 2021: Tuning of Electrical and Magnetic properties of $Sm_{3-x}Ho_xFe_5O_{12}$ $(x = 0.0, 0.2, 0.5)$ (Poster presentation).
2. International Conference on "**Magnetism and Magnetic Materials (MMM)**" held at Minneapolis, United States on 31st October to 4th November, 2022: Tailoring the Magnetic and Electrical properties of Holmium Substituted Samarium Iron Garnet (Poster presentation).
3. **Research and Industrial Conclave (RIC)** held at IIT Indore, India on 20-22 January, 2023: Structural and Magnetic property measurement of Dysprosium Iron Garnet by Cr substitution (Oral presentation).
4. **Research and Industrial Conclave (RIC)** held at IIT Guwahati, India on 14-16 May, 2023: Effect of Al substitution on magnetic and dielectric properties of polycrystalline Gadolinium iron garnet (Poster presentation).
5. **International Conference on Emerging Trends in Magnetism and Magnetic Materials (ICETMM)** held at HBTU Kanpur, India on 6-8 July, 2023: Examination of negative magnetization and multiferroic property of $Ho_{1.2}R_{1.8}Fe_5O_{12}$ $(R = Sm,\ Gd$ and $Dy)$ samples (Oral presentation).
6. **International Conference on Magnetic Materials and Applications (ICMAGMA)** held at Ramoji Film City, Hyderabad, India on 3-5 December, 2023: Study of magnetocaloric effect in $Dy_{1-x}Ho_xFe_5O_{12}$ $(x = 0.4, 0.8)$ (Poster presentation).
7. **International Conference on Nonlinear Dynamics and Applications (ICNDA)** held at SMIT, Sikkim, India on 21-23 February, 2024: Study of Spin reorientation

and dielectric phenomenon in $Sm_{3-x}Bi_xFe_5O_{12}$ $(x = 0.0 - 0.6)$ samples (Conference proceedings).

8. **IEEE International Magnetics Conference (INTERMAG)** held at Rio de Janeiro, Brazil on 5-10 May, 2024: Investigation of Structural, Magnetic and Complex Impedance Studies of High Entropy Garnet Ceramics (Poster presentation).
9. **7th Annual conference on Quantum Condensed Mater (QMAT)** held at IIT Guwahati, India on 20-23, December, 2024: Investigation of Structural, Magnetic, and Dielectric Behavior in Nd-Doped $Gd_3Fe_5O_{12}$ Samples (Oral presentation).
10. **International Conference on Superconductivity and Magnetism (ICSM)** held at Liberty Lykia, Fethiye-Olüdeniz, Mügla, Türkey on 26 April-3 may, 2025: Tuning Garnet Properties: The Role of Cr Substitution in $Sm_3Fe_5O_{12}$ (Conference proceedings).
11. National workshop on **Hands-on training on characterization tools and techniques for material science** held at NIT Meghalaya, India on 8-14 November, 2022.
12. National workshop on **Neutron Scattering (Elastic and Inelastic) and Muon Spectroscopy** held at IIT Guwahati, India on 16-17 February, 2024.

Indian Institute of Technology Guwahati